SAND2016-9297R

Used Fuel Disposition in Crystalline Rocks: FY16 Progress Report

Fuel Cycle Research & Development

Prepared for
U.S. Department of Energy
Used Fuel Disposition
Y. Wang, T. Hadgu, E. A. Kalinina
Sandia National Laboratories
J. Jerden, J. M. Copple, T. Cruse, W. Ebert
Argonne national laboratory
E. Buck, R. Eittman
Pacific Northwest National Laboratory
R. Tinnacher, C. Tournassat, J. Davis
Lawrence Berkeley National Laboratory
H. Viswanathan, S. Chu, T. Dittrich, F. Hyman, S. Karra, N. Makedonska, P. Reimus
Los Alamos National Laboratory
M. Zavarin, C. Joseph
Lawrence Livermore National Laboratory
September 21, 2016
FCRD-UFD-2016-000076
SAND2016-9297R

Sandia National Laboratories is a multi-program laboratory managed and operated by Sandia Corporation, a wholly owned subsidiary of Lockheed Martin Corporation, for the U.S. Department of Energy's National Nuclear Security Administration under contract DE-AC04-94AL85000.

USED FUEL DISPOSITION IN CRYSTALLINE ROCKS: FY16 PROGRESS REPORT

EXECUTIVE SUMMARY

The U.S. Department of Energy Office of Nuclear Energy, Office of Fuel Cycle Technology established the Used Fuel Disposition Campaign (UFDC) in fiscal year 2010 (FY10) to conduct the research and development (R&D) activities related to storage, transportation and disposal of used nuclear fuel and high level nuclear waste. The Mission of the UFDC is

> *To identify alternatives and conduct scientific research and technology development to enable storage, transportation and disposal of used nuclear fuel and wastes generated by existing and future nuclear fuel cycles*.

The work package of Crystalline Disposal R&D directly supports the following UFDC objectives:

- Develop a fundamental understanding of disposal system performance in a range of environments for potential wastes that could arise from future nuclear fuel cycle alternatives through theory, simulation, testing, and experimentation.
- Develop a computational modeling capability for the performance of storage and disposal options for a range of fuel cycle alternatives, evolving from generic models to more robust models of performance assessment.

The objective of the Crystalline Disposal R&D Work Package is to advance our understanding of long-term disposal of used fuel in crystalline rocks and to develop necessary experimental and computational capabilities to evaluate various disposal concepts in such media.

FY16 continued to be a successful year in both experimental and modeling arenas in evaluation of used fuel disposal in crystalline rocks. The work covers a wide range of research topics identified in the R&D plan. The major accomplishments are summarized below:

- *Development of Fuel Matrix Degradation Model (FMDM):* We have formulated, coded and tested an electrochemical steel corrosion module that couples in-package steel corrosion with fuel degradation through the common solution. This module provides the kinetic source of H_2 that may control the used fuel dissolution rates under repository relevant conditions. We have updated and optimized FMDM to improve the efficiency of integration with the GDSA PA model. We have also performed scoping electrochemical tests to build confidence in modeling the H_2 effect mechanism, which has been shown by both experiment and electrochemical modeling to significantly impact source term calculations when in-package steel components are corroding simultaneously with used fuel. It has been shown that the corrosion of steel canister materials will have a significant impact on the radionuclide source terms calculated by PA because of its role as the major source of the H_2, which attenuates the fuel degradation rate. The test runs with the updated FMDM indicate that the peak radionuclide source term from a breached waste package will likely be attenuated by the H_2 effect and the corrosion of steel components (the dominant source of H_2 in the system). In addition, we have shown a potential effect of ferrous iron from waste package corrosion on hydrogen peroxide generation.
- *Uranium Interaction with Engineered Materials:* We developed a new surface complexation model (SCM) that specifically accounts for the 'spillover' of the electrostatic surface potential of basal cation exchange sites on the surface potential of neighboring edge sites. This model allows

us to simulate U(VI) adsorption onto Na-montmorillonite over a wide range of chemical solution conditions with a lower number of fitting parameters than previous SCM concepts, and without including a second site type or the formation of ternary U(VI)-carbonato surface complexes. This SCM allows us to simulate U(VI) sorption onto montmorillonite as a function of chemical solution conditions, while minimizing the number of fitting parameters in subsequent uranium(VI) diffusion models. Modeling results suggest that an accurate description of the unique characteristics of electrostatic surface potentials on montmorillonite edge sites is highly important, in order to accurately predict U(VI) sorption and transport behavior at larger field scales. Similar modeling approaches may also be useful for other charge-unbalanced, layered mineral phases. Our modeling results further emphasize the strong influence of dissolved carbonate ligands on U(VI) sorption, which is driven by the competition between U(VI)-carbonate complexation reactions in solution and U(VI) surface complexation reactions on montmorillonite edge sites.

- *Colloid-Facilitated Radionuclide Transport:* A comprehensive literature review and data synthesis has been conducted on colloid-facilitated radionuclide transport (CFRT), and a scheme for the implementation of the CFRT model in performance assessment has been proposed (the results are reported in a separated report). A comprehensive model interpretation has been performed for the Grimsel Test Site (GTS) CFRT tests, yielding valuable insights for modeling of radionuclide transport, and particularly of CFRT, in saturated fractured crystalline rocks. It is shown that the actinides Th, Pu and Am, and the fission product ^{137}Cs, are the most likely radionuclides to experience colloid-facilitated transport over long time and distance scales (at least for bentonite colloids in a fractured crystalline setting). However, the time and distance scales of the GTS tests were very short relative to time and distance scales of relevance for nuclear waste repository performance assessments, so it should not necessarily be concluded that colloid-facilitated transport of these radionuclides will be a concern in such performance assessments. The GTS results collectively suggest that CFRT is likely to be more efficient at lower radionuclide concentrations than at higher concentrations because a greater fraction of the radionuclide mass will then tend to become associated with strong, low abundance adsorption sites on the colloids.
- D*evelopment and demonstration of Discrete Fracture Network (DFN) model:* We have evaluated the correlation between fracture size and fracture transmissivity. We have characterized how different fracture size-transmissivity relationships influence flow and transport simulations through sparse three- dimensional discrete fracture networks, based on Forsmark fracture characteristics provided by SKB. We observe that adopting a correlation between a fracture size and its transmissivity leads to earlier breakthrough times and higher effective permeability when compared to networks where no correlation is used. While fracture network geometry plays the principal role in determining where transport occurs within the network, the relationship between size and transmissivity controls the flow speed. These observations indicate DFN modelers should be aware that breakthrough times and effective permeabilities can be strongly influenced by such a relationship in addition to fracture and network statistics. We have developed an analysis and visualization tool for the characterization of flow in constrained networks using the concept of a flow topology graph (FTG). Our method allows users to understand and evaluate flow and transport in DFN simulations by computing statistical distributions, segment paths of interest, and cluster particles based on their paths. The new approach enables to evaluate the accuracy of the simulations, visualize features of interest, and compare multiple realizations over a specific domain of interest. It allows to simulate complex transport phenomena modeling large sites for networks consisting of several thousand fractures without compromising the geometry of the network.
- *Comparison of Fracture Continuum Model (FCM) with DFN model:* Both the DFN and FCM fracture models can be used to characterize fractures in crystalline rock. DFN is based on flow and transport in fractures only. FCM is based on both matrix and fracture flow and transport.

Comparison of the two models required significant upgrades in the FCM codes. As part of the comparison the FCM codes were modified to include two fracture generating methods that are close to the DFN model. The first method uses representation of fractures with ellipses to generate fracture network. The second method uses the fracture network generated by DFN. For the second case the properties of the DFN fracture network are converted into the FCM inputs (fracture aperture, spacing, dip, and strike), which are then used to calculate the effective permeability and porosity of the FCM grid blocks. DFN and FCM comparison was made on a domain size of 1 km^3 and common fracture data. The property of the fracture data used for the comparison study are loosely based on the property of the SKB site in Sweden. Results of the two fracture models are similar when the modified FCM methods are used. Results are largely different when the original FCM method is used with matrix diffusion included. It is shown that the rock matrix can play a role in advection as well as in diffusion. The validity of that can be tested using simulations with the use of measured field data. Recommendations for future work are further testing of the fracture models using field data and analysis of numerical dispersion. Two groups of 25 realizations were generated to check statistical stability of the sample size of fracture networks. The effective permeability values calculated for the two groups showed that only two realizations from the first group and four realizations from the second group had effective permeability values above matrix permeability. This indicates that without the manipulation of each realization to create fracture connectivity and use of more realistic matrix permeability, the chances of fracture connectivity are low (12%) and therefore the sample size of 25 may not be large enough to generate meaningful statistics for fracture networks. It anticipated that a relatively large number of realizations might be required for a performance assessment of a crystalline rock geologic repository.

Based on the work accomplished in FY16 and the prior years, the future work is recommended to:

- Continue to focus on two key topics related to deep geologic disposal of spent fuel in crystalline rocks: better characterization and understanding of fractured media and fluid flow and transport in such media, and designing effective engineered barrier systems (EBS) for waste isolation. Specific attention will be given to the development of next-generation buffer materials for waste isolation and to a mechanistic understanding of alteration products (e.g. iron oxides) of EBS components as secondary waste forms for radionuclide retention.
- Help the generic disposal system analysis (GDSA) team to develop a total system performance assessment model and provide the parameter feeds to the model. One goal of this effort is to have a PA model matured enough over next two years to be able to simulate a typical thermal-hydrologic-chemical evolution history of a repository in a crystalline medium. Once such as a model becomes available, various disposal concepts will be explored.
- Continue to synthesize technical results obtained in FY17 and prior years in a few selected areas to demonstrate tangible progress in the research. The focus areas will include thermal limits of bentonite and smectite illitization and modeling approaches of fluid flow and transport in fractured geologic media.
- The modeling work will move towards model demonstrations and applications using actual field data. For the process model development, an emphasis will be placed on the integration with total system model development.
- Fully leverage international collaborations, especially with Sweden Underground Research Lab and DECOVALEX.
- Closely collaborate and integrate with other work packages, especially those on disposal in argillite, deep borehole disposal, and DOE-managed high-level waste (HLW) and spent nuclear fuel (SNF) Research.

CONTENTS

1. GOALS AND OUTLINE

The U.S. Department of Energy Office of Nuclear Energy, Office of Fuel Cycle Technology established the Used Fuel Disposition Campaign (UFDC) in fiscal year 2010 (FY10) to conduct the research and development (R&D) activities related to storage, transportation and disposal of used nuclear fuel and high level nuclear waste. The Mission of the UFDC is

> *To identify alternatives and conduct scientific research and technology development to enable storage, transportation and disposal of used nuclear fuel and wastes generated by existing and future nuclear fuel cycles*.

The work package of Crystalline Disposal R&D directly supports the following UFDC objectives:

- Develop a fundamental understanding of disposal system performance in a range of environments for potential wastes that could arise from future nuclear fuel cycle alternatives through theory, simulation, testing, and experimentation.
- Develop a computational modeling capability for the performance of storage and disposal options for a range of fuel cycle alternatives, evolving from generic models to more robust models of performance assessment.

The objective of the Crystalline Disposal R&D Work Package is to advance our understanding of long-term disposal of used fuel in crystalline rocks and to develop necessary experimental and computational capabilities to evaluate various disposal concepts in such media. FY16 work is aligned with the following considerations and project goals:

- Focus on two key topics related to deep geologic disposal of used fuel in crystalline rocks: (1) better characterization and understanding of fractured media and fluid flow and transport in such media, and (2) designing effective engineered barrier systems (EBS) for waste isolation. Specific attention will be given to the development of scientifically sound thermal limits for various buffer materials.
- Assist the generic disposal system analysis control account to develop a total system performance assessment model and provide the parameter feeds to the model.
- Various disposal concepts will be explored as the total system performance assessment model becomes available, for example, for the concept of borehole disposal vs. drift emplacement, regular waste packages vs. dual purpose canisters (DPCs).
- Start to synthesize technical results obtained in FY16 and prior years in a few selected areas, for example, colloid formation and colloid facilitated transport, to demonstrate tangible progress in the research.
- The modeling work will move towards model demonstrations and applications using actual field data. For the process model development, an emphasis will be placed on the integration with total system model development.
- Fully leverage international collaborations, especially with Korea Atomic Research Institute (KAERI) and Sweden Underground Research Lab and DECOVALEX (especially the next phase of the program).
- Closely collaborate with other work packages, especially those on disposal in argillite, deep borehole disposal, and DOE-managed high-level waste (HLW) and spent nuclear fuel (SNF) research.

The FY 16 work for the Crystalline Disposal R&D Work Package is structured into the following tasks:

- Task 1: (SNL, LANL) Support to develop of a total system performance assessment model for crystalline media. This activity will help the GDSA work package to develop the first version of the PA model for crystalline rocks by providing conceptual and mathematical models as well as model input parameters.

- Task 2: (ANL, PNNL) Development of used fuel degradation and waste package degradation model: This task will continue the development of the fuel degradation model and initiate the waste package degradation model. Due to the budget constraint, this activity will be jointed with the similar effort for the argillite work package.
- Task 3: (LANL, LLNL, SNL) Synthesis of colloid formation and transport-related work: LANL will focus on colloid transport; LLNL will focus on colloid stability; and SNL will focus on the implication of nanogeochemistry to colloid stability and radionuclide transport. The work will be documented in a level 3 milestone report (led by LANL).
- Task 4: (LANL, SNL) Modeling of fluid flow and transport in fractured crystalline rocks: The task will continue to demonstrate the potential application of the discrete fracture network model and the fracture continuum model to actual field testing data obtained from international collaborations. Develop a strategy to integrate these types of process models into a total system performance assessment model.
- Task 5: (LANL, LLNL, SNL, LBNL) Experimental investigation of radionuclide interactions with natural and engineered materials: Continue the work on actinide sorption and diffusion in clays and in granitic materials, with an aim to a comprehensive process model for total system performance assessment and to maintain certain levels of experimental activities.
- Task 6: (SNL) Investigation of thermal limits of clay materials: Start systematical measurements swelling and cation exchange capacities for clays subjected to various thermal treatments. This work may also coordinate with hydrothermal experiments at LANL for the argillite work package.
- Task 7: (LANL, LLNL, SNL, LBNL) International collaborations: International collaborations are crucial for the activities proposed for this work package. These collaborations will include: KURT tests, SKB-BRIE tests, DECOVALEX, Mont Terri and FEBX-DP tests.
- Task 8: (PNNL) Radiolysis Modeling. Activities in this control account will support evaluation of long-term degradation rates for uranium oxide used nuclear fuels in chemically reducing geologic disposal environments

This report summarizes work accomplished in FY16 for the Crystalline Disposal R&D Work Package. The report is outlined as follows:

- Chapter 2 documents the development and implementation the Fuel Matrix Degradation Model (FMDM). The work documented is a jointed effort between the Crystalline Work Package and the Argillite Work Package. (Research topics addressed: S2, S3 and P19; see Wang et al., 2014)
- Chapter 3 focuses a preliminary analysis on a potential effect of ferrous iron on hydrogen peroxide generation. (S2, S3, and P19).
- Chapter 4 summarizes an investigation of uranium interaction with bentonite. (P10)
- Chapters 5 and 6 provide a summary of colloid facilitated radionuclide transport and Np diffusion in compacted bentonite materials (P10 and P11)
- Chapter 7 presents the work on the development and demonstration of Discrete Fracture Network (DFN) model. (P1)
- Chapter 8 provides a comparison between two modeling approaches for flow and transport in fractured crystalline rocks: DFN model and Fracture Continuum Model (FCM). (P1, P8 and P9)
- Chapter 9 provides an overall summary of FY16 accomplishment in Crystalline Work Package.

Wang Y. et al., (2014) *Used Fuel Disposal in Crystalline Rocks: Status and FY14 Progress*, FCRD-UFD-2014-000060, SAND2014, Sandia National Laboratories, Albuquerque, NM.

2. FUEL MATRIX DEGRADATION MODEL: CANISTER CORROSION AND THE EFFECT OF HYDROGEN ON USED FUEL DEGRADATION RATES

2.1 INTRODUCTION

Scientifically-based predictive models of waste form corrosion rates will provide reliable radionuclide source terms for use in repository performance assessments. Furthermore, demonstrating that there is a fundamentals-based, scientific basis for the waste form degradation process models is a key aspect for building confidence in the long-term calculations used for the repository safety case. The objective of the work documented in this section is to develop and implement a fundamentals-based process model for the degradation rate of used fuel that can be readily incorporated into the Generic Disposal System Analyses (GDSA) Performance Assessment (PA) code to provide radionuclide source terms throughout the service life of a disposal system. This model, referred to as the Fuel Matrix Degradation Model (FMDM), is based on the Canadian Mixed Potential Model (King and Kolar, 2003), but has been expanded and customized for application in the ongoing UFD Argillite and Crystalline rock disposal projects. The conceptual context for the FMDM within the generic performance assessment model is shown in Figure 2-1.

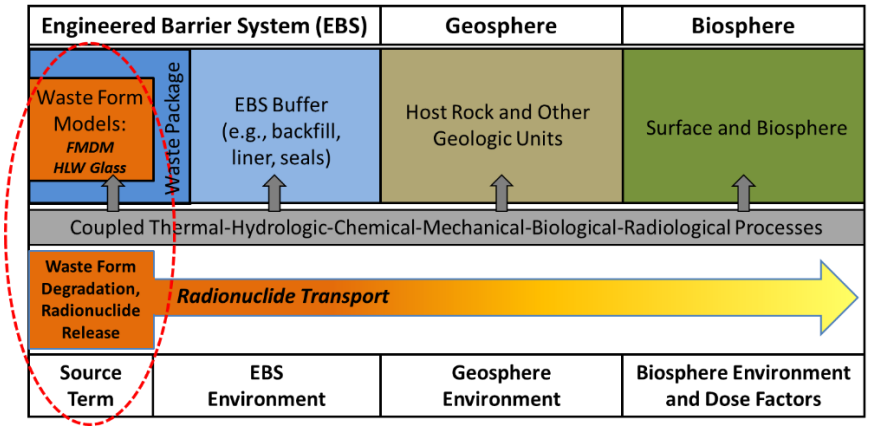

Figure 2-1. Conceptual diagram showing the context for the FMDM. Adapted from Mariner et al., 2015.

The continued development and implementation of the FMDM addresses two high level Features, Events, and Processes (FEPs) that are recognized as high R&D priorities for the UFD (Wang et al., 2014). The FEPs addressed by this model are 2.1.02 (waste form) and 2.1.03 (waste container), which correspond to the high priority research topics P19 (Development of waste form degradation model) and P20 (Development of new waste package concepts and models for evaluation of waste package performance for long-term disposal) identified by Wang et al., 2014.

The FMDM calculates the dissolution rate of used fuel as a function of the interfacial corrosion potential (E_{corr}) that is determined by the kinetic balance between all of the anodic and cathodic half reactions occurring at the fuel/solution boundary. The dissolution rate is relatively high under oxidizing conditions (high E_{corr}) but decreases dramatically at E_{corr} values lower than the U(IV)/U(VI) threshold potential, where only solubility-based chemical dissolution occurs. The FMDM accounts for:

- the generation of radiolytic oxidants as a function of fuel burn-up,
- the catalyzed oxidation of H_2, which protects the fuel from oxidative dissolution,

- the precipitation of secondary phases,
- the complexation of uranyl by carbonate,
- the oxidation of ferrous iron,
- temperature variations (by Arrhenius equations),
- the one-dimensional diffusion of all chemical species,
- the anoxic corrosion of steel components within a breached waste package to provide the flux of H_2 and ferrous iron, which, as discussed below, dominate fuel degradation process (*added and tested in FY-2016*).

Of these processes, the catalysis of H_2 oxidation on Nobel Metal Particles (NMP) on the fuel surface and the generation rate of radiolytic oxidants (determined by dose rate, which is related to fuel burn-up) are the most important for determining the degradation rate of the fuel (Jerden et al., 2015). Since the flux of H_2 to the fuel is determined by the anoxic corrosion rate of steel waste package components (e.g., Shoesmith, 2008), steel corrosion kinetics were added to the FMDM in FY-2016. The new electrochemical steel corrosion module is discussed in Section 2-2.

Specifically, the fuel degradation rate calculated by the FMDM accounts for oxidation of the fuel by radiolytic H_2O_2 (and its decomposition product O_2), the concentration of which is calculated using an analytical form of the radiolysis model developed at Pacific Northwest National laboratory (PNNL) (Buck et al., 2014), and the burn-up/dose rate function described in Section 2-4. Fuel oxidation is counteracted by the catalytic oxidation of H_2 on NMP sites that are present on the fuel surface as a distinct phase.

It was shown in Jerden et al., 2015 that the FMDM accurately reproduces the experimental observation that relatively low concentrations of dissolved H_2 (~0.1mM) can inhibit the oxidative dissolution of the fuel. In the absence of oxidative dissolution, the fuel degrades by solubility based, chemical dissolution, which is over 4 orders of magnitude slower than oxidative dissolution (Röllin et al., 2001).

The present study, which focuses on the degradation behavior of uranium oxide used fuel, shows that interactions between the seepage water contacting the fuel and engineered barrier materials should be accounted for in waste form degradation models. As discussed in this secion, it is particularly important to account for chemical interactions between the corroding used fuel and steel waste package components that occur through a common solution.

Figure 2-2 is a conceptual diagram showing the key interfacial and bulk solution reactions included in the new version of the FMDM (FMDM Version 3) as well as other important source term processes that are not yet included, but may play a key role in radionuclide release and transport (shown in dark red on Figure 2-2).

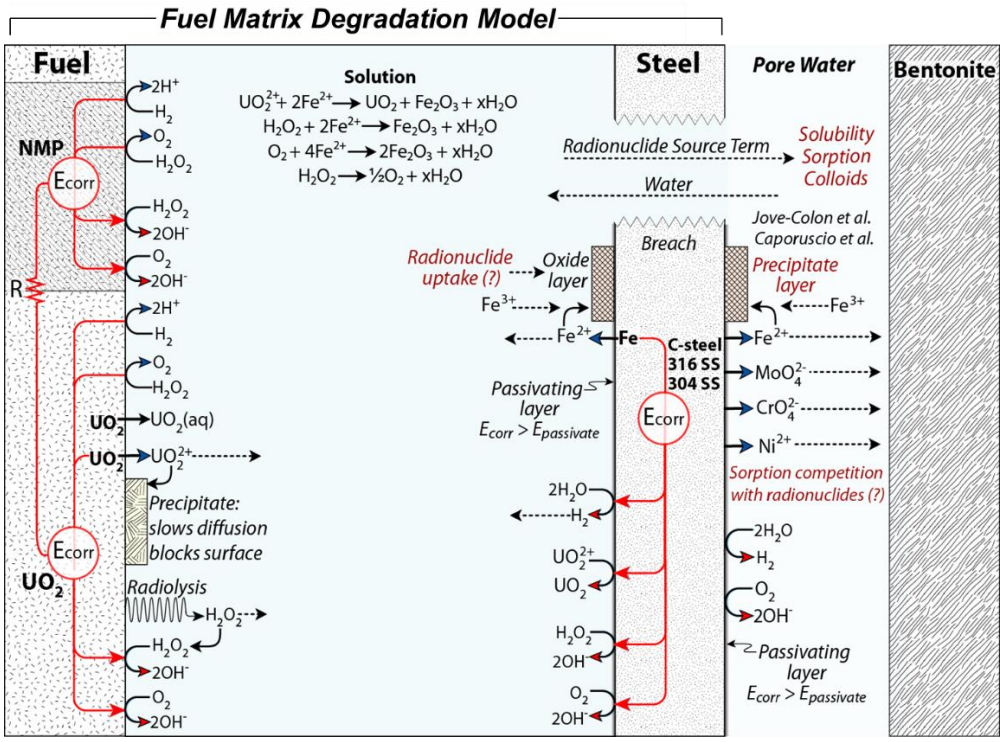

Figure 3-2. Conceptual diagram showing the context for the FMDM. Adapted from Mariner, P., Gardner, P., Hammond, G, Sevougian, D, Stein E., 2015, Application of Generic Disposal System Models, FCRD-UFD-2015-000126, SAND2015-10037, September 22, 2015, 209pp.

2.2 FY-2016 EXTENTION OF THE FUEL MATRIX DEGREDATION MODEL: ELECTROCHEMICAL STEEL CORROSION MODULE

Quantification of the long-term corrosion behavior of steels in relevant environmental conditions is central to developing a scientifically sound performance assessment model for nuclear waste repositories. As shown in Figure 2-3, the used fuel assemblies will be surrounded by and in close contact with steel components within the waste package and disposal canister.

Within a breached canister groundwater will infiltrate open spaces within the canister and begin to corrode steel components (Figure 2-4). This will set up a reaction front that will eventually contact the fuel rods. The steel will corrode and produce H_2 even if the infiltrating groundwater is reducing. This is because the stability field of carbon steels and stainless steels lie below the stability field of water on an Eh vs. pH diagram (Figure 2-5). Therefore, as shown in both Figure 2-5a and Figure 2-6 (steel surface), metallic iron can be oxidized to Fe^{2+} by the reduction of water to $H_2 + 2OH^-$. Assuming that the Zircaloy cladding has failed, the fuel will begin degrading by either relatively rapid oxidative dissolution or by relatively slow chemical dissolution. The dominant dissolution mechanism will be determined by the surface potential established by the solution contacting the fuel surface.

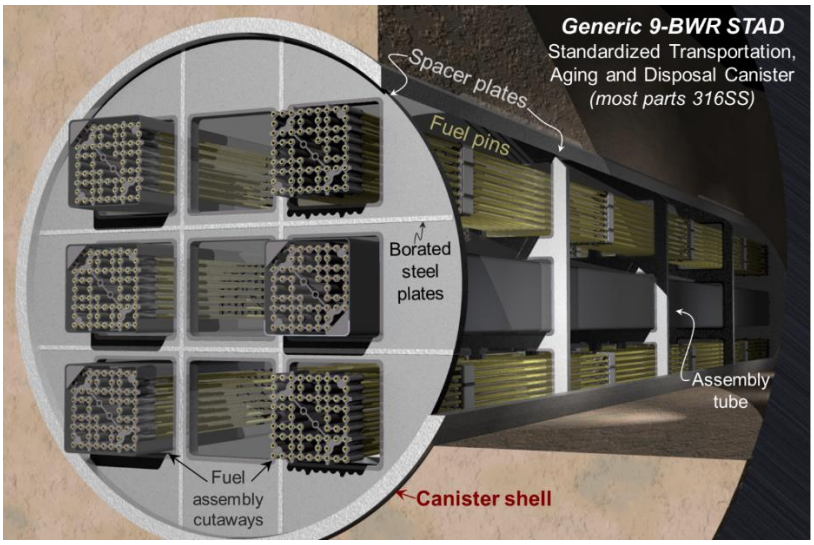

Figure 2-3. Conceptual diagram showing a generic BWR waste package.

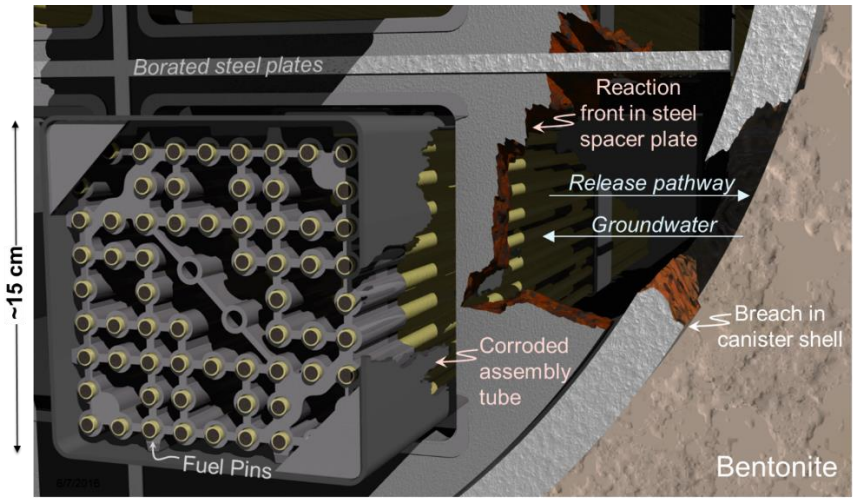

Figure 2-4. Conceptual diagram summarizing the key processes involved in radionucide release from a breached used fuel waste package. Following a breach groundwater will oxidize steel components and eventually reach fuel rods. The key thing to note is that the used fuel will degrade simultaneously with a number of different types of steels. The interactions between the steel corrosion reaction products H_2 and Fe^{2+} have been shown experimentally strongly effect the rate of fuel degradation (e.g., Shoesmith, 2008, Grambow, et al., 2010).

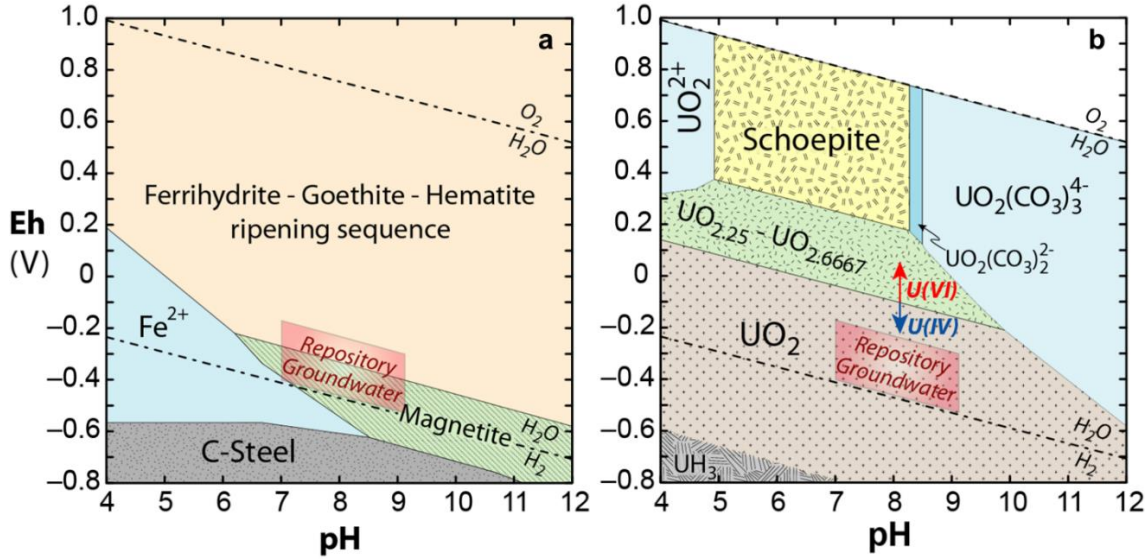

Figure 2-5. Eh – pH diagrams showing the conditions expected for groundwaters in a reducing crystalline rock or argillite repository (from Laaksoharju, et al., 2008). Figure 2-5a was drawn for $1x10^{-3}$ molar iron and the 5b was drawn for $1x10^{-6}$ molar uranium with $1x10^{-4}$ molar carbonate.

The rate of fuel degradation will ultimately be determined by the kinetic balance of five processes:

- rate of radiolytic oxidant production (determined by dose rate, which is determined by fuel burn up and age)
- rate of radiolytic oxidant reduction on fuel surface (cathodic reactions on fuel surface)
- rate of U(IV) → U(VI) oxidation (anodic reactions on fuel surface)
- rate of H_2 production by steel corrosion and H_2 flux to the NMP sites on the fuel surface
- rate of the oxidation of H_2 on the NMP catalytic sites (anodic reaction on fuel surface that anodically "protect" UO_2 from oxidation)

These processes are shown conceptually in Figure 6, which summarizes the reaction scheme for the FMDM.

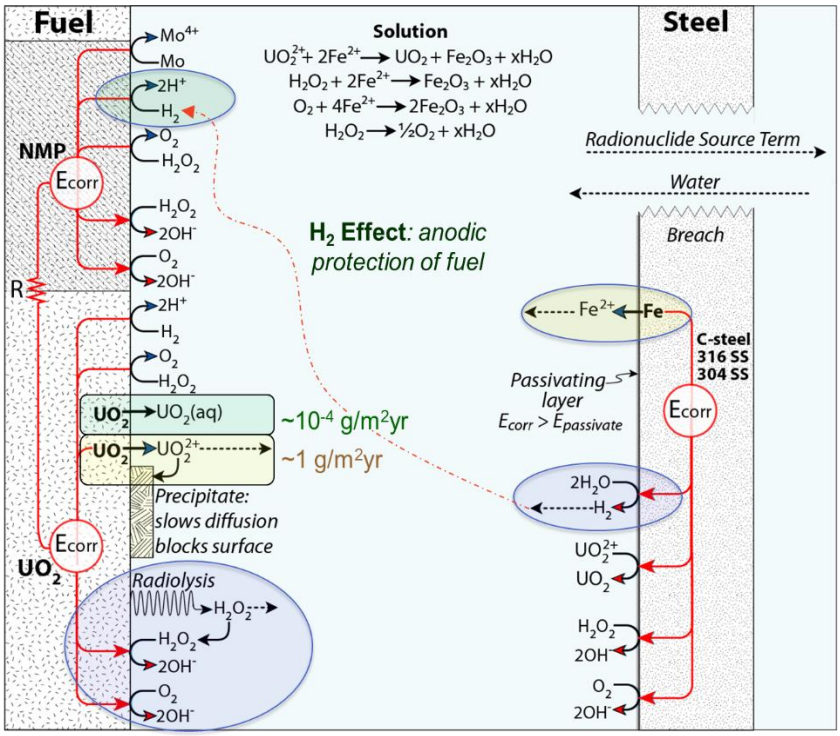

Figure 2-6. Schematic diagram showing the reaction scheme for the FMDM. The key processes in the model are highlighted in yellow (key anodic reactions), blue (key cathodic reactions) and green (the H_2 effect that can provide anodic protection of the UO_2 matrix from oxidative dissolution).

The mixed potential theory on which the FMDM is based Model (King and Kolar, 2003) is also ideal for quantifying steel corrosion because it accounts for the fundamental interfacial electrochemical reactions and couples those reactions with bulk solution chemistry. Therefore, as part of our FY-2016 work, we formulated, coded, and tested a relatively simple mixed potential model for steel corrosion and then added that model to the FMDM as a new module. The interfaces between the modules is presented in Figure 2-7.

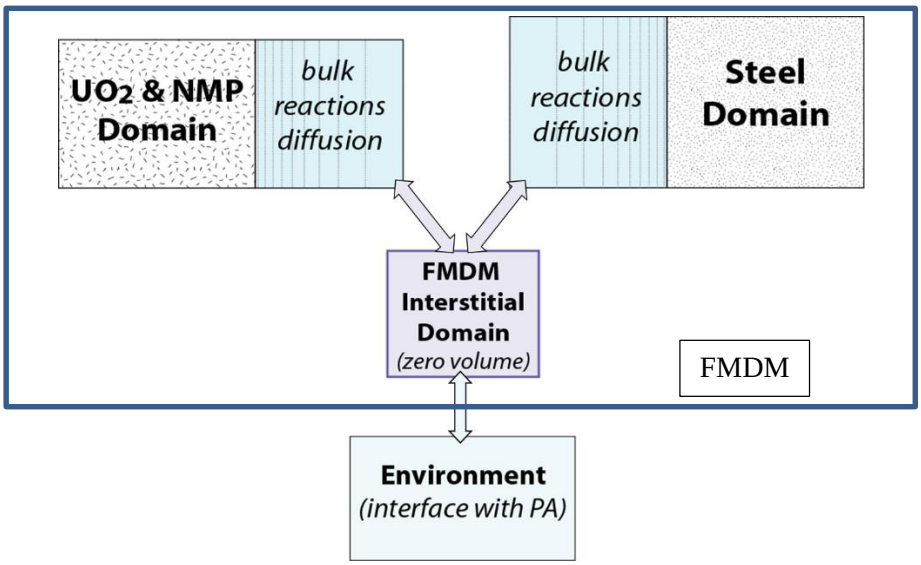

Figure 2-7. Schematic diagram showing the logic for how the steel surface was added to the FMDM.

There are several advantages to the approach of incorporating a separate steel corrosion module directly into the FMDM as shown in Figure 2-7:

- It directly couples fuel degradation and steel corrosion. This is vital, as it has been shown that, even at sub millimolar concentrations, the H_2 produced from the anoxic corrosion of steel can decrease the fuel dissolution rate by over four orders of magnitude (Jerden et al., 2015).
- Directly coupling the fuel and steel degradation allows for the quantification of redox fronts that develop within the waste container due to the diffusion of radiolytic oxidants away from the fuel surface and the reactions of these oxidants with the steel surface and the resulting aqueous Fe^{2+} and H_2. This is also important because these redox fronts represent the Eh of the in-package solutions contacting the waste form and waste container internal components.
- This approach will allow the steel corrosion module to be readily implemented into the GDSA PA PFLOTRAN model, as it will be incorporated into the FMDM, a version of which has already been integrated with PA.

As shown in Figure 2-7 the steel environment (steel surface plus bulk solution) are coupled to the fuel environment through a zero-volume interstitial domain, which can exchange mass fluxes with the fuel environment, the steel environment and the groundwater chemistry within the engineered barrier system adjacent to the waste package.

Table 2-1. Summary of FMDM parameters and data gaps that need to be addressed in future work to improve the accuracy of the model.

Parameter	Description	Data needs to improve accuracy
Dimension of fuel environment	(mm – cm)	To be updated when dimensions of waste package are known
Nodes in fuel environment	(log-space grid: fine-spacing near surface)	To be updated when dimensions of waste package are known
Fuel surface coverage by NMP	(~1%)	From literature
Dimension of steel environment	(mm – cm)	To be updated when dimensions of waste package are known
Nodes in steel environment	(log-space grid: fine-spacing near surface)	To be updated when dimensions of waste package are known
Number of FMDM time steps	(100 – 1000)	Use to optimize PA interface
Fuel alteration layer porosity	(~50%)	From literature
Fuel alteration layer tortuosity	(~0.01)	From literature
Fuel alteration layer radiolysis factor	(*not used*)	*Could be activated to account for radionuclide uptake by U secondary phases*
Alpha particle penetration depth	(35μm)	From literature
Fuel burnup	(25 – 75 GWd/MTU)	Input from PA
Age of fuel (time out of reactor)	30 – 100 yrs	Input from PA
Resistance between fuel and NMP domains	(10^{-3} Volts/Amp)	Interpretation of literature
Temperature history	function	Data need: needs to be input from PA – will depend on repository scenario
Dose rate history	function	Based on MCNPX results of Radulescu, 2011
Spatial dose rate	function (decrease in dose rate with distance from fuel)	Based on MCNPX results of Radulescu, 2011
Rate constants for interfacial reactions in fuel and steel domains	See Figure 6 for summary of specific reactions	Data need: experiments needed due to lacking or inconsistent data in current literature on H_2 reactions on fuel and NMP and steel corrosion under relevant conditions
Charge transfer coefficients for interfacial half-cell reactions in fuel and steel domains	See Figure 6 for summary of specific reactions	Data need: experiments needed due to lacking or inconsistent data in current literature on H_2 reactions on fuel and NMP
Activation energys	T dependence: See Figure 6 for summary of specific reactions	Data need: experiments needed due to lacking or inconsistent data in current literature on H_2 reactions on fuel and NMP and steel corrosion under relevant conditions

Table 2-1. Continued.

Parameter	Description	Data needs to improve accuracy
Standard potentials for interfacial half-cell reactions: fuel and steel	See Fig. 6 for reactions	From literature
Relative area of fuel domain	Default 1:1, depends on waste package design	To be updated when dimensions of waste package are known
Relative area of steel domain	Default 1:1, depends on waste package design	To be updated when dimensions of waste package are known
Environmental leak rate (diffusion barrier factor)	Depends on waste package design, breach	Interpretation of literature
Environmental concentrations	(O_2, H_2, CO_3^{2-}, Fe^{2+})	Input from PA
Rate constants for bulk solution reactions in fuel, steel environments	See Figure 6 for summary of specific reactions	From literature
Activation energy for bulk solution reactions	T dependence, See Figure 6 for reactions	From literature
Passivation potential of steel surface	(85 V_{SCE}) as place-holder	Data need: experiments needed due to lacking or inconsistent data in current literature
Passivation corrosion current density	Calculated internally within FMDM	Function derived from literature
Radiolytic oxidant (H_2O_2) generation value (G_{cond})	Analytical function for conditional G_{H2O2} value from PNNL radiolysis model	Values based on radiolysis model results, Buck et al., 2013. *Would need to be updated, expanded for brine solutions (Cl, Br)*

Within the FMDM no chemistry occurs in the interstitial domain or environment; those regions are zero-volume and only serve to provide an interface/outlet for the active fuel/NMP and steel domains. It is possible to control the interaction between domains by altering (1) the environmental concentrations, (2) the relative total areas of the two reactive domains, and/or (3) the leak rate from the interstitial domain to the environment. The environment domain serves as the input/output interface with the GDSA performance assessment model (the FMDM - PA interface is discussed in more detail below).

In parallel with the addition of the steel surface to the FMDM, the model parameter database was reviewed and updated. As part of this updating process several data gaps were identified to provide priorities for FY-2017 and future work. The main FMDM parameters and the important data gaps are summarized in Table 2-1.

2.3. RESULTS FROM TEST RUNS OF FMDM WITH STEEL CORROSION MODULE AS THE SOURCE OF HYDROGEN

A series of model runs were done using the updated FMDM over a range of relevant conditions assuming that the steel surface was pure iron metal (simulating carbon-steel). The focus of these runs was to quantify the sensitivity of the FMDM-predicted fuel degradation rate to the rate of steel corrosion. The conditions for these sensitivity calculations are listed below and examples of results are shown in Figures 2-8, 2-9 and 2-10.

- The variables that were changed for these sensitivity runs were: the interfacial rate constant for the oxidation of iron (reaction 1 below) and the age of the fuel.
  - The rate constant was varied from 10^{-3} to 1.0 mole/m^2yr (the actual value of this key parameter for different types of steels needs to be determined experimentally).
  - The age of fuel was varied from 20 to 200 years.
- Parameter values (see Table 2-1) for the fuel environment are from Jerden et al., 2015.
- Parameter values (see Table 2-1) for the steel environment are from King and Kolar, 2003.
- The environmental concentrations (constant concentration boundary) were $[H_2] = 10^{-15}$ M, $[O_2] = 10^{-9}$ M, $[Fe^{2+}] = 10^{-9}$ M, $[CO_3^{2-}] = 10^{-6}$ M.
- Temperature was held constant at 40^{o}C for all runs.
- Fuel burnup was 50 GWd/tHM (gigawatt days per metric ton of initial heavy metal: U).

At the corrosion potential of carbon steel, under anoxic conditions, the corrosion rate-determining half-reactions are:

$$Fe^0 \rightarrow Fe^{2+} + 2e^- \quad (2\text{-}1)$$
$$2H_2O + 2e^- \rightarrow H_2 + 2OH^- \quad (2\text{-}2)$$

Mixed potential theory states that, at the corrosion potential, the net sum of the current densities of all anodic and cathodic reactions equals zero. That is, the corrosion potential is defined as the kinetic balance between anodic and cathodic reactions. Therefore, since (2-1) and (2-2) are the dominant reactions on the corroding steel, the rate of H_2 generation will equal the rate of steel corrosion (Fe oxidation) in units of moles H_2 per steel surface area per time at the corrosion potential. So the steel corrosion rates shown in Figures 2-8, 2-9 and 2-10 are directly proportional to the H_2 generation rates.

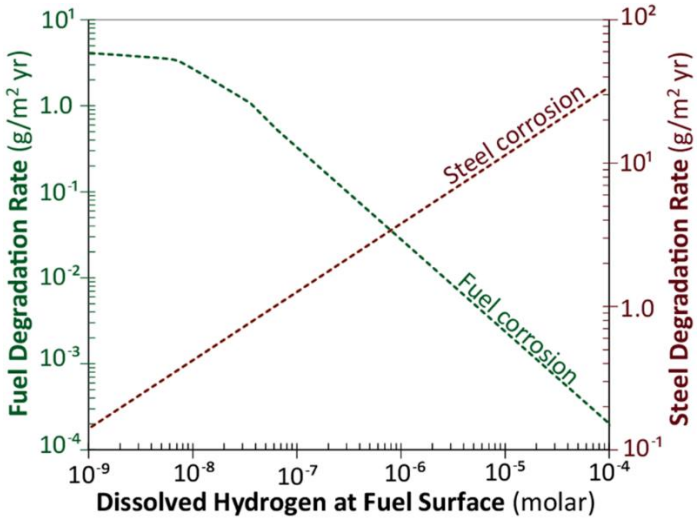

Figure 2-8. Used fuel and steel corrosion rates as functions of the concentration of dissolved H_2 in the common solution. This example is for a 200 year old fuel with a burnup of 50 GWd/tHM. The source of H_2 is the corrosion of steel and is thus its concentration is proportional to the steel corrosion rate (shown in red). For example, at a steel corrosion rate of ~$1.5x10^{-1}$ g/m^2 yr the resulting dissolved H_2 concentration at the fuel surface is 10^{-9} molar and for a steel corrosion rate of ~30 g/m^2 yr the H_2 concentration at the fuel surface is 10^{-4} molar.

Figure 2-8 indicates that, over a relevant range of steel corrosion rates, the concentration of dissolved H_2 that reaches the fuel surface can vary considerably. The variation in H_2 concentrations produced by this range of steel corrosion rates causes the predicted fuel degradation rate to vary from $2x10^{-4}$ g/m^2 yr up to 4.0 g/m^2 yr over a range of nanomolar to 0.1 millimolar H_2 concentrations.

Figures 2-9 and 2-10 show the fuel degradation rates as a function of time when coupled with a range of relevant steel corrosion rates. The dashed curves in Figure 2-9 show the combined effects of radiolysis and steel corrosion and the solid curve shows the effects of radiolysis alone. As mentioned above, for this simple but relevant case of carbon steel corrosion, the rate of iron oxidation is equal to the rate of H_2 production at the steel surface. The fuel degradation rate decreases slowly with time as the dose rate at the fuel surface decreases due to the decreasing production rates of the radiolytic oxidant H_2O_2 and associated O_2. That is, as the amount of radiolytic H_2O_2 decreases it takes less H_2 to anodically protect the fuel from oxidative dissolution. Therefore, the fuel degradation rate decreases to the chemical dissolution rate near 10^{-4} for all steel corrosion rates (see Figure 2-6 for reaction schematic).

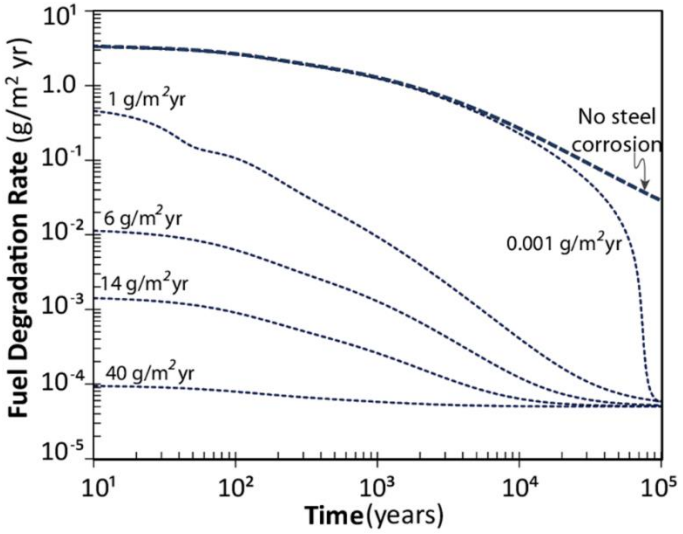

Figure 2-9. Results from the FMDM with the newly added steel corrosion module. All of these runs are for a 10 year old fuel with a burnup of 50 GWd/tHM. The rate of fuel degradation decreases with increasing steel corrosion rates due to the effect of H_2 which is produced at a rate proportional to steel corrosion (see Figure 6 for reaction summary).

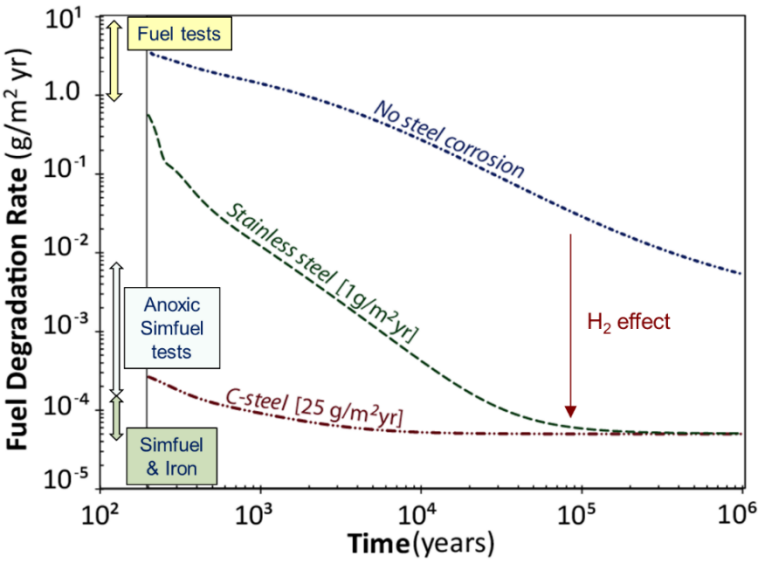

Figure 2-10. Results from the FMDM with the newly added steel corrosion module, comparing predictions with experimental ranges of degradation rates from relevant used fuel and simfuel tests. Fuel data from Cunnane 2004, Simfuel (U^{233} in UO_2) data from Ollila, 2008. These runs are for a 200 year old fuel with a burnup of 50 GWd/tHM.

Figure 2-10 also shows data ranges for used fuel and simulated fuel immersion tests. The fuel tests, compiled by Cunnane, 2004, were performed in oxidizing conditions using ~30 year old fuel that varied in burnup from 25 to 45 GWd/tHM. The temperature for these tests was varied from 25ºC to 80ºC, the pH varied from 7 to 9 and the solution was a buffered DIW with varying concentrations of dissolved carbonate (zero to millimolar). The simfuel tests (Ollila, 2008) involved the immersion of ^{233}U doped UO_2 in buffered DIW at pH 7 – 9 and 25ºC to 90ºC. These tests were performed under both anoxic conditions (argon purged) and reducing conditions (metallic iron added to tests).

The main conclusion drawn from Figure 2-10 is that, while there remains a need for focused electrochemical experiments to both measure parameter values and provide model validation data sets for the FMDM, it is encouraging that our initial results are roughly consistent with the data sets summarized in Figure 2-10 (within the test durations, which is on the order of months).

In order to assess the impact that the steel corrosion/H_2 effect will have on radionuclide source term calculations a hypothetical example was implemented using the radionuclide inventory for a 50 GWd/tHM BWR fuel provided by Carter et al., 2012. For this calculation the fuel dissolution rates from Figure 2-10 were multiplied by an assumed fuel specific surface area ($9.5x10^{-4}$ m^2/g for fuel pellets in a typical BWR assembly, from Fillmore, 2003) to provide the fractional dissolution rate and then by the radionuclide inventory. For the example plots shown in Figures 2-11 and 2-12, the calculated activities of all isotopes were multiplied by biological toxicity factors from 10 CFR, Part 20, Appendix B.

Figure 2-11a shows the radionuclide source term for a case where there is no steel corrosion occurring during used fuel degradation (top line in Figure 2-10). Figure 2-11b shows a case that assumes that the first 30,000 years of fuel degradation is accompanied by carbon steel corrosion that generates relatively high H_2 concentrations (~10^{-4} molar) within the waste package. The discontinuity at 30,000 years indicates the time at which all of the carbon steel has been consumed leading to the cessation of H_2 production and a corresponding increase in fuel dissolution rate. The time at which the carbon steel was all consumed was arbitrarily chosen and is likely unrealistic; however, it is still instructive in a qualitative sense to show how the consumption of steel can influence source term due to the H_2 effect.

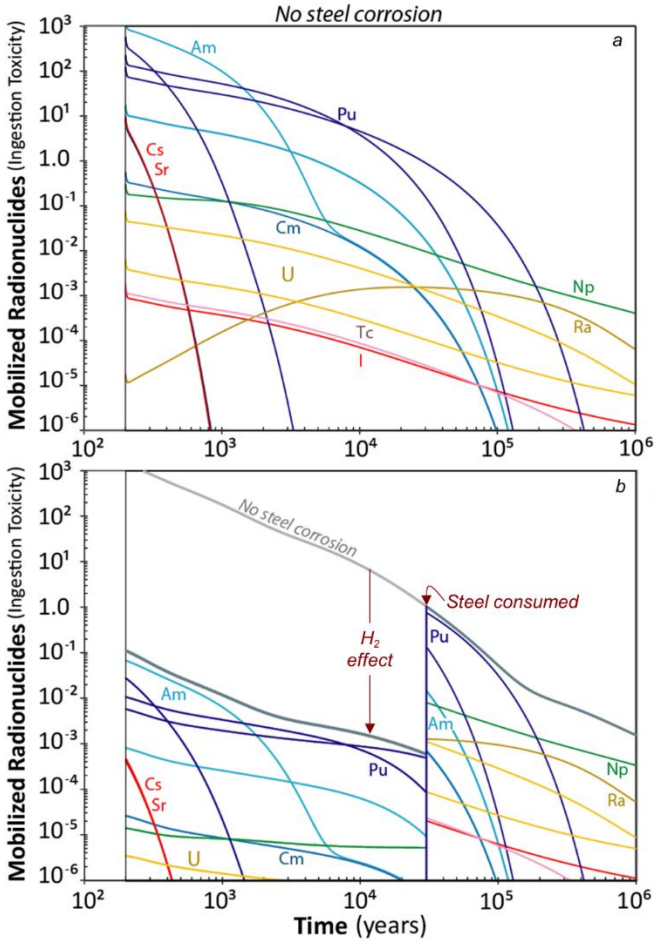

Figure 2-11. Hypothetical radionuclide source term for (a) the case with no steel corrosion, that is no H_2 generation during fuel degradation and (b) a case where carbon steel is corroding simultaneously with the used fuel for the first 30,000 years of the run. This example is for a 200-year-old fuel with a burnup of 50 GWd/tHM. Specific isotopes are not labeled because the purpose of the plot is highlight the elemental output of this hypothetical source term example.

Perhaps a more realistic case is shown in Figure 2-12. In this figure it is assumed that carbon steel corrodes at a rate of 25 g/m^2 yr until it is all consumed at 3,000 years. At this point the more slowly corroding stainless steel (1 g/m^2 yr) dominates H_2 production rates resulting in a higher fuel degradation rate relative to the first 3,000 years. All steel assumed to be consumed by 40,000 years, resulting in the increase of fuel degradation rates due to the absence of H_2. Nevertheless, the benefit of accounting for steel corrosion in the FMDM calculations is revealed by integrating the curves to calculate the total mass that has dissolved.

Although the time frames for the FMDM test runs shown in Figures 2-11 and 2-12 are arbitrary and both the steel and fuel reaction parameters need to be validated by experiments, these hypothetical source term examples are qualitatively instructive. The most important observation is that, due to the H_2 effect, the radionuclide source term may be significantly attenuated. This indicates that having an accurate model for steel corrosion and the associated H_2 effect is essential for accurate source term calculations within the performance assessment model.

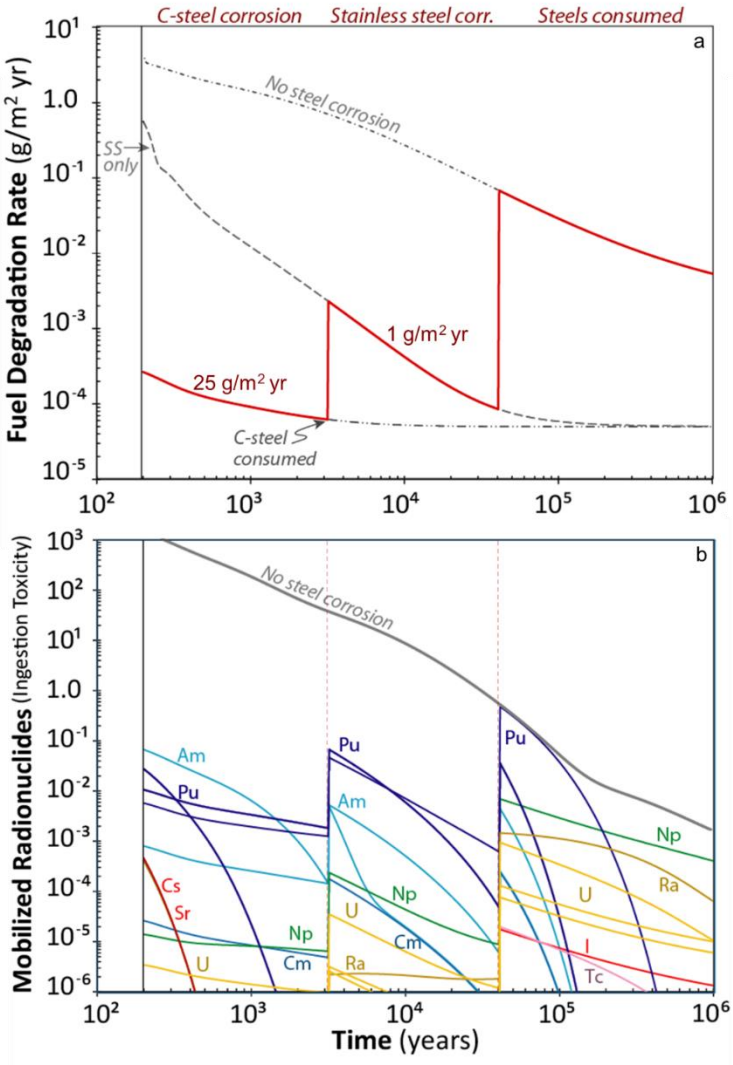

Figure 2-12. Hypothetical radionuclide source terms for the case where carbon steel corrosion dominates the first 3,000 years, followed by stainless steel until 40,000 years at which point all steel has been consumed (a). 12b shows the radionuclide source term for the case diagrammed in 2-12a. This example is for a 200-year-old fuel with a burnup of 50 GWd/tHM. Specific isotopes are not labeled because the purpose of the plot is highlight the elemental output of this hypothetical source term example.

2-4. INTEGRATION OF FMDM WITH THE GENERIC DISPOSAL SYSTEM ANALYSIS PERFORMANCE ASSESMENT MODEL

Although the basic calculations in the FMDM were successfully integrated with GDSA PA reactive transport code PFLOTRAN in FY-2015 (Jerden et al., 2015), there remains a need to extend the code to encompass all chemical processes relevant to source term (e.g., the addition of the steel corrosion as a source of H_2) and optimize the FMDM code to improve performance. In addition to the extension of the FMDM to include the steel corrosion module (see Section 2 above), the FY-2016 integration work also focused on optimizing the FMDM code.

The basic information flow involved in the integration of the FMDM with PFLOTRAN is shown in Figure 2-13.

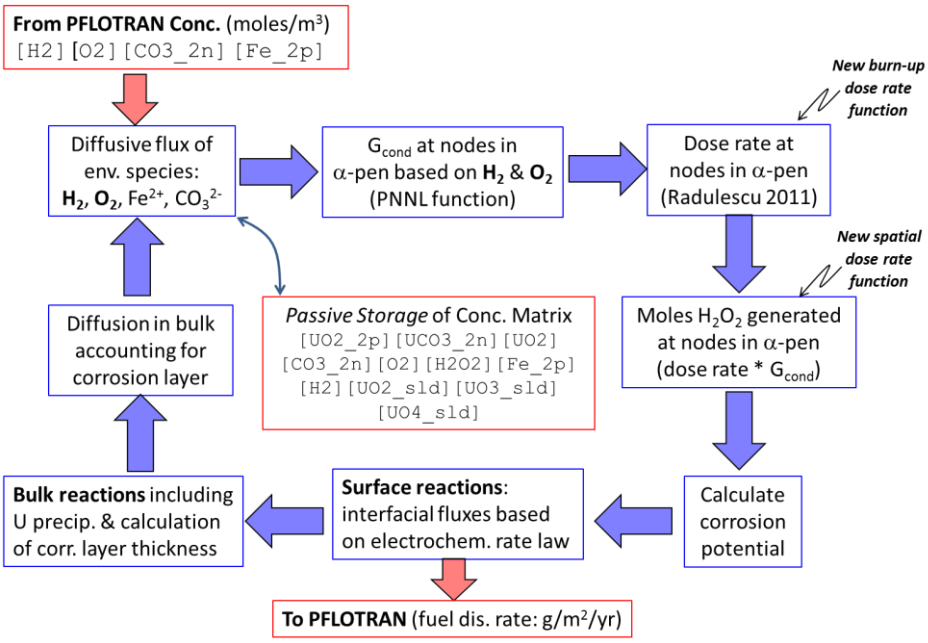

Figure 2-13. Conceptual flow diagram showing the individual calculations within a single time step of the FMDM. Note that the concentrations of all components must be stored and fed back to the FMDM at the beginning of each new time step. G_{cond} refers to the conditional generation value for H_2O_2, which determines the peroxide generation rate within the alpha radiation zone (α–pen). In the FMDM v.2.3 the conditional H_2O_2 generation value is calculated by an analytical function (G_{cond} is a function of $[H_2]$ and $[O_2]$).

The FY-2016 FMDM (V.3) optimization work involved the following activities:

- The dose rate function was re-conditioned to avoid mathematical instability.
- Because Code profiling and sensitivity runs showed that the majority of the computing time of the FMDM is taking place in the bulk chemical reaction module, a plan for streamlining the reaction diffusion equations used in this module was formulated.
- A conceptual plan for integrating the FMDM (V.3) into PFLOTRAN was developed and is summarized in Figures 14 and 15 below.

Update of burnup (BU) - dose rate (RAD) function: The dose rates extrapolated to the fuel surface (distance equals zero) were correlated with the results of Radulescu 2011. The dose rate correlation from the Jerden et. al., 2015 report was replaced because of concerns with non-smooth transitions. For the new dose rate function, the main dose profile is represented using a logistic function, and the Am-241 in-growth was accounted for using a Gaussian. This expression should be globally valid, as long as the burn-up and age-of-fuel are greater than zero.

Figure 2-14 shows how the six process modules that make up the FMDM (V.3) are related to the GDSA PA model. All of the modules are coupled and the flow of information between them is summarized in Figure 2-13. The primary output of the FMDM is the fuel degradation rate in mass per surface area per time, which is used to define the radionuclide source term in PFLOTRAN. in addition to numerical inputs and outputs between FMDM and PFLOTRAN shown in Figure 2-14, there are also a number of places where model parameters need to be coordinated to avoid internal inconsistencies within the PA calculation. These points of coordination include:

- Time at which the waste package is breached.
- The temperature history of the waste package.
- The radionuclide inventory used in PFLOTRAN needs to be consistent with the burnup used in the FMDM.
- The solubility limits used in PFLOTRAN need to be consistent with the solubility limits for U(VI) secondary phases and iron oxides used in the FMDM.
- The specific surface area assumed in the PFLOTRAN source term model needs to be consistent with the relative surfaces of the fuel, steel and NMP domains within the FMDM.

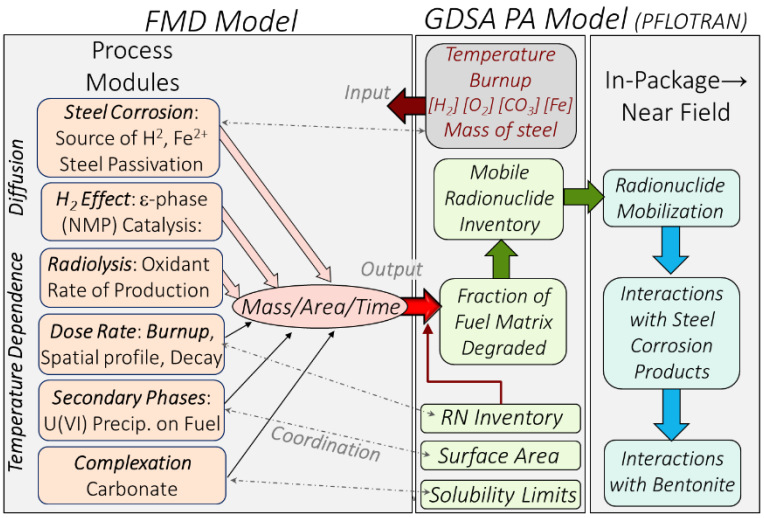

Figure 2-14. Conceptual diagram showing all of the active process modules in the latest version of the FMDM (V.3) and how they are integrated in terms of inputs and outputs with the PA model.

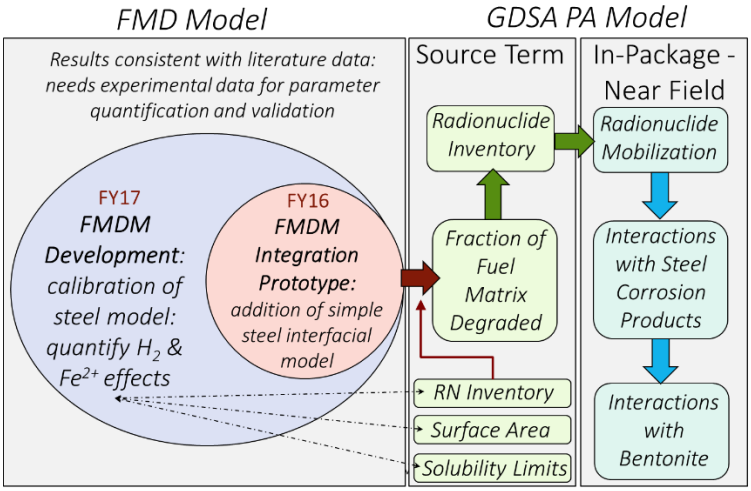

Figure 15. Conceptual diagram highlighting the major objective for FY-2017 in the context of integration with the GDSA PA modeling work.

Figure 2-15 highlights the key objectives of work proposed for FY-2017 in the context of model integration. As discussed in this report, the effect of H_2 produced from the anoxic corrosion of steel will likely dominate the radionuclide source term for relevant repository scenarios. FY-2017 work will focus on quantifying parameter values and calibrating the steel corrosion and H_2 effect modules that are currently in the FMDM. This work will be done in parallel with efforts to optimize the serial performance of the FMDM to minimize run times. Once these modules are appropriately parameterized and tested, they will be added to the FMDM Fortran files that are called by PFLOTRAN to run within the GDSA PA model.

2.5 RESULTS FROM SCOPING EXPERIMENTS ON POISONING CATALYTIC ACTIVITY OF NOBLE METAL PARTICLES

To ensure that the process modules for used fuel degradation and steel corrosion accurately represent reality within the relevant ranges of repository conditions, the model development efforts need to be coupled with a focused experimental program to quantify key parameters and provide data sets for validation. Although the FY-2016 scope for this project did not include a deliverable for experimental work, scoping tests were performed using the radiological electrochemical testing facilities at Argonne to provide confidence that the effect of H_2 on used fuel degradation is accurately represented in the FMDM and thus in the PA model.

As shown in Jerden et al., 2015, and in Section 2-2 above, the catalysis of H_2 oxidation on the NMPs attenuates the used fuel dissolution rate by as much as four orders of magnitude when dissolved H_2 concentrations reach approximately 0.1 mM. Because this NMP – H_2 catalysis process plays such a key role in determining the fuel dissolution rates and its mechanism is not yet fully understood, it is the subject of on-going electrochemical experiments designed to directly inform the process modeling efforts.

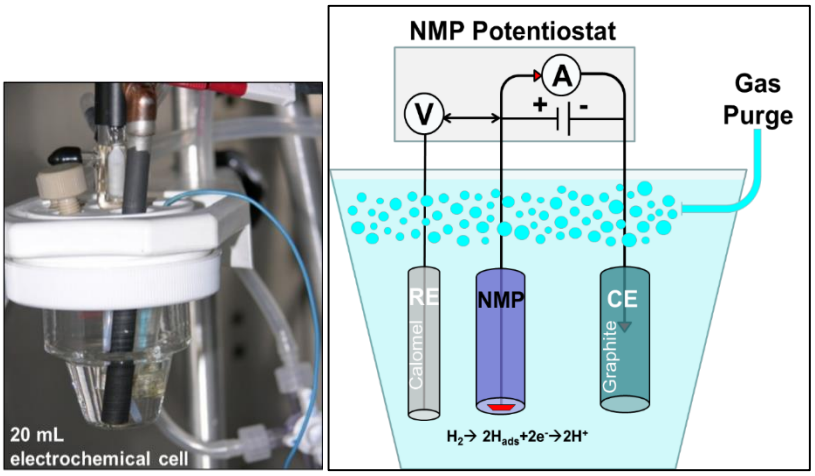

Figure 2-16. Photograph and schematic diagram of the type of cell used for the electrochemical experiments.

The experimental set up for the scoping tests consists of a 20 mL, three-electrode cell in which the experimental cover gas is continuously bubbled during the experiments (Figure 2-16). Multiple cells (experiments) are run simultaneously within an oven in a radiological laboratory. Multiple power supplies and potentiostats are available so that tests with two or more working electrodes (e.g., NMP and UO_2) can also be performed. The electrodes are characterized pre- and post-experiment by optical and Scanning Electron Microscopy (SEM). The solutions from selected tests are analyzed for electrode constituents (Ru, Mo, Pd, Rh, Tc, U, and other dopants such as REE) by Inductively coupled plasma mass spectrometry (ICP-MS). Tests performed in FY-2015 through FY-2016 focused on the interfacial reactions of H_2 with electrodes composed of a technetium bearing noble metal partial, which serves as a

simulant for the fission product alloy present in spent fuel and modeled in the FMDM (NMP on Figures 2-2 and 2-6 above). Other tests were performed with electrodes made of the most abundant pure elements present in the NMP (Ru, Mo, and Pd). The NMP simulant electrode was made in house (Argonne) from an alloy produced by Steve Frank at Idaho National Laboratory that closely matches the composition and homogeneity (single alloy phase) of the NMP (ε-phase) found in used fuel. The NMP alloy used to make the electrode has a composition of $Ru_{56}Mo_{20}Rh_{11}Pd_{11}Tc_2$ and, based on characterization by SEM and energy dispersive x-ray analyses (EDS), appears to be composed of a single phase with trace amounts of TcO_2.

The EDS analyses of several locations on the NMP alloy used in our experiments show that this material falls within the compositional range of the fission product alloys generated in UO_2 light water reactor fuels (Figure 2-17).

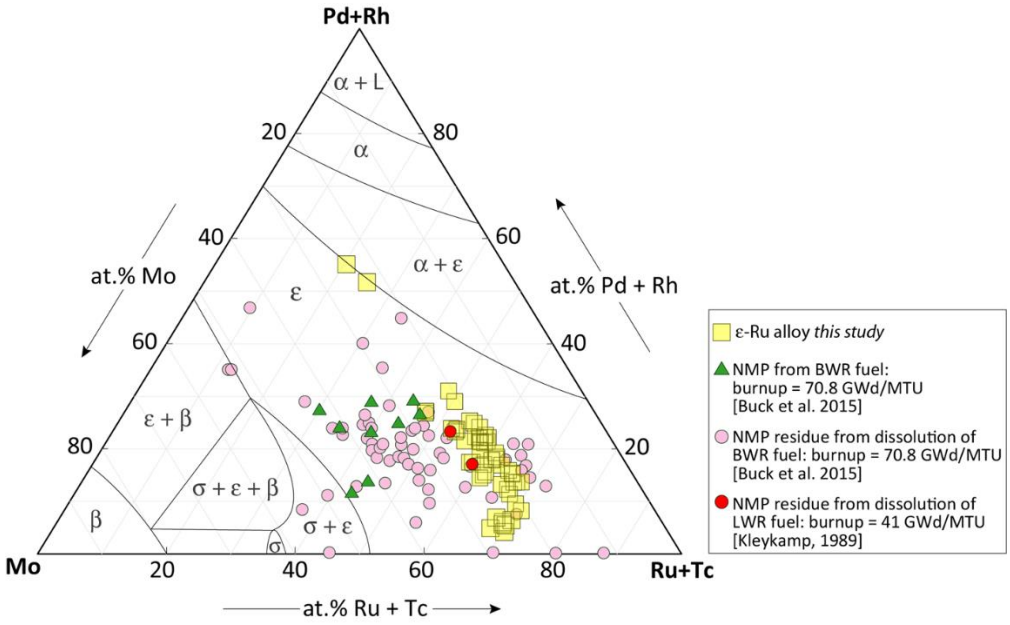

Figure 17. Energy dispersive x-ray analyses of the NMP alloy used in the scoping experimental studies (yellow squares). Note that the alloy falls within the ε-Ru phase field and is thus representative of the fission product alloy phase present in used fuel. The phase fields are for the 1700ºC plot of this system from Kleykamp, 1989.

One of the most important experimental observations made regarding the role of H_2 in used fuel dissolution is that the presence of dissolved halides, particularly Br^-, seems to counteract the H_2 effect (Metz et al., 2008). Although the mechanism is poorly understood, our new results (Figure 2-18) suggest that the NMP surfaces may be poisoned by halides and reduce their catalytic efficiency (i.e., counteract the protective H_2 effect). The effects of poisoning and alteration of the NMP surfaces are not currently accounted for in the FMDM, because these processes are not well understood or quantified. However, due to the importance of the H_2 effect these processes are deemed high priorities for experimental investigations.

To investigate the reaction of H_2 on the NMP and other metal electrodes, scoping tests were performed in which the open circuit potential (OCP) of the electrode was measured for up to 80 hours in 1 mM NaCl purged by bubbling either air, Ar or 2% H_2 in Ar through the solution. The possible poisoning effect of

Br^- was also investigated by performing the 2% H_2 cover gas tests in solutions containing 1 mM NaBr. The pH for all tests remained relatively constant at around 7.0. Typical results are shown in Figure 2-18.

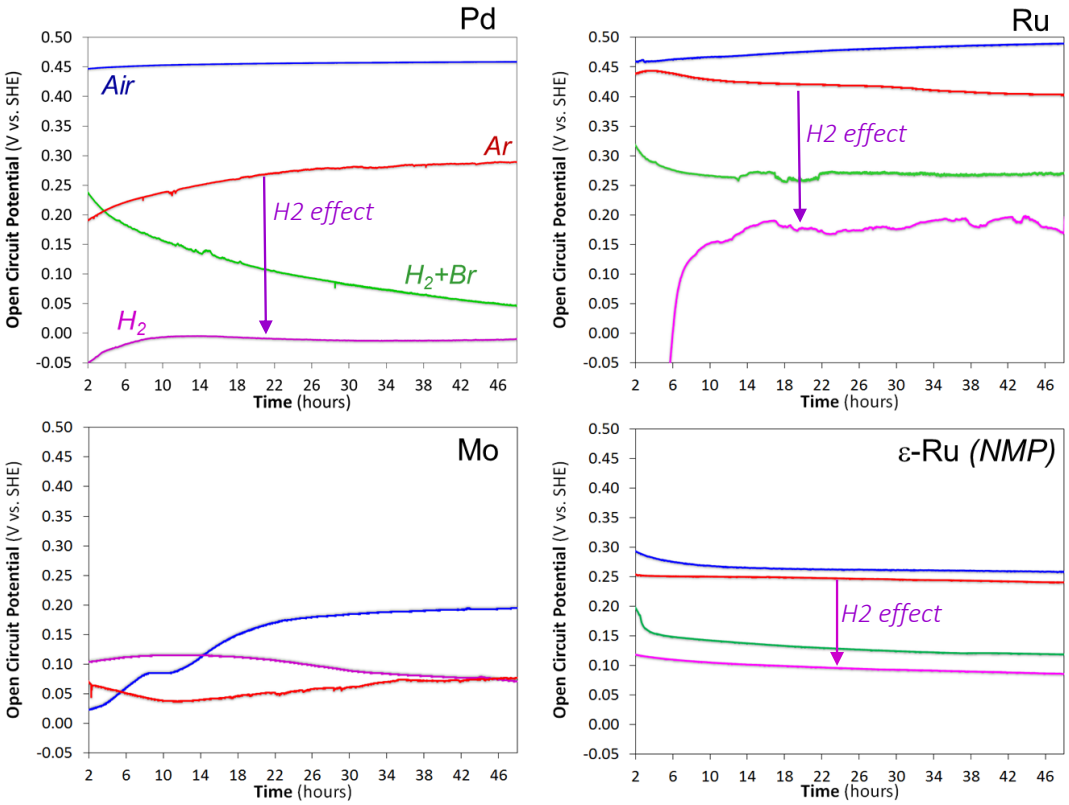

Figure 2-18. Results from scoping electrochemical tests showing the open circuit potentials of the $Ru_{56}Mo_{20}Rh_{11}Pd_{11}Tc_2$ (NMP) and pure Pd, Ru and Mo electrodes in 1 mM NaCl solution purged with air (blue curves), Ar (red curves), or H_2/Ar (violet curves) and 1 mM NaCl + 1 mM BrCl solution purged with H_2/Ar (green curves). Note that the presence of Br^- partially counteracts the H_2 effect on all of the electrode materials except for Mo. The Mo results were inconsistent due to the formation of an oxide layer (MoO_2) during the test.

The results of tests with the NMP electrode show a pronounced H_2 effect that causes a decrease in the open circuit potential from greater than 260 mV (vs. SHE) for the air cover gas tests down to around 100 mV for tests performed with 2% H_2 in Ar as the cover gas. That this large potential drop is not seen when the test is performed in pure Ar indicates that it is due to H_2 oxidation occurring on the NPM electrode. This shows that, under near neutral conditions, the NMP surface is hosting anodic reactions that can be generalized as:

$$H_2 \rightarrow 2H_{adsorbed} + 2e^- \rightarrow 2H^+ \qquad (2\text{-}4)$$

As indicated by the green curves in Figure 2-18, the presence of 1 mM Br^- partially counteracts the H_2 effect, resulting in the NMP surface potential being approximately 60 mV higher than in its absence. The relative effects of both H_2 and Br^- on the OCP are significantly greater for reactions on the Ru and Pd electrodes; however, the results for the Mo electrode are confounded by the growth of an oxide layer (MoO_2) during the tests. It is likely that a thin (undetectable by SEM) MoO_2 layer is generated on the NMP electrode during the test.

Figure 2-19 shows the Eh – pH diagrams for the main constituents of the NMP. Of particular interest in Figure 2-19 is the observation that the MoO_2 stability field overlaps the field for repository relevant conditions. This is interesting because it implies that Mo within the NMP will likely oxidize when exposed to in-package solutions, which may impact the catalytic activity of the NMP surfaces. The Eh – pH diagrams also indicate that sulfur may play an important role in the surface chemistry of Ru (the dominant element in the NMP) and thus should be accounted for in future experimental and modeling efforts.

Figure 2-19 also indicates that MoO_2 and perhaps Ru sulfides could play an important role in the evolution of the NMP surfaces under repository relevant solutions. This is important because the NMP surfaces are responsible for the H_2 effect that anodically protects used fuel from oxidation (see Figure 2-7 above). This indicates that future experimental and modeling efforts should account for the evolution of the NMP surface in relevant solutions.

The results in Figure 18 also show that even over short time frames (minutes) the presence of Br^- has an effect on the NMP – H_2 reaction. This is a significant observation as it identifies a key chemical process, that could counteract the protective H_2 effect that is not currently accounted for in the FMDM.

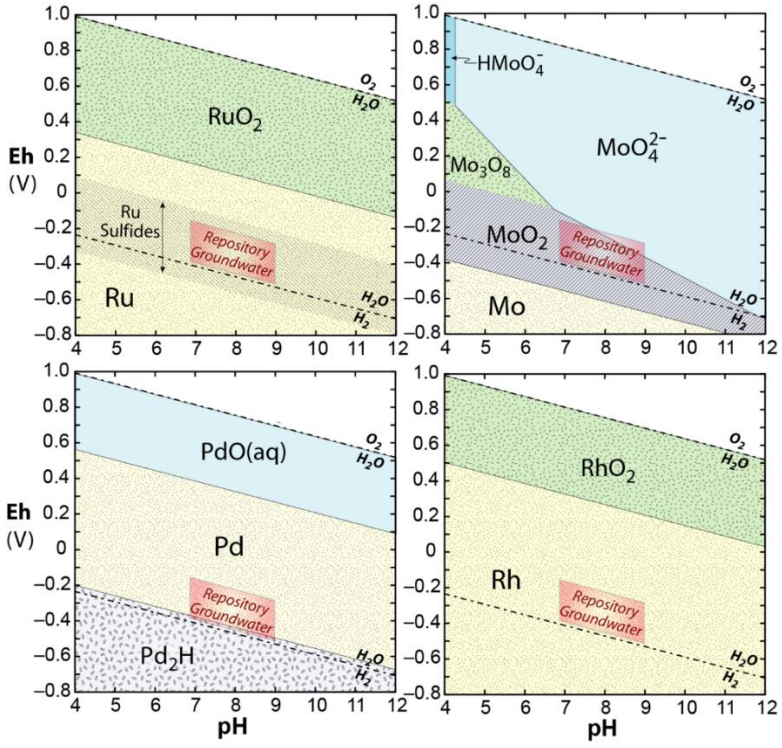

Figure 2-19. Eh – pH diagrams for the major constituents of the noble metal particle alloy (NMP) present in used fuel.

Future experimental work will also involve a series of electrochemical tests with simulated used fuel that consists of NMP in a UO_2 matrix. These tests will be used to generate a validation data set for the FMDM.

2.6 CONCLUSIONS AND FUTURE WORK

The primary purpose of this project is to develop a process model to calculate the degradation rate of used fuel based on fundamental underlying processes used to determine radionuclide source terms for reactive transport calculations in the Generic Disposal System Analysis PA model.

The main accomplishments for the FY2016 work on the Fuel Matrix Degradation Model (FMDM) development project are as follows:

- Formulated, coded and tested an electrochemical steel corrosion module that couples in-package steel corrosion with fuel degradation through the common solution. This module provides the kinetic source of H_2 that may control the used fuel dissolution rates under repository relevant conditions.
- Updated and optimized FMDM to improve the efficiency of integration with the GDSA PA model.
- Performed scoping electrochemical tests to build confidence in modeling the H_2 effect mechanism, which has been shown by both experiment and electrochemical modeling to significantly impact source term calculations when in-package steel components are corroding simultaneously with used fuel.

The key finding of the FY-2016 work was that the corrosion of steel canister materials will have a significant impact on the radionuclide source terms calculated by PA because of its role as the major source of the H_2, which attenuates the fuel degradation rate. The test runs with the updated FMDM indicate that the peak radionuclide source term from a breached waste package will likely be attenuated by the H_2 effect and the corrosion of steel components (the dominant source of H_2 in the system).

These processes have been added in the FMDM V.3; however, there remains a need for coupled experimental and process modeling work to accurately parameterize and validate the model. This future work is particularly important because the FMDM is currently being used to provide the radionuclide source term in the PA model. Thus, future improvements to the FMDM process model will have a direct impact on the accuracy of the existing GDSA PA model.

FY-2017 activities of particular importance are:

- Extend the FMDM Fortran – PFLOTRAN interface files to account for the corrosion of the steel components and the associated H_2 effect that anodically protects the fuel from oxidative degradation.
- Take next step in integration of FMDM with PA: demonstrate sensitivity of the Argillite PA model to key variables in the FMDM such as burnup, surface area, steel corrosion/H_2 production rates and the dissolved concentrations of H_2, O_2, carbonate and ferrous iron.
- Perform focused electrochemical experiments to determine the effect of halides and other possible poisons on the catalytic efficiency of the NMP. These tests will quantify processes that may counteract the protective H_2 effect.

- Account for the effect of poisons (e.g., Br, S) or other processes that counteract the protective H_2 effect in the FMDM.

Furthermore, the recognition and quantification of the interactions between the corrosion of steel waste package components and waste form degradation suggests that our models may provide important insights as to the types of steel that could be used to optimize the long-term performance of the waste package and canister materials.

2.7 REFERENCES

Buck E., Jerden, J., Ebert, W., Wittman, R., (2013) Coupling the Mixed Potential and Radiolysis Models for Used Fuel Degradation, FCRD-UFD-2013-000290.

Buck, E., Mausolf, E., McNamara, B., Soderquist, C., Schwantes, J., 2015, Nanostructure of Metallic Particles in Light Water Reactor Used Nuclear, *Journal of Nuclear Materials* 461, 2015, 236–243

Cunnane, J.C., 2004, CSNF Waste Form Degradation: Summary Abstraction, Bechtel SAIC Company LLC Technical Report, ANL-EBS-MD-000015 REV 02, August 2004

Fillmore, D.L., 2003, Parameter Selection for Department of Energy Spent Nuclear Fuel to be Used in the Yucca Mountain License Application, Idaho National Engineering and Environmental Laboratory Report, INEEL/EXT-03-01032 Revision 1, October 2003

Grambow, B., Bruno, J., Duro, L., Merino, J., Tamayo, A., Martin, C., Pepin, G., Schumacher, S., Smidt, O., Ferry, C., Jegou, C., Quiñones, J., Iglesias, E., Rodriguez Villagra, N., Nieto, J., Martínez-Esparza, A., Loida, A., Metz, V., Kienzler, B., Bracke, G., Pellegrini, D., Mathieu, Wasselin-Trupin, G., Serres, C., Wegen, D., Jonsson, M., Johnson, L., Lemmens, K., Liu, J., Spahiu, K., Ekeroth, E., Casas, I., de Pablo, J., Watson, C., Robinson, P., Hodgkinson, D., 2010, Model Uncertainty for the Mechanism of Dissolution of Spent Fuel in Nuclear Waste Repository, European Commission, Final Report for MICADO Project, EUR 24597, 2010.

Jerden J. Copple J., Frey K. Ebert W., 2014, Prototype Fortran Version of the Mixed Potential Process Model for Used Fuel Degradation, Used Fuel Disposition Campaign Milestone: M4FT-15AN0806012, October 15, 2014

Jerden J., Glenn Hammond, G., Copple J., Cruse, T., Ebert W., 2015, Fuel Matrix Degradation Model: Integration with Performance Assessment and Canister Corrosion Model Development, FCRD-UFD-2015- 000550, July 21, 2015

Jerden J. Frey K. Ebert W., 2015, A Multiphase Interfacial Model for the Dissolution of Spent Nuclear Fuel, *Journal of Nuclear Materials*, 462, 135–146

Joe T. Carter, J., Luptak, A., Gastelum, J., Stockman, C., Miller, A., 2012, Fuel Cycle Potential Waste Inventory for Disposition, FCR&D-USED-2010-000031 Rev 5, July 2012

King F. and Kolar M., (2003). The Mixed-Potential Model for UO_2 Dissolution MPM Versions V1.3 and V1.4., Ontario Hydro, Nuclear Waste Management Division Report No. 06819-REP-01200-10104 R00.

Kleykamp, H., Constitution and Thermodynamics of the Mo-Ru, Mo-Pd, Ru-Pd and Mo-Ru-Pd Systems, *Journal of Nuclear Materials*, 167 (1989), 49-63

Laaksoharju M., Smellie, J., Tullborg, E-L., Gimeno, M., Hallbek, L., Molinero, J., Waber, N., 2008, Bedrock hydrogeochemistry Forsmark site descriptive modeling SDM-Site Forsmark, SKB R-Report (R-08-47), SKB, Stockholm, Sweden

Mariner, P., Gardner, P., Hammond, G, Sevougian, D, Stein E., 2015, Application of Generic Disposal System Models, FCRD-UFD-2015-000126, SAND2015-10037, September 22, 2015, 209pp.

Metz V., Loida A., Bohnert E., Schild D., Dardenne K., (2008) Effects of Hydrogen and Bromide on the Corrosion of Spent Nuclear Fuel and γ-irradiated UO_2(s) in NaCl Brine, *Radiochim. Acta* 96, 637–648

NRC Regulations, Title 10, Code of Federal Regulations, PART 20—STANDARDS FOR PROTECTION AGAINST RADIATION, Appendix B to Part 20—Annual Limits on Intake

(ALIs) and Derived Air Concentrations (DACs) of Radionuclides for Occupational Exposure; Effluent Concentrations; Concentrations for Release to Sewerage

Ollia, K., 2008, Dissolution of Unirradiated UO_2 and UO_2 Doped with ^{233}U in Low- and High-Ionic-Strength NaCl Under Anoxic and Reducing Conditions, Posiva Working Report 2008-50

Radulescu, G., (2011) Repository Science/Criticality Analysis, Oak Ridge National Laboratory, Reactor and Nuclear Systems Division, FTOR11UF0334, ORNL/LTR-2011, Oak Ridge National Laboratory, Oak Ridge, TN.

Röllin S., Spahiu K., Eklunda U., (2001), Determination of Dissolution Rates of Spent Fuel in Carbonate Solutions Under Different Redox Conditions with a Flow-through Experiment, *Journal of Nuclear Materials*, 297, 231–243

Shoesmith, D., 2008, The Role of Dissolved Hydrogen on the Corrosion/Dissolution of Spent Nuclear Fuel, Nuclear Waste Management Organization, Toronto, Ontario, Canada, TR-2008-19, November 2008.

Wang Y. et al., (2014) *Used Fuel Disposal in Crystalline Rocks: Status and FY14 Progress*, FCRD-UFD-2014-000060, SAND2014, Sandia National Laboratories, Albuquerque, NM.

3. EFFECT OF IRON ON RADIOLYTIC HYDROGEN PEROXIDE GENERATION

3.1 INTRODUCTION

The U.S. Department of Energy Office of Nuclear Energy (DOE-NE), Office of Fuel Cycle Technology has established the Used Fuel Disposition Campaign (UFDC) to conduct the research and development activities related to storage, transportation, and disposal of used nuclear fuel (UNF) and high-level radioactive waste. Within the UFDC, the components for a general system model of the degradation and subsequent transport of UNF is being developed to analyze the performance of disposal options [Sassani et al., 2012]. Two model components of the near-field part of the problem are the ANL Mixed Potential Model and the PNNL Radiolysis Model.

This section is in response to the desire to integrate the two models as outlined in [Buck, E.C, J.L. Jerden, W.L. Ebert, R.S. Wittman, (2013) "Coupling the Mixed Potential and Radiolysis Models for Used Fuel Degradation," FCRD-UFD-2013-000290, M3FT-PN0806058]. This section gives the details on the effect of iron chemistry on H_2O_2 decomposition under radiolytic condition at the surface of used nuclear fuel under repository conditions. Additionally, suggestions are offered on what further data or measurements would be required for model verification and applicability. The listings of the reactions considered in this report are given in Appendix.

3.2 RADIOLYSIS MODEL WITH IRON REACTIONS

A radiolysis model sensitivity study [Wittman RS and EC Buck. 2012] has shown that, of the approximately 100 reactions [Pastina, B. and LaVerne, J. A., 2001] describing water radiolysis, only about 37 are required to accurately predict H_2O_2 to one part in 10^5. The intended application of that radiolysis model (RM) was to calculate H_2O_2 production for an electrochemical based mixed potential model (MPM) [Jerden, J., Frey, K., Cruse, T., and Ebert, W., 2013] developed to calculate the oxidation/dissolution rate of used nuclear fuel [Shoesmith, D.W., Kolar, M., and King, F., 2003] under disposal conditions where O_2 is expected to be at low concentrations and H_2 is generated from oxidation of steel containers.

As an initial approximation, that model (MPM) was developed under the assumption that H_2O_2 is generated at a rate determined only by its radiolytic *G*-value. Ideally, for a full RM-MPM integration, the MPM would use a reaction kinetics based model to predict H_2O_2 for various water chemistries. As a further step in that direction, this section presents the effect of small concentration of [Fe(II)] on H_2O_2 concentration and explains the mechanism of that effect.

To better understand how integration of the PNNL Radiolysis Model (RM) can be integrated with the ANL Mixed Potential Fuel Degradation Model in the environment of iron containing species we consider iron reactions in the RM. Since our goal is to consistently account for the chemistry in both models we focus on the mechanism and effect of iron on prediction H_2O_2 decomposition affecting the UO_2 degradation rate.

The main approach is as follows.

- Identify the significant reactions that govern the chemical and radiolytic decomposition of H_2O_2 in water with known dose rate and concentrations of iron species (De Laat, et al., 1999 and Bouniol, 2010).
- Determine if iron chemistry is well understood enough to accurately represent its effects on decomposition of H_2O_2 in the RM.

Progress on bullet one above is summarized here and bullet two is left as an open question.

Figure 1 of reference (De Laat, et al., 1999) was reproduced by our current kinetics model as a check of the numerical solution and our understanding of the model definition. Assuming 38 water reactions from previous radiolysis model work (Wittman and Buck 2012) and approximately 60 additional iron containing reactions of Refs. (De Laat, et al., 1999 and Bouniol, 2010) we initially find that approximately 60 total reactions are sufficient to reproduce the H_2O_2 concentration.

Figure 3-1 shows both the radiolytic and iron concentration effects on the H_2O_2 concentration. Without dose, the initial 0.01 molar H_2O_2 concentration is initially catalytically decomposed at a rate of 160 times faster than thermal decomposition (25°) alone. Additionally, at a dose rate of 25 krad/s the steady-state H_2O_2 concentration is about 160 times lower with an initial 1 μM concentration of Fe(II) that is converted to 1 μM of Fe(II). For these comparisons pH is fixed at 7.0 and no constraints were put on oxygen and hydrogen concentrations. The effect of those constraints with diffusion out of the alpha radiation zone is currently being explored.

Further work is in progress to confirm the applicability of the reaction kinetics for pH and iron concentrations required by Mixed Potential UO_2 Fuel Degradation Model. Also, further work is in progress to confirm the applicability of the reaction kinetics for pH and iron concentrations required by Mixed Potential UO_2 Fuel Degradation Model.

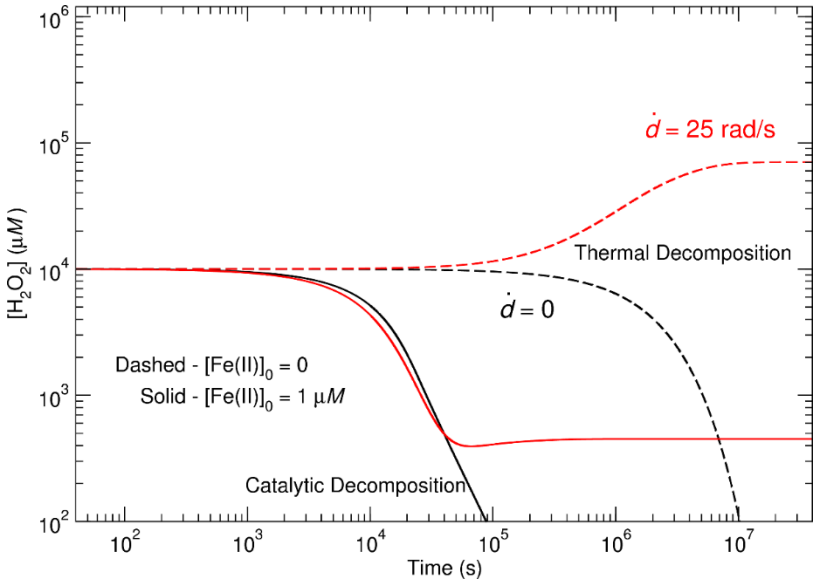

Figure 3-1. Effect of an initial micro-molar concentration of Fe(II) on H_2O_2 generation. Comparison of with and without dose rate (red and black). Comparison of with and without Fe(II) (solid and dashed curves).

Table 2-1 was found to be a sufficient set of reactions to describe the main features of Figure 3-1 and contains the mechanism that H_2O_2 decomposes or shifts its steady-state concentration. The main process responsible for H_2O_2 decomposition is Fenton's reaction (51 of Table 2-1) (Fenton, H.J.H., (1894) where Fe(II) attains a secular equilibrium with a lower concentration of Fe(III). The effective equilibrium arises because ·OH radicals react with water forming O_2^- which reduces Fe(III) back to Fe(II) (58 and 60 of Table 3-1).

Table 3-1. Subset of reactions sufficient to represent the primary mechanisms for H_2O_2 generation in the full RM (Appendix A) [Iron from Ref. (De Laat, et al., 1999)].

	Reaction	k_r
3	$H_2O_2 \rightarrow H^+ + \cdot HO_2^-$	1.1×10^{-1}
4	$H^+ + \cdot HO_2^- \rightarrow H_2O_2$	5.0×10^{10}
15	$\cdot HO_2 \rightarrow O_2^- + H^+$	1.3×10^{6}
16	$O_2^- + H^+ \rightarrow \cdot HO_2$	5.0×10^{10}
23	$e^- + H_2O_2 \rightarrow \cdot OH + OH^-$	1.1×10^{10}
26	$\cdot H + H_2O_2 \rightarrow \cdot OH + H_2O$	9.0×10^{7}
27	$\cdot H + O_2 \rightarrow \cdot HO_2$	2.1×10^{10}
33	$\cdot OH + H_2 \rightarrow \cdot H + H_2O$	4.3×10^{7}
34	$\cdot OH + H_2O_2 \rightarrow \cdot HO_2 + H_2O$	2.7×10^{7}
35	$\cdot HO_2 + O_2^- \rightarrow \cdot HO_2^- + O_2$	8.0×10^{7}
36	$H_2O_2 \rightarrow \cdot OH + \cdot OH$	2.5×10^{-7}
41	$Fe^{3+} + 2H_2O \rightarrow Fe(OH)_2^+ + 2H^+$	1×10^{5}
42	$Fe(OH)_2^+ + 2H^+ \rightarrow Fe^{3+} + 2H_2O$	1.3×10^{11}
51	$Fe^{2+} + H_2O_2 \rightarrow Fe^{3+} + \cdot OH + OH^-$	63.0
52	$Fe^{2+} + \cdot OH \rightarrow Fe^{3+} + OH^-$	3.2×10^{8}
58	$Fe^{3+} + O_2^- \rightarrow Fe^{2+} + O_2$	5×10^{7}
60	$Fe(OH)_2^+ + O_2^+ \rightarrow Fe^{2+} + O_2 + 2OH^-$	5×10^{7}

The mechanism can be understood by focusing on a few species during H_2O_2 decomposition (Figure 3-2). Figure 3-2 shows that without the reducing reactions (58 and 60 of Table 3-1) the Fe(II) quickly oxidizes to Fe(III), resulting in little or no decomposition of H_2O_2. Depending on solution pH the Fe(III) will remain or precipitate from solution. The solid lines show that the iron reducing reaction creates an effective fixed concentration of Fe(II) which enables decomposition – while both Fe(II) and Fe(III) participate in reactions, the Fe(II)/Fe(III) equilibrium effectively acts like a catalyst. Therefore, the decomposition mechanism requires the Fe(III) reduction reactions to preserve even a small concentration of Fe(II). It's this last point that make the inclusion of this mechanism unclear for the RM because if Fe(III) drops out of solution at a rate faster than it can be reduced back to Fe(II) the RM will non-conservatively predict lower than actual H_2O_2 production rates. The current fuel degradation model assumption is that Fe(III) precipitates on formation without subsequent reduction to Fe(II). While Figure 3-2 shows that the concentration of Fe(III) is almost 10X less than Fe(II), the solubility of Fe(III) and its precipitation rate is an open question for conditions (pH, etc.) appropriate for UO_2 degradation.

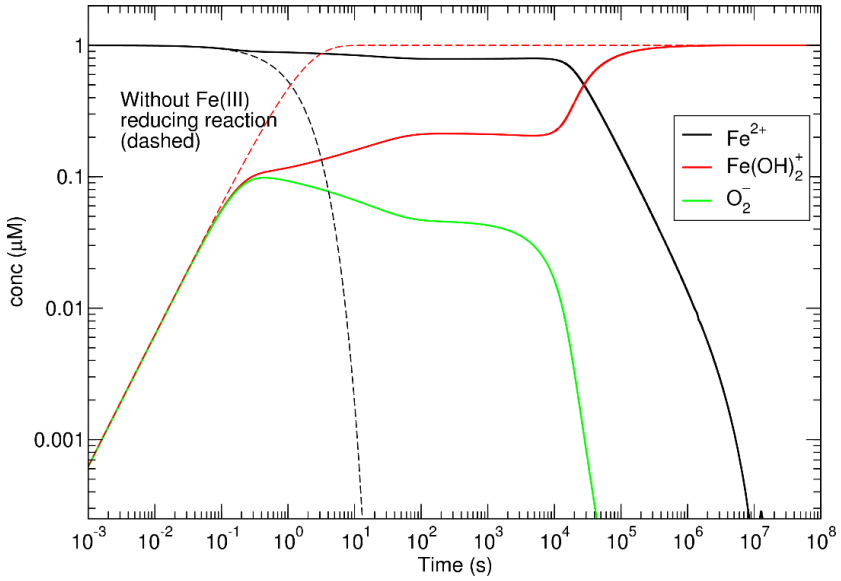

Figure 3-2. Concentrations of Fe(II), Fe(III) and O_2^- during H_2O_2 decomposition.

3.3 CONCLUSION AND FUTURE WORK

While this work identifies a mechanism for an effective Fe(II)/Fe(III) equilibrium to catalytically reduce H_2O_2 production rates, it cannot guarantee that the mechanism operates under the repository conditions of spent nuclear fuel. Future work that would measure Fe(III) solubility and precipitation rates, preferably under radiolytic conditions, are necessary for a confident inclusion of iron reaction in the RM.

3.4 REFERENCES

Buck, E.C, J.L. Jerden, W.L. Ebert, R.S. Wittman, (2013) *Coupling the Mixed Potential and Radiolysis Models for Used Fuel Degradation*, FCRD-UFD-2013-000290, M3FT-PN0806058.

Bouniol, P., (2010) *The influence of iron on water radiolysis in cement-based materials*, Journal of Nuclear Materials **403**,167–183.

De Laat , Joseph, and Gallard, Herve, (1999) *Catalytic Decomposition of Hydrogen Peroxide by Fe(III) in Homogeneous Aqueous Solution: Mechanism and Kinetic Modeling* Environ, Sci. Technol., **33**, 2726-2732.

Fenton, H.J.H. (1984). *Oxidation of tartaric acid in presence of iron*, J. Chem. Soc., Trans. 65 (65): 899–911.

Jerden, J., Frey, K., Cruse, T., and Ebert, W. (2013). *Waste Form Degradation Model Status Report: ANL Mixed Potential Model, Version 1. Archive*. FCRD-UFD-2013-000057.

Jerden, James L., Frey, Kurt, and Ebert, William (2015), *A multiphase interfacial model for the dissolution of spent nuclear fuel*, Journal of Nuclear Materials, 462: 135-146.

Sassani et al., 2012 *Integration of EBS Models with Generic Disposal System Models*, U.S. Department of Energy, Used Fuel Disposition Campaign milestone report: M2FT-12SN0806062, September, 7 2012

Shoesmith, D.W., Kolar, M., and King, F. (2003). A Mixed-Potential Model to Predict Fuel (Uranium Dioxide) Corrosion Within a Failed Nuclear Waste Container, *Corrosion*, *59*, 802-816.

Wittman RS and EC Buck. 2012. "Sensitivity of UO_2 Stability in a Reducing Environment on Radiolysis Model Parameters." In *Actinides and Nuclear Energy Material, MRS Spring 2012 Proceedings*, vol. 1444, 3-8, ed. D Andersson, et al. Cambridge University Press, Cambridge, United Kingdom. DOI:10.1557/opl.2012.1449.

3.5 APPENDIX A: REACTION LISTING FOR FULL RM

```
Equilibrium constants:
H2O  <--> H+  +  OH- : RKeq(2) = 10^(-13.999)
H2O2 <--> H+  +  HO2-: RKeq(3) = 10^(-11.65)
OH   <--> H+  +  O-  : RKeq(4) = 10^(-11.9)
HO2  <--> H+  +  O2- : RKeq(5) = 10^(- 4.57)
H    <--> H+  +  E-  : RKeq(6) = 10^(- 9.77)

        Reactions                          Rate constans (M^-n/s)
1       H+ + OH- = H2O                                 1.4d11
2       H2O = H+ + OH-                rk( 2) = rk( 1)*RKeq(2)
3       H2O2 = H+ + HO2-              rk( 3) = rk( 4)*RKeq(3)
4       H+ + HO2- = H2O2                               5.0d10
5       H2O2 + OH- = HO2- + H2O                        1.3d10
6       HO2- + H2O = H2O2 + OH-       rk( 6) = rk( 5)*RKeq(2)/RKeq(3)
7       E- + H2O = H + OH-                             1.9d1
8       H + OH- = E- + H2O                             2.2d7
9       H = E- + H+                   rk( 9) = rk(10)*RKeq(6)
10      E- + H+ = H                                    2.3d10
11      OH + OH- = O- + H2O                            1.3d10
12      O- + H2O = OH + OH-           rk(12) = rk(11)*RKeq(2)/RKeq(4)
13      OH = O- + H+                  rk(13) = rk(14)*RKeq(4)
14      O- + H+ = OH                                   1.0d11
15      HO2 = O2- + H+                rk(15) = rk(16)*RKeq(5)
16      O2- + H+ = HO2                                 5.0d10
17      HO2 + OH- = O2- + H2O                          5.0d10
18      O2- + H2O = HO2 + OH-         rk(18) = rk(17)*RKeq(2)/RKeq(5)
19      E- + H2O2 = OH + OH-                           1.1d10
20      E- + O2- + H2O = HO2- + OH-                    1.3d10
21      E- + HO2 = HO2-                                2.0d10
22      E- + O2 = O2-                                  1.9d10
23      H + H2O = H2 + OH                              1.1d1
24      H + H = H2                                     7.8d9
25      H + OH = H2O                                   7.0d9
26      H + H2O2 = OH + H2O                            9.0d7
27      H + O2 = HO2                                   2.1d10
28      H + HO2 = H2O2                                 1.8d10
29      H + O2- = HO2-                                 1.8d10
30      OH + OH = H2O2                                 3.6d9
31      OH + HO2 = H2O + O2                            6.0d9
32      OH + O2- = OH- + O2                            8.2d9
33      OH + H2 = H + H2O                              4.3d7
34      OH + H2O2 = HO2 + H2O                          2.7d7
35      HO2 + O2- = HO2- + O2                          8.0d7
36      H2O2 = OH + OH                                 2.25d-7
37      OH + HO2- = HO2 + OH-                          7.5D9
38      HO2 + HO2 = H2O2 + O2                          7.0d5
38      HO2 + HO2 = H2O2 + O2                          7.0d5
39      Fe+3 + H2O = FeOH+2 + H+                         1d5
40      FeOH+2 + H+ = Fe+3 + H2O                        0.d0
41      Fe+3 + H2O + H2O = Fe(OH)2+ + H+ + H+            1d5
42      Fe(OH)2+ + H+ + H+ = Fe+3 + H2O + H2O           0.d0
43      Fe+3 + Fe+3 + H2O + H2O = Fe2(OH)2+4 + H+ + H+         1d5
44      Fe2(OH)2+4 + H+ + H+ = Fe+3 + Fe+3 + H2O + H2O         0.d0
45      Fe+3 + H2O2 = Fe(HO2)+2 + H+                           1d5
46      Fe(HO2)+2 + H+ = Fe+3 + H2O2                           0.d0
47      FeOH+2 + H2O2 = Fe(OH)(HO2)+ + H+                      1d5
48      Fe(OH)(HO2)+ + H+ = FeOH+2 + H2O2                      0.d0
49      Fe(HO2)+2 = Fe+2 + HO2                                 2.7e-3
50      Fe(OH)(HO2)+ = Fe+2 + HO2 + OH-                        2.7e-3
51      Fe+2 + H2O2 = Fe+3 + OH + OH-                          63.0
52      Fe+2 + OH = Fe+3 + OH-                                 3.2e8
```

53	Fe+2 + HO2 = Fe(HO2)+2	1.2e6
54	Fe+2 + O2- + H+ = Fe(HO2)+2	1.0e7
55	Fe+3 + HO2 = Fe+2 + O2 + H+	1.9e3
56	FeOH+2 + HO2 = Fe+2 + O2 + H2O	1.9e3
57	Fe(OH)2+ + HO2 = Fe+2 + O2 + H2O + OH-	1.9e3
58	Fe+3 + O2- = Fe+2 + O2	5e7
59	Fe2(OH)2+4 + O2- = 2Fe+2 + O2 + OH-	5e7
60	Fe(OH)2+ + O2- = Fe+2 + O2 + OH- + OH-	5e7

4. URANIUM INTERACTION WITH BENTONITE MATERIALS

4.1 INTRODUCTION

Due to mining, milling and fuel processing operations, numerous sites have been contaminated with uranium in the past, with 38 proposed or final Superfund sites on the Environmental Protection Agency (EPA) National Priority List in the U.S. alone (NIH, 2016). In the future, the long-term storage of nuclear waste has the potential to create additional sources of uranium contamination affecting subsurface environments and drinking water resources, since spent nuclear fuel consists to approximately 95% of uranium. Chemically-induced, acute effects of uranium in humans, such as an inflammation of the kidneys (nephritis), have been reported (Hursh and Spoor, 1973), while chronic health effects and carcinogenicity are less well understood (World Health Organization, 2004). At this point in time, the World Health Organization has proposed a provisional guideline value of 15 µg uranium L^{-1} in drinking water (World Health Organization, 2004); the current U.S. EPA Maximum Contaminant Level (MCL) is set at 30 µg uranium L^{-1} (U.S. EPA, 2001). Hence, a sound scientific understanding of uranium mobility is needed in order to evaluate risks to humans and the environment, to optimize the management of nuclear waste and to take appropriate remediation actions if necessary.

While the U.S. has not yet decided on the geologic media for its long-term nuclear waste repository, in most scenarios, bentonite and clays are either the host rock media or the proposed backfill material in the engineered barrier systems (EBS) in close proximity to waste containers (Tournassat et al. 2015b). From a mineralogical perspective, sodium-montmorillonite clay is the major component of bentonite, and largely responsible for bentonite properties relevant for contaminant mobility. Given the low porosity and permeability, and the swelling properties of montmorillonite, diffusion is expected to be the primary transport mechanism in engineered barrier systems. Hence, accurate predictions of uranium(VI) transport behavior in the near- and far-fields will be dependent on a realistic conceptual understanding of uranium(VI) diffusion in clays and bentonite close to the source term.

Uranium(VI) mobility on the field-scale is ultimately controlled by the parameters and processes effective at micro- and nanometer scales. First, uranium(VI) sorption onto bentonite and sodium-montmorillonite is an important, and potentially limiting, process affecting uranium(VI) fluxes and contaminant retardation. Second, the small-scale diffusion-accessible porosities of montmorillonite will largely determine the magnitude of uranium(VI) fluxes across the EBS. A prediction of uranium(VI) adsorption and diffusion processes in clay-rich media, however, is complicated by: (1) the complex uranium(VI) solution speciation, which can include cationic, neutral, and anionic species, depending on chemical solution conditions, and (2) the complexity of the mineralogical structure of montmorillonite clay, in terms of its pore-size distributions, diffusion-accessible porosities, and available surface site types.

First, with regard to solution speciation, uranium can exist at oxidation states of IV or VI, but U(VI) is the most relevant oxidation state in most surface waters and in oxic groundwaters (Choppin, 2006). In reducing environments, the low solubility of U(IV) mineral phases greatly decreases uranium mobility. Furthermore, numerous studies have demonstrated the impacts of pH, bicarbonate and calcium concentrations on U(VI) solution speciation, adsorption and transport behavior (Davis et al. 2004; Curtis et al. 2006; Fox et al. 2006; Hartmann et al. 2008; Yabusaki et al. 2008; Ma et al. 2010; Kerisit et al. 2010; Bradbury and Baeyens 2011; Joseph et al. 2011).

Potential changes in chemical solution conditions and contaminant solution speciation over time and space are especially relevant for uranium, given the long half-lives of uranium isotopes and complex transport pathways in engineered barrier systems and the natural environment. For instance, in nuclear waste repositories, pore-water pH is buffered at values between 7 and 8 in the bentonite backfill material of the EBS surrounding waste canisters and/or in the clay host-rock (Muurinen and Lehikoinen 1999;

Bradbury and Baeyens 2003; Wersin 2003; Wersin et al. 2004; Tournassat et al. 2015c). However, more alkaline pH conditions are expected in close proximity to steel canisters (pH 8 – 11) due to corrosion processes (Bildstein and Claret, 2015), as well as in cementitious leachates at bentonite-concrete boundaries (pH>13 for Ordinary Portland Cement and pH 9 – 11 for low alkali cement) due to the chemical degradation of cement (Savage et al. 1992; Gaucher and Blanc 2006; Gaboreau et al. 2012b; Milodowski et al. 2016). Furthermore, dissolved calcium concentrations may also vary over time and space due to the progressive degradation of cement-based engineered barriers, the specific calcite contents in clay host rocks or changing concentrations in carbonate minerals along transport pathways (Hartmann et al. 2008; Gaboreau et al. 2012a; Adinarayana et al. 2013).

These chemical gradients in waste scenarios are important for the fate and transport of uranium, since U(VI) aqueous speciation is very complex and controls the extent and processes behind U(VI) adsorption reactions (e.g., cation exchange versus surface complexation reactions), as well as the U(VI) diffusion-accessible porosities and diffusion pathways (e.g., anion exclusion from clay interlayer spaces for anions versus 'surface diffusion' along basal cation exchange sites for cations). For instance, the uranyl cation (UO_2^{2+}) typically dominates speciation at low pH, while neutral and anionic U(VI)-hydroxyl and carbonate complexes become predominant at higher pH conditions. In a dilute U(VI) solution at pH 7 in the absence of carbonate, the predominant U(VI) species is the neutral $UO_2(OH)_2^0$. In comparison, for the same solution in equilibrium with atmospheric CO_2, the predominant species is the anion $(UO_2)_2CO_3(OH)_3^-$ (for a 1 µM solution). However, groundwater solutions are typically in equilibrium with partial pressures of CO_2 at 1% or greater, and may contain considerable concentrations of calcium due to the presence of carbonate minerals. At 1% CO_2, pH 7 and in the *absence* of Ca, U(VI) solution speciation is dominated by the anion $UO_2(CO_3)_2^{2-}$ (Figure 4-1). For a comparable solution in equilibrium with calcite, the predominant U(VI) species is the neutral $Ca_2UO_2(CO_3)_3^0$ (Figure 4-2).

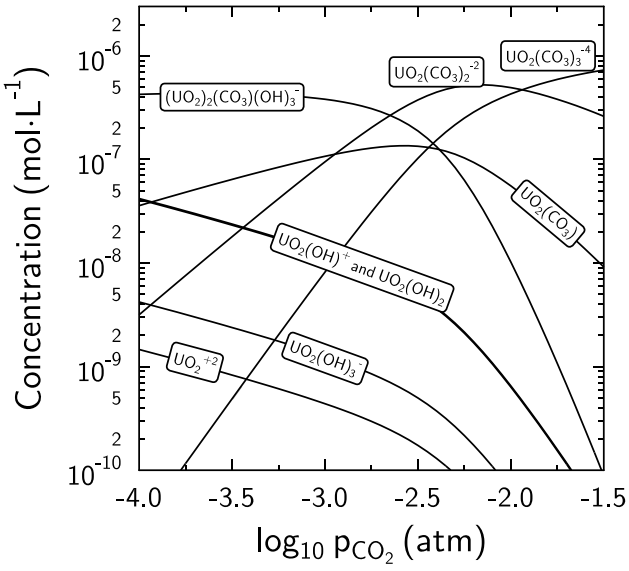

Figure 4-1. Uranium(VI) speciation as a function of the partial pressure of CO_2 in a 1 µM U(VI) solution in 0.1 M NaCl at pH 7 in the absence of Ca. Calculations were made with PHREEQC and the THERMOCHIMIE database (Giffaut et al. 2014).

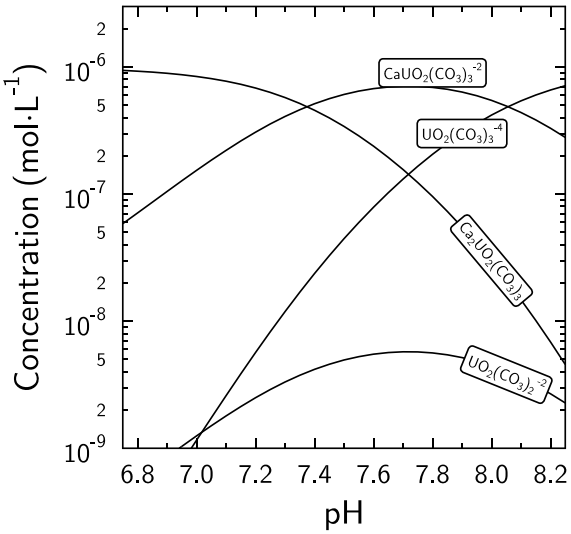

Figure 4-2. Uranium(VI) speciation as a function of pH in a 1 µM U(VI) solution in 0.1 M NaCl in equilibrium with a partial pressure of CO_2 at 1% and in equilibrium with calcite. Calculations were made with PHREEQC and the THERMOCHIMIE database (Giffaut et al. 2014).

The second major factor complicating a prediction of contaminant mobility in the EBS is the complex mineralogical structure of sodium-montmorillonite, the major component of bentonite in barrier systems, which affects both contaminant adsorption and diffusive transport behavior. Montmorillonite is a smectite, a 2:1-layer-type dioctahedral phyllosilicate with a large specific surface area (~750 $m^2 \cdot g^{-1}$) and cation exchange capacity (~1 $mol_c \cdot kg^{-1}$). Each montmorillonite layer has a thickness of ~1 nm and carries negative surface charges due to isomorphic substitutions of Al(III) for Si(IV) and Mg(II)/Fe(II) for Al(III) in its phyllosilicate framework (Brigatti et al. 2013). Due to its mineralogical structure, montmorillonite provides two types of surfaces and surface site types: (1) cation exchange sites with a permanent surface charge on basal planar surfaces, and (2) surface complexation sites, with variable surface charges as a function of pH, on edge surfaces of clay particles.

A fundamental understanding of U(VI) adsorption processes and the resulting U(VI) surface speciation on Na-montmorillonite is essential for an accurate prediction of uranium(VI) retardation and the magnitude of U(VI) diffusive fluxes across the EBS. As a result, many research groups have investigated the surface speciation of adsorbed U(VI) on montmorillonite with Extended X-ray Absorption Fine Structure (EXAFS) absorption spectroscopy (Dent et al. 1992; Chisholm-Brause et al. 1994; Giaquinta et al. 1997; Sylwester et al. 2000; Hennig et al. 2002; Catalano and Brown, 2005; Schlegel and Descostes, 2009; Marques Fernandes et al. 2012; Troyer et al. 2016). The analysis of the spectra obtained at various ionic strengths has revealed the presence of U(VI) outer-sphere complexes at low pH and/or low ionic strengths, and of U(VI) inner-sphere complexes at other conditions. These interpretations of EXAFS data are in qualitative agreement with the duality of adsorption mechanisms on montmorillonite surfaces, i.e. cation exchange on basal planar surfaces at low pH/ionic strength and surface complexation on edge surfaces at other conditions, as also evinced by other spectrometric techniques for a range of different specifically adsorbed cations (Morris et al. 1994; Chisholm-Brause et al. 2001; Kowal-Fouchard et al. 2004; Wolthers et al. 2006).

The formation of inner-sphere bonds of U(VI) with surface groups at montmorillonite edge sites at neutral pH and high ionic strengths was deduced from the splitting of the U(VI) oxygen equatorial shell into two distinct contributions at ~2.3 Å and ~2.5 Å in EXAFS spectra. However, there is considerable uncertainty in the interpretation of second neighbor atoms involved in these surface complexes. Hennig et al. (2002) concluded that surface mononuclear bidentate complexes formed at aluminol sites. Schlegel and Descostes (2009) also proposed a U-Al shell, in agreement with Hennig et al. (2002). Additional Polarized-EXAFS (P-EXAFS) characterizations allowed them to conclude that the U complex was located on the particle edges and corresponded to a mononuclear bidentate complex. In contrast, Catalano and Brown (2005) suggested that the primary surface group second neighbors were Fe atoms, where Fe has substituted for Al in the octahedral sheets. In addition, Catalano and Brown (2005) fitted their data with a U-C shell and suggested that ternary uranyl-carbonato species formed at the surface in the presence of carbonate. However, more recently, Marques Fernandes et al. (2012) and Troyer et al. (2016) concluded that it was not possible to conclusively distinguish between Fe, Al, and Si as second neighbor atoms in U(VI) EXAFS spectra. Furthermore, Marques Fernandes et al. (2012) did not find spectroscopic evidence for uranyl-carbonato complexes at the montmorillonite surface, despite the fact that their surface complexation model included this species. Troyer et al. (2016) were not able to confirm the presence of ternary uranyl-carbonato surface complexes from their EXAFS data either, but made a strong conclusion about the presence of such species from laser-induced fluorescence spectroscopy (LIFS) data. The LIFS results, however, were obtained at very high U(VI) equilibrium concentrations and U(VI)/clay ratios. The total U(VI) concentration was 100 µM and solid-to-liquid ratio was 0.2 $g \cdot L^{-1}$, leading to an equilibrium U(VI) solution concentration of ~70 µM. Although it is not known, these conditions might have favored the formation of uranyl carbonate complexes driven by a high total uranium-carbonate ratio. In short, current results from spectroscopic sorption studies are still associated with a large degree of uncertainty regarding the relevance of ternary uranyl-carbonato surface complexes and the interpretation of second neighbor atoms involved in U(VI) surface complexes at montmorillonite edge sites.

Nevertheless, an accurate prediction of uranium mobility in clay-rich environments is dependent upon the development of adsorption models that can capture: (1) the complex uranium solution and surface speciation as a function of chemical solution conditions, and (2) the complexity of montmorillonite and its implications for the conceptual description of adsorption processes. Surface complexation models (SCMs) have the ability to directly link U(VI) adsorption behavior with U(VI) solution speciation based on existing thermodynamic data, which allows the models to predict changes in adsorption as a function of chemical solution conditions over time and space.

Several research groups have developed surface complexation models (SCMs) for the U(VI)-montmorillonite system (Pabalan and Turner 1996; Turner et al. 1996; Hyun et al. 2001; Bradbury and Baeyens 2005, 2011; Marques Fernandes et al. 2012). Surface complexation modeling studies predict that U(VI) adsorption decreases at alkaline pH when carbonate anions are present, due to the formation of strong uranyl-carbonato solution complexes (see Figure 4-1, and aqueous speciation diagrams in Davis et al. 2004 and Fox et al. 2006). The quantification of this effect was however dependent on the consideration, or not, of a retention mechanism of these uranyl-carbonato solution complexes on the clay surfaces. For example, in the model of Marques Fernandes et al. (2012), the authors found it necessary to include ternary uranyl-carbonato surface complexes to describe U(VI) adsorption onto montmorillonite in the presence of various concentrations of aqueous carbonate. Analogous U(VI) surface species have also been proposed on iron oxides and imogolite (Waite et al. 1994; Villalobos et al. 2001; Arai et al. 2006). For U(VI) adsorption on montmorillonite, however, in the absence of clear spectroscopic evidence, the need to add such additional surface complexes was solely guided by the quality of the fit between the model and the data. This fitting criterion may however be impaired by inadequate hypotheses in the modeling exercise. For example, the model of Marques Fernandes et al. (2012) was a non-electrostatic model, which means that the ionic nature of the sorbent and its interaction with the electrostatic potential field surrounding the montmorillonite particles is inherently not included. Given the complex U(VI)

solution speciation described above, it is important to take into account that the interactions of cationic, neutral or anionic U(VI) solution species with the surface electrostatic field is influenced by their charge. Hence, an electrostatic model is needed in order to test whether the importance of this electrostatic interaction is of first order to quantify U(VI) adsorption processes accurately, and whether it has an impact on the need to include ternary uranyl-carbonato surface complexes in the model.
However, currently available electrostatic surface complexation models for montmorillonite have mostly been based on the classical surface complexation models for oxides. These models include the hypothesis that surface charges are homogeneously distributed on a flat and infinite surface, which is invalid for clay minerals for the following two reasons. First, the edge surface is very different from a flat infinite surface in terms of its specific surface area and electrostatic surface potential. Second, the surface potential developed by the permanent charges of the basal surfaces interacts with the surface potential at the edge surfaces with pH-dependent charges (Tournassat et al. 2013, 2016a). This unique and relevant feature, called the 'spillover' effect, must be taken into account in the development of an electrostatic model for montmorillonite edge surfaces.

Given the current uncertainties associated with results from spectroscopic studies and the modeling needs described above, our goals with regards to U(VI) adsorption processes onto Na-montmorillonite were:

1) to improve the current mechanistic understanding of uranium(VI) adsorption onto montmorillonite as a function of chemical conditions, with a specific focus on the role of dissolved inorganic carbon; and
2) to develop an electrostatic surface complexation model that accounts for the impacts of the electric-double-layer (EDL) spillover effect on U(VI) surface reactions.

Besides U(VI) adsorption processes, the complexity of the montmorillonite structure will also affect the diffusive transport behavior of U(VI) in the EBS. For instance, the 'co-existence' of small interlayer pores within particles and larger macropores between clay particles can create two types of clay porosities and diffusion pathways. The relevance of the individual porosities and pathways is strongly dependent on system characteristics, such as the degree of bentonite compaction, chemical solution conditions, and the charge of contaminant species in solution. For example, a partial or full exclusion of anions from negatively charged clay interlayer spaces can change the effective 'anion-accessible' porosity and decrease the diffusive flux of these solutes under steady state conditions. As a result, diffusive fluxes can vary substantially between cations, anions and uncharged solutes. Furthermore, radionuclides that show dramatic changes in their chemical solution speciation as a function of pH, such as uranium(VI) are expected to show different diffusive transport behavior under varying chemical solution conditions.

Based on the literature we have reviewed, at present full or partial anion exclusion effects have not been clearly demonstrated experimentally for anionic uranium(VI) species, despite the theoretical understanding of the uranium(VI)-montmorillonite system described above. This is, at least in part, due to the difficulties associated with the experimental approach of so-called uranium(VI) through-diffusion experiments, which monitor the breakthrough and diffusive fluxes of uranium(VI) across a diffusion cell over the course of an experiment. Almost all previously reported uranium(VI)-montmorillonite/bentonite diffusion experiments were based on an evaluation of total uranium(VI) concentrations (dissolved plus sorbed concentrations) as a function of distance in the clay packing after the completion of experiments. While this approach still allows determining apparent uranium diffusion coefficients and sorption distribution coefficients (K_D values) based on the simulation of the concentration profile, the associated model parameters are less constrained, and direct observations of solute retardation, diffusive fluxes, and any potential kinetic effects are not possible.

Hence, our research goals with regard to U(VI) diffusion in Na-montmorillonite were:

(1) to provide clear, direct experimental evidence for U(VI) anion exclusion effects in through-diffusion experiments at alkaline pH conditions; and
(2) to complete a set of two, parallel uranium(VI) through-diffusion experiments, started during FY 2015, which also required a detailed, analytical characterization of the chemical composition of sample solutions in order to allow for a simulation of U(VI) solution speciation in later diffusion models.

In this section, we will first describe our experimental and modeling efforts regarding the investigation of uranium(VI) sorption behavior onto Na-montmorillonite, followed by a summary of experimental setups and results for U(VI) diffusion experiments. Finally, we will present our overall summary and conclusions and end with an outlook on planned future work.

4.2 DEVELOPMENT OF URANIUM(VI)-MONTMORILLONITE SURFACE COMPLEXATION MODEL

4.2.1 Materials and Methods

For the development of U(VI) surface complexation models, it is important to carefully characterize the compositions of experimental solutions, because various other solutes may affect U(VI) solution or surface speciation. Uranium(VI) adsorption onto Na-montmorillonite was investigated here as a function of total U(VI) and calcium concentrations and partial pressures of CO_2 (Table 4-1). Experimental blanks, standards and sample suspensions were analyzed for U(VI), calcium and dissolved inorganic carbon (DIC) concentrations, and monitored for elements that could indicate clay dissolution or inadequate solid-liquid phase separation. Analysis of DIC concentrations in supernatant solutions was of particular importance in our experiments, given the relevance of carbonate for U(VI) speciation. Measured DIC concentrations allowed us to back-calculate actual pCO_2 values for all samples individually. In addition, analytical detection limits and experimental background values for DIC solution concentrations were determined as described in further detail below.

Materials: Glassware was cleaned by soaking in acid (10% (v/v) HCl) over 12 to 24 hours, followed by thorough rinsing with Nanopure water and air-drying. All aqueous solutions were prepared with Nanopure water (Barnstead ultrapure water system) using chemicals of reagent grade or better. Acids, bases and salt solutions used in adsorption experiments were of TraceSelect grade (Sigma Aldrich), in order to minimize calcium background concentrations in particular. Uranium(VI) solutions contained U-238, either from an in-house or a commercially available uranyl nitrate stock solution (1.30 mM stock provided by Drs. David Singer and Wayne Lukens at Lawrence Berkeley National Laboratory, or various dilutions of a 1000 µg U/mL Inorganic Ventures ICP-MS standard).

A well-characterized, standardized source clay (Na-montmorillonite, Standardized Na-montmorillonite source clay from Wyoming, provided by the Clay Minerals Society (SWy-2), Clay Minerals Society) was selected as the sorbent. Since this material is known to contain considerable impurities of quartz (8%), feldspars (16%) and calcite (Chipera and Bish 2001; Costanzo and Guggenheim 2001; Mermut and Cano 2001), it was pretreated to avoid uncontrolled impacts of calcite dissolution on U(VI) solution speciation during adsorption experiments. The major purification steps, which have been described in detail elsewhere (Tinnacher et al. 2016), included: (1) dissolution of calcite impurities in 1 M sodium acetate/0.564 M acetic acid solution at pH 5, (2) conversion of the clay into its Na form, (3) separation of quartz and feldspar impurities from the <2 µm clay fraction by centrifugation, and (4) oven-drying of the clay mineral phase at 45 °C. Afterwards, clay stock suspensions of 10 or 20 g L^{-1} were prepared in Nanopure water, and exact solid concentrations determined by weighing volume fractions before and after drying at 45 °C.

Batch Adsorption Experiments: Uranium(VI) adsorption onto Na-montmorillonite was characterized as a function of total U(VI) and calcium concentrations and "target" partial pressures of CO_2 (atmospheric CO_2, 2 % CO_2 and CO_2-free atmospheres). An overview of all experimental conditions is provided in Table 4-1. Batch adsorption experiments were conducted at room temperature (22.5 – 23.5 °C) at an ionic strength of 0.1 M, and a Na-montmorillonite concentration of 0.5 $g \cdot L^{-1}$ (except for experiment 7 with a solid concentration, m_s, of 0.24 $g \cdot L^{-1}$). The pH values ranged from 4.0 to 10.0. The reaction time was 48.5 hours, which closely approached or was sufficient to reach steady-state conditions. This reaction time is comparable to adsorption time-frames over 20-72 hours used in other, similar studies (Chisholm-Brause et al. 1994; Hyun et al. 2001; Bradbury and Baeyens, 2005; Schlegel and Descostes, 2009). Total calcium concentrations varied from low micromolar background concentrations (see Table 2-1) to the higher concentration of 2.1 mM in the experiment with added Ca.

Table 4-1. Experimental conditions for U(VI) batch adsorption experiments.

.Exp.	Actual, total U(VI) conc. ($\mu mol \cdot L^{-1}$)	Target CO_2 partial pressures	Back-calculated range of CO_2 partial pressures [1]			Ca concentrations ($\mu mol \cdot L^{-1}$) [2]
			log pCO_2 (atm)	pCO_2 (%)	pCO_2 (ppm)	
1	0.11	Laboratory air	-3.5 to -2.8	0.03 - 0.16	316 - 1585	6.7 - 8.5
2	0.96	Laboratory air	-3.6 to -3.1	0.03 - 0.08	251 - 794	6.4 - 1.9
3	2.6	Laboratory air	-3.5 to -2.8	0.03 - 0.16	316 - 1585	9.1 - 13
4	0.98	Laboratory air	-3.5 to -3.1	0.03 - 0.08	316 - 794	2100
5	1.1	Zero	-7 to -3.1	0.00 - 0.08	0 - 794	7.7 - 9.8
6	0.81	2% CO_2	-4 to -2	0.01 - 1.00	100 - 10000	10 - 27
7	0.98	2% CO_2	-2.7 to -2.1	0.20 - 0.79	1995 - 7943	10 - 13

[1] Based on back-calculation with measured DIC concentrations in sample solutions.

[2] Ca concentration in experiments 1 – 3 and 5 – 7 represent background values without any Ca additions.

Solutions were in contact with three different gas phases that varied in terms of their *target* partial pressures of CO_2: (1) atmospheric CO_2 in laboratory air (~0.04%, 400 ppm), (2) CO_2-"free" atmosphere (glove box, filled with 95% N_2/5% H_2 gas mixture), and (3) a *target* 2% CO_2 atmosphere. With respect to the last concentration, experiment 6 was conducted with a disposable Sigma Aldrich glove bag purged with certified 2% CO_2/balance nitrogen gas mixture. Experiment 7 was conducted in a COY anaerobic chamber filled with a 2% CO_2/98% nitrogen mix).

In the experiments performed under atmospheric or elevated CO_2 levels, additions of aliquots of $NaHCO_3$ solution were used to facilitate equilibration with the gas phases for samples with pH values of 7.0 or greater. Added aliquots of background electrolyte (NaCl) were decreased to account for the contributions of $NaHCO_3$ or $CaCl_2$ to the ionic strengths of the solutions. Fifty-mL polycarbonate centrifuge vials ('Oakridge centrifuge tubes') were used as sample vials to minimize U(VI) wall adsorption effects. In addition to samples containing Na-montmorillonite and U(VI) (1 replicate per pH condition), each

experiment included experimental standards (in duplicate) to determine values of total, initial U(VI) solution concentrations. These standards had the same volume of U(VI) stock solution added to a vial in the absence of a mineral phase with the pH adjusted to 2.0. In addition, electrolyte blanks (in duplicate) containing 0.1 M NaCl but no U(VI) or solid were used to determine calcium and uranium-238 background concentrations in the absence of solid phases.

The main steps in the batch adsorption experiments were: (1) pre-equilibration of Na-montmorillonite with a background electrolyte solution at the specified pH and chemical solution conditions, (2) U(VI) adsorption equilibration with the mineral phase, and (3) sampling and analysis of supernatant fractions after removal of the solid phase by centrifugation. At the beginning of experiments, aliquots of Nanopure water, Na-montmorillonite stock suspension, 1 M NaCl solution, and 1 M or 0.1 M $NaHCO_3$ solution were transferred into sample vials to yield the target solid concentrations and ionic strengths in the final sample volumes. pH values were adjusted with small volumes of HCl or NaOH solutions, and solutions were pre-equilibrated in closed sample vials by shaking for 12 to 24 hours.

After pre-equilibration with the electrolyte solution, aliquots of U(VI) stock solution were added to obtain the desired total U(VI) concentrations in the experiments. After re-adjustment of pH, the vials were shaken for 48.5 hours. Afterwards, final pH values were recorded while attempting to minimize gas exchange during pH measurements (discussed further below). Then, the sample suspensions were centrifuged to remove particles larger than approximately 50 nm from solution, as calculated based on Stokes law (Beckman Coulter Allegra 64R, F0850 rotor, centrifugation at 26 900 g for 61 minutes). Aliquots of supernatant solution were collected to analyze for metal concentrations by ICP-MS (Perkin-Elmer SCIEX ICP-Mass Spectrometer ELAN DRC II, after sample acidification with TraceSelect grade HNO_3 (2% v/v)), and dissolved inorganic carbon (DIC) concentrations on a Shimadzu TOC-V_{CSH}.

Experimental results for batch adsorption experiments are reported in terms of distribution coefficients (K_D values, in $L \cdot kg^{-1}$) and fractions of U(VI) adsorbed ($f_{U(VI)_{adsorbed}}$ in %) after adsorption for 48.5 hours. Adsorbed U(VI) fractions and K_D values were computed based on concentration differences in supernatant solutions between experimental standards and samples:

$$f_{U(VI)_{adsorbed}} = \frac{U_{Std,supernat.} - U_{Sample,supernat.}}{U_{Std,supernat.}} \times 100 \quad (4\text{-}1)$$

$$K_D = \frac{f_{U(VI)_{adsorbed}} \times U_{Std,supernat.}}{100 \cdot m_s \cdot U_{Sample,supernat.}} \quad (4\text{-}2)$$

where $U_{supernat.}$ represents U(VI) concentrations in supernatant solutions for standards (subscript *Std*) and individual sample vials (subscript *Sample*), and m_S the solid concentration in kg L^{-1}.

Analytical Detection Limits and Background Values for Dissolved Inorganic Carbon: The manufacturer of the Shimadzu TOC-V_{CSH} instrument reports a detection limit of 4 $\mu g \cdot L^{-1}$ carbon. However, actual method detection limits are often dependent on the specific purity of water and reagents used to prepare calibration standards. Hence, following recommendations by the U.S. EPA (1995), the Method Detection Limit (MDL) and Minimum Level (ML) were determined for the specific setup of our DIC analysis on two separate days. The MDL represents the minimum DIC concentration that can be identified, measured and reported with a 99 % confidence that the concentration is greater than zero (U.S. EPA 1995). The ML is defined as the smallest measured concentration of a constituent that may be reliably reported using a given analytical method. Its value corresponds to the limit of quantitation (LOQ) established by the American Chemical Society, and is computed by multiplying the MDL by a factor of 3.18.

Furthermore, potential DIC contributions from various sources in the CO_2-"free" batch adsorption experiment, performed in a 95% N_2/5% H_2 glove box environment, were quantified. In particular, as will be discussed later, it was necessary to understand if measured DIC concentrations had been present in solution during U(VI) adsorption equilibration, or if they represent a DIC contamination that was introduced into samples at a later point in time. For this particular experimental setup, potential sources of DIC contamination include: (1) DIC background concentrations in Milli-Q Water (MQW) (before and after purging with nitrogen gas) used for the later preparation of montmorillonite suspensions in the glove box, (2) handling of open sample vials in the glove box, if CO_2 was not fully excluded from the glove box atmosphere (maximum handling time for open vials estimated at 3-4 hours), (3) introduction of CO_2 into closed sample vials during centrifugation under atmospheric CO_2 outside the glove box, and (4) diffusion of atmospheric CO_2 into refrigerated, closed sample vials during a six-day storage period prior to DIC analysis.

Experimental Challenges in Experiments at Elevated CO_2 Partial Pressures: In experiment 6, it was difficult to create a controlled 2% CO_2 atmosphere using a disposable glove bag (Sigma Aldrich), which was repeatedly purged with a 2% CO_2/balance nitrogen gas mixture. In experiment 7, some of the problems associated with the disposable glove bag were avoided by using a Coy gas chamber. However, similarly to experiment 6, results from the DIC analysis of supernatant solutions suggest that samples were not fully equilibrated with the intended CO_2 partial pressure of 2% (see Experimental Results section 4.3 for details).

Despite these problems, DIC measurements in the final solutions allowed for an individual calculation of U(VI) aqueous speciation for each experimental sample. Although it was desired to have identical partial pressures of CO_2 for each series of vials in a particular experiment so that data could be illustrated and compared under identical conditions, DIC measurements showed that the solutions were not completely equilibrated with the respective gas phases, particularly for the elevated CO_2 atmospheres. Fortunately, for the purpose of creating an equilibrium geochemical model (and SCM) that describes the effect of dissolved carbonate on U(VI) speciation and adsorption, it was not necessary to have the same partial pressure of CO_2 in each vial. By measuring DIC in all sample solutions, including those from the laboratory air experiment, the equilibrium geochemical model determined the U(VI) aqueous speciation for each experimental data point rather than assuming a constant specific partial pressure of CO_2 in equilibrium with the aqueous phase. As will be discussed further below, this was very important in describing the observed U(VI) adsorption behavior in the SCM.

4.2.2 Experimental Results

Equilibration of Solutions with CO_2 in Gas Phases

Dissolved Inorganic Carbon Detection Limits and Background Contributions: Based on two analyses performed on different days, the Method Detection Limit (MDL) and Minimum Level (ML) were determined to be 0.051 and 0.161 $mg \cdot L^{-1}$ DIC (4.2E-6 and 1.3E-5 $mol \cdot L^{-1}$ DIC). Taking into account the offset due to DIC background concentrations in (MQW), calibration curves showed linearity down to the lowest concentration standard at 0.025 $mg \cdot L^{-1}$ (2.1E-6 $mol \cdot L^{-1}$) of added DIC.

The characterization of DIC background concentrations showed similar values for MQW before (0.121 $mg \cdot L^{-1}$, 1.0E-5 mol $mg \cdot L^{-1}$) and after (0.125 $mg \cdot L^{-1}$, 1.0E-5 mol L^{-1}) purging with nitrogen gas. The handling of open sample vials in the glove box atmosphere in the CO_2-"free" adsorption experiment, centrifugation of closed vials under atmospheric CO_2 conditions, and the refrigeration of closed vials outside the glove box prior to DIC analysis were each evaluated for their potential to increase measured DIC concentrations in N_2-purged MQW samples. Sample handling and centrifugation, which took place prior to supernatant sampling in the CO_2-"free" adsorption experiment, resulted in 0.344 and 0.277 $mg \cdot L^{-1}$

DIC (2.9E-5 and 2.3E-5 mol·L^{-1} DIC) concentrations during the test experiment. Storage of solutions in the refrigerator, which occurred after supernatant sampling in the adsorption experiments, resulted in a concentration of 0.331 mg·L^{-1} DIC (2.8E-5 mol·L^{-1} DIC) during testing.

Given the similarity of DIC contributions from these potential sources and the series of steps in the CO_2-"free" adsorption experiment, it can be assumed that open handling of sample solutions in the not-fully CO_2-"free" glove box atmosphere represented the major source of DIC contamination in the CO_2-"free" adsorption experiment. However, since most of the open handling of sample solutions occurred prior to the U(VI)-montmorillonite adsorption equilibration step in closed sample vials, we can further assume that measured DIC values represent actual DIC concentrations, present in sample suspensions during U(VI) sorption equilibration steps.

Measured DIC concentrations in batch adsorption experiments: A summary of measured DIC concentrations and calculated pCO_2 data are also plotted in Figure 4-3 (two bottom and top right panels). The calculations of pCO_2 were carried out with measured solution compositions (specifically DIC and pH) using PHREEQC v.3 (Parkhurst and Appelo, 2013) with the THERMOCHIMIE database (Giffaut et al. 2014). Experiments carried out in the presence of atmospheric CO_2 ($\sim 10^{-3.45}$ atm) resulted in measured DIC concentrations roughly in agreement with geochemical model calculations for this pCO_2. Samples from the CO_2-"free" glove box experiment had DIC concentrations similar to solutions observed under atmospheric conditions for pH< 6, suggesting CO_2 contamination as described above. However, in samples at pH>6 DIC concentrations, and consequently the calculated pCO_2 values, were much lower than those under atmospheric conditions (Figure 4-1).

In experiments with a target value of 2% CO_2 in the gas phase (experiments 6 and 7), DIC results suggest that the gas bag or gas chamber was not sufficiently purged with the 2% CO_2/balance N_2 gas to achieve the intended 2% partial pressure. This was the case despite multiple purge volumes that were used to clear the bag and gas chamber in these experiments. In experiment 6, solutions up to a pH of 7.24 exhibited DIC concentrations that suggested equilibration with a gas phase composition closer to ~1% CO_2. Samples from supernatants at higher pH values had DIC concentrations consistent with even lower partial pressures of CO_2. This trend is most likely due to insufficient purging combined with a lack of fast CO_2 equilibration between the aqueous phase and the local atmosphere in the gas bag.

In experiment 7, the calculated low pCO_2 values at acidic pH suggest that the Coy gas chamber was also not sufficiently flushed to achieve the target CO_2 partial pressure. Although the solutions contained added $NaHCO_3$ such that they would be equilibrated with a 2% CO_2 gas phase, DIC data indicate that some CO_2 outgassed from solutions into the chamber atmosphere, driven by a pCO_2 value lower than 2%. Despite these problems, DIC measurements in the supernatant solutions allowed for an individual calculation pCO_2 values and U(VI) solution speciation in each sample.

U(VI) Adsorption Behavior under Varying Chemical Conditions

Effect of Variable pCO_2: Under atmospheric CO_2, U(VI)-montmorillonite K_D values varied over four orders of magnitude as a function of pH (Figure 4-3, left panel). At low pH, U(VI) adsorption is assumed to be limited due to its competition with protons at surface complexation sites (Stumm 1992). At high pH, low uranium adsorption is attributed to increasing carbonate concentrations, leading to weakly sorbing or non-sorbing aqueous U(VI)-carbonate complexes (Hsi and Langmuir 1985; Waite et al. 1994; Davis et al. 2004).

In the CO_2-"free" system, the shape of the U(VI) adsorption envelope is different compared to atmospheric CO_2 systems. In the low-pH region, U(VI) adsorption characteristics remain similar with comparable K_D values in the pH range from 4 to 6; above pH 6.5, however, U(VI) adsorption is much

stronger at very low concentrations of CO_2. The greater U(VI) adsorption at high pH under low CO_2 conditions can be attributed to much lower concentrations of aqueous U(VI)-carbonate complexes that compete effectively with binary U(VI) surface complexation. A similar effect of the competition between aqueous carbonate and surface sites for U(VI) complexation is also observed when comparing U(VI) adsorption in systems at elevated at atmospheric CO_2 conditions, where U(VI) adsorption is lower at higher dissolved carbonate concentrations at pH values above 5.5 (Figure 4-3).

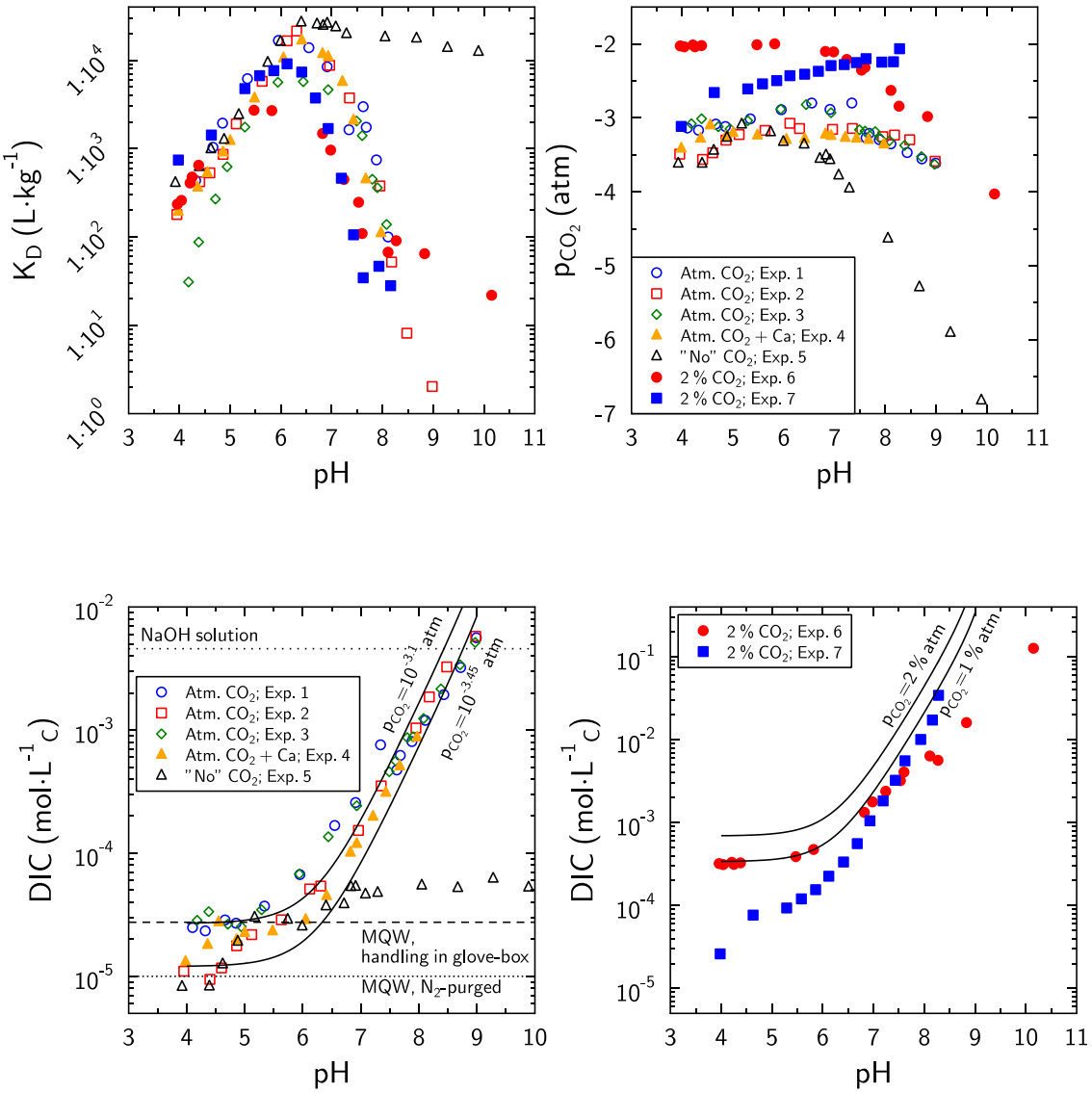

Figure 4-3. Top left: U(VI) adsorption as a function of pH and target pCO_2 partial pressures. Top right: Actual pCO_2 partial pressures calculated from DIC concentrations measured in supernatant samples as depicted in two bottom panels.

Effect of Variable Calcium Concentrations: Under atmospheric CO_2 conditions, U(VI) adsorption appeared to be approximately the same in the presence of 2.1 mM $CaCl_2$ compared to Ca background concentrations (Figure 2-1, left). At pH~8, the U(VI) K_D value appeared to be lower by approximately a

half an order of magnitude (compare experiments 2 and 4 with similar total U(VI) concentrations). However, it is difficult to be certain of this effect because of differences in experimentally observed DIC concentrations. In this pH region, U(VI) aqueous speciation changes in the presence of 2 mM Ca concentrations, which leads to the formation of aqueous ternary Ca-U(VI)-carbonate complexes at pH>7.5 (Figure 4-4). This effect is evaluated further in the modeling section, where calculations are made at a constant pCO_2 partial pressure.

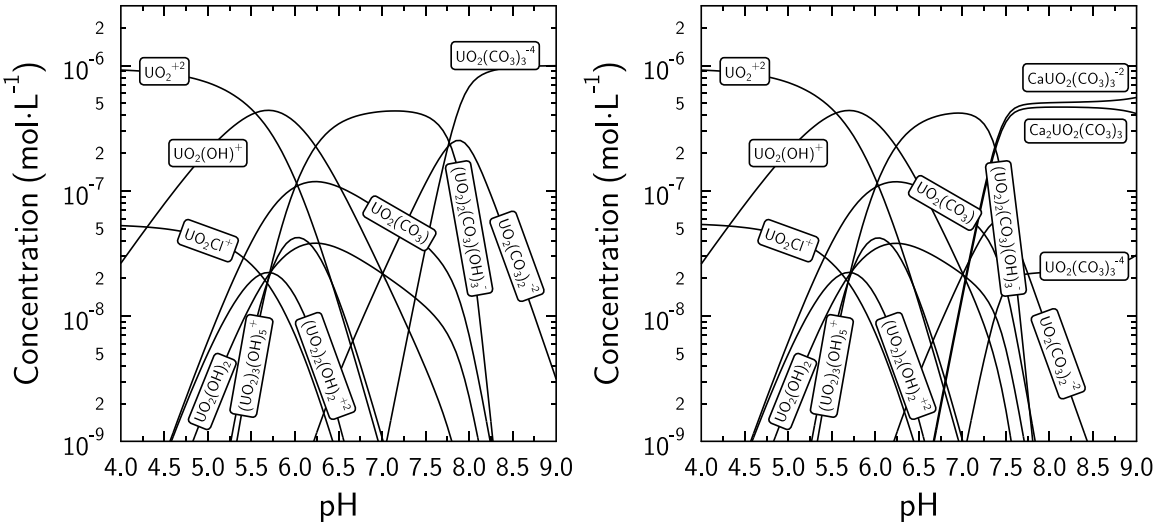

Figure 4-4. Aqueous speciation of a 1 μM U(VI) solution in 0.1 M NaCl in equilibrium with atmospheric CO_2 (log CO_2 = -3.45) in the absence (left) and presence of 2 mM Ca (right). Vertical axis is the negative log of the concentration of each U(VI) species.

4.2.3 Modeling and Discussion

Surface Complexation Modeling Strategy: An analysis of the literature shows that considerable uncertainty remains on the nature of inner-sphere complexes on montmorillonite edge surfaces. Surface complexation modeling cannot elucidate the nature of clay atoms present on surface sites, i.e., decipher the contributions of aluminol, silanol and Fe-substituted sites. However, modeling allows for an estimation of the likelihood of a reaction, such as the adsorption of uranyl carbonate complexes, and an understanding of the effect of Ca-CO_3-U(VI) solution complexes on the extent of U(VI) adsorption in calcium-rich environments. In the process, it is necessary to follow a parsimony rule, i.e., to build a model with the fewest adjustable parameters as possible in order to avoid correlations between fitting parameters. Accordingly, the chosen modeling strategy was based on a four-step approach, as follows. In a first step, U(VI) adsorption model parameters were fitted using experimental data from the CO_2-"free" experiment. In a second step, we applied these parameters to predict the data obtained in the other experiments: a good match of the prediction with experimental data would suggest that the adsorption of uranyl carbonate complexes is not important, while an underestimation of the adsorption extent would indicates that a uranyl carbonate complex must have formed at the surface (e.g., see the modeling approach of Waite et al. 1994). In a third step, we applied our model to a large range of data obtained from the literature in order to test its robustness. In a fourth and final step, factors influencing U(VI) adsorption, such as pCO_2 or Ca^{2+} concentrations, are discussed on the basis of predictive calculations using the model.

Surface Complexation Model for Montmorillonite Edge Surfaces: The objective of the modeling work presented here was to develop a model that was as mechanistic as possible, but without adding too

many fitting parameters. Accordingly, the speciation model for SWy-2 edge surfaces was directly taken from Tournassat et al. (2016a). This surface complexation model explicitly takes into account the spillover effect of the basal surface potential on the edge surface potential. This effect is typical for layered minerals with structural charges and renders classical surface complexation models developed for oxide surfaces incorrect for modeling clay mineral edge surface properties (Bourg et al. 2007; Tournassat et al. 2013, 2015a, 2016a).

Briefly, the negative surface charge created by the isomorphic substitutions in the montmorillonite lattice creates a negative electrostatic potential field that interacts with the electrostatic field created by the amphoteric edge surface sites (Chang and Sposito 1994, 1996). Consequently, if the edge surface charge is zero, the edge surface potential remains negative. This effect can be adequately captured by setting the relationship between surface charge (Q_{edge} in C·m^{-2}) and surface potential (ψ_{edge} in V) to:

$$\frac{F\psi_{edge}}{RT} = A_1 \operatorname{asinh}\left(A_2\left(Q_{edge} + A_3\right)\right) \quad (4\text{-}3)$$

where A_1, A_2, and A_3 are fitted parameters, F is the Faraday constant (96485 C·mol^{-1}), R is the gas constant (8.314 J·K^{-1}·mol^{-1}) and T is the temperature (K). For montmorillonite at 25 °C, Tournassat et al. (2013) refined the values of these parameters to: A_1 = 1.4 -1.2 log I, A_2 = 11 + log I, and A_3 = -0.02 × (-log I)$^{1.60}$, where I refers to the ionic strength (unitless). This equation is comparable to the classic equation of the diffuse layer model (DLM) for oxides (Davis et al. 1978) that is implemented in most geochemical calculation codes (Steefel et al. 2015), but that is not adapted to model the properties of clay edge surfaces (Tournassat et al. 2013, 2015a, 2016a):

$$\frac{F\psi}{RT} = 2\operatorname{asinh}(B \cdot \sigma) \text{ with } B = \frac{1}{\sqrt{8\varepsilon\varepsilon_0 RT \cdot 1000 \cdot I}} \quad (4\text{-}4)$$

where $\varepsilon\varepsilon_0$ is the dielectric constant for water. The site densities, stoichiometries and protonation/deprotonation constants were taken from Tournassat et al. (2016a). Site densities were calculated from crystallographic considerations and structural formulas; protonation/deprotonation constants were obtained from the predictions of first-principle molecular dynamics calculations (Liu et al. 2013, 2014, 2015a, b).

Edge surfaces with different crystallographic orientations exhibit amphoteric sites of different natures and with different site densities (Tournassat et al. 2016a). Two kinds of edge surfaces can be found in this model, corresponding to the AC and B chains that were first described by White and Zelazny (1988). The relative proportions of these two kinds of surfaces (AC and B) on SWy-2 particle edges and the total edge specific surface area (~15 m^2·g^{-1}) were fitted from titration curves. The value of the edge specific surface area that was fitted by Tournassat et al. (2016a) compared well with the value measured by the low-pressure gas adsorption method (~19 m^2·g^{-1}) (Duc et al. 2005). This value, however, was different from the SWy-2 N_2-BET specific surface area value. Nitrogen-BET specific surface area measurements have been commonly used for the calibration of surface complexation models for clay minerals in the literature, even though these values are not representative of the edge specific surface area for the following reason. Nitrogen-BET measurements probe both edge and external basal surface areas of the particles, and the latter contribution always dominates over the first for montmorillonite particles (Tournassat et al. 2003, 2013, 2015a, 2016a; b).

None of the parameters of the above described surface model was changed during the modeling exercises, leaving only the speciation of U(VI) surface complexes and the related association constants as fitting parameters. Only U(VI) surface complexes on the B-chain surface type were considered in the model, in

agreement with the results obtained with P-EXAFS on the orientation of the U(VI) surface complexes (Schlegel and Descostes, 2009; Marques Fernandes et al. 2012). In the absence of any supporting spectrometric evidence on the nature of the surface sites involved in U(VI)-specific adsorption, we hypothesized that the formation of U(VI) surface complexes took place on the most abundant, non-substituted Si_T-Al_{Oc}-Si_T edge sites, where subscripts T and Oc refer to the tetrahedral and octahedral sheets of the layer respectively (Table 4-2). Note that the influence of cation exchange reactions was negligible under our experimental conditions, compared to the strong relevance of U(VI) surface complexation reactions for overall U(VI) adsorption behavior.

Table 4-2. U(VI) surface complexation reactions on SWy-2 particle edges and related association constants used for modeling[a]. The partial charges were calculated by adding up all bond valences of cations and anions from the clay structure that surround the surface site.

Edge surface areas	Total	$15\ m^2 \cdot g^{-1}$
	Edge surface of B type	$9\ m^2 \cdot g^{-1}$
Protonation/deprotonation reactions	Log K	
	Si_T-Al_{Oc}-Si_T	Si_T-Fe^{III}_{Oc}-Si_T
$>SiteH_4^+ = >SiteH_3^+ + H^+$	-3.1	-1.2
$>SiteH_3 = >SiteH_2^- + H^+$	-7	-5.1
$>SiteH_2^- = >SiteH^{2-} + H^+$	-7	-8.6
$>SiteH^{2-} = >Site^{3-} + H^+$	-8.3	-8.6
	Si_T-Mg_{Oc}-Si_T	Si_T-Fe^{II}_{Oc}-Si_T
$>SiteH_4^{+0.67} = >SiteH_3^{-0.33} + H^+$	-10.8	-6.6
$>SiteH_3^{-0.33} = >SiteH_2^{-1.33} + H^+$	-10.8	-10.2
$>SiteH_2^{-1.33} = >SiteH^{-2.33} + H^+$	-13.2	-10.2
$>SiteH^{-2.33} = >Site^{-3.33} + H^+$	N.A.	-11.2
	Al_T-Al_{Oc}-Si_T	
$>SiteH_4^{+0.75} = >SiteH_3^{-0.25} + H^+$	-4.9	
$>SiteH_3^{-0.25} = >SiteH_2^{-1.25} + H^+$	-7	
$>SiteH_2^{-1.25} = >SiteH^{-2.25} + H^+$	-8.5	
$>SiteH^{-2.25} = >Site^{-3.25} + H^+$	-15.1	

U(VI) adsorption reactions on Si_T-Al_{Oc}-Si_T sites	Log K
$>SiteH_3 + UO_2^{2+} = >SiteH_3UO_2^{2+}$	3.8
$>SiteH_3 + UO_2^{2+} = >SiteHUO_2 + 2\ H^+$	-5
$>SiteH_3 + UO_2^{2+} + 2\ H_2O = >SiteUO_2(OH)_2^{-3} + 5\ H^+$	-25.4

[a] The surface speciation model of Tournassat et al. (2016a) provides information on surface types and areas, site types and protonation/deprotonation constants.

An in-house version of PHREEQC, which was modified to handle Eq. (4-3), was used to carry out the calculations, together with the database THERMOCHIMIE v. 9b0 for thermodynamic parameters of solute species (Giffaut et al. 2014). This database is available in various formats including PHREEQC format at the following address: https://www.thermochimie-tdb.com/.

Calibration of the U(VI) Surface Complexation Model in the "Absence" of CO_2: Carrying out all the steps of an adsorption experiment in the complete absence of CO_2 is very difficult. The DIC measurements indicate that carbonate was not fully excluded from the solutions despite the efforts to achieve this goal. Despite the observed carbonate contamination, the adsorption results from the CO_2-"free" experiments were qualitatively similar to other literature data for carbonate-free systems (Bradbury and Baeyens 2005; Marques Fernandes et al. 2012), i.e. showing a sharp increase in U(VI) adsorption from pH 4 to pH 6 and a limited decrease of U(VI) adsorption at pH>6 (Figure 4-3).

While actual DIC concentrations are usually not considered in CO_2-"free" U(VI) adsorption models in the literature, they were specifically taken into account in the model calculations discussed here. Only three edge surface reactions were necessary to reproduce the data (Figure 2-3 and Table 2-2). The effect of cation exchange was negligible because of the effective competition between Na^+ versus UO_2^{2+} for cation exchange sites under our experimental conditions (0.1 M NaCl background electrolyte). The calculation made with the same reference model parameters, but using a zero DIC value instead of the measured one, illustrates how sensitive the calculation is to the consideration of actual DIC values (dashed lines in Figure 4-5 represent the model predictions while assuming zero DIC; solid lines are based on the reference model using measured DIC values). Even at the low DIC concentrations observed in the CO_2-"free" experiment, dissolved carbonates provide highly competitive ligands for U(VI) complexation reactions relative to mineral surface sites.

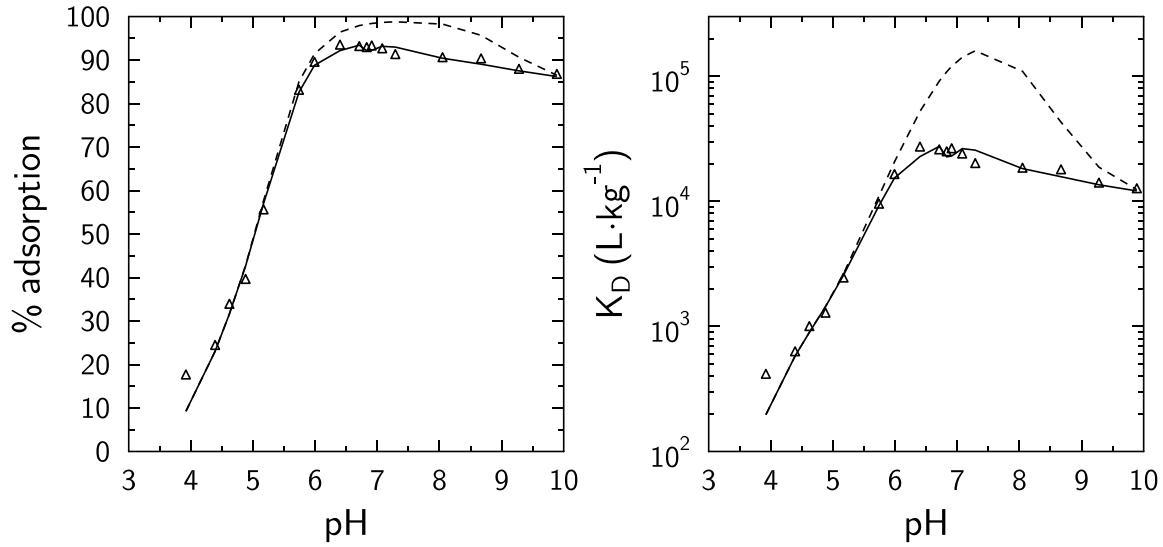

Figure 4-5. U(VI) adsorption results in the CO_2-"free" experiment (symbols: data; lines: model predictions) plotted as percentages of U(VI) adsorbed (left) and adsorption distribution coefficients (K_D, right). The reference model (solid line) was calculated taking into account individually measured DIC concentrations for each data point. The dashed line corresponds to a prediction using the same model parameters but while assuming zero DIC concentrations. Solid concentration = 0.52 g·L^{-1}, total U(VI) concentration = $1.1 \cdot 10^{-6}$ M, ionic strength=0.1 M NaCl.

Blind Prediction of U(VI) Adsorption in the Presence of CO_2: The minimal set of adsorption parameters obtained from the fitting of CO_2-"free" adsorption data were directly used to predict the results of experiments carried out at atmospheric CO_2 partial pressure (log pCO_2 ~ -3.45). Instead of assuming the expected pCO_2 value for every point in the calculations, however, the individually measured DIC concentrations were used to calculate the aqueous composition and U(VI) speciation. The blind prediction of U(VI) adsorption data was surprisingly good (Figure 4-4). Furthermore, in the experiment at $U(VI)_{tot}$ = 0.1 µM, the $NaHCO_3$ aliquot addition was twice of what it should have been for the sample at pH = 7.34, due to an experimental error (see point circled in left panel of Figure 2-4). The related decrease in U(VI) adsorption due to U(VI) aqueous complexation with carbonate was perfectly reproduced by the model, without a need for including the adsorption of uranyl carbonate complexes on the montmorillonite surface. This suggests that our doubts regarding the existence of such ternary surface complexes (on montmorillonite) under atmospheric pCO_2 conditions, triggered by the uncertainties associated with spectroscopic data, are probably justified. The experimental error in the $NaHCO_3$ addition for the sample at pH 7.34 also demonstrates that the solution was slow to re-equilibrate with the atmosphere outside of the closed sample vial, and confirms that measured DIC values correspond to DIC concentrations during U(VI) sorption equilibration.

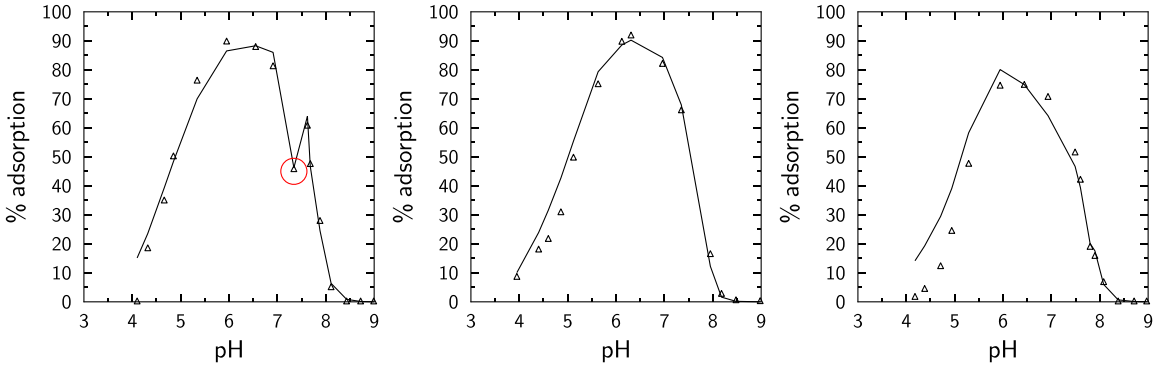

Figure 4-6. U(VI) adsorption results in the presence of atmospheric pCO_2 in a NaCl background electrolyte concentration of 0.1 M (symbols: data; line: model predictions). The model was calculated for each data point taking into account individually measured DIC concentrations. The solid concentration was ~0.52 $g \cdot L^{-1}$. From left to right, the total U(VI) concentration was $1.1 \cdot 10^{-7}$, $9.6 \cdot 10^{-7}$, or $2.6 \cdot 10^{-6}$ M. $NaHCO_3$ aliquot addition was twice of what it should have been for the sample at pH = 7.34 and $1.1 \cdot 10^{-7}$ M U(VI) (circled experimental point).

The robustness of the model was further tested as a function of ionic strength, and, again, the model predicted the data well (Figure 4-7). Under the conditions of this experimental dataset, the influence of cation exchange reactions was negligible for pH >5. The apparent effect of ionic strength on the extent of U(VI) adsorption is due to the changes in electrostatic potential as a function of ionic strength, as well as to small changes in pH values (see Figure 4-7 caption).

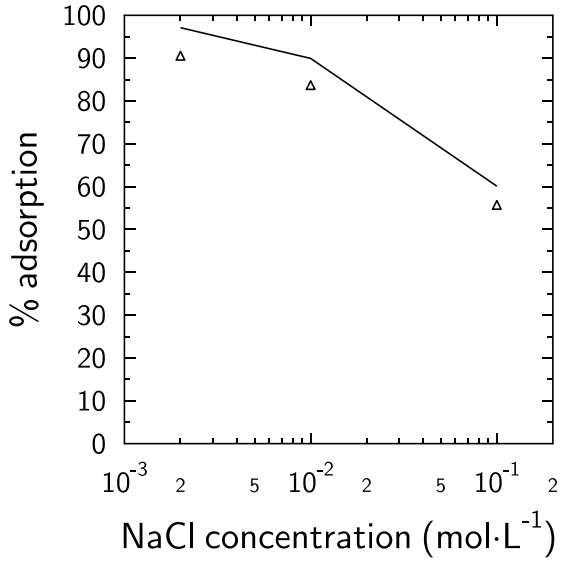

Figure 4-7. U(VI) adsorption as a function of ionic strength in the presence of atmospheric pCO_2 (symbols: data; line: model predictions). The model was calculated for each data point taking into account individually measured DIC concentrations and pH values (5.6, 5.4, 5.2 at 0.002, 0.01 and 0.1 M NaCl, respectively). The solid concentration was 0.52 $g \cdot L^{-1}$; the total U(VI) concentration $9.5 \cdot 10^{-7}$ M.

At greater DIC concentrations (due to pCO_2 values higher than atmospheric), U(VI) adsorption data were also correctly predicted by the model without changing fitting parameters, or adding new surface complexes. The model underpredicted the measured values in percent U(VI) adsorbed by 15% or less (Figure 4-8). However, it was not possible to enhance the quality of the fit by including a uranyl-carbonato surface complex without deteriorating the data fits obtained at atmospheric pCO_2 or CO_2-"free" conditions.

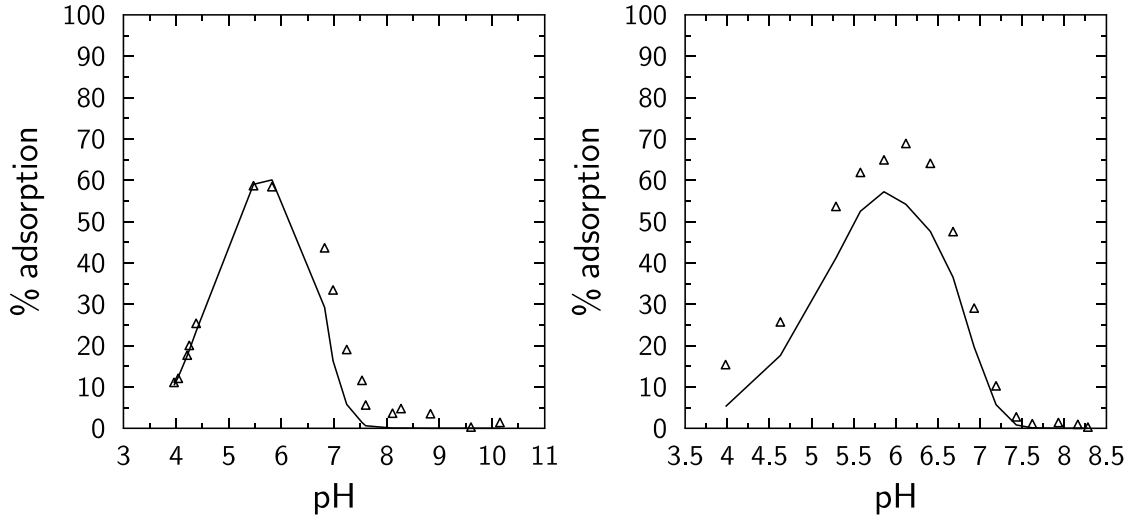

Figure 2-6. U(VI) adsorption in the presence of elevated pCO_2 (symbols: data; line: model predictions). The model was calculated for each data point taking into account individually measured DIC concentrations. Solid concentrations were 0.52 $g \cdot L^{-1}$ (left) or 0.24 $g \cdot L^{-1}$ (right). Total concentrations of U(VI) were $8.1 \cdot 10^{-7}$ M (left) and $9.8 \cdot 10^{-7}$ M (right).

Model Predictions of Literature Data: A wide range of literature data is available for U(VI) adsorption on montmorillonite (McKinley et al. 1995; Pabalan and Turner 1996; Turner et al. 1996; Hyun et al. 2001; Bradbury and Baeyens 2005; Marques Fernandes et al. 2015; Troyer et al. 2016). Thus, it was possible to test the predictive capabilities of the model over a wider range of conditions than those tested in the experiments described above. However, the limitations of this benchmarking approach are at least two-fold. First, the origin and preparation of the clay material (fine fraction separation and further chemical purification) can influence adsorption results because of variations in reactive surface area and surface chemistry. Second, DIC concentrations were not reported in previous studies, while the results presented here demonstrate the paramount importance of this parameter.

The following modeling and data presentation strategies were applied in order to avoid any misinterpretations regarding the quality of the model predictions. Data from the literature were first compared with a blind modeling prediction without any adjustment of model parameters given in Table 4-2 (reference model). In the case of experiments carried out under atmospheric conditions, a $\log_{10}(pCO_2)$ value of -3.45 was assumed for these reference calculations. In case of CO_2-"free" conditions, a $\log_{10}(pCO_2)$ value of -99 was applied. In a second step, various hypotheses were tested to achieve a better fit of the data, if necessary. In particular, as our reference model did not include cation exchange reactions, it was necessary to include these reactions to reproduce U(VI) adsorption data obtained at low ionic strength and low pH (pH<4) conditions.

The data of Troyer et al. (2016) were acquired in the presence of atmospheric pCO_2 on a clay material similar to the one used in this study (< 2 µm fraction of SWy-2 montmorillonite), but in the presence of a

0.01M NaCl electrolyte, thus promoting cation exchange reactions compared to our conditions. We tested the model on the authors' three adsorption isotherms obtained at pH 4, 6 and 8. The error bands were based on adsorption data as follows:

$$\Delta C_{ads} = \frac{2}{m_{clay}}\sqrt{uC_{tot}{}^2 + uC_{eq}{}^2} = \frac{2}{m_{clay}}\sqrt{(0.02 \cdot C_{tot})^2 + \left(0.02 \cdot C_{eq}\right)^2} \qquad (4\text{-}5)$$

Data obtained at pH 6 could be adequately reproduced without changing any parameter from the reference model (Figure 4-9). Data obtained at pH 4 could be reproduced only by adding a cation exchange reaction to the reference model (Table 4-3). Data at pH 8 were not satisfactorily reproduced in the first calculations. However, a slight change in the pH value (7.8 instead of 8) or pCO_2 value (-3.7 instead of -3.45 in $\log_{10}$ value) made it possible to fit the data very well, again showing the great sensitivity of the system to pH/pCO_2 over this range of conditions.

Table 4-3. Cation exchange reaction parameters added to the reference model in order to reproduce literature data obtained at low ionic strength[a].

Surface reactions on montmorillonite basal surfaces	$\log_{10}$ K	
X^- + Na+ = XNa	0	
Cation exchange reactions with U(VI) species (as a function of literature data)	$\log_{10}$ K	CEC (mol·kg^{-1}) [b]
Troyer et al. (2016), Hyun et al. (2001)		
2 XNa + UO_2^{2+} = X_2 UO_2 + 2 Na^+	0.95	0.85
Pabalan and Turner (1996)		
2 XNa + UO_2^{2+} = X_2 UO_2 + 2 Na^+	0.75	1.2
McKinley et al. (1995)		
2 XNa + UO_2^{2+} = X_2 UO_2 + 2 Na^+	1.2	0.8
Turner et al. (1996)		
2 XNa + UO_2^{2+} = X_2 UO_2 + 2 Na^+	0.9	0.41

[a] Cation exchange reactions were modeled with a classic diffuse layer model that was already calibrated for Na^+ and Ca^{2+} by Tinnacher et al. (2016). The total specific surface area for cation exchange reactions was set to the crystallographic surface area for montmorillonite, i.e. ~750 m^2·g^{-1} (Tournassat and Appelo, 2011; Tournassat et al. 2011, 2015b; Tournassat and Steefel 2015).
[b] Values measured in the reference papers.

Some data at high U(VI) surface coverage could not be predicted by the model, even after changing some of the parameters. The origin of this problem can be understood by comparing the measured U(VI) surface coverage with the maximum available surface site density. If we consider a site density of 2.06 sites·nm^{-2} (Bourg et al. 2007; Tournassat et al. 2016a) and a specific surface area of 15 m^2·g^{-1}, the maximum adsorption capacity for U(VI) complexes should be ~0.05 mol·kg^{-1}. If we further assume that

no U multinuclear complexes form at the surface, this value decreases to ~0.025 mol·kg^{-1} (perfect ordering). This value is similar to the maximum adsorbed concentration value measured in Troyer et al. (2016) at pH 6, but far lower than the maximum value measured at pH 8. Hence, the much higher measured than simulated extent of U(VI) adsorption cannot be explained by the formation of isolated mononuclear bidentate U(VI) surface complexes alone. These data must include additional uptake processes that are not described in the model developed here, and are beyond the scope of this study, e.g. polymerization on the surface, or precipitation. The latter cannot be fully ruled out at elevated U(VI) concentrations, since a supersaturation of schoepite was predicted at 1.3 and 62 µM U(VI) at pH 6 and pH 8 respectively, based on the U(VI) aqueous speciation model by Troyer et al. (2016).

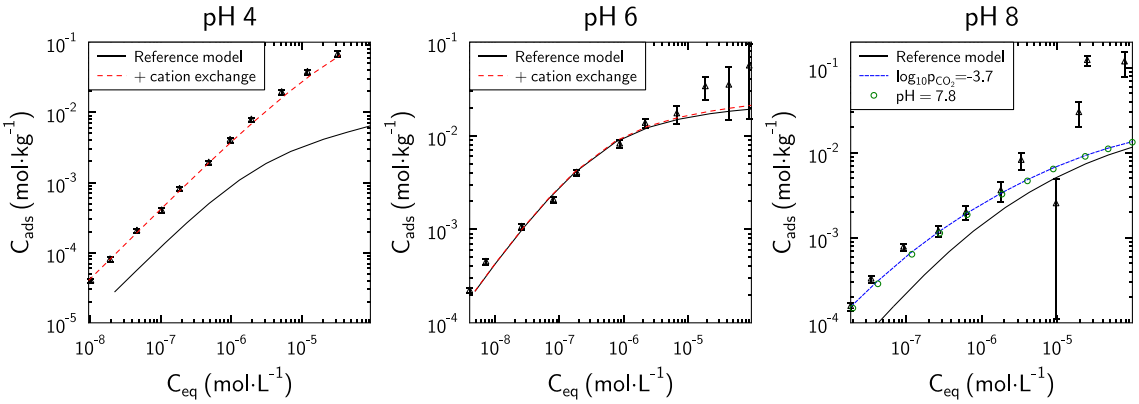

Figure 4-9. Comparison of model predictions with the U(VI) adsorption data on montmorillonite by Troyer et al. (2016).

The data of Hyun et al. (2001) were also acquired in the presence of atmospheric pCO_2 on a clay material similar to the one used in this study (fine fraction of SWy-2 montmorillonite). Uranium(VI) adsorption was characterized at two fixed total U(VI) concentrations (10^{-7} and 10^{-5} mol·L^{-1}), with variable pH, and for two ionic strengths (I=0.001 and I=0.1), and at a relatively high solid concentration (~6-7 g·L^{-1}). The reference model provided a good prediction of the data (Figure 4-10).

At low ionic strength, the addition of cation exchange reactions, with the same parameters as for the study of Troyer et al. (2016), had almost no influence on the results. At pH 4 and low ionic strength, the high level of adsorption is mainly due to the increase in the surface potential value at edge surfaces. At high pH, the disagreement between experimental data and model predictions could be attributed to the fact that carbonate concentrations were not constrained experimentally (Hyun et al. 2001). Pabalan and Turner (1996) reported that, under some conditions, an equilibration period of ten days with the atmosphere was necessary to reach equilibrium between DIC and atmospheric CO_2. Insufficient time of equilibration with the atmosphere in the experiments of Hyun et al. (2001) could have led to pCO_2 values that were lower than the atmospheric value considered in the calculations: fitted value were log pCO_2 = -4.4 at pH 9 and -5.05 at pH 9.55 (blue line in Figure 4-10 right).

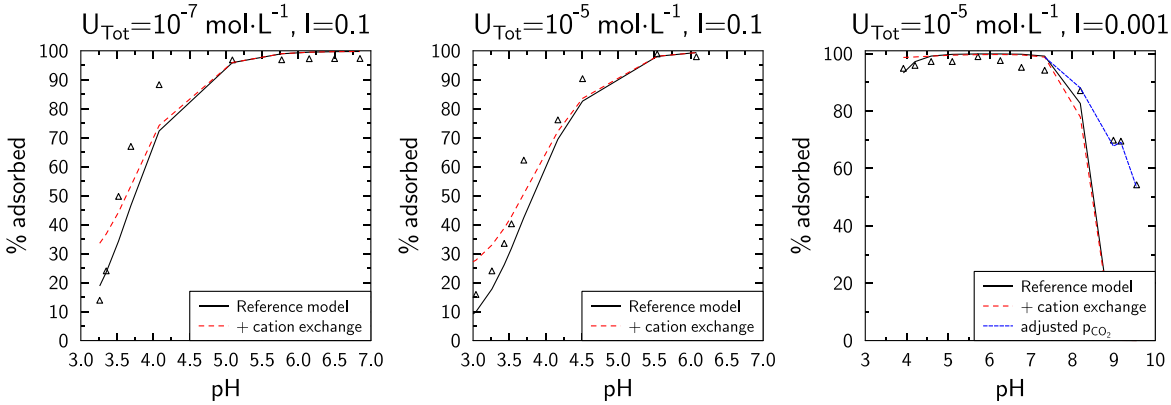

Figure 4-10. Comparison of model predictions with the U(VI) adsorption data on montmorillonite by Hyun et al. (2001).

The data of Pabalan and Turner (1996) were obtained in the presence of atmospheric pCO_2 on a clay material, SAz-1, that was different from SWy-2. Experimental conditions were otherwise quite similar to those used in the present study. In particular, close equilibrium with atmospheric pCO_2 was ensured by the addition of bicarbonate to the solutions. Again, the predictions of the model were in very good agreement with the experimental data without any further adjustments (Figure 4-11), despite the different nature of the clay.

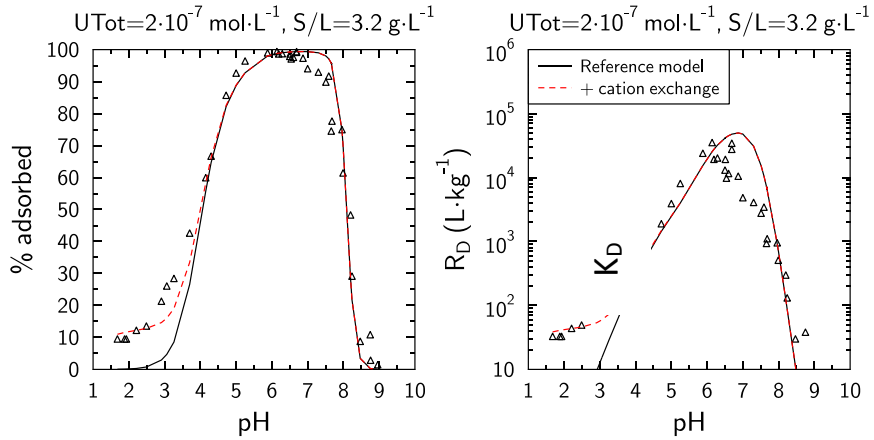

Figure 4-11. Comparison of model predictions with U(VI) adsorption data by Pabalan and Turner (1996). Cation exchange parameters are given in Table 2-3. Solid concentration = 3.2 $g \cdot L^{-1}$; total U(VI) concentration = $2 \cdot 10^{-7}$M. The results are presented in percentage adsorbed (left) and in $\log_{10} K_D$ values (right) for a better evaluation of model fits at low (left) and high (right) U(VI) adsorption.

McKinley et al. (1995) reported U(VI) adsorption data on the <2 µm fraction of Swy-1 montmorillonite as a function of pH and ionic strength. At first sight, these data were not satisfactorily reproduced by the reference model (Figure 2-10). The addition of cation exchange reactions improved predictions at low pH, but U(VI) adsorption at pH>5.5 was still overestimated. However, these discrepancies can be satisfactorily explained by taking into account that the edge specific surface area of the Swy-1 sample from McKinley et al. (1995) was lower than the area of the Swy-2 sample, i.e. 10.5 $m^2 \cdot g^{-1}$ instead of 15 $m^2 \cdot g^{-1}$. Both values are within the range of montmorillonite edge surface area values reported in the literature, which vary from 5 $m^2 \cdot g^{-1}$ to 25 $m^2 \cdot g^{-1}$ (Tournassat et al. 2016a).

Turner et al. (1996) reported U(VI) adsorption data on the <2 µm fraction of a smectite isolate from a sedimentary rock fraction (Kenoma scmectite). Kenoma smectite is a beidellite, meaning that most of its structural charge originates from tetrahedral isomorphic substitutions, instead of octahedral substitutions for montmorillonite. Despite this difference, U(VI) adsorption data could be fitted equally well using the same approach as for the data of McKinley et al. (1995). Only U(VI) adsorption data obtained at very low ionic strength (I=0.001) were overestimated (Figure 4-13). Since the solid/liquid separation was achieved by centrifugation, it may be possible that finer particles were not completely removed from solution at this ionic strength, causing a lower apparent extent of U(VI) adsorption: at low ionic strength, separation of solids from solution based on density differences is more difficult, due to the increased intensity of electrostatic repulsive interactions between montmorillonite layers (Van Olphen 1992).

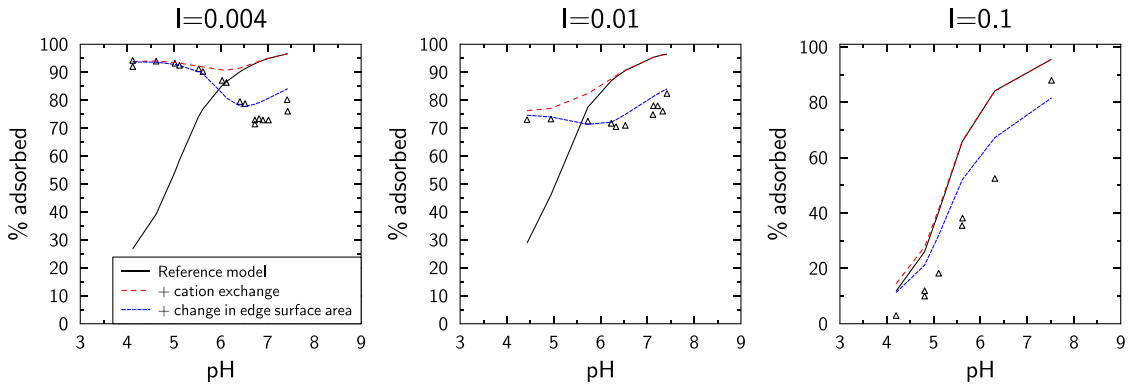

Figure 4-12. Comparison of model predictions with U(VI) adsorption data by McKinley et al. (1995). The edge surface area was set to 10.5 $m^2 \cdot g^{-1}$ instead of 15 $m^2 \cdot g^{-1}$ in the reference model. Cation exchange parameters are given in Table 4-3.

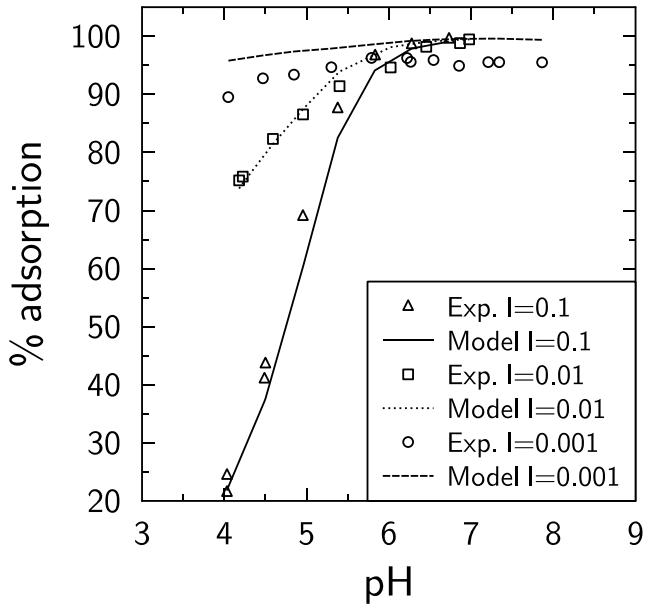

Figure 4-13. Comparison of model predictions (lines) with U(VI) adsorption data by Turner et al. (1996) (symbols). Cation exchange parameters are given in Table 4-3.

Marques Fernandes et al. (2012) conducted U(VI) adsorption experiments on the <0.5 µm fraction of a SWy-1 montmorillonite over a wide range of pH and total U(VI) concentrations while varying pCO_2. Experimental data at pH>7, in the presence and absence of atmospheric pCO_2 (actual DIC concentrations were not measured), were predicted satisfactorily by the reference model without further modifications (Figure 4-14). Experimental data obtained at lower pH, however, had higher adsorption than predicted by the reference model. The position of the pH adsorption edge could only be reproduced by increasing the edge surface area by a factor 10. This is obviously not a justifiable assumption, even if we consider that the authors used a finer clay fraction (<0.5 µm) than in most other reported studies (< 2 µm). With the large edge surface area, U(VI) adsorption was also greatly overestimated at pH>7 (Figure 4-14). The SWy-1 montmorillonite material of Marques Fernandes et al. (2012) thus exhibits U(VI) adsorption properties that are significantly different from the SWy-1 material studied by McKinley et al. (1995) and all other montmorillonite materials studied in the literature, given the otherwise good agreement between experimental data and our model predictions for a large number of other studies.

Based on the quality of fit, Marques Fernandes et al. (2012) attributed the very high adsorption affinity of SWy-1 montmorillonite to "strong sites", with a specific site density of ~2 mmol·kg^{-1}. However, if present, the influence of such strong sites should have been apparent in the many other studies discussed above, where the U(VI) to solid concentration ratio was lower than the putative "strong site" density. Hence, it appears that, for most other solid materials previously studied, these strong sites either do not exist or are present at a far lower site density than the reported value of ~2 mmol·kg^{-1} (Marques Fernandes et al. 2012). Differences in material preparation procedures could potentially explain this difference in reactivity; e.g., Marques Fernandes et al. (2012) acidified their clay sample to pH 3.5 to remove acid-soluble impurities, while pH 5 was used in this and other previous studies.

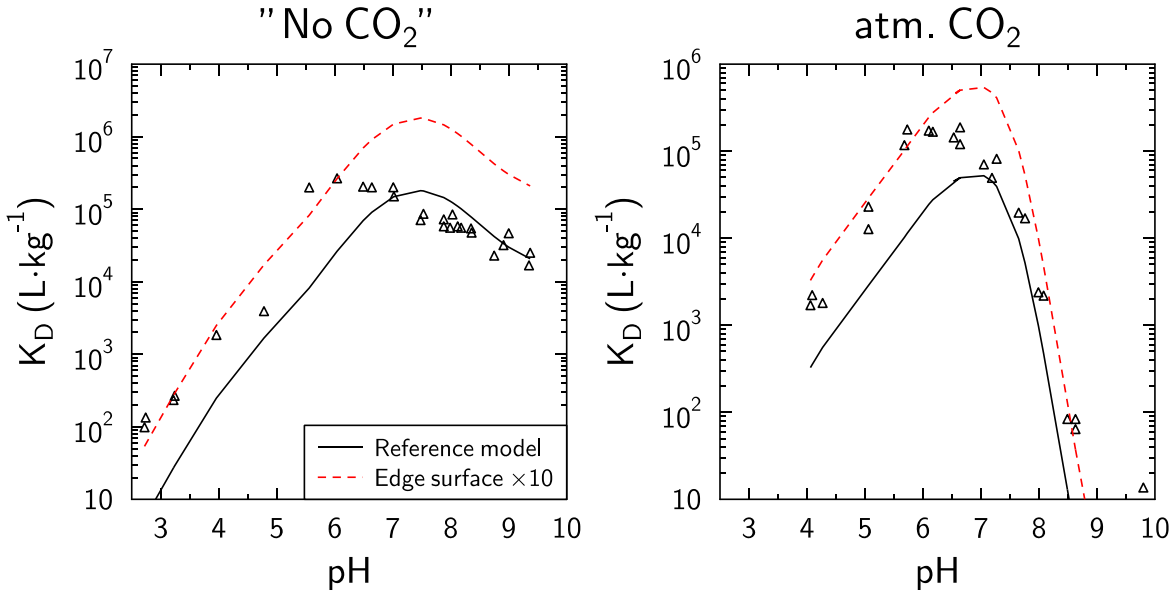

Figure 4-14. Comparison of model predictions (lines) with experimental U(VI) adsorption data on montmorillonite by Marques Fernandes et al. (2012) (symbols).

Summary of Modeling Results: The reference U(VI) adsorption model presented here is based on a state-of-the-art description of the reactivity of montmorillonite clay edges that specifically takes into account the spillover effect of the basal surface potential on the edge surface potential (Bourg et al. 2007; Tournassat et al. 2013, 2015a, 2016a). This model accurately predicts adsorption of U(VI) on

montmorillonite surfaces over a wide range of experimental conditions, with only one specific adsorption site, three different U(VI) complexes at the surface, and one cation exchange reaction.

Within the limits of data accuracy, there was no need to include the formation of uranyl-carbonato surface complexes in the model to simulate the experimental data. Including such a species would only be justified if: (1) the discrepancies between experimental data and model predictions (without including these surface complexes) were larger than the combined uncertainties associated with experimental errors and formation constants for aqueous U(VI)-carbonate complexes, and (2) if actual measurement data are available for all solution parameters, including DIC concentrations (or alternatively, alkalinity). Without these data, we consider the uncertainties of assumed pCO_2 values too large to draw any conclusions regarding the presence of ternary U(VI)-carbonato surface complexes.

For illustration, the effect of varying pCO_2 conditions on U(VI) adsorption is shown in Figure 4-15. Based on these calculations with the reference model, at pH>9 a "true" absence of CO_2 can be interpreted only if it can be demonstrated that actual pCO_2 values are lower than 10^{-6} atm. This partial pressure corresponds to 1 ppm CO_2 in the surrounding atmosphere, i.e., experimental conditions that could be met only with great difficulty in the laboratory, even in a specially equipped glove box. It can be concluded that an "absence of CO_2" at pH>9 (ideally corresponding to $pCO_2=10^{-99}$ atm in Figure 4-15) is in fact obtained because of slow gas exchange rates between degassed solutions and the surrounding atmosphere, and not a true equilibrium with atmospheric CO_2. Under these conditions, it is thus necessary to measure DIC concentrations to assess the exact concentrations in solutions exposed to low levels of pCO_2. To our knowledge, this type of measurement has never been performed in previously reported U(VI) adsorption studies on montmorillonite. Most likely, this has sometimes led to false assumptions that previous experiments were conducted at pCO_2 levels that did not impact U(VI) adsorption.

For example Schlegel and Descostes (2009) reported U(VI) adsorption results in the "absence of CO_2" that clearly show evidence of pCO_2 at higher values than ~10^{-5} atm (compare their Figure 1 with Figure 4-15 of this report). Even a precise interpretation of data obtained at atmospheric pCO_2 may be problematic. The value of atmospheric pCO_2 can fluctuate as a function of geographic location, season, and above all the presence of humans in an enclosed lab setting because of respiration and poor ventilation. Also, a slight change in pH after pre-equilibration of the clay, following for example the introduction of a mildly acidic U(VI) spike, can impact the final pCO_2 value if the time-frame of the pH re-adjustment is too short to allow for full gas-solution re-equilibration and the following sorption equilibration is performed in closed sample vials. A pCO_2 of $10^{-3.2}$ instead of $10^{-3.45}$ bar has a significant effect on the prediction of U(VI) adsorption at pH>7. Hence, even with a 'forced' pre-equilibration of background electrolyte solutions with $NaHCO_3$ buffer, the CO_2 exchange with the surrounding atmosphere and other experimental artefacts add a significant uncertainty to the modeling results, unless actual DIC concentrations are used during the model fitting process. This effect is well illustrated with the modeling of U(VI) adsorption data by Troyer et al. (2016) at pH~8 (Figure 4-13).

While actual values of DIC concentrations are critical parameters in the evaluation of U(VI) adsorption, the combined presence of Ca and carbonate further increases the level of complexity and uncertainty in the model calculations. This is due to the formation of aqueous calcium-uranyl-carbonate complexes (Meleshyn et al. 2009), with variable adsorption impacts (Fox et al. 2006). According to the reference model, the effect of the formation of this complex on U(VI) adsorption could be significant for Ca^{2+} concentrations larger than 2 mmol·L^{-1}, which is in agreement with our experimental results (Figure 4-16).

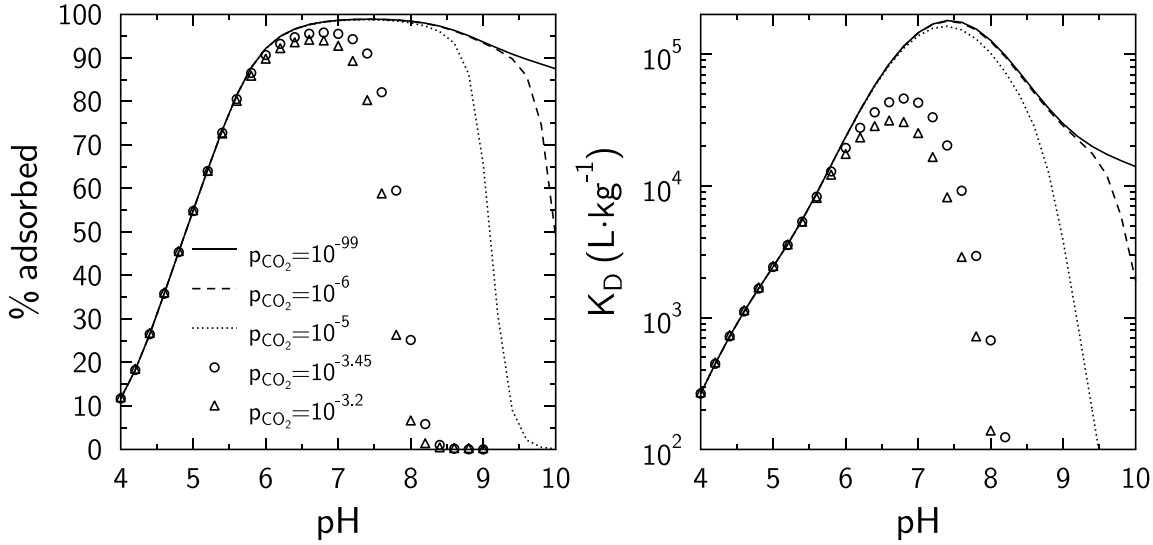

Figure 4-15. Predicted effect of pCO_2 on U(VI) adsorption onto montmorillonite using our reference model with a solid concentration of 0.5 g·L^{-1} , a 0.1M NaCl background electrolyte and a total U(VI) concentration of 10^{-7} M.

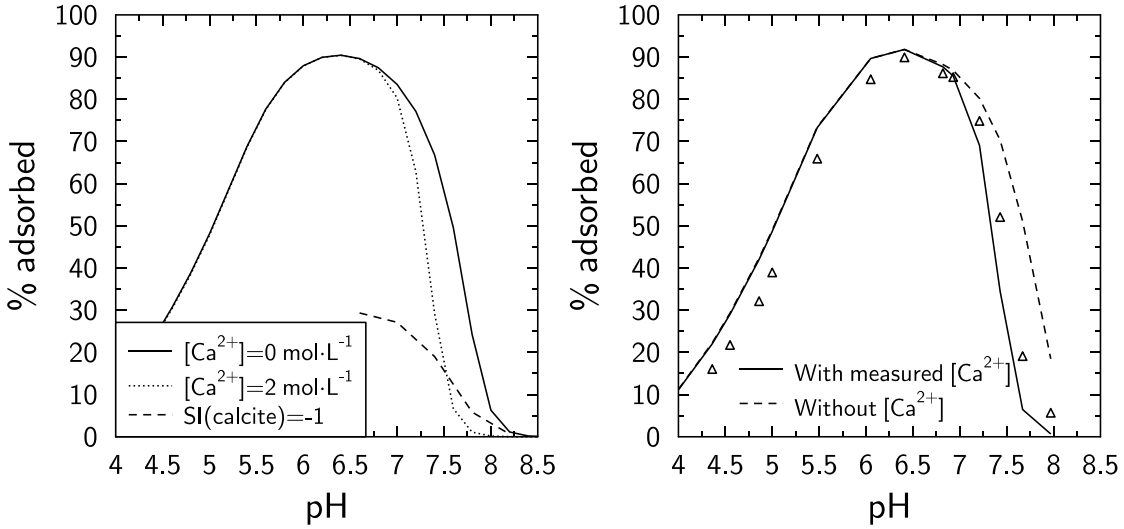

Figure 4-16. Left: Predicted effect of Ca^{2+} concentration on U(VI) adsorption using our reference model with a solid concentration of 0.5 g·L^{-1}, a 0.1 M NaCl background electrolyte, a total U(VI) concentration of 10^{-6} M, and a $pCO_2=10^{-3.2}$ bar. Solubility index (SI) for calcite is plotted for comparison. Right: Comparison of our experimental data with model results with and without taking into consideration the impact of Ca^{2+} on U(VI) solution speciation.

4.3 URANIUM(VI)-MONTMORILLONITE DIFFUSION EXPERIMENTS AT ALKALINE PH CONDITIONS

4.3.1 Materials and Methods

Chemicals and Solutions: All chemicals used in this study were reagent grade or better. Acids, bases, and salt solutions used in diffusion and batch kinetic sorption experiments were of TraceSelect grade (Sigma Aldrich) in order to minimize calcium background concentrations. Aqueous solutions were prepared with Nanopure water (ThermoScientific ultrapure water system). Glassware was cleaned by soaking in acid (10 % (v/v) HCl) for 12 to 24 hours, followed by thorough rinsing with Nanopure water and air-drying.

A U-233 stock solution provided by Dr. Heino Nitsche (Nuclear Sciences Division, Lawrence Berkeley National Laboratory, deceased) was utilized for these experiments. However, a purification of the stock solution was necessary in order to remove accumulated daughter products (Th-229, Ra-225, Ac-225), and to ensure that U-233 was present as uranium (VI) and in a known chemical solution matrix. The purification procedure was based on the separation of uranium from impurities using an Eichrom UTEVA resin column (2-mL cartridges, 50-100 μm UTEVA resin, Eichrom P/N: UT-R50-S), while largely following the recommendations provided in Method ACW02, Rev. 1.4 (Uranium in Water) by Eichrom Technologies, LLC. Very briefly, the original U-233 stock solution (5 mL, 25 μCi total, nominal activity) was carefully dried in a Savillex PFA vial on a hot plate and, after a series of other steps, loaded onto the preconditioned resin column in 10 mL of 3 M nitric acid-1 M aluminum nitrate solution plus 1 mL of 3.5 M $NaNO_2$. After a series of additional steps, the purified U-233 was eluted from the column into three separate Savillex vials using 1 M HCl (twice) and 0.5 M HCl (once). Based on the weighing and liquid scintillation counting of the resulting, purified stock solutions, we estimated 100% recovery of U-233 after purification.

Montmorillonite: A commercially available, well-characterized, standardized Source Clay (Na-montmorillonite, SWy-2, Clay Minerals Society) was used as the solid material in all experiments. Given its known amounts of impurities in terms of quartz (8%), feldspars (16%) and calcite (Chipera and Bish 2001; Costanzo and Guggenheim 2001; Mermut and Cano 2001), the Source Clay was purified prior to its use in experiments, as described in detail elsewhere (Tinnacher et al. 2016).

Furthermore, dry, purified Na-montmorillonite was pre-equilibrated with the background electrolyte solutions at the specified pH-conditions (pH-8.75 and pH-8.95) in batch systems in order to accelerate the pH-equilibration in 0.1 M NaCl/$NaHCO_3$ background electrolyte prior to any diffusion experiments. The specific compositions of background electrolyte solutions at pH 8.75 and 8.95 and a total ionic strength of 0.1 M (pH-8.75: 9.52E-2 M NaCl, 4.32E-03 M $NaHCO_3$, 4.49E-4 M NaOH; pH-8.95: 9.22E-2 M NaCl, 7.05E-3 M $NaHCO_3$, 1.13E-03 M NaOH) were based on aqueous speciation calculations, taking into account the ionic strength contributions of the buffer (sodium bicarbonate) and the base (sodium hydroxide) to be added for initial pH adjustments.

Two-liter electrolyte solutions were prepared using high-purity chemicals (Fluka TraceSelect NaCl and NaOH; Alfa Aesar Puratronic $NaHCO_3$). After an initial equilibration of solutions with atmospheric CO_2 over two days, the pH was further adjusted by adding small volumes of high-purity HCl or NaOH. Then, six aliquots of approximately 1 gram of Na-montmorillonite were added to six acid-washed 40-mL polycarbonate centrifuge vials (Oakridge tubes). After adding 33 mL of pH-adjusted background electrolyte solutions to each vial (three vials per pH condition), the clay was first mixed by hand and then on a rotary shaker over four days. Afterwards, the pH values of the clay suspensions were recorded, and the clay separated from solutions in two consecutive centrifugation steps (Avanti J-E centrifuge, JA-17

rotor, 16,000 rpm; 31,511 average g-force, for 33 minutes each). After re-combining all clay fractions in the original polycarbonate vials, 20 mL of fresh background electrolyte solutions were added to each individual vial, and the clay mixing and equilibration steps repeated for a total number of 10 steps over three weeks (individual equilibration times of 4, 0.8, 0.8, 1, 3.8, 0.9, 1, 0.9, 2.9, and 1 days). Afterwards, three pH fine-adjustments were performed by adding small volumes of HCl and NaOH solutions directly to the individual vials over three days, while allowing for system equilibration over about one day after each adjustment. The first and second pH values determined for pH-8.75 and pH-8.95 clay suspensions were pH 7.5 and 7.9, and pH 7.9 and 8.4, respectively. Over the course of the repeated exchange of electrolyte solutions and the pH fine-adjustments, the incremental increases in pH between equilibration steps became smaller. Over this time-frame, the pH values in electrolyte control solutions not in contact with clay remained stable. Pre-equilibrated clay samples were then isolated from solutions by centrifugation as described above, dried in a convection oven at 45 °C over five days, and ground on a Retsch MM 400 ball mill with tungsten-carbide balls (frequency of 30/sec for 2 minutes) prior to their use in experiments. No relevant changes in sample mineralogy were observed due to pH pre-equilibration, based on the elemental analysis of solid samples before and after (total digestion of ~1 gram of solids combined with XRF analysis and a Ca colorimeter measurement).

Uranium(VI) Through-Diffusion Experiments: Uranium(VI) through-diffusion experiments were set up with the goal to investigate the effects of two processes on U(VI) diffusion at the same time: (1) the potential exclusion of anionic uranium(VI) solution species from montmorillonite interlayer spaces, and (2) U(VI) sorption onto montmorillonite. Given this goal, and to ensure U(VI) breakthrough within reasonable experimental time-frames, a careful selection of experimental conditions in terms of pH, total uranium(VI) concentration and degree of clay compaction was necessary.

With regard to pH, the selected target pH conditions had to ensure: (1) a predominance of negatively-charged uranium(VI) species in solution to evaluate potential anion exclusion effects, and (2) a sufficiently low U(VI) sorption affinity in order to avoid strong U(VI) retardation and unreasonably long experimental time-frames. For the latter, results from preliminary transport calculations indicated that log K_D values between 0.7 and 1 [L kg^{-1}] (K_D=5-10 [L kg^{-1}]) would be appropriate. The first requirement leads to the selection of alkaline pH conditions; the second further narrows the pH range to values between 8 and 9 based on previous U(VI) batch sorption experiments with the same solid (see sections above). Hence, we decided to perform two parallel through-diffusion experiments at target pH values of 8.75 and 8.95, with the expectation that clay interactions with the pH-adjusted electrolyte solutions could potentially further lower pH, given our experience from a previous diffusion experiment (Tinnacher et al. 2016).

We selected uranium-233 as the only uranium isotope to be used in these diffusion experiments due to its short half-life relative to other uranium isotopes. At a nominal total U(VI) concentration of 2.35×10^{-6} M, this allows for better detection limits of low uranium(VI) concentrations in solution, a relatively straight-forward and fast analysis by liquid scintillation counting, and hence a close and timely monitoring of diffusive fluxes over the course of diffusion experiments.

Last, a low degree of clay compaction (~ 0.8 kg dm^{-3}) was chosen to facilitate a reasonably fast diffusive transport of U(VI), and to allow for a simulation of Ca diffusion and its effects on U(VI) solution speciation, sorption and diffusive transport, if necessary, based on previous experimental Ca diffusion data at the same degree of compaction (Tinnacher et al. 2016). While we purified our solid material in order to avoid this additional level of complexity (see details above), the dissolution of trace calcite impurities in montmorillonite, or release of Ca from montmorillonite cation exchange sites, could still potentially lead to Ca solution concentrations affecting U(VI) sorption and transport behavior.

Uranium(VI) through-diffusion experiments largely followed procedures previously described in the literature (Molera and Eriksen 2002; Van Loon et al. 2003a, b; Tinnacher et al. 2016). The experimental setup consists of a set of two diffusion cells, each connected to high- and low-concentration reservoirs with Teflon tubings, and a peristaltic pump circulating solutions over both ends of the diffusion cells. These experiments include a series of steps which can be summarized as follows: (1) dry-packing of the pH-equilibrated montmorillonite samples into diffusion cells, (2) saturation of the initially dry clay packings with background electrolyte solutions at the specified, target pH, (3) a through-diffusion experiment with tritiated water (HTO) tracer to determine the total porosity of the clay packing in each cell, and (4) the uranium(VI) through-diffusion experiment, which is a HTO out-diffusion experiment at the same time.

At the beginning of the experiment, dry, pH-equilibrated Na-montmorillonite samples were packed into the diffusion cells (PEEK; D=1.0 cm, L=0.5 cm; Alltech 2 µm stainless-steel frits, P/N 721825) by hand with the goal to obtain a dry bulk density of approximately 0.8 kg dm^{-3}. The clay was carefully compacted with a custom-made PEEK rod, and then saturated with the individual background electrolyte solutions (0.1 M NaCl, pH-8.75 or pH-8.95; for exact composition see above) by circulating electrolyte solutions for about 3 ½ weeks (two 200-mL reservoirs per cell; estimated flow rate of 0.78 mL min^{-1}). Prior to their contact with the mineral phase, these electrolyte solutions had been repeatedly adjusted to the target pH values of pH 8.75 and 8.95 using small volumes of acid/base solutions (TraceSelect grade NaOH and HCl) while equilibrating with atmospheric CO_2. The exact dry densities of the clay packings (pH-8.75: 0.766 kg dm^{-3}; pH-8.95: 0.772 kg dm^{-3}) were calculated after determining the water content of dry, pH-equilibrated clay fractions from the same batches of solids used in diffusion experiments (drying at 150 °C for approximately five days).

After clay saturation, tracer tests with tritiated water (HTO) were initiated by replacing the reservoir solutions with 200 mL of background electrolytes at pH-8.75 or pH-8.95 containing ~24 nCi/mL (~890 Bq mL^{-1}) HTO (high-concentration reservoirs) on one end of each diffusion cell, and 20 mL reservoirs containing fresh, HTO-free electrolyte solutions (low-concentration reservoirs) on the opposite ends. Over the following weeks, the circulation of solutions was continued at the same flow rate. Electrolyte solutions in the low-concentration reservoirs were repeatedly replaced in order to maintain a nearly constant concentration gradient between the high- and low-concentration reservoirs. The exchanged low-concentration reservoir vials were weighed to correct for volume losses due to evaporation in the hood. Solutions were sampled for tritium analysis by liquid scintillation counting (PerkinElmer Liquid Scintillation Analyzer Tri-Carb 2900TR; Ultima Gold XR liquid scintillation cocktail), and their solution pH values were recorded. This procedure was continued until a series of data points had been collected under steady-state conditions for HTO diffusive fluxes.

The solutions in the high-concentration reservoirs were then replaced with HTO-free background electrolyte solutions at pH-8.75 and pH-8.95 containing a nominal concentration of 2.35×10^{-6} M uranium(VI) in the form of U-233 (exact concentrations were 2.36×10^{-6} M U-233 or 5.35 nCi mL^{-1} = 198 Bq mL^{-1} for pH-8.75, and 2.34×10^{-6} M U-233 or 5.30 nCi mL^{-1} = 196 Bq mL^{-1} for pH-8.95). Again, low-concentration reservoir solutions were continuously replaced, and uranium-233 and tritium activities analyzed (PerkinElmer Liquid Scintillation Analyzer Tri-Carb 2900TR; Ultima Gold XR liquid scintillation cocktail), with the goal to collect a sufficient number of data points under steady-state conditions for uranium(VI) diffusive fluxes in each system.

After the pH values in low-concentration reservoir solutions were recorded, solution fractions were collected for later ICP-MS analysis and alkalinity titrations. Metals analysis by ICP-MS (1:1 dilution with 2% TraceSelect HNO_3, Perkin-Elmer SCIEX ICP-Mass Spectrometer ELAN DRC II) focused on elements that could either be relevant for uranium(VI) solution speciation (Ca, Mg) or indicate any potential montmorillonite degradation (Si, Al, Fe, etc.). Alkalinity titrations had the goal to constrain

carbonate concentrations for later U(VI) solution speciation, sorption and transport modeling. For this purpose, Gran alkalinity titrations were performed on 5-ml fractions of selected low concentration reservoir solutions using 0.02 eq/L sulfuric acid (Manufacturer: BDH). Precision reference standards (pH 4.000, 7.000 and 10.000, Ricca Chemical Company) were used for the calibration of the VWR pH meter. Since a pH drift to higher pH values was observed during initial titrations, possibly due to slow gas exchange with atmospheric CO_2, solutions were first titrated from the initial sample pH to a pH value of around 4, then allowed to reach pH stabilization over 27-46 hours. Afterwards, sample titrations were continued to the final end point at pH~3.2.

It is important to note that, with the replacement of HTO high-concentration reservoir solutions with HTO-free U-233 high-concentration reservoir solutions, we essentially started an 'out-diffusion' experiment for tritium. At the end of the tritium tracer test, and after reaching steady-state conditions, a linear HTO concentration profile had been established across the clay packing in the diffusion cell. By replacing the high-concentration reservoir with a HTO-free solution and continuously exchanging low-concentration reservoir solutions during the uranium(VI) diffusion experiments, new concentration gradients between HTO in the diffusion cells and the reservoir solutions are established. Hence, HTO diffuses out of the cells in both directions, and is accumulated in both, the high- and low-concentration reservoir solutions. As a result, low HTO concentrations are detected in low-concentration reservoir solutions during the uranium(VI) through-diffusion experiments. These 'out-diffusion' data for HTO (data not reported) allow us to further constrain total porosity values that are inferred from simulations of HTO through-diffusion data.

Furthermore, given the high importance of pH for U(VI) solution speciation and sorption behavior, we performed two additional types of pH measurements at two other points in the experimental setup during uranium(VI) diffusion experiments. First, a small pH probe was repeatedly immersed directly into the two high-concentration reservoir solutions containing U-233. In addition, we collected small volumes (3-5 mL) of 'flow-back' solutions directly from Teflon tubings. These samples represent high-concentration reservoir solutions that had been in contact with the clay packings in the diffusion cells, and were in the process of flowing back into the high-concentration reservoirs. After these pH measurements, collected solution fractions were returned to their respective reservoirs. These 'flow-back' solution measurements were taken in order to evaluate whether the pH values directly recorded in high-concentration reservoir solutions actually represented the pH conditions of solutions in contact with the clay packings. This consideration is based on the large dilution effect occurring in high-concentration reservoirs during the circulation of solutions (200 mL of reservoir volume versus 0.78 mL min^{-1} flow-rate for the circulating solution). However, both of these types of measurements were performed much less frequently than pH measurements of low-concentration reservoir solutions in order to minimize any potential disturbances to experiments.

Last, over the course of the 81-day uranium(VI) through-diffusion experiments, plastic tubings in the peristaltic pump were repeatedly replaced. Nonetheless, one of the tubings delivering high-concentration reservoir solution to the pH-8.95 diffusion cell failed, sometime after the sampling event on day 35. After the problem was noticed, the continuous flow of solutions was stopped for both cells in order to replace peristaltic tubings as well as the lost pH-8.95 high-concentration reservoir solution. The results reported in the following only cover time-frames (1) before the tubing failure, and (2) after the continuous flow of reservoir solutions was resumed and both systems stabilized again after the flow interruption.

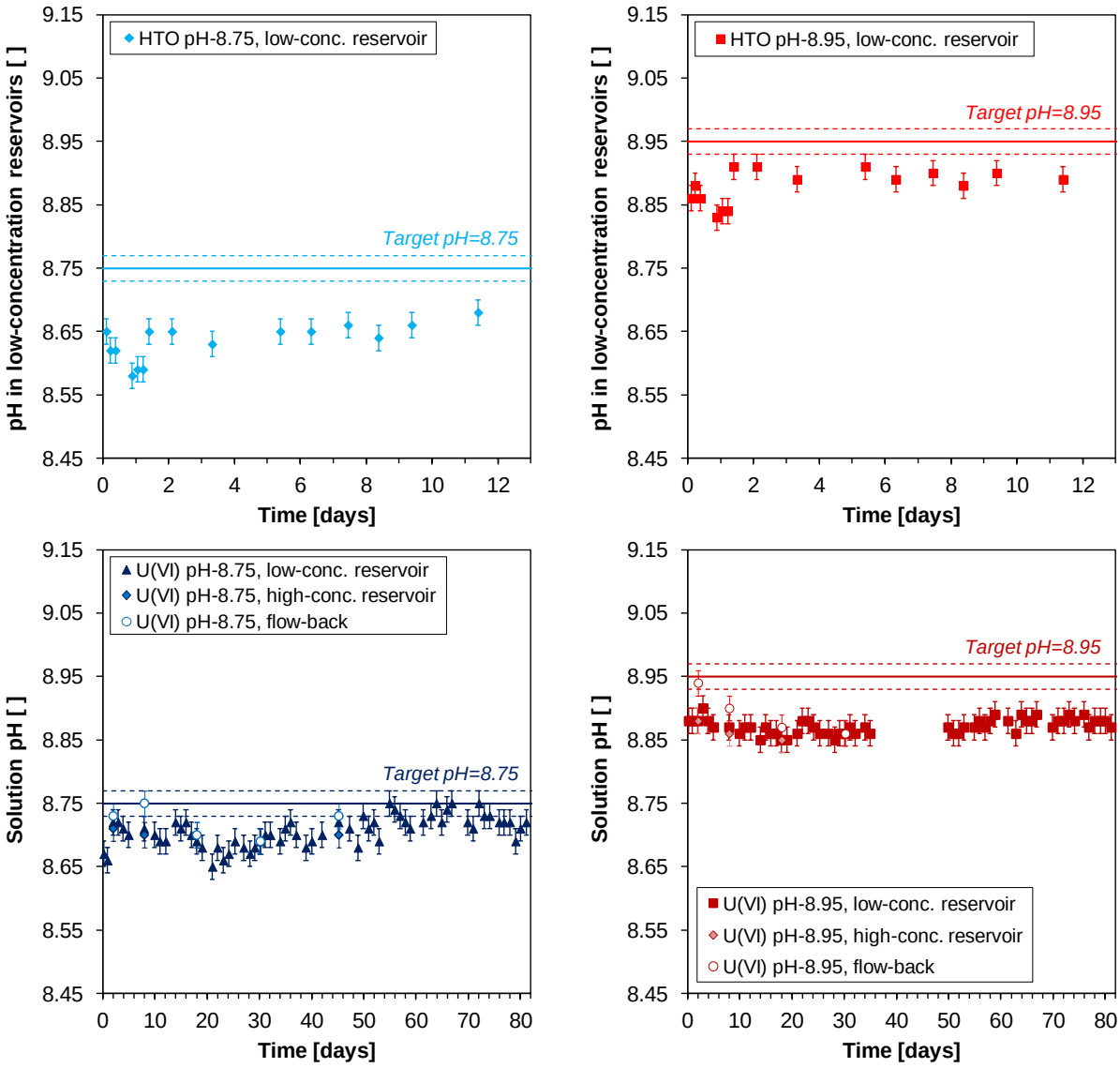

Figure 4-17. pH monitoring data for through-diffusion experiments with tritiated water (HTO, top) and uranium(VI) (bottom) in two, parallel diffusion cells set up at target pH values of pH 8.75 and 8.95. Data series include pH measurements for low-concentration reservoir, high-concentration reservoir and 'flow-back' solutions. High-concentration reservoir and 'flow-back' solutions were only analyzed at a few, selected time-points during U(VI) through-diffusion experiments. Measured pH values in 'flow-back' and high-reservoir solutions were the same, wherever data points for high-concentration reservoir solutions are not clearly visible.

4.3.2 Results and Discussion

pH Monitoring Data for High- and Low-Concentration Reservoir Solutions: In Figure 4-17, we show a summary of pH monitoring data recorded during the consecutive through-diffusion experiments with tritiated water (HTO), then uranium(VI), for both diffusion cells, set up at target pH values of pH 8.75 and 8.95. While a drop in pH was observed due to the contact of the background electrolyte solutions with the clay packings in both systems, pH conditions remained reasonably stable over the course of

experiments. During U(VI) through-diffusion experiments, the average pH values measured in low-concentration reservoir solutions were calculated at pH 8.71 and 8.87 for the systems at target pH values of pH 8.75 and 8.95, respectively. Values of pH recorded in high-concentration and 'flow-back' solutions were generally in the same range than those measured in low-concentration reservoir solutions. Furthermore, no systematic differences in pH values between high-concentration reservoir and 'flow-back' solutions could be observed.

Normalized Flux Data for Through-Diffusion Experiments with Tritiated Water: As described in last year's annual report, normalized mass flux densities reaching the low-concentration reservoir (J_N in m day^{-1}) were calculated with the following expression:

$$J_N = \frac{C_{low}}{C_{high}} \frac{V_{low}}{A\Delta t} \quad (4\text{-}6)$$

where C_{low} is the concentration of the species of interest measured in the low-concentration reservoir at a sampling event, C_{high} is the constant concentration in the high-concentration reservoir, Δt is the time interval since the previous sampling event (in days), A is the cross sectional area available for diffusion (0.785 cm^2), and V_{low} is the volume of the low-concentration reservoir (about 20 mL).

Figure 4-18 depicts the results for normalized HTO fluxes recorded during the HTO through-diffusion experiments. Based on these data, the normalized HTO flux under steady-state conditions, and hence the total porosity of the clay packing, appear to be slightly higher in the pH-8.75 than the pH-8.95 system. This agrees well with our estimated dry density values for the two cells, with 0.766 and 0.772 kg dm^{-3} for the pH-8.75 and pH-8.95 systems, respectively. Slightly higher dry densities and degrees of clay compaction would result in slightly lower total porosities of the clay packing. A later simulation of both experimental data sets will allow us to determine the total porosity and water diffusion coefficients in each system.

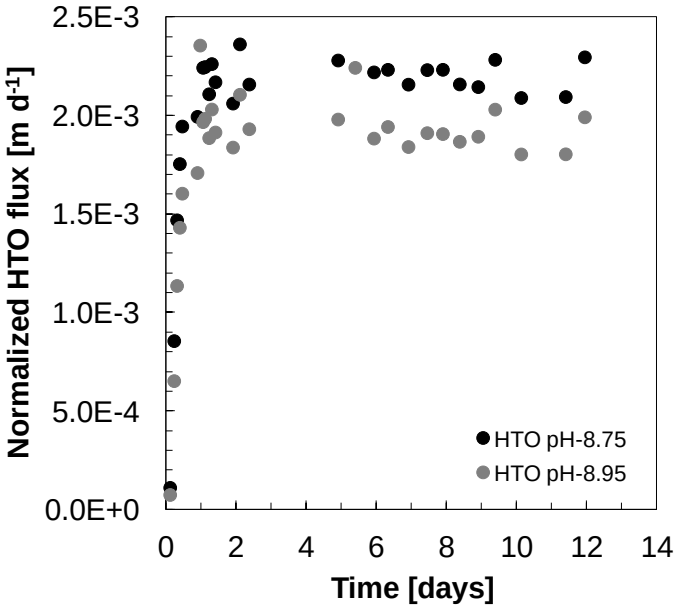

Figure 4-18. Normalized diffusive fluxes of tritiated water (HTO) during HTO through-diffusion experiments at target pH values of 8.75 and 8.95, which are used to determine the total porosities in each diffusion cell prior to U(VI) through-diffusion experiments.

Normalized Flux Data for Through-Diffusion Experiments with Uranium(VI): Observed normalized fluxes for uranium(VI) are about one order of magnitude lower than fluxes for tritiated water (Figure 4-19). This difference in diffusive fluxes between a non-reactive tracer (HTO) and U(VI) provides direct, experimental evidence for a full or partial exclusion of anionic U(VI) solution species from montmorillonite interlayer spaces. This anion exclusion leads to a decrease in the diffusion-accessible porosity and normalized diffusive fluxes for U(VI) under steady-state conditions. This effect is expected to become even more relevant at the higher degrees of clay/bentonite compaction proposed for future nuclear waste repositories (dry density of ~1.65 kg dm^{-3}), than the one tested in this through-diffusion experiment (dry density of ~0.8 kg dm^{-3}). At high degrees of compaction, montmorillonite interlayer spaces will become the primary contributor to the total porosity in the clay packing. Hence, an exclusion of U(VI) from interlayer spaces effectively minimizes its overall diffusion-accessible porosity and diffusive fluxes.

Furthermore, under both pH conditions, uranium(VI) breakthrough is clearly retarded relative to the non-reactive tracer tritium due to U(VI) sorption onto montmorillonite. A greater U(VI) retardation is observed at target pH-8.75 than pH-8.95, given the different time-points of the initial breakthroughs of U(VI). The latter is in good agreement with uranium(VI) sorption data, which suggest higher uranium(VI) sorption affinities and K_D values at pH-8.75 than pH-8.95. Uranium(VI) K_D values estimated from U(VI) through-diffusion data (2.0 L kg^{-1} for pH-8.75 and 1.3 L kg^{-1} for pH-8.95) following an approach by Van Loon et al. (2003b) are in the same range of values as would be expected from batch adsorption data.

Based on our newly developed surface complexation model, U(VI) adsorption onto montmorillonite is dominated by surface complexation reactions on montmorillonite edge sites, not cation exchange reactions on basal surfaces, under the chemical solution conditions tested in U(VI) through-diffusion experiments. This modeling result is further supported by the experimental results from the diffusion experiments. A strong influence of cation exchange reactions would most likely lead to higher U(VI) diffusive fluxes at steady-state conditions relative to the non-reactive tracer (HTO), similar to the diffusion behavior of Ca^{2+}, previously observed in a comparable system (Tinnacher et al. 2016). The latter is due to the 'surface diffusion' of cations along basal cation exchange sites, which are predominantly present within montmorillonite interlayer spaces. Our experimental U(VI) diffusion results, however, indicate a decrease and not an increase in U(VI) diffusive fluxes, compared to the non-reactive tracer.

Last, there appears to be a stronger kinetic limitation for uranium(VI) sorption reactions in the system at pH-8.75 than the one at pH-8.95 (Figure 4-19), since a longer time-frame seems to be required to reach steady-state conditions for U(VI) diffusive fluxes after the initial breakthrough. This indicates a potential overall rate dependence of U(VI) surface complexation reactions on the aqueous speciation of uranium(VI). For instance, the dissociation kinetics of different aqueous uranium(VI) complexes prior to the formation of uranium(VI) surface complexes at montmorillonite edge sites could be different. This hypothesis, however, is currently under further testing (data not reported), based on U(VI)-montmorillonite batch kinetic sorption experiments at the same chemical solution conditions.

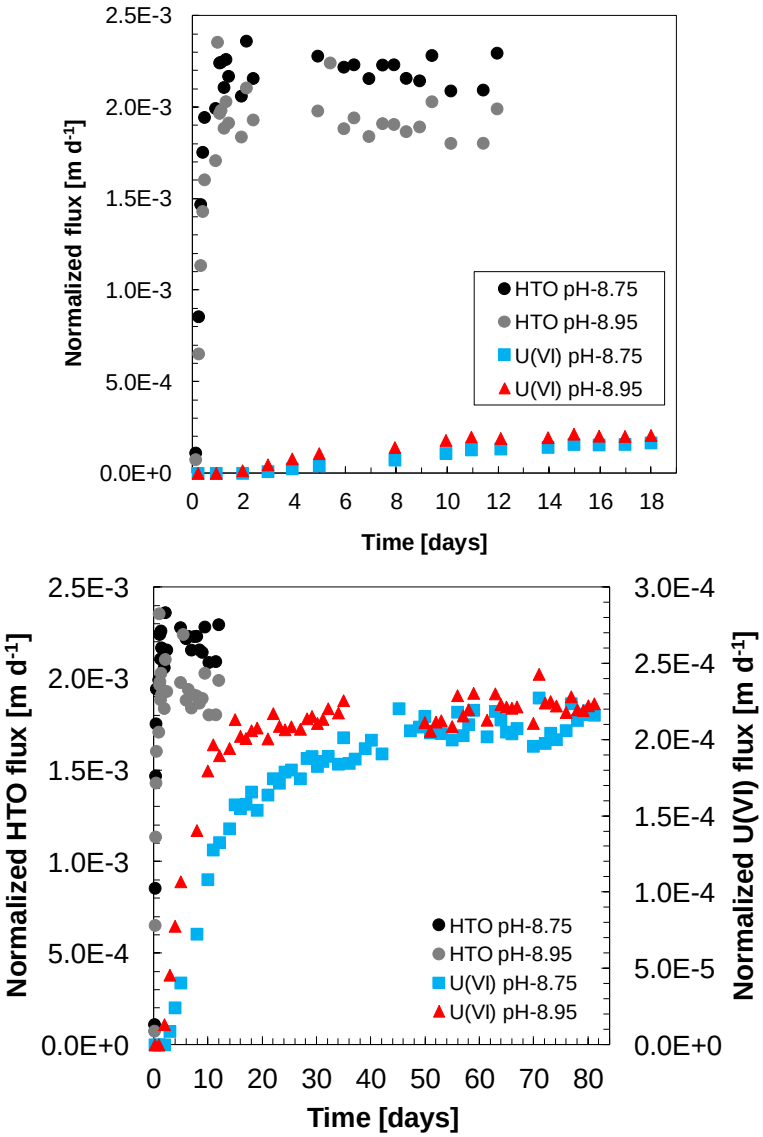

Figure 4-19. Comparison of normalized diffusive fluxes of tritiated water (HTO) and uranium(VI) observed during through-diffusion experiments at target pH values of 8.75 and 8.95 using the same (top) or different (bottom) scales for diffusive fluxes.

Characterization of Chemical Compositions of Low-Concentration Reservoir Solutions: The following results from the characterization of chemical compositions of low-concentration reservoir solutions will allow us to accurately compute U(VI) solution speciation in later simulations of U(VI) diffusion in these through-diffusion experiments. In this context, concentrations of dissolved inorganic carbon/carbonate alkalinity and metals directly affecting U(VI) solution speciation (Ca, Mg) are especially important.

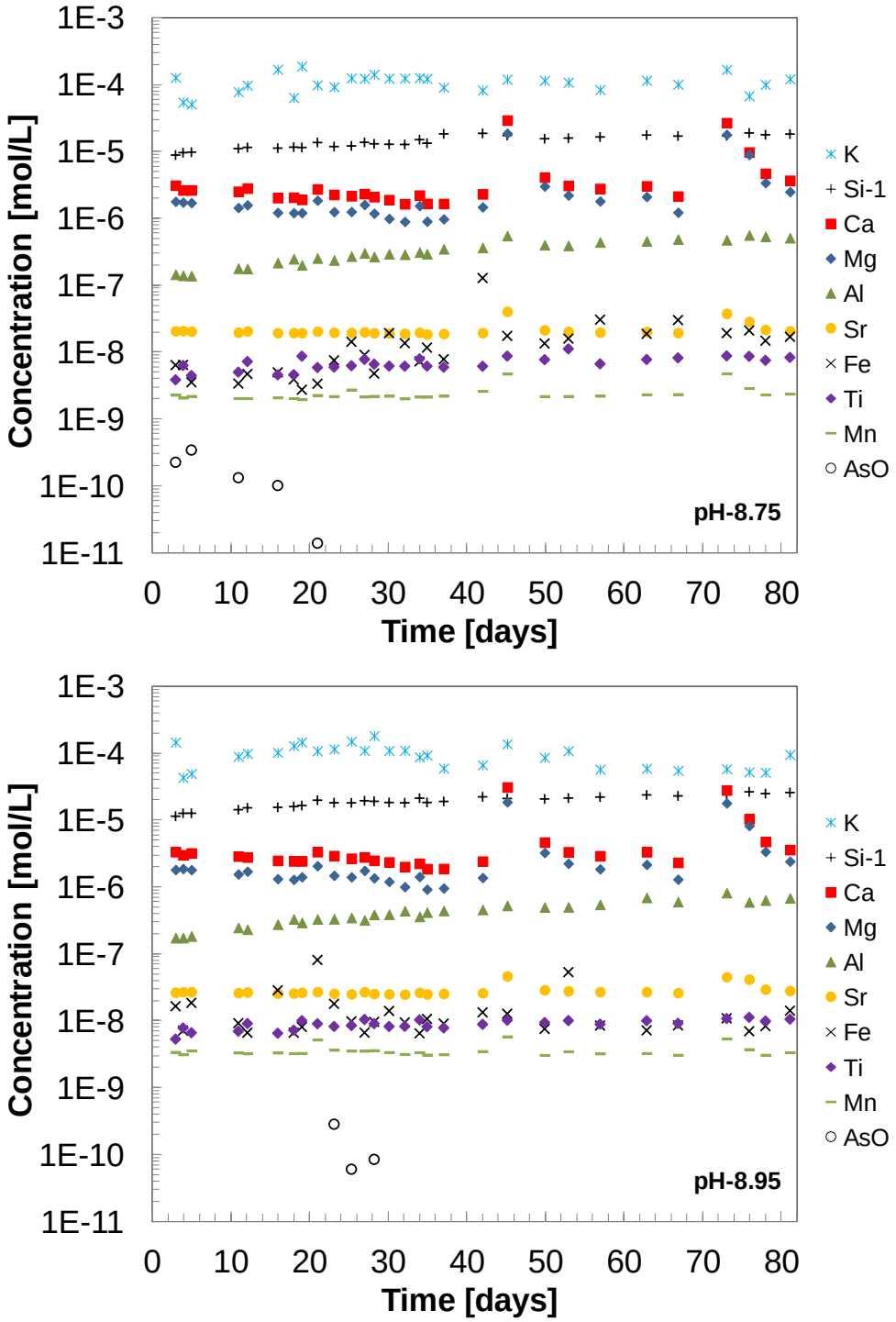

Figure 4-20. Metal concentrations observed in low-concentration reservoir solutions over the course of U(VI) through-diffusion experiments.

Table 4-4. Summary of results for Gran alkalinity titrations of low-concentration reservoir solutions in U(VI) through-diffusion experiments.

		pH-8.75		**pH-8.95**	
Sample ID	Time	Alkalinity	Alkalinity	Alkalinity	Alkalinity
[ ]	[days]	[meq/L]	[mg/L as CaCO3]	[meq/L]	[mg/L as CaCO3]
U-5	3.90	5.31	265.54	7.60	380.14
U-10	12.09	5.29	264.55	7.56	377.76
U-16	19.02	5.31	265.44	7.58	379.18
U-22	26.99	5.34	266.79	7.57	378.37
U-28	33.99	5.29	264.30	7.54	377.08
U-60	75.92	5.32	265.91	7.50	375.03
Average		**5.31**	**265.42**	**7.56**	**377.93**
Std. Dev.		**0.02**	**0.91**	**0.04**	**1.78**

Gran alkalinity titrations indicate stable carbonate concentrations in low-concentration reservoir solutions over the course of U(VI) through-diffusion experiments in both diffusion cell systems (Table 4-4). Alkalinity concentrations are consistently higher in solutions with the higher target pH value, as expected for systems in contact with atmospheric CO_2.

Metal concentrations in low-concentration reservoir solutions, measured by ICP-MS analysis, are summarized in Figure 4-20. Based on previous U(VI) speciation calculations in the presence of Ca (Fox et al. 2006), we conclude at this point that Ca solution concentrations were not high enough to affect U(VI) solution speciation during our U(VI) through-diffusion experiments.

4.4 SUMMARY AND FUTUREWORK

With regard to our research on uranium(VI) adsorption onto Na-montmorillonite, we can summarize the major findings and implications as follows:

1. We developed a new surface complexation model (SCM) that specifically accounts for the 'spillover' of the electrostatic surface potential of basal cation exchange sites on the surface potential of neighboring edge sites. This model allows us to simulate U(VI) adsorption onto Na-montmorillonite over a wide range of chemical solution conditions with a lower number of fitting parameters than previous SCM concepts, and without including a second site type or the formation of ternary U(VI)-carbonato surface complexes. This SCM allows us to simulate U(VI) sorption onto montmorillonite as a function of chemical solution conditions, while minimizing the number of fitting parameters in subsequent uranium(VI) diffusion models.
2. Modeling results suggest that an accurate description of the unique characteristics of electrostatic surface potentials on montmorillonite edge sites is highly important, in order to accurately predict U(VI) sorption and transport behavior at larger field scales. Similar modeling approaches may also be useful for other charge-unbalanced, layered mineral phases.
3. Our modeling results further emphasize the strong influence of dissolved carbonate ligands on U(VI) sorption, which is driven by the competition between U(VI)-carbonate complexation reactions in solution and U(VI) surface complexation reactions on montmorillonite edge sites. As a consequence, predictive U(VI) transport models need to capture potential changes in dissolved inorganic carbon (DIC) concentrations over time and space, e.g. in case of variable contents in carbonate minerals along transport pathways and/or fluctuating pH conditions. For instance,

calcite impurities in bentonite, the proposed buffer material at future nuclear waste repositories, may affect U(VI) sorption by providing a source of dissolved carbonate concentrations.

4. Lastly, a measurement of DIC concentrations appears to be crucial for accurate simulations of U(VI) aqueous speciation during the development and calibration of SCMs. Assumptions of a full exclusion of inorganic carbon from sample solutions in CO_2-"free" adsorption experiments, or a complete solution equilibration with atmospheric/elevated CO_2 levels in the local atmosphere, may often not be justified. This is due to the generally challenging nature of CO_2-"free" adsorption experiments, and the potentially slow CO_2 gas exchange between sample solutions and the local atmosphere under atmospheric/elevated CO_2 conditions. Hence, we recommend that DIC analysis or alkalinity titrations are included as routine measurements in future U(VI) adsorption studies. Furthermore, future experimental designs should also take into account the experimental challenges experienced in this study, with regards to achieving constant pCO_2 conditions across a series of sample solutions in a given adsorption experiment.

Our experimental results from U(VI)-montmorillonite diffusion experiments at alkaline pH can be briefly summarized as follows:

1. Our experimental data provide a first, direct experimental evidence of a full or partial exclusion of anionic U(VI) solution species from montmorillonite interlayer spaces in through-diffusion experiments at alkaline pH and low degrees of clay compaction. This anion exclusion effect results in a significant decrease in the U(VI) diffusion-accessible porosities and U(VI) diffusive fluxes by about one order of magnitude compared to a tritiated water tracer at a compaction of 0.8 kg dm^{-3}. At higher degrees of compaction, and with a larger relevance of clay interlayer spaces for the total porosity in the system, this phenomenon should be even further pronounced, possibly leading to extremely low diffusive fluxes of U(VI).
2. In addition, the U(VI) diffusion results further emphasize the importance of U(VI) adsorption reactions onto Na-montmorillonite in controlling U(VI) retardation during diffusive transport, even at fairly alkaline pH values, where U(VI) adsorption is typically low compared to more circum-neutral pH conditions.
3. Lastly, apparent kinetic limitations were observed for U(VI) sorption reactions in the diffusion cell at a target pH value of pH-8.75, compared to the system at pH-8.95. These apparent kinetic effects, however, need to be further evaluated experimentally and/or based on the simulation of U(VI) diffusion behavior. If relevant, they could affect the time-frames needed to reach full steady-state conditions for U(VI) diffusive fluxes across engineered barrier systems.

All of these results need to be taken into account for the conceptual development of U(VI)-montmorillonite adsorption and diffusion 'sub-models', as part of higher-level performance assessment models.

For the upcoming fiscal year (FY 2017), we plan to:

(1) Simulate the U(VI) diffusion behavior, observed at alkaline pH conditions and low degree of compaction in previous U(VI) through-diffusion experiments, while applying the newly developed U(VI)-montmorillonite surface complexation model to capture U(VI) adsorption processes.
(2) Test experimentally if U(VI) diffusion in Na-montmorillonite can be measured at the extremely low fluxes expected at alkaline pH and the high degrees of compaction (~1.65 kg dm^{-3}) proposed for nuclear waste repositories. If this is the case, then future performance assessment models could possibly rule out U(VI) as a potential contaminant of concern for a certain range of system conditions, e.g., at alkaline pH and high degrees of clay compaction.

Then, we would like to focus our efforts on bentonite samples from the second dismantling phase of the FEBEX heater test. These FEBEX samples represent unique, 'natural' samples with regards to realistic degrees of bentonite compaction (bentonite 'rock') and mineralogical impurities in the solid. The latter is expected to lead to a more complex chemical solution composition in the pore water, e.g. in terms of non-radioactive cations competing for cation exchange sites at low pH and ionic strength. Furthermore, these heat-treated samples also allow us to investigate the potential impacts of a ten-year bentonite exposure to moderate heat (at various water saturation levels) on mineralogical changes in bentonite and possible impacts on U(VI) sorption behavior. Hence, we plan the following experimental work with these FEBEX samples:

(1) Evaluate if U(VI) adsorption affinities onto bentonite have changed due to the heat treatment; and
(2) Characterize potential impacts of mineral impurities in bentonite on the overall diffusion-accessible porosities and U(VI) anion exclusion effects at alkaline pH.

4.5 REFERENCES

Adinarayana, K.N.V., Sasidhar, P., Balasubramaniyan, V., 2013. Modelling of calcium leaching and its influence on radionuclide migration across the concrete engineered barrier in a NSDF. *Journal of environmental radioactivity* 124, 93–100.

Arai, Y., McBeath, M., Bargar, J. R., Joye, J., and Davis, J. A., 2006. Uranyl adsorption and surface speciation at the imogolite-water interface: Self-consistent spectroscopic and surface complexation models. *Geochim. Cosmochim. Acta* 70, 2492-2509.

Bildstein, O., and Claret, F., 2015. Chapter 5- Stability of clay barriers under chemical perturbations. In: Tournassat, C., Steefel, C.I., Bourg, I.C., Bergaya, F. (Eds.), *Natural and Engineered Clay Barriers, Developments in Clay Science*. Elsevier, pp. 155–188.

Bourg, I.C., Sposito, G., Bourg, A.C.M., 2007. Modeling the acid-base surface chemistry of montmorillonite. *Journal of Colloid and Interface Science* 312, 297–310.

Bradbury, M.H., and Baeyens, B., 2003. Porewater chemistry in compacted re-saturated MX-80 bentonite. *Journal of Contaminant Hydrology* 61, 329–338.

Bradbury, M.H., and Baeyens, B., 2005. Modelling the sorption of Mn(II), Co(II), Ni(II), Zn(II), Cd(II), Eu(III), Am(III), Sn(IV), Th(IV), Np(V) and U(VI) on montmorillonite: Linear free energy relationships and estimates of surface binding constants for some selected heavy metals and actinides. *Geochimica et Cosmochimica Acta* 69, 875–892.

Bradbury, M.H., and Baeyens, B., 2011. Predictive sorption modelling of Ni(II), Co(II), Eu(IIII), Th(IV) and U(VI) on MX-80 bentonite and Opalinus Clay: A "bottom-up" approach. *Applied Clay Science* 52, 27–33.

Brigatti, M.F., Galán, E., Theng, B.K.G., 2013. Chapter 2 - Structure and Mineralogy of Clay Minerals. In: Bergaya, F., Lagaly, G. (Eds.), *Handbook of Clay Science, Developments in Clay Science*. Elsevier, pp. 21–81.

Catalano, J.G., and Brown, G.E. Jr., 2005. Uranyl adsorption onto montmorillonite: Evaluation of binding sites and carbonate complexation. *Geochimica et Cosmochimica Acta* 69, 2995–3005.

Chang, F.R.C., Sposito, G., 1994. The electrical double layer of a disked-shaped clay mineral particle: effect of particle size. *Journal of Colloid and Interface Science* 163, 19–27.

Chang, F.R.C., and Sposito, G., 1996. The electrical double layer of a disked-shaped clay mineral particle: effect of electrolyte properties and surface charge density. *Journal of Colloid and Interface Science* 178, 555–564.

Chipera, S. J. and Bish, D. L., 2001. Baseline studies of The Clay Minerals Society Source Clays: Powder X-ray diffraction analyses. *Clay Clay Min.* 49, 398-409.

Chisholm-Brause, C., Conradson, S.D., Buscher, C.T., Eller, P.G., Morris, D.E., 1994. Speciation of uranyl sorbed at multiple binding sites on montmorillonite. *Geochimica et Cosmochimica Acta* 58, 3625–3631.

Chisholm-Brause, C.J., Berg, J.M., Matzner, R.A., Morris, D.E., 2001. Uranium (VI) sorption complexes on montmorillonite as a function of solution chemistry. *Journal of Colloid and Interface Science* 233, 38–49.

Choppin, G.R., 2006. Actinide speciation in aquatic systems. *Marine Chemistry* 99, 83–92.

Costanzo, P. A. and Guggenheim, S., 2001. Baseline studies of The Clay Minerals Society Source Clays: Preface. *Clay Clay Min.* 49, 371-371.

Curtis, G. P., Davis, J. A., and Naftz, D. L., 2006. Simulation of reactive transport of uranium(VI) in groundwater with variable chemical conditions. *Water Resources Research* 42.

Davis, J.A., James, R.O., Leckie, J.O., 1978. Surface ionization and complexation at the oxide/water interface: I. Computation of electrical double layer properties in simple electrolytes. *Journal of Colloid and Interface Science* 63, 480–499.

Davis, J.A., Meece, D.E., Kohler, M., Curtis, G.P., 2004. Approaches to surface complexation modeling of Uranium(VI) adsorption on aquifer sediments. *Geochimica et Cosmochimica Acta* 68, 3621–3641.

Dent, A.J., Ramsay, J.D., Swanton, S.W., 1992. An EXAFS study of uranyl ion in solution and sorbed onto silica and montmorillonite clay colloids. *Journal of colloid and interface science* 150, 45–60.

Duc, M., Gaboriaud, F., Thomas, F., 2005. Sensitivity of the acid-base properties of clays to the methods of preparation and measurement: 2. Evidence from continuous potentiometric titrations. *Journal of Colloid and Interface Science* 289, 148–156.

Fox, P.M., Davis, J.A., Zachara, J.M., 2006. The effect of calcium on aqueous uranium (VI) speciation and adsorption to ferrihydrite and quartz. *Geochimica et Cosmochimica Acta* 70, 1379–1387.

Gaboreau, S., Claret, F., Crouzet, C., Giffaut, E., Tournassat, C., 2012a. Caesium uptake by Callovian–Oxfordian clayrock under alkaline perturbation. *Applied Geochemistry* 27, 1194–1201.

Gaboreau, S., Lerouge, C., Dewonck, S., Linard, Y., Bourbon, X., Fialips, C.I., Mazurier, A., Pret, D., Borschneck, D., Montouillout, V., Gaucher, E.C., Claret, F., 2012b. In-Situ Interaction of Cement Paste and Shotcrete with Claystones in a Deep Disposal Context. *American Journal of Science* 312, 314–356.

Gaucher, E.C., and Blanc, P., 2006. Cement/clay interactions - A review: Experiments, natural analogues, and modeling. *Waste Management* 26, 776–788.

Giaquinta, D., Soderholm, L., Yuchs, S., Wasserman, S., 1997. The speciation of uranium in a smectite clay: evidence for catalysed uranyl reduction. *Radiochimica Acta* 76, 113–122.

Giffaut, E., Grivé, M., Blanc, P., Vieillard, P., Colàs, E., Gailhanou, H., Gaboreau, S., Marty, N., Madé, B., Duro, L., 2014. Andra thermodynamic database for performance assessment: ThermoChimie. *Applied Geochemistry* 49, 225–236.

Hartmann, E., Baeyens, B., Bradbury, M.H., Geckeis, H., Stumpft, T., 2008. A Spectroscopic Characterization and Quantification of M(III)/Clay Mineral Outer-Sphere Complexes. *Environmental Science & Technology* 42, 7601–7606.

Hennig, C., Reich, T., Dähn, R., Scheidegger, A., 2002. Structure of uranium sorption complexes at montmorillonite edge sites. *Radiochimica Acta* 90, 653–657.

Hsi, C.D., and Langmuir, D., 1985. Adsorption of uranyl onto ferric oxyhydroxides: application of the surface complexation site-binding model. *Geochimica et Cosmochimica Acta* 49, 1931–1941.

Hursh, J., Spoor, N., 1973. Data on man. In: *Uranium· Plutonium Transplutonic Elements*. pp. 197–239.

Hyun, S.P., Cho, Y.H., Hahn, P.S., Kim, S.J., 2001. Sorption mechanism of U(VI) on a reference montmorillonite: binding to the internal and external surfaces. *Journal of Radioanalytical and Nuclear Chemistry* 250, 55–62.

Joseph, C., Schmeide, K., Sachs, S., Brendler, V., Geipel, G., and Bernhard, G., 2011. Sorption of uranium(VI) onto Opalinus Clay in the absence and presence of humic acid in Opalinus Clay pore water. *Chem. Geol.* 284, 240-250.

Kerisit, S. and Liu, C. X., 2010. Molecular simulation of the diffusion of uranyl carbonate species in aqueous solution. *Geochim. Cosmochim. Acta* 74, 4937-4952.

Kowal-Fouchard, A., Drot, R., Simoni, E., Ehrhardt, J.J., 2004. Use of spectroscopic techniques for uranium(VI)/montmorillonite interaction modeling. *Environmental Science & Technology* 38, 1399–1407.

Ma, R., Zheng, C., Prommer, H., Greskowiak, J., Liu, C., Zachara, J., and Rockhold, M., 2010. A field-scale reactive transport model for U(VI) migration influenced by coupled multirate mass transfer and surface complexation reactions. *Water Resources Research* 46.

Liu, X., Cheng, J., Sprik, M., Lu, X., Wang, R., 2014. Surface acidity of 2:1-type dioctahedral clay minerals from first principles molecular dynamics simulations. *Geochimica et Cosmochimica Acta* 140, 410–417.

Liu, X., Cheng, J., Sprik, M., Lu, X., Wang, R., 2015a. Interfacial structures and acidity of edge surfaces of ferruginous smectites. *Geochimica et Cosmochimica Acta* 168, 293–301.

Liu, X., Lu, X., Cheng, J., Sprik, M., Wang, R., 2015b. Temperature dependence of interfacial structures and acidity of clay edge surfaces. *Geochimica et Cosmochimica Acta* 160, 91–99.

Liu, X., Lu, X., Sprik, M., Cheng, J., Meijer, E.J., Wang, R., 2013. Acidity of edge surface sites of montmorillonite and kaolinite. *Geochimica et Cosmochimica Acta* 117, 180–190.

Marques Fernandes, M., Baeyens, B., Dähn, R., Scheinost, A.C., Bradbury, M.H., 2012. U(VI) sorption on montmorillonite in the absence and presence of carbonate: A macroscopic and microscopic study. *Geochimica et Cosmochimica Acta* 93, 262–277.

Marques Fernandes, M., Ver, N., Baeyens, B., 2015. Predicting the uptake of Cs, Co, Ni, Eu, Th and U on argillaceous rocks using sorption models for illite. *Applied Geochemistry* 59, 189–199.

McKinley, J.P., Zachara, J.M., Smith, S.C., Turner, D.R., 1995. The influence of uranyl hydrolysis and multiple site-binding reactions on adsorption of U(VI) to montmorillonite. *Clays and Clay Minerals* 43, 586–598.

Meleshyn, A., Azeroual, M., Reeck, T., Houben, G., Riebe, B., Bunnenberg, C., 2009. Influence of (calcium-) uranyl- carbonate complexation on U (VI) sorption on Ca-and Na-bentonites. *Environmental science & technology* 43, 4896–4901.

Mermut, A. R. and Cano, A. F., 2001. Baseline studies of The Clay Minerals Society Source Clays: Chemical analyses of major elements. *Clay Clay Min.* 49, 381-386.

Milodowski, A.E., Norris, S., Alexander, W.R., 2016. Minimal alteration of montmorillonite following long-term interaction with natural alkaline groundwater: Implications for geological disposal of radioactive waste. *Applied Geochemistry* 66, 184–197.

Molera, M., and Eriksen, T., 2002. Diffusion of $^{22}Na^{+}$, $^{85}Sr^{2+}$, $^{134}Cs^{+}$ and $^{57}Co^{2+}$ in bentonite clay compacted to different densities: experiments and modeling. *Radiochim. Acta* 90, 753–760.

Morris, D.E., Chisholm-Brause, C.J., Barr, M.E., Conradson, S.D., Eller, P.G., 1994. Optical spectroscopic studies of the sorption of UO22+ species on a reference smectite. *Geochimica et Cosmochimica Acta* 58, 3613–3623.

Muurinen, A., Lehikoinen, J., 1999. Porewater chemistry in compacted bentonite. *Engineering Geology* 54, 207–214.

NIH, 2016. U.S. National Library of Medicine, TOXMAP classic Environmental Health Maps: http://toxmap-classic.nlm.nih.gov/toxmap/superfund/mapControls.do; accessed on 05-24-2016.

Pabalan, R.T., Turner, D.R., 1996. Uranium (6+) sorption on montmorillonite: Experimental and surface complexation modeling study. *Aquatic Geochemistry* 2, 203–226.

Parkhurst, D.L., and Appelo, C.A.J., 2013. Description of Input and Examples for PHREEQC Version 3–a Computer Program for Speciation, Batch-reaction, One-dimensional Transport, and Inverse Geochemical Calculations.

Savage, D., Bateman, K., Hill, P., Hughes, C., Milodowski, A.E., Pearce, J.M., Rae, E., Rochelle, C.A., 1992. Rate and mechanism of the reaction of silicates with cement pore fluids. *Applied Clay Science* 7, 33–45.

Schlegel, M.L., and Descostes, M., 2009. Uranium uptake by hectorite and montmorillonite: a solution chemistry and polarized EXAFS study. *Environmental science & technology* 43, 8593–8598.

Steefel, C.I., Appelo, C.A.J., Arora, B., Jacques, D., Kalbacher, T., Kolditz, O., Lagneau, V., Lichtner, P.C., Mayer, K.U., Meeussen, J. C. L., Molins, S., Moulton, D., Shao, H., Šimunek, J., Spycher, N., Yabusaki, S.B., Yeh, G.T., 2015. Reactive transport codes for subsurface environmental simulation. *Computational Geosciences* 19, 445–478.

Stumm, W., 1992. Chemistry of the solid-water interface: processes at the mineral-water and particle-water interface in natural systems. John Wiley & Son Inc.

Sylwester, E.R., Hudson, E.A., Allen, P.G., 2000. The structure of uranium (VI) sorption complexes on silica, alumina, and montmorillonite. *Geochimica et Cosmochimica Acta* 64, 2431–2438.

Tinnacher, R.M., Holmboe, M., Tournassat, C., Bourg, I.C., Davis, J.A., 2016. Ion adsorption and diffusion in smectite: molecular, pore, and continuum scale views. *Geochimica et Cosmochimica Acta* 177, 130–149.

Tournassat, C., and Appelo, C.A.J., 2011. Modelling approaches for anion-exclusion in compacted Na-bentonite. *Geochimica et Cosmochimica Acta* 75, 3698–3710.

Tournassat, C., Bizi, M., Braibant, G., Crouzet, C., 2011. Influence of montmorillonite tactoid size on Na-Ca cation exchange reactions. *Journal of Colloid and Interface Science* 364, 443–454.

Tournassat, C., Bourg, I.C., Steefel, C.I., Bergaya, F., 2015a. Chapter 1 - Surface Properties of Clay Minerals. In: Tournassat, C., Steefel, C.I., Bourg, I.C., Bergaya, F. (Eds.), *Natural and Engineered Clay Barriers*, *Developments in Clay Science*. Elsevier, pp. 5–31.

Tournassat, C., Davis, J A, Chiaberge, C., Grangeon, S., Bourg, I.C., 2016a. Modeling acid/base properties at montmorillonite edge surfaces: A review. *Environmental Science* In review.

Tournassat, C., Gaboreau, S., Robinet, J.-C., Bourg, I.C., Steefel, C.I., 2016b. Impact of microstructure on anion exclusion in compacted clay media. *CMS Workshop lecture series* 21, 137–149.

Tournassat, C., Grangeon, S., Leroy, P., Giffaut, E., 2013. Modeling specific pH dependent sorption of divalent metals on montmorillonite surfaces. A review of pitfalls, recent achievements and current challenges. *American Journal of Science* 313, 395–451.

Tournassat, C., Neaman, A., Villiéras, F., Bosbach, D., Charlet, L., 2003. Nanomorphology of montmorillonite particles: Estimation of the clay edge sorption site density by low-pressure gas adsorption and AFM observations. *American Mineralogist* 88, 1989–1995.

Tournassat, C., Steefel, C., Bourg, I., Bergaya, F., 2015b. Natural and Engineered Clay Barriers. Elsevier.

Tournassat, and C., Steefel, C.I., 2015. Ionic transport in nano-porous clays with consideration of electrostatic effects. *Reviews in Mineralogy and Geochemistry* 80, 287–330.

Tournassat, C., Vinsot, A., Gaucher, E.C., Altmann, S., 2015c. Chapter 3 - Chemical conditions in clay-Rocks. In: Tournassat, C., Steefel, C.I., Bourg, I.C., Bergaya, F. (Eds.), *Natural and Engineered Clay Barriers*, *Developments in Clay Science*. Elsevier, pp. 71–100.

Troyer, L.D., Maillot, F., Wang, Z., Wang, Z., Mehta, V.S., Giammar, D.E., Catalano, J.G., 2016. Effect of phosphate on U (VI) sorption to montmorillonite: Ternary complexation and precipitation barriers. *Geochimica et Cosmochimica Acta* 175, 86–99.

Turner, G.D., Zachara, J.M., McKinley, J.P., Smith, S.C., 1996. Surface-charge properties and UO_2^{2+} adsorption of a subsurface smectite. *Geochimica et Cosmochimica Acta* 60, 3399–3414.

U.S. EPA, 1995; https://nepis.epa.gov/Exe/ZyNET.exe/9101IMKK.TXT?ZyActionD=ZyDocument&Client=EPA&Index=1995+Thru+1999&Docs=&Query=&Time=&EndTime=&SearchMethod=1&TocRestrict=n&Toc=&TocEntry=&QField=&QFieldYear=&QFieldMonth=&QFieldDay=&IntQFieldOp=0&ExtQFieldOp=0&XmlQuery=&File=D%3A%5Czyfiles%5CIndex%20Data%5C95thru99%5CTxt%5C00000033%5C9101IMKK.txt&User=ANONYMOUS&Password=anonymous&SortMethod=h%7C-&MaximumDocuments=1&FuzzyDegree=0&ImageQuality=r75g8/r75g8/x150y150g16/i425&Di

splay=hpfr&DefSeekPage=x&SearchBack=ZyActionL&Back=ZyActionS&BackDesc=Results%20page&MaximumPages=1&ZyEntry=1&SeekPage=x&ZyPURL; accessed on 08-19-2016. Development of Compliance Levels From Analytical Detection and Quantitation Levels.

U.S. EPA, 2001; http://nepis.epa.gov/Exe/ZyPDF.cgi?Dockey=30006644.txt; accessed on 05-25-2016. Radionuclides Rule: A Quick Reference Guide.

Van Loon, L.R., Soler, J.M., Bradbury, M.H., 2003a. Diffusion of HTO, $^{36}Cl^-$ and $^{125}I^-$ in Opalinus Clay samples from Mont Terri: Effect of confining pressure. *J. Contam. Hydrol.* 61, 73–83.

Van Loon, L.R., Soler, J.M., Jakob, A., Bradbury, M.H., 2003b. Effect of confining pressure on the diffusion of HTO, 36Cl- and 125I- in a layered argillaceous rock (Opalinus Clay): diffusion perpendicular to the fabric. *Appl. Geochem.* 18, 1653–1662.

Van Olphen, H., 1992. Particle associations in clay suspensions and their rheological implications. In: Güven, N., Pollastro, R.M. (Eds.), *Clay-water interface and its rheological implications*. The clay minerals society, pp. 191–210.

Villalobos, M., Trotz, M.A., Leckie, J.O., 2001. Surface complexation modeling of carbonate effects on the adsorption of Cr (VI), Pb (II), and U (VI) on goethite. *Environmental science & technology* 35, 3849–3856.

Waite, T.D., Davis, J.A., Payne, T.E., Waychunas, G.A., Xu, N., 1994. Uranium (VI) adsorption to ferrihydrite: Application of a surface complexation model. *Geochimica et Cosmochimica Acta* 58, 5465–5478.

Wersin, P., 2003. Geochemical modelling of bentonite porewater in high-level waste repositories. *Journal of Contaminant Hydrology* 61, 405–422.

Wersin, P., Curti, E., Appelo, C.A.J., 2004. Modelling bentonite–water interactions at high solid/liquid ratios: swelling and diffuse double layer effects. *Applied Clay Science* 26, 249–257.

White, G.N., and Zelazny, L.W., 1988. Analysis and implications of the edge structure of dioctahedral phyllosilicates. *Clays and Clay Minerals* 36, 141–146.

Wolthers, M., Charlet, L., Tournassat, C., 2006. Reactivity of bentonite. An additive model applied to uranyl sorption. In: Lützenkirchen, J. (Ed.), *Surface complexation modelling*. Elsevier.

World Health Organization, 2004. Uranium in drinking-water – Background document for development of WHO guidelines for drinking-water quality. Available at http://www.who.int/water_sanitation_health/dwq/chemicals/en/uranium.pdf.

Yabusaki, S. B., Fang, Y., and Waichler, S. R., 2008. Building conceptual models of field-scale uranium reactive transport in a dynamic vadose zone-aquifer-river system. *Water Resources Research* 44.

5. KNOWLEDGE FOR COLLOID FACILITATED RADIONUCLIDE TRANSPORT AND UPDATE ON ACTINIDE DIFFUSION IN BENTONITE BACKFILL

5.1 INTRODUCTION

This section summarizes research conducted at Lawrence Livermore National Laboratory (LLNL) within the Crystalline Disposal R&D Activity Number FT-16LL080303051 and Crystalline International Collaborations Activity Number FT-16LL080303061. The focus of this research is the interaction of radionuclides with Engineered Barrier System (EBS) and host rock materials at various physico-chemical conditions relevant to subsurface repository environments. They include both chemical and physical processes such as solubility, sorption, and diffusion. The scope of the FY16 effort included the following:

- Summarizing the state of knowledge for colloid-facilitated transport and parameterizing our data and conceptual model for use in reactive transport and Performance Assessment models
- Supporting Np(IV) diffusion experiments through bentonite backfill material. The result of this effort will provide sorption/diffusion data for the Np oxidation state most likely to be present in repository scenarios and least studied in the literature.
- Publication of a long-term U(VI) diffusion experiments. These data provide unique information on the long-term performance of bentonite backfill material.
- Supporting the involvement of the Used Fuel Disposition campaign in the Nuclear Energy Agency Thermodynamic Database Development (NEA-TDB, supported through the International Work Package Number FT-16LL08030306)

The colloid facilitated transport effort focused on preparation of a draft manuscript summarizing the state of knowledge and parameterization of colloid facilitated transport mechanisms in support of reactive transport and performance assessment models for generic crystalline repositories. This draft manuscript is being submitted as a level 3 milestone with LANL as the primary author. LLNL's contribution to that effort is summarized only briefly in the present section. A manuscript summarizing long-term U(VI) diffusion experiments through bentonite backfill material was recently accepted for publication; the contents of that manuscript are summarized below. The Np(IV) diffusion experiments were started mid-year and are ongoing. The completion of these experiments is planned for early FY17. Our progress in quantifying Np(IV) diffusion in bentonite backfill is summarized in this section. Our involvement with the NEA TDB project was summarized in a recent Argillite Disposal activity report. It is not included in this report.

5.2 COLLOID FACILITATED TRANSPORT

Due to their importance as backfill material and repository host rock, the interaction of radionuclides with aluminosilicate clay minerals has been the subject of intense study. Recent efforts at LLNL have focused on the potential role of montmorillonite colloids in facilitating Pu migration. In these studies, the focus has been on understanding both the mechanisms and rates of Pu sorption and desorption from montmorillonite clay (Begg et al., 2014; Begg et al., Submitted; Begg et al., 2015; Begg et al., 2013; Benedicto et al., 2014; Zavarin et al., 2008). In our contribution to the report co-authored with Paul Reimus (LANL) "Colloid-Facilitated Radionuclide Transport: Current State of Knowledge from a Nuclear Waste Repository Risk Assessment Perspective" (referred to as the LANL report), we summarized the experimental results and numerical modeling approach used to quantify the observed Pu interaction behavior with aluminosilicate clays. Importantly, these experiments were focused on adsorption and desorption processes rather than transport behavior. Thus, the numerical approach did not include processes associated with colloid transport or filtration. However, the adsorption and desorption

processes were based on the same simple first order reaction equations that were employed to describe radionuclide behavior in field and column flowthrough experiments summarized in the LANL report. As a result, values determined in LLNL experiments could be applied and compared to the values determined from field and column flowthrough experiments summarized in the LANL report. Based on these comparisons, it appears that the numerical approaches and the associated constants reported in the LANL report provide a consistent roadmap for incorporation of colloid-facilitated transport processes into nuclear waste repository performance assessment.

Colloid-facilitated transport may occur via intrinsic or pseudocolloid transport processes. The majority of the discussion in the LANL report was focused in pseudocolloid transport. However, we did include some insight into the behavior of intrinsic Pu colloids as well. From a transport modeling perspective, the numerical approach to simulating the behavior of intrinsic and pseudocolloids is quite similar. The ability of radionuclides to migrate downgradient will still be a function of the colloid filtration rate and the chemical stability of the radionuclide. For pseudocolloids, this chemical stability is governed by the rate of radionuclide desorption. For intrinsic colloids, the chemical stability is principally governed by the rate of intrinsic colloid dissolution.

Based on our Pu intrinsic colloid experiments, it appears that the conditions of Pu nanoparticle formation will have a significant impact on their stability over time. Pu precipitation under mild temperature and solution conditions will lead to unstable Pu nanoparticle formation while higher heat loads and/or acidic conditions may produce more stable nanoparticles. The results suggest that nuclear repository scenarios that include higher heat loading may result in stabilization of Pu oxide phases, which can lead to greater migration of intrinsic Pu nanoparticles.

The repository temperature history, combined with the predicted timing of canister failure, re-saturation of the repository near field, presence of natural and anthropogenic colloids, and other factors will all play a role in the evolution of any specific repository scenario and the potential for colloid facilitated radionuclide mobilization. While uncertainties associated with each of the mechanisms that affect colloid facilitated transport remain, numerical approaches and the associated constants are sufficiently well developed to provide a roadmap for incorporation of colloid-facilitated transport processes into nuclear waste repository performance assessment.

5.3 NP(IV) DIFFUSION THROUGH BENTONITE

In FY16, we continued our efforts in the determination of actinide diffusion coefficients under repository conditions. We began our investigation of ^{237}Np diffusion, which represents a highly radiotoxic component in high-level nuclear waste with a long half-live of 2.144×10^6 a.

In the case of the rupture of waste containers, Np can be mobilized by inflowing water. Under the reducing repository conditions, it will be mainly present as Np(IV). In addition, due to the radioactive decay of the waste, elevated temperatures are expected in this near-field of the waste container (between 50-280°C in the first 1,000 years (Jové Colón et al., 2014)). This will influence the radionuclides' mobility further.

One potential barrier to limit the radionuclides' entry to the biosphere is the clay-rich rock bentonite which is proposed as backfill material between host rock and waste containers. Bentonite will acquire bulk densities ranging from 1.5 to 1.8 g/cm^3 depending on the design of confinement (Keto et al., 2007). Under these conditions, molecular diffusion is expected to be the main transport process for waste-released radionuclides such as Np(IV). The bentonite pore water composition varies based on the pH and redox potential ranges expected under repository conditions. This affects the partial pressure of CO_2.

Conservative modeling results assume partial pressures of up to $10^{-1.5}$ bar (Curti and Wersin, 2002) to be present in the repository.

To mimic repository conditions as close as feasible in the laboratory, we are studying the ^{237}Np(IV) diffusion through compacted MX-80 bentonite (1.6 g/cm^3) at room and elevated temperatures (25, 65, 85°C) under controlled atmosphere conditions (pO_2 < 10 ppm, pCO_2 = 3.2 vol.% = $10^{-1.5}$ bar).

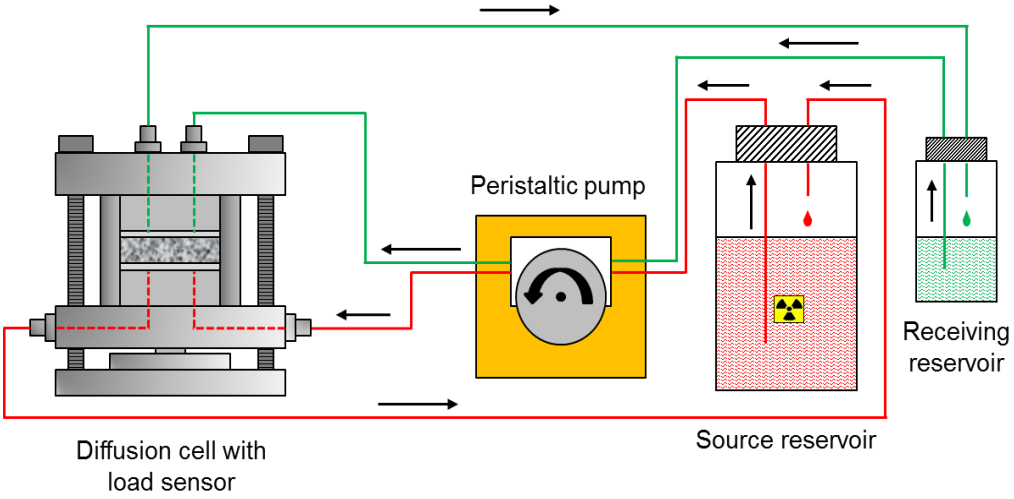

Figure 5-1. Experimental set-up of the diffusion experiments (taken from Joseph et al., 2016).

In Figure 5-1, the general set-up of the experiment at room temperature is given, consisting of a stainless steel diffusion cell containing compacted bentonite (Ø = 0.73'', *L* = 0.39'') and equipped with a load sensor, a peristaltic pump, and two reservoirs: the source reservoir, which contains the radioactive tracer, and the tracer-free receiving reservoir, each of them connected to one end plate of the diffusion cell. For the experiments at elevated temperature, the diffusion cells are placed in aluminum beads baths, which are put on a hot plate together with the reservoirs.

As mobile phase, synthetic bentonite pore water is used in the diffusion experiments (cf. Table 5-1). Its composition is based on the modeling results found in (Van Loon et al., 2007) for a MX-80 bentonite density of 1.6 g/cm^3. However, the salt load needed to be adjusted to hinder carbonate precipitation.

Before the actual diffusion experiment started, the bentonite was equilibrated with the synthetic pore water. This guaranteed the presence of a pore-water-saturated clay. To monitor the saturation of the clay, the swelling pressures were measured daily using the attached load cells. After about 25 days, the three samples (at 25, 65, and 85°C) were regarded to be fully saturated.

Table 5-1. Composition of synthetic MX-80 bentonite pore water.

Cation	*c* / mol/L	Anion	*c* / mol/L
Na^+	2.9×10^{-1}	Cl^-	1.8×10^{-2}
K^+	3.1×10^{-3}	SO_4^{2-}	9.6×10^{-2}
Mg^{2+}	1.2×10^{-4}	F^-	2.2×10^{-4}
Ca^{2+}	9.8×10^{-5}	CO_3^{2-}	8.0×10^{-2}
I	0.51 mol/L		
pH	8		

To characterize the clay samples porosity under the applied conditions, HTO through- and out-diffusion experiments were performed. The diffusive flux and accumulated HTO activity in the receiving reservoir solution was measured at distinct time steps. Figure 5-2 depicts the measured diffusive flux as a function of time and temperature for the through- and out-diffusion experiments. With increasing temperature, the diffusive flux increased in the HTO through-diffusion experiments. In the case of the HTO out-diffusion experiments, the diffusive flux at 65°C was slightly higher than at 85°C. However, both fluxes were increased compared to the flux for the experiment performed at room temperature.

Based on a slope analysis (Van Loon and Soler, 2004), first values for the effective diffusion coefficient and effective porosity could be estimated. The results are summarized in Table 5-2. The results reflect the findings for the flux, with increasing temperature the effective diffusion coefficient increases. The slope analysis reveals that the accessible porosity of the clay for diffusing HTO decreases with increasing temperature.

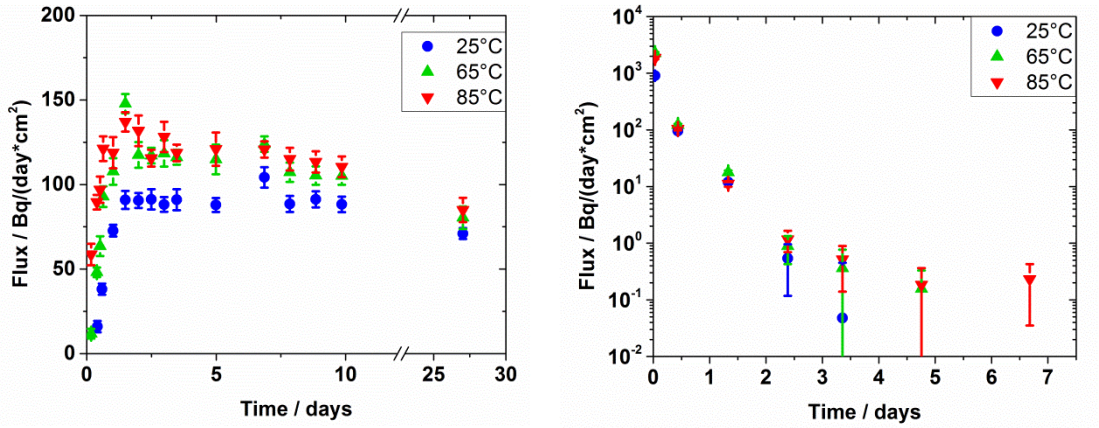

Figure 5-2. Diffusive flux as a function of time and temperature for the HTO (left) through-diffusion and (right) out-diffusion. Activities were measured in the receiving reservoir solution.

Currently, a $^{237}Np(IV)$-carbonate stock solution has been prepared via electrolysis under controlled atmosphere. The oxidation state was checked by UV/vis spectroscopy to be Np(IV); solvent extraction is underway (Bertrand and Choppin, 1982). A total of 3 Np(IV) diffusion experiments (25, 65, and 85 ºC) are underway. The Np(IV) diffusion experiment will continue for about two months at an initial concentration of 1×10^{-6} mol/L. Under our conditions, the aqueous complexes $Np(OH)_3CO_3^-$ (59.8%) and $Np(OH)_2(CO_3)_2^{2-}$ (38.6%) (calculated with EQ3/6, Wolery, 1992) should be the dominant diffusing

species in solution. Characterization of the bentonite material will be performed at the end of the diffusion experiments (early FY17) to quantify Np(IV) diffusion rates.

Table 5-2. First estimates of the effective porosity ε_{eff}, and the effective diffusion coefficient, D_e, obtained via slope analysis (Van Loon and Soler, 2004).

Temperature	c_0 **/ Bq/g**	ε_{eff} **/ –**	D_e **/ m^2/s**
25°C	884 ± 18	0.44 ± 0.02	(1.19 ± 0.03) ×10^{-10}
65°C	882 ± 18	0.30 ± 0.03	(1.51 ± 0.04) ×10^{-10}
85°C	906 ± 18	0.11 ± 0.03	(1.53 0.04) ×10^{-10}

5.4 A NEW VIEW OF URANIUM DIFFUSION THROUGH COMPACTED BENTONITE: REVELATIONS FROM A 6-YEAR STUDY

The manuscript by Joseph, C., Mibus, J., Trepte, P., Müller, Ch., Brendler, V., Park, D.M., Jiao, Y., Kersting, A.B., and Zavarin, M., entitled "Long-term diffusion of U(VI) in bentonite: Dependence on density" was recently accepted for publication in Science of the Total Environment. This work summarizes a multi-year study of the long-term diffusion behavior of U(VI) in bentonite. Importantly, the results suggest that radionuclide diffusion rates will tend to decrease with time which could substantially reduce the long-term risk of radionuclide diffusion through bentonite backfill material and release into the environment.

To protect the environment and people from the ecological and health risks of high-level nuclear waste, one internationally accepted concept is to safely isolate the waste in deep geologic formations. This manuscript, resulting from an international collaboration between the LLNL Glenn T. Seaborg Institute, USA, and the Institute of Resource Ecology at Helmholtz-Zentrum Dresden-Rossendorf, Germany, represents an important contribution to the risk assessment of long-term storage of high-level nuclear waste. The clay, bentonite, is considered as potential buffer material in most of the nuclear waste repository concepts regardless of the surrounding host rock. Our results of a unique 6-year laboratory study on uranium (U) diffusion through MX-80 bentonite as a function of clay dry density suggest that long-term diffusion of U(VI) through clay will be significantly slower than most short-term diffusion experiments have indicated (Figure 5-1). Our long-term diffusion experiments yield diffusivities that are about two orders of magnitude lower than previously reported (the majority of published studies were conducted for less than one year). We propose that the bentonite porosity and pore connectivity decreases with time and hinders U(VI) diffusion through the bentonite. The results of these experiments improve our understanding of long-term performance of proposed nuclear waste repositories and may significantly change the long-term outlook for safety assessment of nuclear waste storage worldwide.

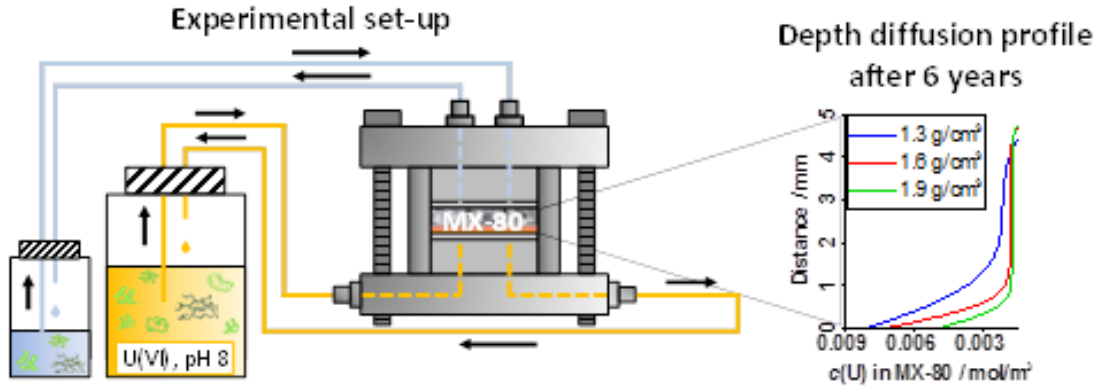

Figure 5-3. Diagram of the diffusion cell used to determine long-term U diffusion rates and a simplified plot of the observed density-dependent diffusion profiles.

5.5 PLANNED FY17 EFFORTS

In FY17, we plan to continue our efforts in data collection and model development in support of the UFD program. In particular, our research will focus on identification, quantification, and parameterization of processes relevant for the evaluation of the performance of various repository scenarios under investigation by the UFD program. Our specific FY17 goals for the crystalline and international work pages are the following:

- Completion of the Np(IV) diffusion experiments and quantification of the diffusion rates.
- Evaluation of the radionuclide sequestration potential of corrosion products produced during canister breaching and radionuclide release (described below)
- Continued engagement with the NEA TDB project through the support of Dr. Atkins-Duffin as the UFD representative for international thermodynamic database development effort.
- Continued collaboration with HZDR thermodynamic and sorption database development groups in support of the database needs of the UFD program

Our interest in radionuclide sequestration by corrosion products stems from (1) the potential for this process to significant inhibit radionuclide release during canister breaching and (2) from the absence of such processes in most repository performance assessments. Discussions with James Jergens (Argonne National Laboratory) suggest that a model of radionuclide incorporation can be added to the waste package cell of the GDSA model and may lead to a reduction in the source term of mobile radionuclides. Steel corrosion rates are already implemented in the GDSA. Thus, only the partitioning of radionuclides into those corrosion products needs to be quantified to evaluate the effect of radionuclide sequestration on downgradient radionuclide migration.

We will evaluate this process from both an experimental and modeling perspective. Experimentally, LLNL has been in the process of developing methodologies to grow various iron oxides phases (goethite, hematite, magnetite) in the presence of radionuclides. We will perform a small number of binary (RN-mineral) coprecipitation experiments to test radionuclide (Pu, Am, Np, and U) partitioning. These data will form the basis for testing our modeling approach, described below.

Several parameters can be used to quantify metal sorption to surfaces and coprecipitation into solid phases. A distribution coefficient, D, relates the solution concentration to the solid concentration (Mn sorption/coprecipitation used as an example):

$$D = (Fe)/(Mn) \times X_{MnOx}/X_{FeOx}$$

where (Fe) and (Mn) are the solution activities and X_{MnOx} and X_{FeOx} are the solid solution concentrations. The value D is appropriate for measuring partitioning in coprecipitation experiments but not for adsorption experiments since partitioning in adsorption samples is a function of the surface area and not the mass of the bulk solid. For adsorption experiments, the results can be related to surface partitioning ratios. A surface partitioning coefficient can be described by:

$$D^* = (Fe)/(Mn) \times Q_{Mn}/Q_{Fe}$$

where Q_{Mn} and Q_{fe} are the surface concentrations of those elements. A comparison between D and D* values can be used to determine if sorption and coprecipitation results follow the Doerner-Hoskins rule in which partitioning by coprecipitation is assumed to behave as a continuum of surface sorption partitioning due to the constant formation of new surface sites. If the Doerner-Hoskins rule applies, a model of radionuclide partitioning into corrosion products can be, at least qualitatively, developed based on the relatively rich radionuclide adsorption data already available in the literature. The efficacy of this approach will be evaluated in FY17.

5.6 REFERENCES

Begg, J. D., Zavarin, M., and Kersting, A. B., 2014. Plutonium Desorption from Mineral Surfaces at Environmental Concentrations of Hydrogen Peroxide. *Environmental Science & Technology* **48**, 6201-6210.

Begg, J. D., Zavarin, M., and Kersting, A. B., Submitted. Desorption of plutonium from montmorillonite: An experimental and modeling study. *Geochimica et Cosmochimica Acta*.

Begg, J. D., Zavarin, M., Tumey, S. J., and Kersting, A. B., 2015. Plutonium sorption and desorption behavior on bentonite. *Journal of Environmental Radioactivity* **141**, 106-114.

Begg, J. D., Zavarin, M., Zhao, P., Tumey, S. J., Powell, B., and Kersting, A. B., 2013. Pu(V) and Pu(IV) Sorption to Montmorillonite. *Environmental Science & Technology* **47**, 5146-5153.

Benedicto, A., Begg, J. D., Zhao, P., Kersting, A. B., Missana, T., and Zavarin, M., 2014. Effect of major cation water composition on the ion exchange of Np(V) on montmorillonite: NpO2+-Na+-K+-Ca2+-Mg2+ selectivity coefficients. *Applied Geochemistry* **47**, 177-185.

Bertrand, P. A. and Choppin, G. R., 1982. Separation of actinides in different oxidation states by solvent extraction. *Radiochim. Acta* **31**, 135-137.

Curti, E. and Wersin, P., 2002. Assessment of porewater chemistry in the bentonite backfill for the Swiss SF/HLW repository*Technical Report 02-09*. Nagra, Wettingen.

Joseph, C., Mibus, J., Trepte, P., Müller, C., Brendler, V., Park, D. M., Jiao, Y., Kersting, A. B., and Zavarin, M., 2016. Long-term diffusion of U(VI) in bentonite: Dependence on density. *Science of the Total Environment* **accepted**.

Jové Colón, C. F., Weck, P. F., Sassani, D. H., Zheng, L., Rutqvist, J., Steefel, C., Kim, K., Nakagawa, S., Houseworth, J., Birkholzer, J., Caporuscio, F. A., Cheshire, M., Rearick, M. S., McCarney, M. K., Zavarin, M., Benedicto, A., Kersting, A. B., Sutton, M., Jerden, J., Frey, K. E., Copple, J. M., and Ebert, W., 2014. Fuel Cycle Research and Development: Evaluation of Used Fuel Disposition in Clay-Bearing Rock (FCRD-UFD-2014-000056)*SAND2014-18303 R*. Sandia National Laboratories, Albuquerque, New Mexico.

Keto, P., Gunnarsson, D., Johannesson, L.-E., and Hansen, J., 2007. Assessment of backfilling materials and methods for deposition tunnels*Clays in Natural & Engineered Barriers for Radioactive Waste Confinement*. Andra, Lille.

Van Loon, L. R., Baeyens, B., Glaus, M. A., Bradbury, M. H., Müller, W., and Schaible, A., 2007. NF-PRO Report, Contract Number: FI6W-CT-2003-02389, RTD Component: 2, Work Package: 2.5*Deliverable (D-N°: 2.5.20), Reporting period: 01/01/04 - 31/12/07*. European Commission - Community Research.

Van Loon, L. R. and Soler, J. M., 2004. Diffusion of HTO, $^{36}Cl^-$, $^{125}I^-$, and $^{22}Na^+$ in Opalinus Clay: Effect of Confining Pressure, Sample Orientation, Sample Depth and Temperature*PSI Report 04-03*. Paul Scherrer Institute, Villigen PSI.

Wolery, T. J., 1992. *EQ3/6, A software package for the geochemical modeling of aqueous systems, UCRL-MA-110662 Part I*. Lawrence Livermore National Laboratory, Livermore.

Zavarin, M., Bourbin, M., Kersting, A. B., Powell, B. A., and P.Zhao, 2008. Examination of the Effects of Ionic Strength and pH on Np(V) and Pu(V) Sorption to Montmorillonite*American Chemical Society - Geochemistry Division/Clay Minerals Society Symposium*, New Orleans, LA.

6 INTERPRETATION OF COLLOID-FACILITATED RADIONUCLIDE TRANSPORT EXPERIMENTS IN A CRYSTALLINE GRANODIORITE AT THE GRIMSEL TEST SITE, SWITZERLAND

6.1 INTRODUCTION

Three colloid-facilitated radionuclide transport experiments were conducted at the Grimsel Test Site (GTS) between 2002 and 2013. Additionally, a fourth test involving radionuclides but no colloids was also conducted in 2002. The GTS is an Underground Research Laboratory in a crystalline granodiorite in the Swiss Alps. The tests were conducted in a saturated shear zone at the GTS, called the MI shear zone, which is dominated by a steeply-dipping planar flow feature that intersects a major access tunnel (the AU tunnel). Fig. 6-1 shows the locations of selected boreholes within the MI shear zone, including the injection and extraction locations for each of the three colloid-facilitated radionuclide transport experiments and also the experiment in which radionuclides were injected without colloids.

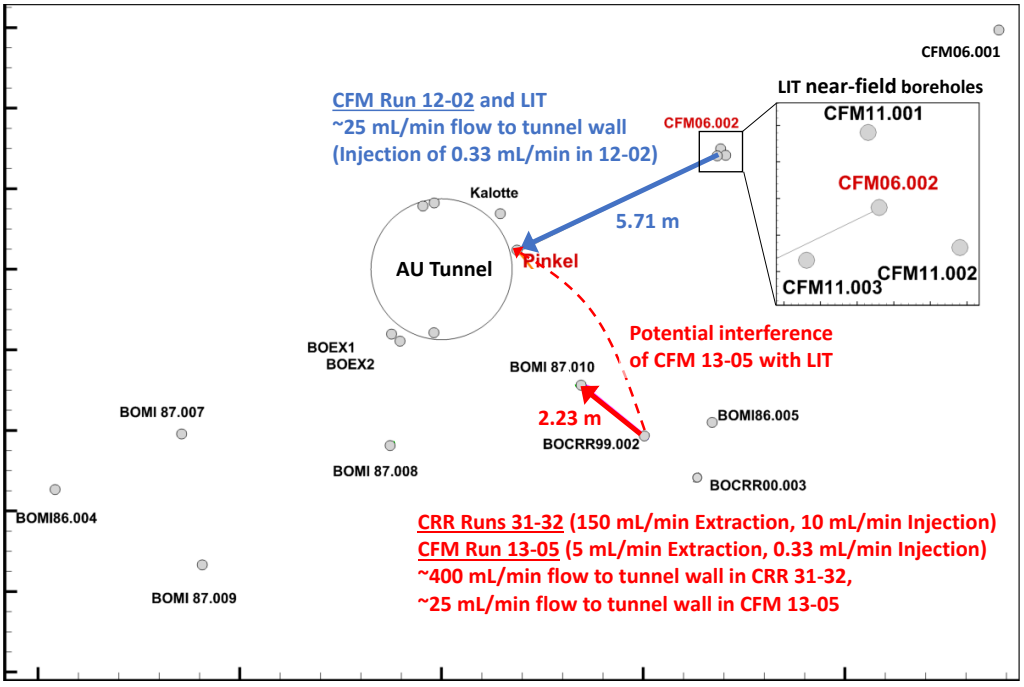

Figure 6-1. Configurations and flows in the GTS MI shear zone for the colloid-facilitated radionuclide transport experiments discussed in this report (underlined). LIT refers to the long-term in-situ test involving emplacement of a radionuclide-doped bentonite plug into CFM 06.002.

The first of the three colloid-facilitated radionuclide transport tests was conducted as part of the Colloids and Radionuclide Retention (CRR) program in 2002. This test, CRR Run 32, was a 'dipole test' that was carried out between two boreholes intersecting the shear zone, with the radionuclide/colloid 'cocktail' being injected at ~10 mL/min into borehole CRR 99.002 and the pextraction hole, BOMI 87.010, being pumped at ~150 mL/min (Fig. 6-1). The mean conservative tracer residence time in the shear zone in this

dipole configuration was on the order of about 2 hours, which ensured high recoveries of injected radionuclidesand minimal spread of contamination in the shear zone. CRR Run 32 was preceded by a radionuclide cocktail injection without colloids (CRR Run 31), which was conducted in an identical flow configuration as Run 32, thus offering the opportunity to compare the transport behavior of the same radionuclides in both the absence and presence of colloids. Details of the CRR transport experiments at the GTS, including Runs 31 and 32, are provided in Möri (2004).

A second colloid-facilitated radionuclide transport experiment was conducted in the MI shear zone in 2012 as part of the Colloids Formation and Migration (CFM) program, a successor program to the CRR program that was initiated in 2004. The U.S. Department of Energy participated as a partner in the CFM program from 2013 to 2015. In this second colloid-facilitated radionuclide transport experiment, CFM Run 12-02, a radionuclide-colloid cocktail was injected at ~0.33 mL/min into shear-zone borehole CFM 06.002, and the extraction location was a surface packer at the AU tunnel wall (called the Pinkel packer) that received shear zone water at a flow rate of ~25 mL/min (Fig. 2-1). The tunnel wall acts as a hydraulic sink for the shear zone, and it flows at several hundred mL/min if the flow is not held back with surface packers. An interpretation of this test was previously provided by the author in Chapter 2 of Wang et al. (2013); it was concluded that the mean water residence time in the shear zone in this test was about 36 hours, or about 18 times longer than in CRR Run 32. The injection interval for this test has since been filled with a radionuclide-doped bentonite plug that is being allowed to swell and erode to release radionuclides and colloids into the shear zone. This test is being called the Long-Term In-Situ Test, or LIT (Kontar and Rösli, 2014). Sampling for the LIT is being conducted both from three small boreholes completed near CFM 06.002 (see Fig. 2-1 inset) and at the Pinkel surface packer at the tunnel wall, which continues to receive shear zone water at ~25 mL/min.

A third colloid-facilitated radionuclide transport experiment, CFM Run 13-05, was conducted in 2013 using the same two boreholes as in CRR Runs 31 and 32 but with the injection and extraction flow rates reduced to 0.33 mL/min and 5 mL/min, respectively. This test was preceded by a series of conservative dye tracer tests that established that the injection of radionuclides and colloids into CRR 99.002 would not interfere with the LIT and also that high recoveries of injected radionuclides at BOMI 87.010 could still be expected despite the much lower flow rates than in CRR Runs 31 and 32. The mean conservative tracer residence time in CFM Run 13-05 was similar to that for CFM Run 12-02, i.e., over an order of magnitude greater than in CRR Run 32.

The purpose of this section is to provide internally consistent interpretations of the three colloid-facilitated radionuclide transport experiments so that the model parameters describing colloid-facilitated transport can be compared and contrasted in the same configuration at different shear zone residence times (CRR Run 32 and CFM Run 13-05) and also in different parts of the shear zone but at similar residence times (CFM Runs 12-02 and 13-05). These comparisons were expected to yield insights into both the time-scaling behavior of colloid-facilitated radionuclide transport and also heterogeneity of transport properties with the MI shear zone. This effort complements a previous effort by Kosakowski and Smith (2004) to model the CRR experiments.

6.2 SUMMARY OF TRACER TESTS CRR 31-32, CFM 12-02 AND CFM 13-05

The experimental parameters and test conditions associated with each of the GTS colloid-facilitated radionuclide transport experiments, including CRR Run 31 which had radionuclides but no colloids, are summarized in Table 6-1. The normalized tracer breakthrough curves (extraction concentrations divided by injection masses as a function of time) in each test are shown in Figures 6-2 through 6-5. The estimated percent recoveries of each radionuclide are listed in parentheses next to the radionuclide names in the legends of these figures. Additional information about each experiment can be obtained from Möri (2004) for the CRR tests and from the Quick-Look reports issued for CFM Runs 12-02 and 13-05 (Kontar

and Gräfe, 2012 and Kontar et al., 2013, respectively). Several points are worthy of mention regarding the tests:

1. For the two CRR runs, ^{131}I was used as a conservative (nonreactive) tracer, and no fluorescent dyes were used. The radionuclide-colloid injections in both CRR tests were accomplished by interrupting the 10 mL/min flow of untraced shear zone water into CRR 99.002 with a 100-ml slug of the cocktail solution injected at the same flow rate (10 mL/min) for 10 minutes and then immediately switching back to a 10 mL/min flow of untraced shear zone water.
2. For the two CFM runs, Amino-G Acid (AGA) was used as a conservative tracer. In these tests, a 2250 mL container of radionuclide-colloid cocktail was inserted into a flow loop of approximately 1000 mL to create an injection circuit of approximately 3250 mL that contained all of the injection cocktail. The solution in this circuit was circulated through the packed-off injection interval in the shear zone at a rate of about 20 mL/min while maintaining a net inflow rate of ~0.33 mL/min to slowly force the cocktail into the shear zone. The circulation between the shear zone and the access tunnel allowed the injection circuit to be sampled over time. This injection method resulted in approximately an exponential decay of tracer/radionuclide concentrations in the injection circuit over time. The decay in concentrations occurred over time scales that were quite long relative to the transport time in the shear zone. Therefore, the resulting injection functions for the CFM tests had to be properly accounted for in test interpretations to ensure that transport parameters were estimated only for the time that radionuclides and colloids spent in the shear zone, not in the injection/circulation loop.
3. The colloids used in each experiment were generated from natural FEBEX bentonite (taken from a mine in Spain) by dispersing the bentonite in a synthetic GTS groundwater, collecting the colloidal fraction, ensuring the stability of the colloidal fraction over time, and then diluting the colloids to the target injection concentration (Möri, 2004). A "cocktail" was prepared for injection by adding all the radionuclides to the colloid dispersion prepared in this manner. The fraction of each radionuclide adsorbed to the colloids at the time of injection was determined by analyzing the supernatant of an ultra-centrifuged sample of the injection cocktail at approximately the time of injection. The colloid concentration in the CRR Run 32 injection cocktail was 20 mg/L, whereas the colloid concentration in the two CFM cocktails was ~100 mg/L.
4. The concentrations of the actinides Th, Pu, Am, U and Np were measured by ICP-MS at the Karlsruhe Institute of Technology (KIT), Karlsruhe, Germany. ^{99}Tc, which was used only in CRR Run 32, was also analyzed by ICP-MS at KIT. The concentrations of ^{22}Na, ^{85}Sr, ^{137}Cs and ^{133}Ba were measured by gamma spectrometry at KIT. Bentonite colloid concentrations and size distributions were measured in the field using a mobile laser-induced breakdown detection (LIBD) system operated by KIT personnel, and they were also measured offsite by LIBD at KIT. Additionally, for the two CFM runs, colloid concentrations were determined at KIT by background-subtracted ICP-MS measurements of Ni, as the bentonite colloids in these tests were labeled with Ni (Reinholdt et al., 2013), which had a very low background concentration in the shear zone water. The LIBD data were used to generate the colloid breakthrough curves for CRR Run 32, and the ICP-MS Ni data were used to generate the colloid breakthrough curves for the CFM tests.
5. As Table 6-1 indicates, the radionuclide associations with colloids (numbers in parentheses listed directly below each radionuclide mass) varied significantly in the different tests for some radionuclides. The most notable differences were for ^{133}Ba, ^{137}Cs, U, and ^{237}Np. The reasons for these differences are not readily explainable, but the most likely explanations are: (1) For ^{137}Cs, the concentrations in the CRR Run 32 injection cocktail were much higher than in the CFM cocktails, and the colloid concentration was lower in the CRR 32 cocktail than in the CFM cocktails; so it is likely that the combination of these factors resulted in suppression of the overall fraction of ^{137}Cs adsorbed to the colloids in the CRR run. (2) The times at which colloid associations were measured for the CRR Run 32 and CFM 12-02 cocktails were within a week of

cocktail preparation, but the colloid associations in the CFM 13-05 cocktail were measured approximately 400 days after cocktail preparation (and the injection was also conducted long after cocktail preparation), so the longer contact times between the radionuclides and colloids may have resulted in significantly different colloid associations in CFM Run 13-05 than in the other tests. It is also possible that the U(VI) and Np(V) added to the CFM 13-05 cocktail partially reduced to U(IV) and Np(IV), respectively, during the long time that this cocktail was stored. These lower oxidation states would be expected to be more strongly associated with the colloids than the higher oxidation states. The different initial radionuclide associations were accounted for explicitly in the model interpretations of the respective tests.

Table 6-1. Summary of experimental parameters and test conditions in the colloid-facilitated radionuclide transport tests (see Fig. 2-1 for test configurations).

Parameter	CRR 31	CRR 32	CFM 12-02	CFM 13-05
Extraction Flow Rate, mL/min	150	150	25	5
Injection Flow Rate, mL/min	10	10	0.33	0.33
Injection Volume, mL (includes circulation loop volume for CFM tests)	100	100	3218	3218
Injection Loop Circulation Flow Rate, mL/min	N/A	N/A	20	20
Amino G Acid Injected, mg	---	---	3.7	4.45
Colloid Mass Injected, mg	---	~2	~225	~225
^{131}I mas injected, μg	1.63×10^{-5}	1.21×10^{-5} (0)	---	---
^{22}Na mass injected, μg	---	---	0.005 (0-3.5%)	0.0065 (3.9%)
^{85}Sr mass injected, μg	1.09×10^{-4}	9.41×10^{-5} (0)	---	---
^{99}Tc mass injected, μg	---	0.103 (12%)	---	---
^{133}Ba mass injected, μg	---	---	0.21 (24-34%)	1.02 (59.3%)
^{137}Cs mass injected, μg	---	0.19 (8%)	0.24 (97-98%)	0.27 (63.9%)
^{232}Th mass injected, μg	0.26	0.255 (94%)	---	2.35 (99.1%)
$^{233 \text{ or } 238}$U mass injected, μg	22.6	20.2 (6%)	---	0.225 (83.5%)
^{237}Np mass injected, μg	22.4	25.8 (0.5%)	4.8 (<1%)	4.59 (30.9%)
$^{241 \text{ or } 243}$Am mass injected, μg	0.144	0.016 (99%)	0.035 (99+%)	0.235 (99.6%)
$^{238, 242 \text{ or } 244}$Pu mass injected, μg	0.242	0.165 (84%)	1.6 (99+%)	1.09 (99.6%)

Note: Numbers in parentheses listed beneath each radionuclide mass are the percentage of injected mass estimated to be associated with colloids at the time of injection. Note that the colloid associations are quite different in the different tests. Differences between CFM 12-02 and CFM 13-05 may have been influenced by the different times after cocktail preparation that the associations were measured: 2-7 days for CFM 12-02 and 401 days for CFM 13-05. There were no colloids in the CRR 31 injection cocktail. Injection concentrations can be calculated by dividing injection masses by the injection volumes listed in the third row of the table.

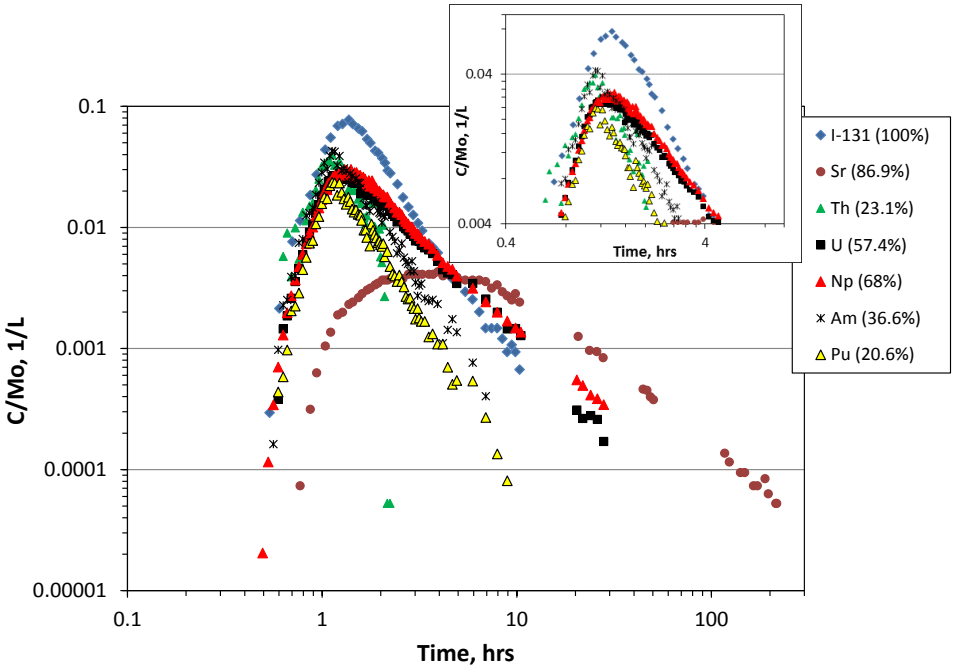

Figure 6-2. Normalized breakthrough curves in CRR Run #31 (recoveries indicated in parentheses). Inset shows details near peak concentrations.

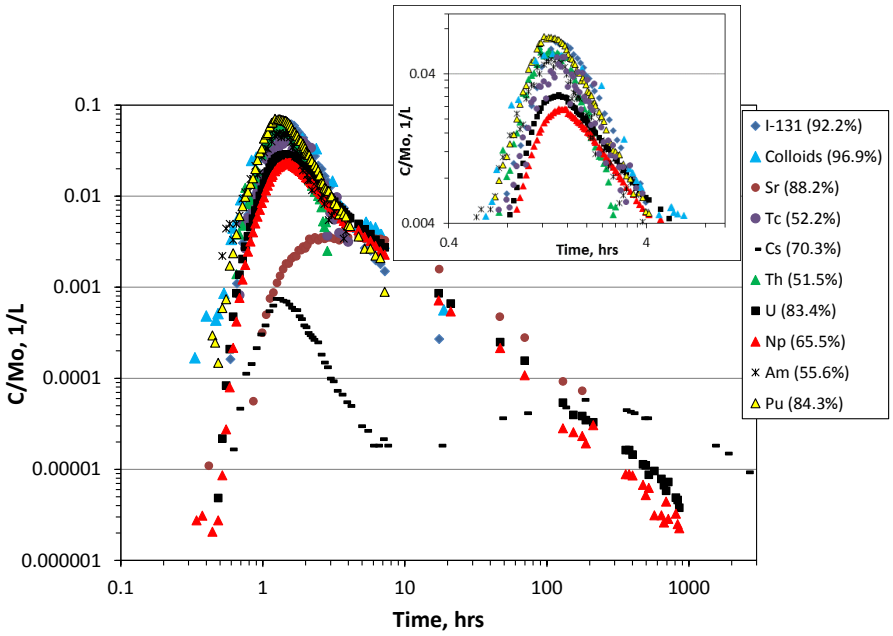

Figure 6-3. Normalized breakthrough curves in CRR Run #32 (recoveries indicated in parentheses). Inset shows details near peak concentrations.

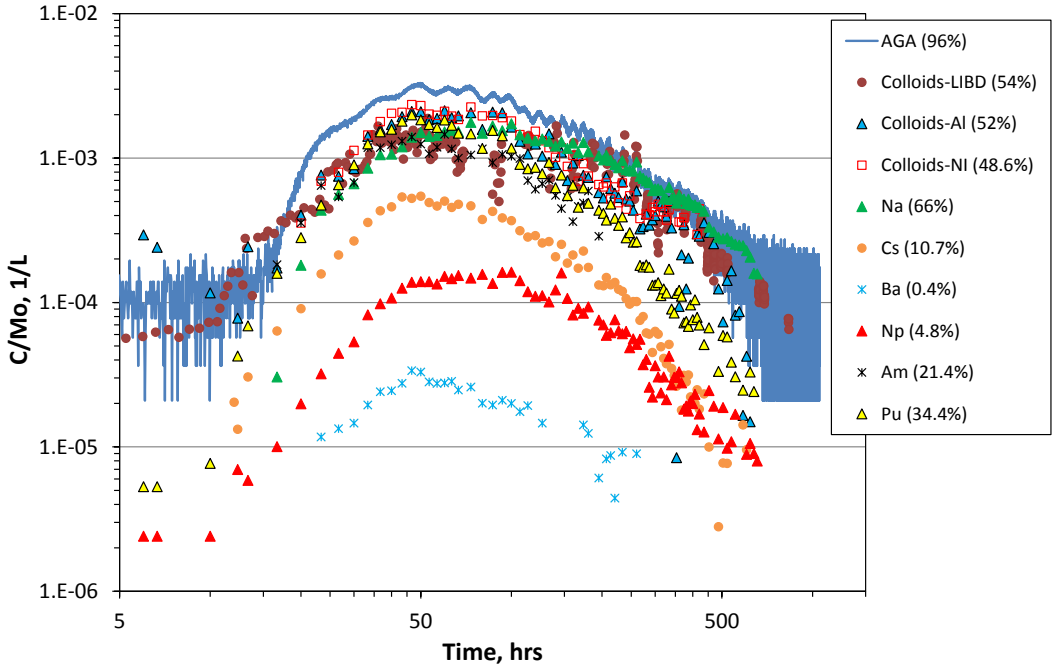

Figure 6-4. Normalized breakthrough curves in CFM Run 12-02 (recoveries indicated in parentheses).

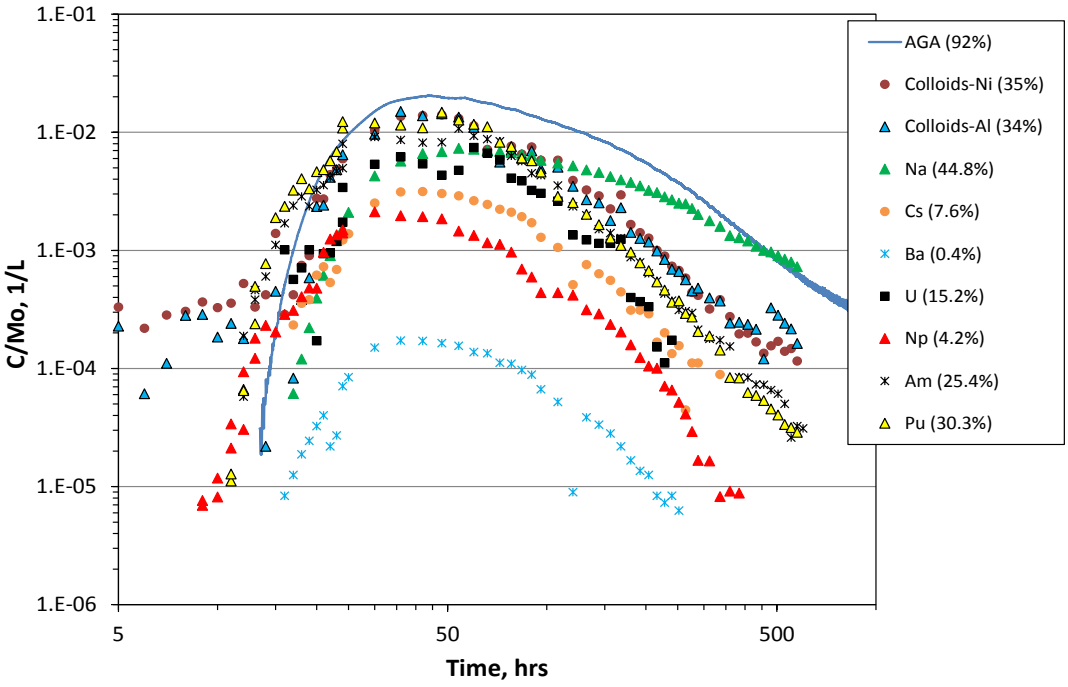

Figure 6-5. Normalized breakthrough curves in CFM Run 13-05 (recoveries indicated in parentheses).

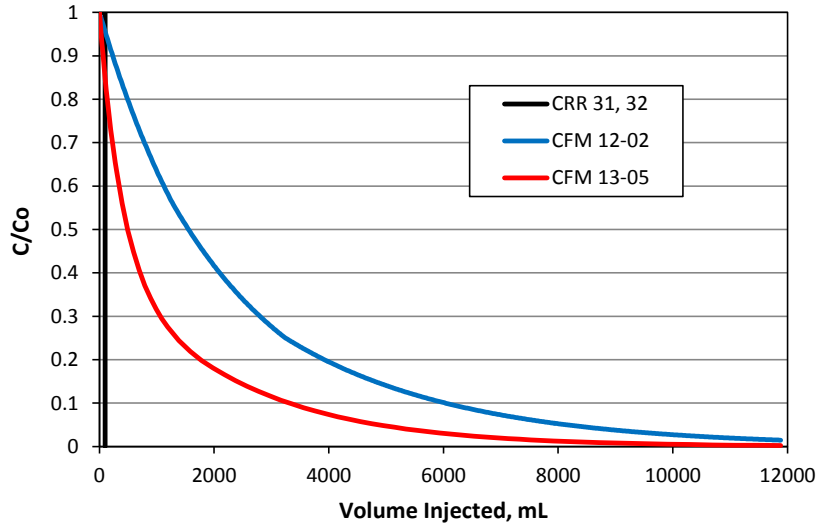

Figure 6-6. Normalized injection concentration histories as function of volume injected in the four radionuclide-colloid experiments. Note that CRR Runs 31 and 32 had same histories that were very short (100-mL) pulses.

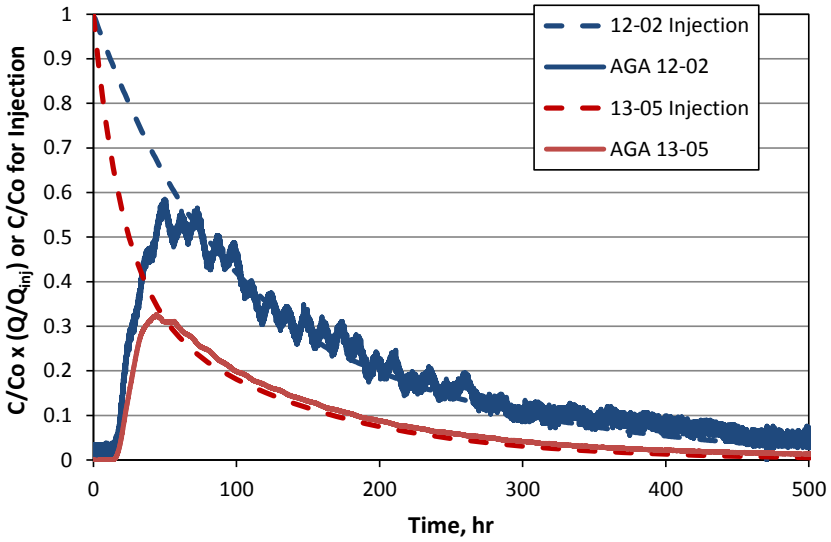

Figure 2-7. Normalized extraction and injection concentration histories in the two CFM tests.

Fig. 6-6 shows the normalized injection concentration histories (smoothed) for each of the four tests plotted as a function of volume injected. The injection histories for the two CRR tests were not measured but are inferred to be simple 100-ml pulses based on descriptions of how the tests were conducted. The injection histories for the two CFM tests were measured by sampling the injection circulation loops, and they show the roughly exponential decay of tracer concentration during the tests. Fig. 6-7 shows how the extraction concentration histories closely follow the injection concentration histories in both CFM tests after accounting for dilution (dilution factor = extraction rate divided by injection rate). This figure shows that much of the tailing in both of the CFM tests can be attributed to the slow decline in injection

concentrations and not to dispersion of tracers in the shear zone. Note that the cyclic fluctuations in the extraction concentration history for CFM Run 12-02 shown in Fig. 6-7 were typical of all tests conducted between borehole CFM 06.002 and the Pinkel surface packer at the tunnel wall. These fluctuations are believed to be caused by cyclic changes in flow patterns in the shear zone caused by a combination of barometric effects and earth tides.

In Fig. 6-8 it is apparent that despite the two CFM tests having the same controlled injection rate of 0.33 mL/min, the Run 13-05 injection concentrations declined significantly faster than the 12-02 concentrations, which suggests that the actual injection rate in Run 13-05 was significantly faster than in Run 12-02 (at least during the early portion of the tests). The negative of the slope of a plot of the natural log of injection concentration vs. time multiplied by the circulation interval volume provides an estimate of the instantaneous injection rate in any given test. Fig. 2-8 shows the resulting estimated instantaneous injection rates as a function of time in the two CFM tests along with a dashed line to indicate the intended injection rate of 0.33 mL/min. Both tests exhibited greater-than-intended injection rates in the early portions of the tests, with a leveling off of the injection rates after a little more than 100 hours. The injection rate early in Run 13-05 greatly exceeded the planned injection rate. Furthermore, whereas the Run 12-02 injection was defined by two distinct injection rates with a clear break at around 120 hours, the Run 13-05 injection exhibited a continuous decline in injection rate up until about that same time. The reasons for this decline are unknown, but it is important that it be accounted for when interpreting the tracer test because the observed extraction concentrations are highly dependent on the rate at which tracers/colloids/radionuclides leave the injection interval and enter the shear zone. The variations in injection rate also cause a time dependence of the dilution factor (ratio of extraction to injection rate), which must be accounted for when interpreting a test using a transport model that assumes only 1-D flow, as was done for this report (see next section). For Run 12-02, the injection rate variations were not large enough to cause significant errors in modeled concentrations, but for Run 13-05, the variations during the early portion of the test were large enough to have a big impact on modeled concentrations and thus a significant impact on test interpretations. Indeed, the magnitude of the Run 13-05 injection rate variations were far greater than in any previous CFM tracer test that the author has interpreted.

To account for the variations in apparent injection rates in CFM Run 13-05, the first step taken was to determine the mass associated with the injection function by effectively integrating the product of the deduced instantaneous injection flow rate and the observed instantaneous conservative tracer (AGA) injection concentration over time. The mass obtained by this procedure was about 1.2 times greater than the reported injection mass, which implies that either the estimated flow rates are too high or the observed concentrations are too high, or both.

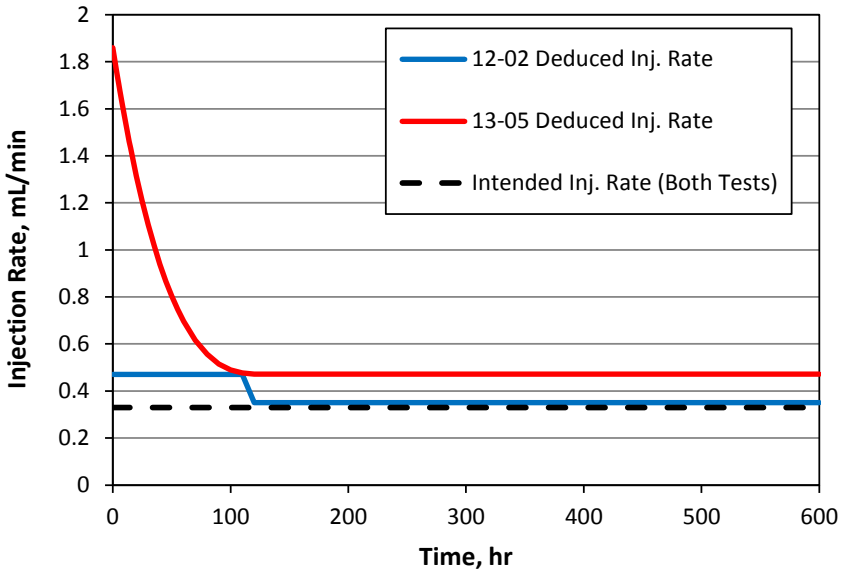

Figure 6-8. Estimated injection rates as a function of time in the two CFM tests based on the slope of the natural log of concentration vs. time multiplied by injection loop volume. The dashed line is the intended injection rate.

Because it is not possible to know whether the flow rate or concentrations are erroneous, two methods of ensuring mass balance were employed. In the first method, the injection flow rate for the entire test was assumed to be the flow rate that was observed after 120 hours (0.47 mL/min), and the initial injection concentration was assumed to be the reported injection mass divided by the injection interval volume. This approach guaranteed perfect mass balance in the injection interval. The second approach was to use the deduced flow rates, but to reduce the initial concentration in the injection interval by a factor of 1.2 to achieve mass balance. The resulting assumed AGA injection functions relative to the observed injection function are shown in Fig. 6-9. Although the constant-rate injection function has greater area under its curve in this figure, the mass associated with the two solid curves are the same because of the larger injection flow rate in the early portion of the test for the varying-inflow curve.

The interpretive modeling approach used in this report (discussed in the next section) involved the application of a numerical model that assumes only 1-dimensional flow, so there is no transverse dispersion to account for spatial variations of tracer concentrations that must occur near the injection borehole when injection rates vary. Instead, a dilution factor (ratio of extraction to injection flow rates) must be explicitly incorporated into the model calculations; i.e., the modeled extraction concentrations are divided by the dilution factor. The dilution factor in the case of assuming a constant-rate injection function was constant throughout the test (5/0.47 = 10.64), which is easy to implement in the model; but in the case of the varying-rate injection function, the dilution factor must be varied throughout the test. This poses a problem because the tracer arrival time at the extraction point is delayed relative to its injection time, so the instantaneous dilution factor at the time of tracer arrival can be quite different than the dilution factor at the time of injection. When the instantaneous dilution factors associated with the varying-inflow injection function were used without any time adjustments, it was found that the modeled tracer extraction mass recovery was far less than the injection mass because the dilution factors were always greater at the time of tracer recovery than the time of tracer injection. To address this problem, the dilution factor applied at any given time was taken to be the ratio of extraction to injection flow rates that occurred at an earlier time during the test. The offset in time was fixed throughout the test, and it was adjusted by trial-and-error until the calculated AGA tracer mass recovery was approximately 100%. It

was found that a time offset of 50 hours, with the dilution factor during the first 50 hours of the test assumed to be equal to the initial dilution factor, yielded 100% mass recovery, so this offset was assumed for all the varying inflow rate test interpretations.

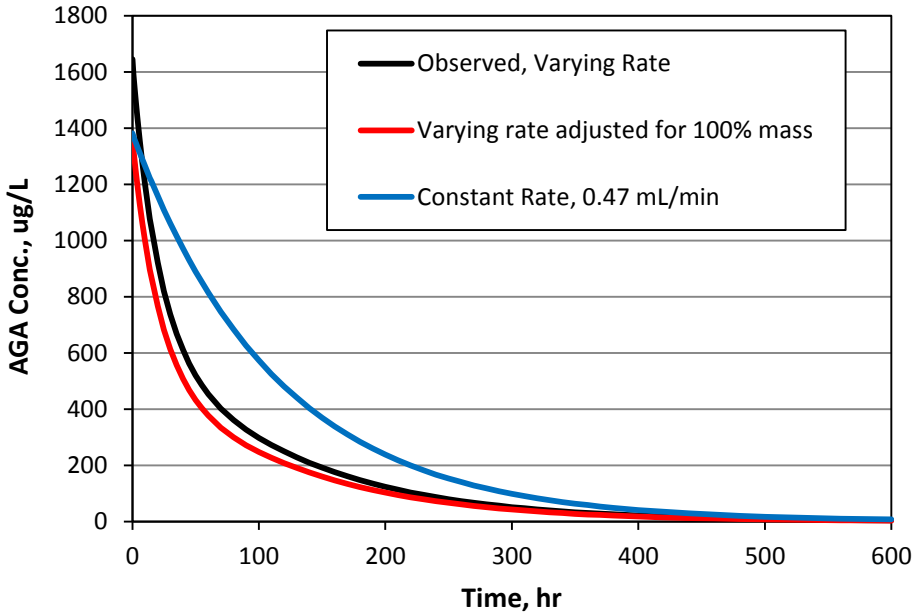

Figure 6-9. Observed (black) and two different assumed injection functions in CFM Run 13-05. The observed curve yields 120% mass injection, whereas the two assumed curves correspond to 100% mass injection.

Because colloid filtration and radionuclide interactions with shear zone surfaces are assumed to occur only while colloids and radionuclides are in the shear zone, it is important to know the conservative tracer residence time distributions in the shear zone for each of the tests. Fig. 6-10 shows the shear-zone-only residence time distributions for each test plotted as a function of volume extracted. There curves were obtained by effectively deconvoluting the conservative tracer injection functions from the conservative tracer extraction functions in each test. This deconvolution was accomplished by matching the extraction functions using a 1-D advection-dispersion model while assuming that the injection functions were the observed injection concentration histories (or inferred concentration histories in the case of the CRR tests). The curves of Fig. 6-10 were calculated assuming that a 0.02-hr tracer pulse was injected directly into the shear zone, with the normalized concentrations being divided by the extraction flow rate in each test to make the areas under the curves the same. The shear-zone mean residence times and Peclet numbers (transport distance divided by longitudinal dispersivity) deduced for each test and used to generate the curves of Figure 6-10 are listed in Table 2-2. It is clear that the shear-zone transport functions for the two different CFM 13-05 injection functions are significantly different, with their only common feature being the extracted volume at which the peak concentration occurs. These different shear zone transport functions have a big effect on model-deduced transport parameters for the CFM 13-05 test. In this report, the model parameters deduced for both of the CFM 13-05 injection functions are treated as a reflection of parameter uncertainty resulting from uncertainty in knowledge of the true injection function. However, it will be shown later that the varying-rate injection function appeared to be superior to the constant rate injection function because the latter required time-dependent filtration and desorption rate constants to provide good model matches to the breakthrough curves of colloids and several radionuclides in CFM 13-05.

Table 6-2. Deduced mean residence times and Peclet numbers in shear zone for curves of Figure 6-10.

Parameter	CRR 31	CRR 32	CFM 12-02	CFM 13-05 Constant	CFM 13-05 Varying
Mean Residence Time, hr	1.8	1.9	36	28	140
Peclet number	9.5	11.5	10	27	1.5

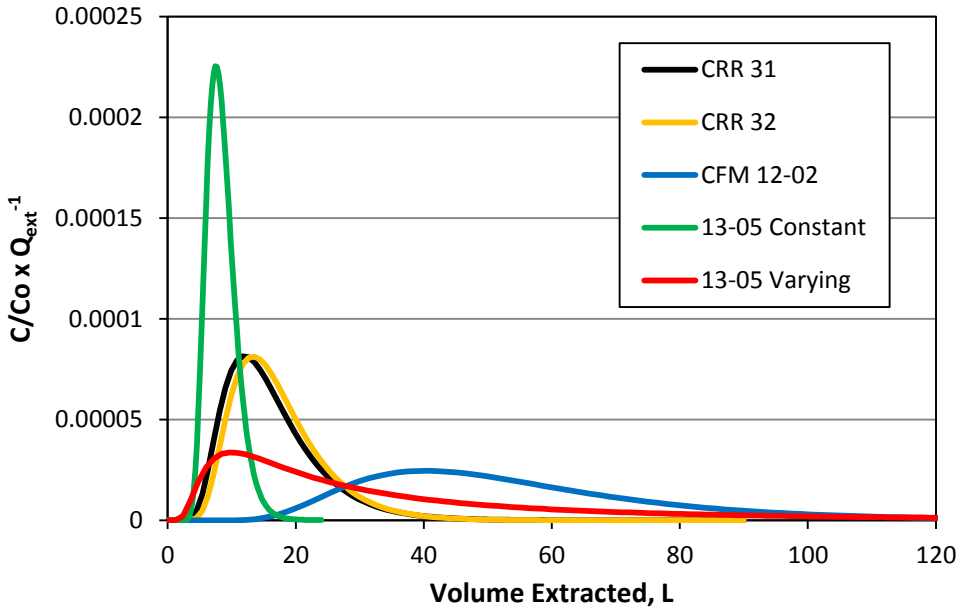

Figure 6-10. Deduced shear-zone-only residence time distributions in each test. For CFM 13-05, "constant" and "varying" refers to constant and varying injection rate functions.

6.3 INTERPRETIVE MODELING APPROACH

The first step in the interpretive modeling procedure was to use the RELAP (REactive transport LAPlace transform) semi-analytical model (Reimus et al., 2003) to approximately fit the conservative tracer extraction breakthrough curves by adjusting the mean residence time and Peclet number in the shear zone (Peclet number is transport distance divided by longitudinal dispersivity) as well as the fractional tracer mass participation in each test. This model was used to generate the shear-zone-only residence time distributions of Fig. 2-10 after the injection functions had been effectively deconvoluted from the extraction functions using the numerical model described below. Exponential-decay injection functions with a constant decay rate (i.e., constant injection flow rate) can be directly implemented in RELAP, but RELAP cannot accommodate varying injection rates, so for the CFM tests, RELAP provided only approximate estimates of the mean residence time and Peclet number to use as first guesses in the numerical model (which was then used to refine the estimates). RELAP was used to do all model

interpretations of the CRR tests because these tests involved simple pulse injections that RELAP can readily accommodate.

RELAP is a semi-analytical model that uses a Fourier transform inversion method to solve the Laplace-domain transport equations in either a single- or a dual-porosity system. The model can account for diffusion between fractures and matrix, as well as linear, first-order reactions in both fractures and matrix. The very rapid execution of the model makes it ideal for the numerous simulations needed for transport parameter estimation. The fractional mass participation in each test was allowed to be an adjustable parameter because some of the tests did not have complete tracer recovery, indicating that some of the tracer mass drifted out of the hydraulic capture zone induced by extraction at the BOMI 87.010 borehole (or at the Pinkel surface packer in the case of CFM Run 12-02). A matrix porosity of 0.02 that extended 1 cm into the matrix from the fracture wall(s) was assumed in the shear zone for all test interpretations (the matrix was assumed to have a porosity of zero at distances greater than 1 cm from the fracture walls), and a solute matrix diffusion coefficient of 1×10^{-6} cm^2/sec was also assumed in all interpretations. Also, a shear-zone effective fracture aperture of 2 mm was assumed in all test interpretations, and the effective porosity within the shear zone was assumed to be 0.5 to allow for sorption to occur within the shear zone. The mean residence time, Peclet number and fractional mass participation estimated for the conservative tracers using the above matrix diffusion parameters were not significantly different from estimates obtained assuming no matrix diffusion. However, matrix diffusion and sorption were found to be necessary to explain the transport behavior of the reactive solutes that were not strongly associated with colloids, so a small amount of matrix diffusion was allowed.

In addition to providing estimates of shear-zone transport parameters for the conservative tracers, RELAP was also used to estimate colloid transport parameters (filtration and resuspension rate constants) and reactive solute transport parameters (fracture and matrix adsorption and desorption rate constants for solutes not strongly associated with colloids, and colloid desorption rate constants for solutes strongly associated with colloids). These estimates were obtained by assuming that the mean residence time, Peclet number and fractional mass participation estimated for the conservative tracers also applied to the colloids and reactive solutes, and then the appropriate rate parameters were adjusted to fit the colloid or solute data.

The resulting best-fitting parameters from RELAP were used as initial parameter estimates in a 2-D numerical model that could account for processes that RELAP does not explicitly account for. The most important of these processes was the variable injection flow rates observed in the CFM tests and the simultaneous transport of colloids and reactive solutes (RELAP does not account for interacting species). In effect, RELAP was used to obtain initial estimates for the more robust numerical model. This procedure was found to be highly effective for refinement of parameter estimates; only relatively minor adjustments to the RELAP-estimated parameters were necessary, and these adjustments could be made rather quickly by hand. The mean residence times and Peclet numbers of the shear zone listed in Table 6-2 were obtained using this refinement procedure. Note that the 2-D model still simulated only 1-D flow, as the second dimension (perpendicular to flow) was used only to account for diffusive mass transport.
The 2-D numerical model simultaneously solves the following equations:

Colloid Transport in Fractures:

Mobile: $$\frac{\partial C_{col}}{\partial t} + v_f \frac{\partial C_{col}}{\partial x} - D_c \frac{\partial^2 C_{col}}{\partial x^2} + k_{fc} C_{col} - k_{rc} S_{col} + k_{fci} C_{col} - P_{col} = 0 \qquad (6\text{-}1)$$

Immobile: $$\frac{\partial S_{col}}{\partial t} - k_{fc} C_{col} + k_{rc} S_{col} - k_{fci} C_{col} = 0 \qquad (6\text{-}2)$$

Solute Transport in Fractures:

$$\frac{\partial C}{\partial t} + v_f \frac{\partial C}{\partial x} - D_f \frac{\partial^2 C}{\partial x^2} + k_{1f} C C_{col}\left(1-\frac{C_1}{C_{col}S_1^0}\right) + k_{2f} C\, C_{col}\left(1-\frac{C_2}{C_{col}S_2^0}\right) + \left(\frac{\rho_f}{\eta}\right)k_{fa} C\left(1-\frac{S_a}{S_a^0}\right) + \left(\frac{\rho_f}{\eta}\right)k_{fb} C\left(1-\frac{S_b}{S_b^0}\right) + k_{1f} C S_{col}\left(1-\frac{C_{filt,1}}{S_{col}S_1^0}\right) + k_{2f} C S_{col}\left(1-\frac{C_{filt,2}}{S_{col}S_2^0}\right) - k_{1b} C_1 - k_{2r} C_2 - k_{1b} C_{filt,1} - k_{2r} C_{filt,2} - \left(\frac{\rho_f}{\eta}\right)k_{ra} S_a - \left(\frac{\rho_f}{\eta}\right)k_{rb} S_b - \frac{\phi D_m}{b\eta}\frac{\partial C_m}{\partial y}\bigg|_{y=b} = 0 \quad (6\text{-}3)$$

Solute Transport on mobile colloids (in fractures) while adsorbed to colloid sites 1 and 2:

$$\frac{\partial C_1}{\partial t} + v_f \frac{\partial C_1}{\partial x} - D_c \frac{\partial^2 C_1}{\partial x^2} - k_{1f} C C_{col}\left(1-\frac{C_1}{C_{col}S_1^0}\right) - k_{rc} C_{filt,1} + k_{1r} C_1 + k_{fc} C_1 - P_{col} S_a = 0 \quad (6\text{-}4)$$

$$\frac{\partial C_2}{\partial t} + v_f \frac{\partial C_2}{\partial x} - D_c \frac{\partial^2 C_2}{\partial x^2} - k_{2f} C C_{col}\left(1-\frac{C_2}{C_{col}S_2^0}\right) - k_{rc} C_{filt,2} + k_{2r} C_2 + k_{fc} C_2 - P_{col} S_b = 0 \quad (6\text{-}5)$$

Solute Transport in Matrix:

$$\frac{\partial C_m}{\partial t} - D_m \frac{\partial^2 C_m}{\partial y^2} + \left(\frac{\rho_b}{\phi}\right)k_{fam} C_m\left(1-\frac{S_{am}}{S_{am}^0}\right) + \left(\frac{\rho_b}{\phi}\right)k_{fbm} C_m\left(1-\frac{S_{bm}}{S_{bm}^0}\right) - \left(\frac{\rho_b}{\phi}\right)k_{ram} S_{am} - \left(\frac{\rho_b}{\phi}\right)k_{rbm} S_{bm} = 0 \quad (6\text{-}6)$$

Immobile Solute in Fractures (sorption sites a and b):

$$\frac{\partial S_a}{\partial t} - k_{fa} C\left(1-\frac{S_a}{S_a^0}\right) + k_{ra} S_a = 0 \quad (6\text{-}7)$$

$$\frac{\partial S_b}{\partial t} - k_{fb} C\left(1-\frac{S_b}{S_b^0}\right) + k_{rb} S_b = 0 \quad (6\text{-}8)$$

Immobile Solute in Matrix (sorption sites a_m and b_m):

$$\frac{\partial S_{am}}{\partial t} - k_{fam} C\left(1-\frac{S_{am}}{S_{am}^0}\right) + k_{ram} S_{am} = 0 \quad (6\text{-}9)$$

$$\frac{\partial S_{bm}}{\partial t} - k_{fbm} C \left(1 - \frac{S_{bm}}{S_{bm}^0}\right) + k_{rbm} S_{bm} = 0 \quad (6\text{-}10)$$

Immobile Solute adorbed onto Immobile Colloids in Fractures (colloid sites 1 and 2):

$$\frac{\partial C_{filt,1}}{\partial t} - k_{1f} C S_{col} \left(1 - \frac{C_{filt,1}}{S_{col} S_1^0}\right) - (k_{fc} + k_{fci}) C_1 + k_{rc} C_{filt,1} + k_{1r} C_{filt,1} = 0 \quad (6\text{-}11)$$

$$\frac{\partial C_{filt,2}}{\partial t} - k_{2f} C S_{col} \left(1 - \frac{C_{filt,2}}{S_{col} S_2^0}\right) - (k_{fc} + k_{fci}) C_2 + k_{rc} C_{filt,2} + k_{2r} C_{filt,2} = 0 \quad (6\text{-}12)$$

where, C_{col} = concentration of colloids in solute phase, g/cm^3
S_{col} = colloid concentration on fracture surfaces, g/cm^3
C = solution concentration of solute in fractures, g/cm^3
C_m = solution concentration of solute in matrix, g/cm^3
S_a = sorbed concentration of solute on fracture surface site *a*, g/g
S_b = sorbed concentration of solute on fracture surface site *b*, g/g
C_1 = concentration of solute sorbed to site 1 on mobile colloids, g/cm^3
C_2 = concentration of solute sorbed to site 2 on mobile colloids, g/cm^3
$C_{filt,1}$ = concentration of solute sorbed to site 1 on immobile colloids, g/cm^3
$C_{filt,2}$ = concentration of Pu on sorbed to site 2 on immobile colloids, g/cm^3
S_{am} = sorbed concentration of solute on matrix surface site a_m, g/g
S_{bm} = sorbed concentration of solute on fracture surface site b_m, g/g
P_{col} = colloid production rate in fractures, g/cm^3-s
v_f = fluid velocity in fractures, cm/s
D_f = solute dispersion coefficient in fractures, cm^2/s
D_c = colloid dispersion coefficient in fractures, cm^2/s
D_m = solute molecular diffusion coefficient in matrix, cm^2/s
ρ_f = effective bulk density within fractures, g/cm^3
ρ_B = bulk density in matrix, g/cm^3.
η = porosity within fractures
ϕ = matrix porosity
b = fracture half aperture, cm
k_{fc} = colloid filtration rate constant (1/s) = λv_f, where λ = filtration coefficient (1/cm)
k_{rc} = reverse colloid filtration (detachment) rate constant, 1/s.
k_{fci} = irreversible colloid filtration rate constant, 1/s
k_{fa} = rate constant for sorption of solute onto fracture surface site *a*, ml/g-s
k_{ra} = rate constant for desorption of solute from fracture surface site *a*, 1/s
k_{fb} = rate constant for sorption of solute onto fracture surface site *b*, ml/g-s
k_{rb} = rate constant for desorption of solute from fracture surface site *b*, 1/s
k_{fam} = rate constant for sorption of solute onto matrix surface site a_m, ml/g-s
k_{ram} = rate constant for desorption of solute from matrix surface site a_m, 1/s
k_{fbm} = rate constant for sorption of solute onto matrix surface site b_m, ml/g-s
k_{rbm} = rate constant for desorption of solute from matrix surface site b_m, 1/s
k_{1f} = rate constant for sorption of solute onto colloid surface site 1, ml/g-s
k_{1r} = rate constant for desorption of solute from colloid surface site 1, 1/s
k_{2f} = rate constant for sorption of solute onto colloid surface site 2, ml/g-s

k_{2r} = rate constant for desorption of solute from colloid surface site 2, 1/s
S_1^0 = maximum solute capacity on colloid sorption site 1, g/g colloid
S_2^0 = maximum solute capacity on colloid sorption site 2, g/g colloid
S_a^0 = maximum solute capacity on fracture sorption site *a*, g/g solid
S_b^0 = maximum solute capacity on fracture sorption site *b*, g/g solid
S_{am}^0 = maximum solute capacity on matrix sorption site a_m, g/g solid
S_{bm}^0 = maximum solute capacity on matrix sorption site b_m, g/g solid

Figure 6-11 shows the system geometry and boundary conditions assumed in the numerical model. The parallel-plate fracture domain is one node wide, implying that concentration gradients across the fracture aperture are rapidly leveled by diffusion and/or advective mixing. Solute diffusion between fractures and matrix is assumed to be perpendicular to the fracture flow direction. The matrix nodes can be specified to have variable spacing with different porosities and different solute diffusion coefficients as a function of distance away from the fracture wall. Thus, fracture coatings or gradients in porosity or diffusion coefficients can be simulated. The above equations and the geometry of Figure 6-11 also apply to RELAP, although simplifications are necessary to use the RELAP semi-analytical solution method (Reimus et al., 2003).

The reaction processes accounted for by equations 6-1 to 6-12 are depicted in Figure 6-12 (including diffusion between the fractures and matrix). Solutes can adsorb to and desorb from two different sorption sites that are assumed to be present on (1) fracture surfaces, (2) matrix surfaces, (3) mobile colloid surfaces, and (4) immobile colloid surfaces. The adsorption sites on each surface can be specified as being irreversible by simply specifying a zero desorption rate constant for that site. Colloids can attach either reversibly or irreversibly to fracture surfaces, but they are not allowed to diffuse into the matrix. When the colloids attach or detach, they carry any adsorbed solutes with them, although the solutes can still independently adsorb or desorb from colloids after the colloid transition. Additionally, colloid generation from fracture surfaces is allowed. The model ensures that a background colloid concentration given by P_{col}/k_{fci} is always maintained in the system, satisfying the steady-state condition that the colloid production rate must be balanced by an irreversible filtration rate (if this were not true either all colloids would disappear from the system or the system would plug with colloids). Each arrowhead in Figure 2-12 has a reaction rate that can be specified by the user (or a diffusion coefficient in the case of diffusion into/from the matrix).

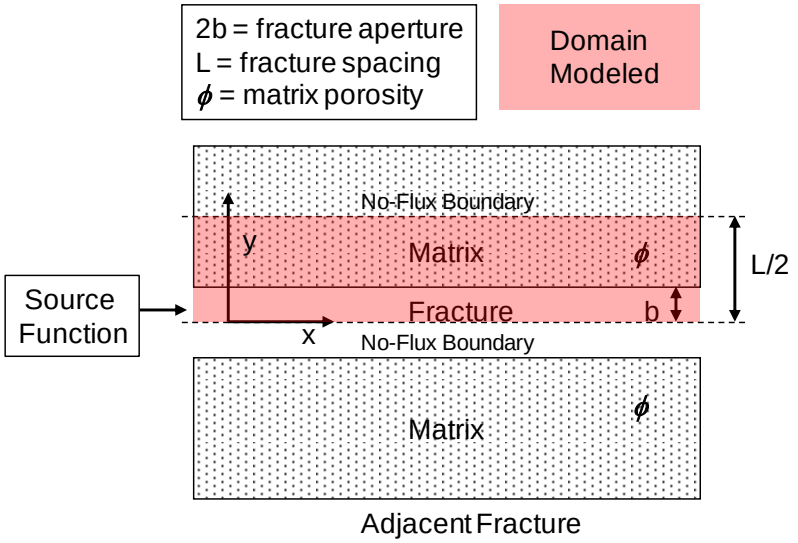

Figure 6-11. System geometry and boundary conditions assumed in the numerical model (also applies to the RELAP model).

With a few exceptions, the red-outlined boxes in Figure 2-12 were the only ones that were actually used to model the colloid and solute data from the colloid-radionuclide tracer tests. Specifically, only a single type of sorption site was assumed to be present on each of the surfaces present in the system (although the fracture, matrix, and colloid sites were allowed to have different adsorption and desorption rates). It was found that reasonable fits to the tracer data could be obtained without the black-outlined boxes, and it was considered desirable to not complicate the model with additional processes and parameters that did not significantly improve the fits.

6.4 TEST INTERPRETATIONS

The RELAP model matches to the radionuclide and colloid breakthrough curves for CRR Runs 31 and 32 are shown in Fig. 6-13 to 6-18. Each figure shows model results for multiple radionuclides or colloids. Figs. 6-19 and 6-20 show the results of numerical model matches to the AGA, radionuclides and colloids in CFM Run 12-02 (these were previously reported in Chapter 2 of Wang et al., 2013, although they are updated here). Finally, Fig. 6-21 shows the AGA and colloid model matches for CFM Run 13-05, and Figs. 6-22 through 6-28 show each individual radionuclide model match for CFM 13-05 along with the AGA data and the colloid model curves for comparison. For each of the CFM Run 13-05 figures, a pair of plots is shown: one for the constant-rate injection function and one for the varying-rate injection function. The best-fitting model parameters in each of the tests are listed by colloids or radionuclide in Tables 6-3 through 6-5. Table 6-3 lists the filtration rate constants for the colloids in each of the tests (note that a single irreversible filtration rate constant was used for all the tests, as the model matches to the colloid breakthrough curves were not significantly improved by assuming a reversible filtration reaction). Table 6-4 lists model parameters for the radionuclides that tended to be less strongly associated with colloids (although Cs was quite strongly associated with colloids in the CFM runs), and Table 6-5 lists the parameters for the actinides Th, Am and Pu, which tended to be quite strongly associated with colloids in all tests. In each table, two sets of parameters are listed for CFM Run 13-05; one assuming the constant-rate injection function, and another assuming the varying-rate injection function.

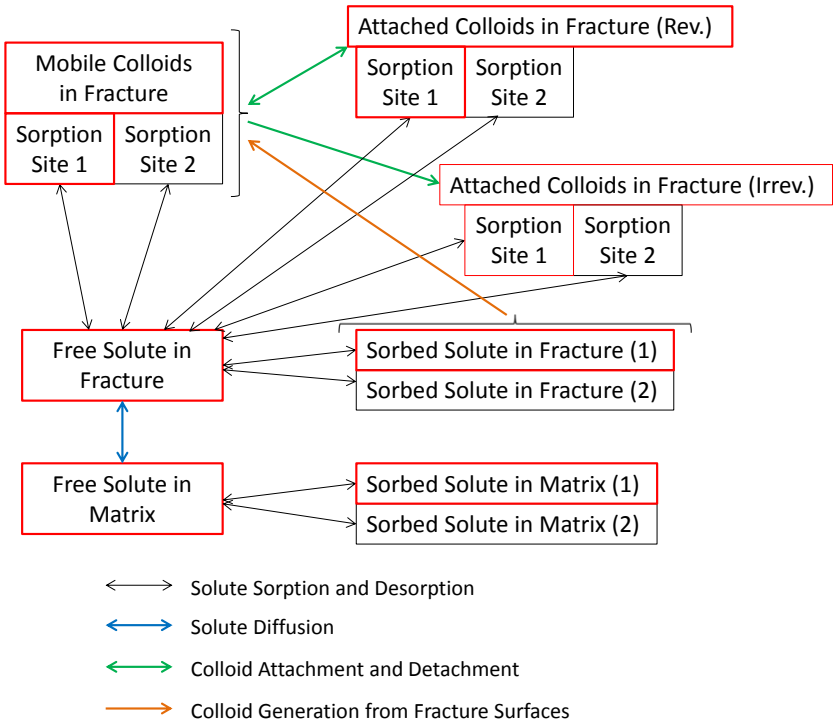

Figure 6-12. Reaction processes accounted for by equations 6-1 to 6-12 and implemented in the numerical transport model. Note that the red-outlined boxes were the only boxes actually used in the interpretation of the colloid-homologue or colloid-radionuclide tracer tests.

An underlying strategy in the test interpretations was to try to match the breakthrough curves for a given radionuclide using, to the extent possible, the same model parameters in each test in which the radionuclide was injected. The rationale for this was that the tests were all conducted in the same shear zone within a relatively short distance of each other, so the radionuclide transport parameters should be very similar in the different tests. A little more flexibility was allowed in the case of the parameter estimates for CFM Run 12-02 because this test was conducted in a different portion of the shear zone than all the other tests, which were performed in the same dipole (CRR 99.002 to BOMI 87.010). Because some of the model parameters were rather poorly constrained in any given test, this strategy helped reduce the nonuniqueness of the parameter estimates to a greater degree than any single test could.

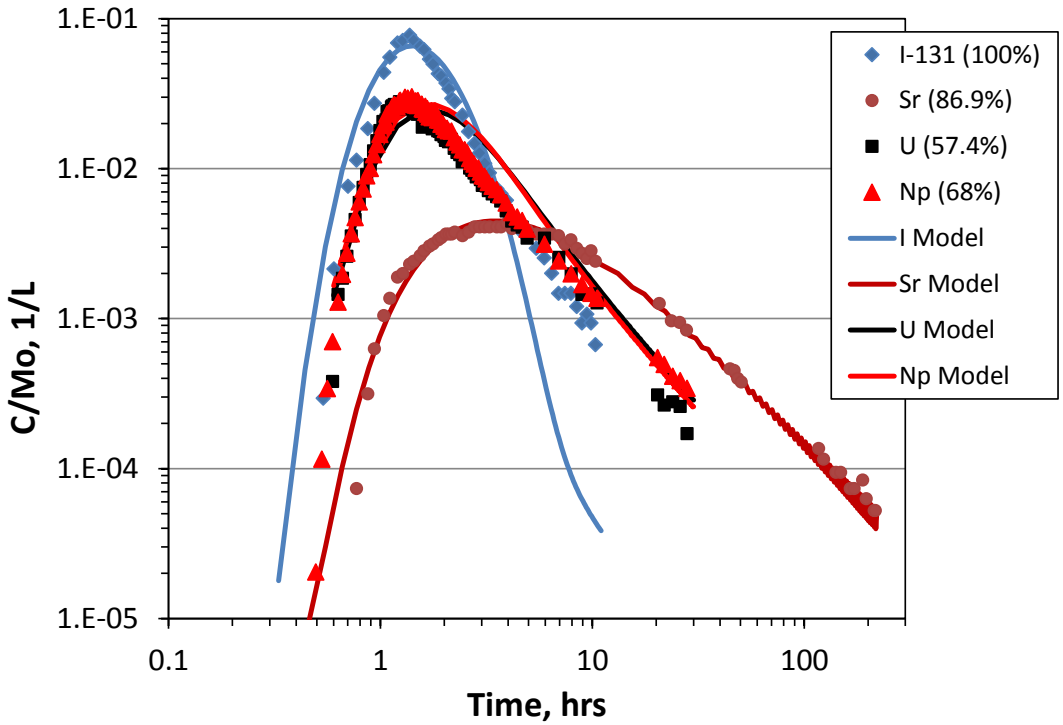

Figure 6-13. Model matches to ^{131}I, Sr, U, and Np data from CRR Run 31.

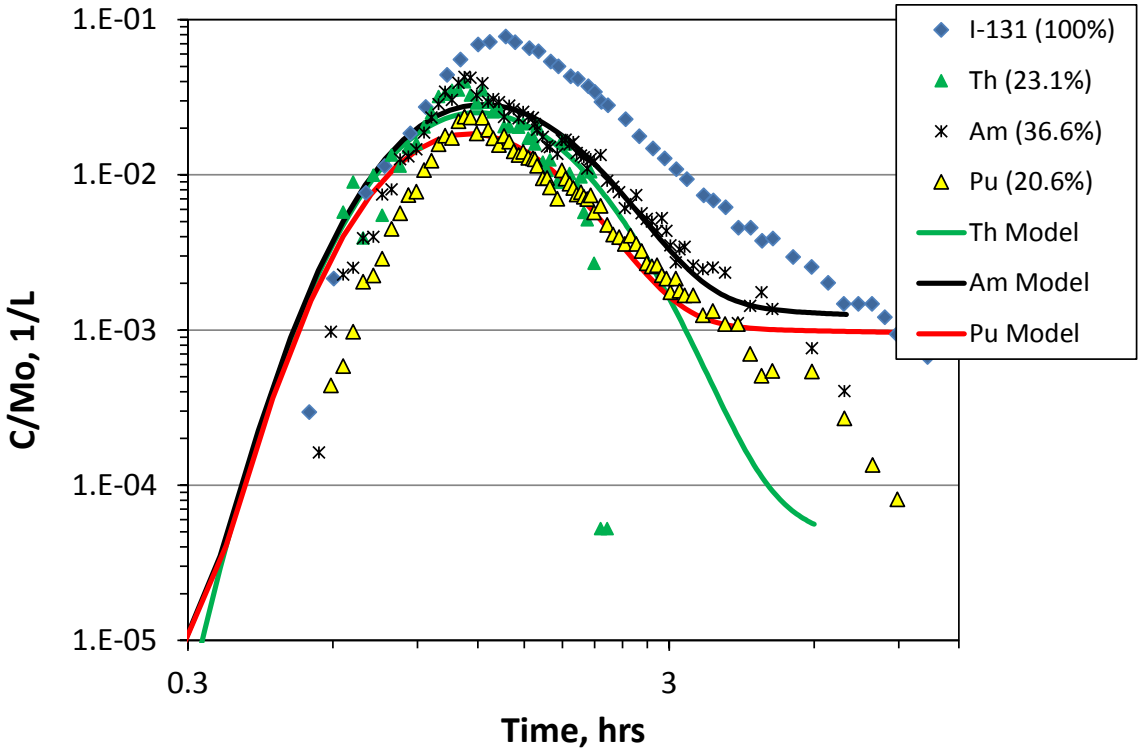

Figure 6-14. Model matches to Th, Am, and Pu data from CRR Run 31.

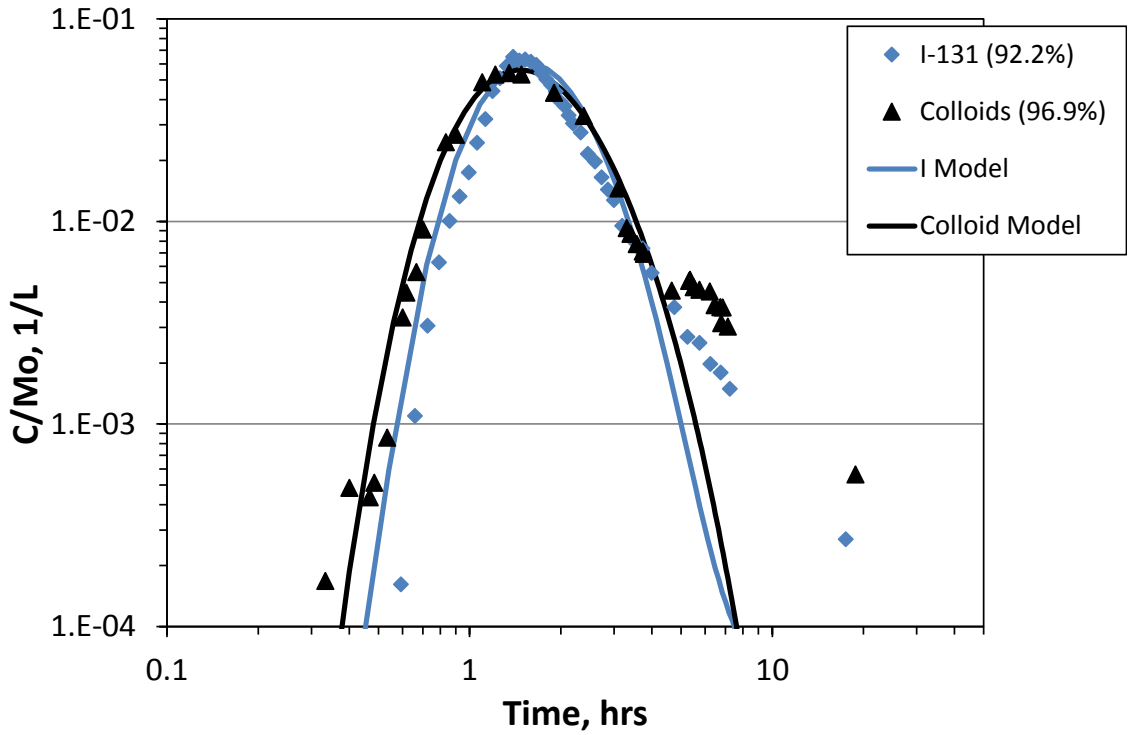

Figure 6-15. Model matches to ^{131}I and colloid data from CRR Run 32.

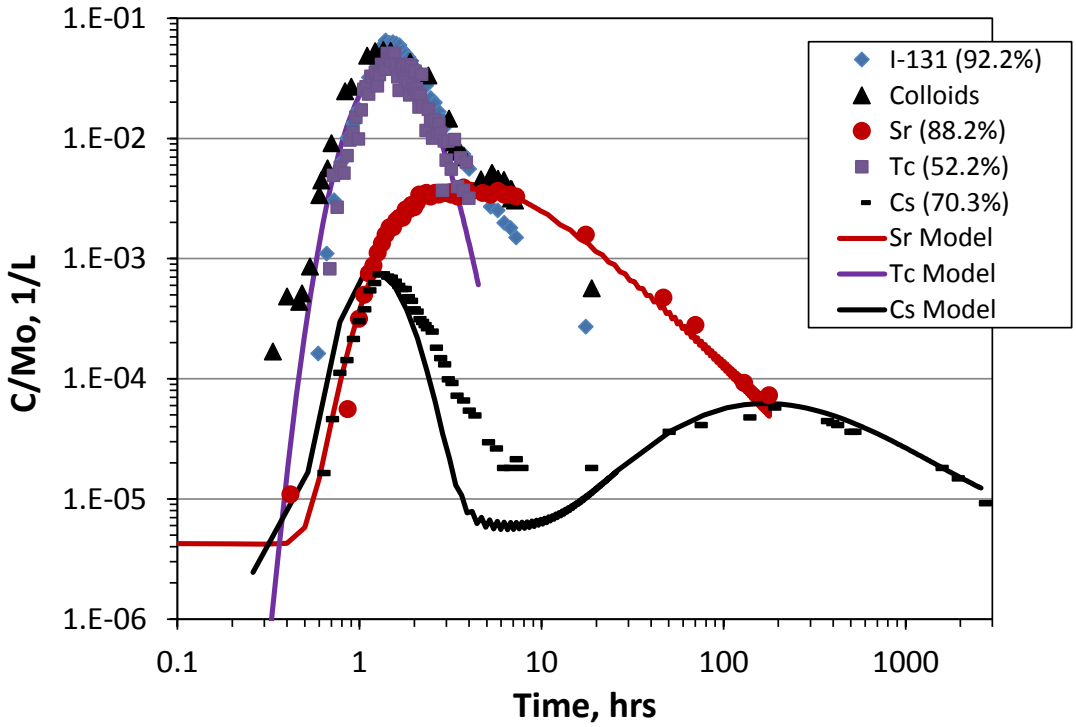

Figure 6-16. Model matches to ^{131}I, Sr, Tc,and Cs data from CRR Run 32. Sr and Tc modeled as solute transport. Cs early peak modeled as colloid-facilitated transport and late peak modeled as solute transport.

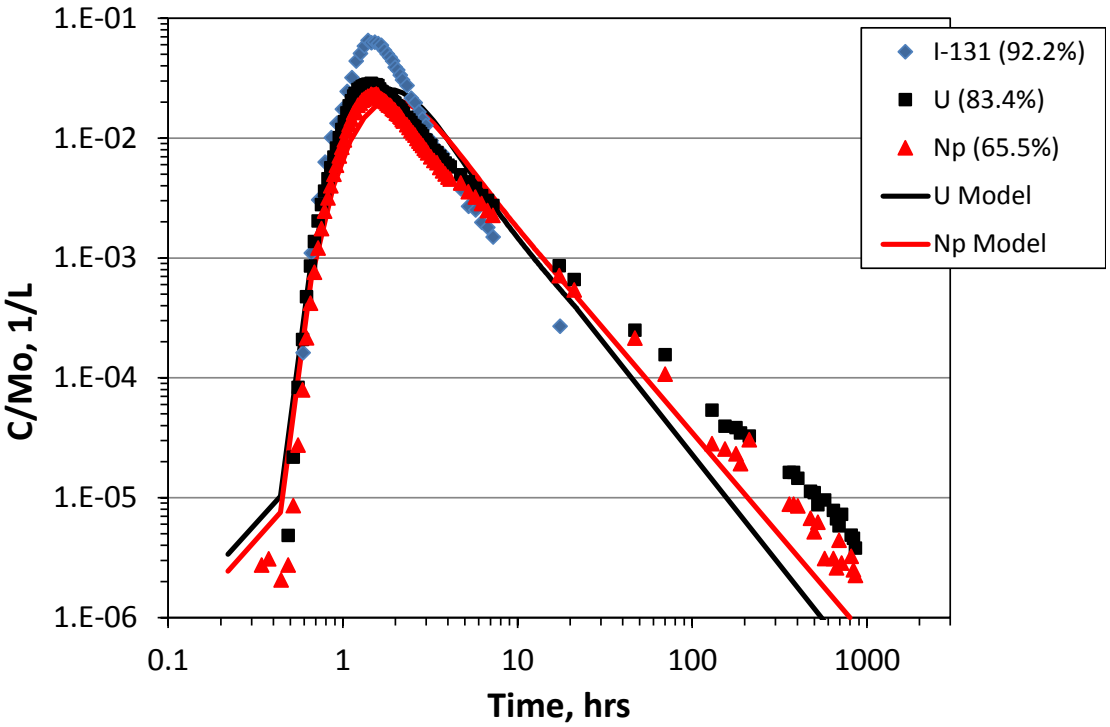

Figure 6-17. Model matches to U and Np data from CRR Run 32. Both species modeled as being dominated by solute transport (not colloid-facilitated transport).

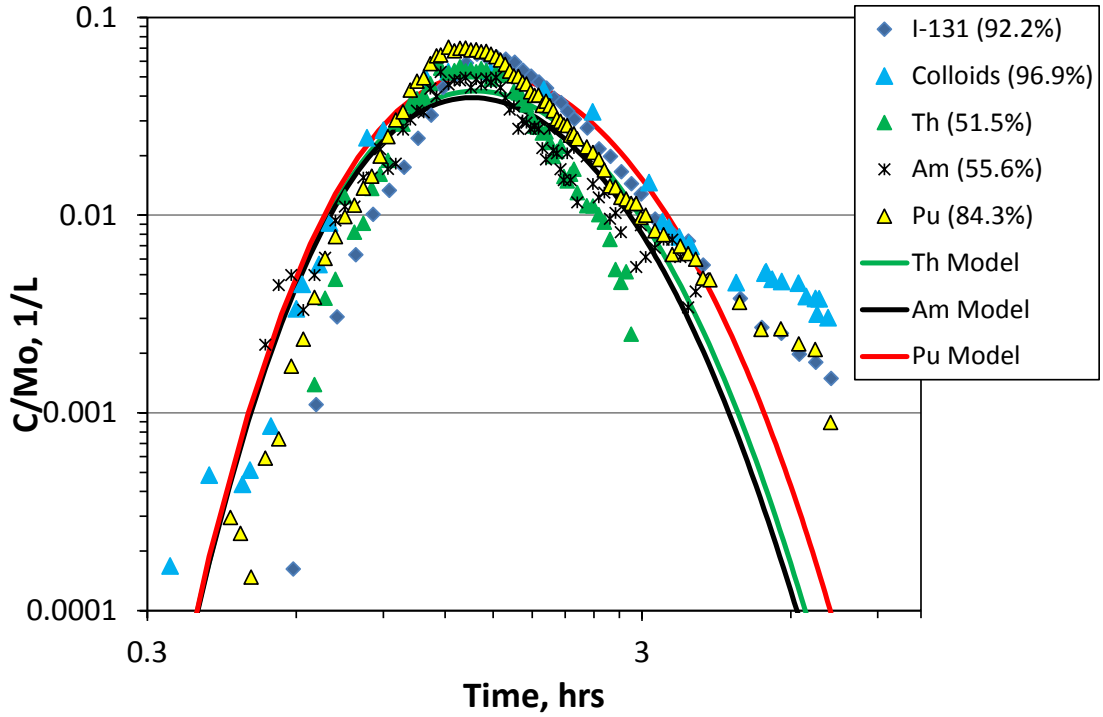

Figure 6-18. Model matches to Th, Am and Pu data from CRR Run 32. All species modeled as dominated by colloid-facilitated transport.

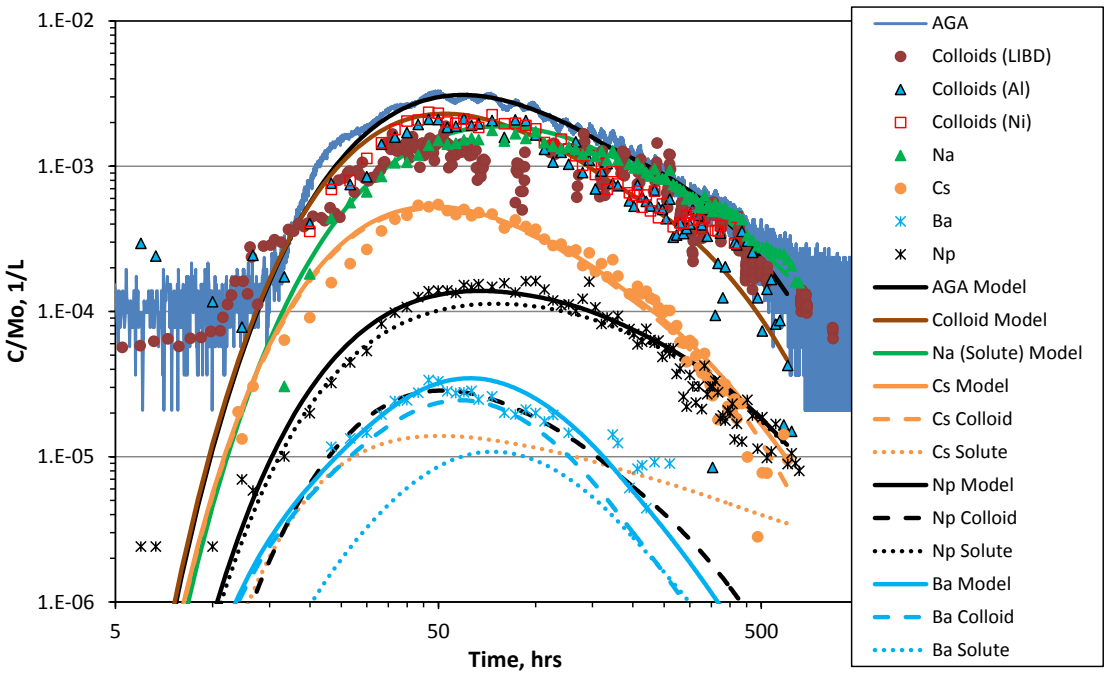

Figure 6-19. Model matches to the AGA, colloid, Na, Cs, Ba and Np breakthrough curves of CFM Run 12-02. Modeled solute and colloid contributions shown.

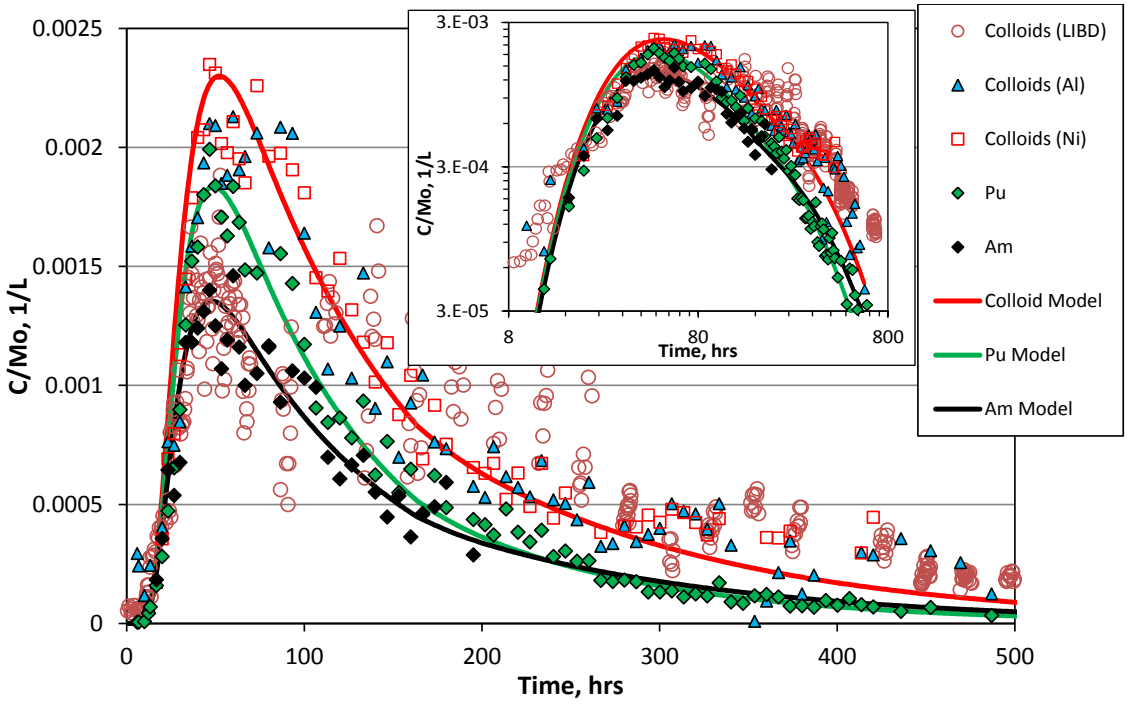

Figure 6-20. Model matches to the colloid, Pu, and Am breakthrough curves of CFM Run 12-02. Both species modeled as colloid-facilitated transport.

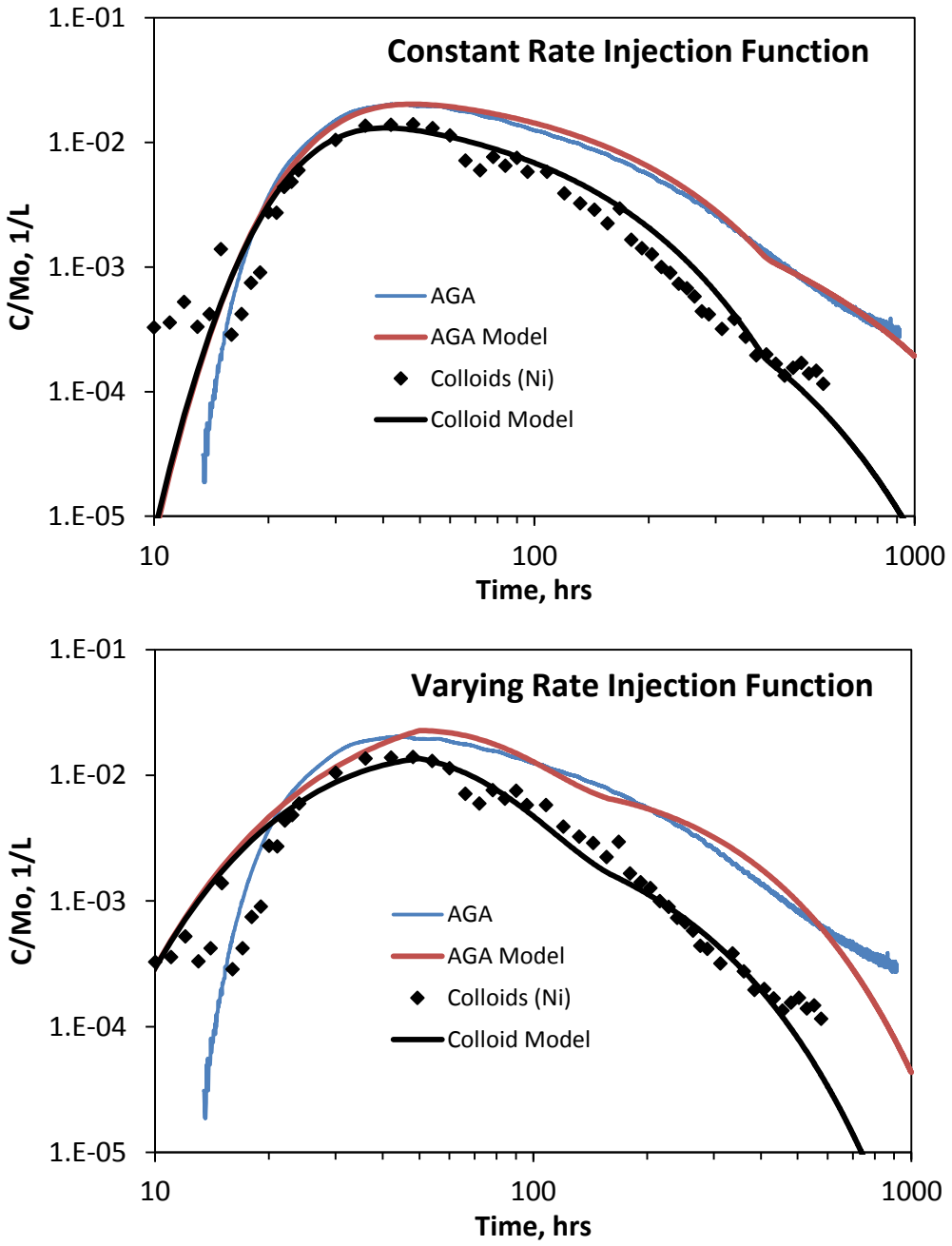

Figure 6-21. Model matches to the AGA and colloid breakthrough curves of CFM Run 13-05 assuming the two different injection functions.

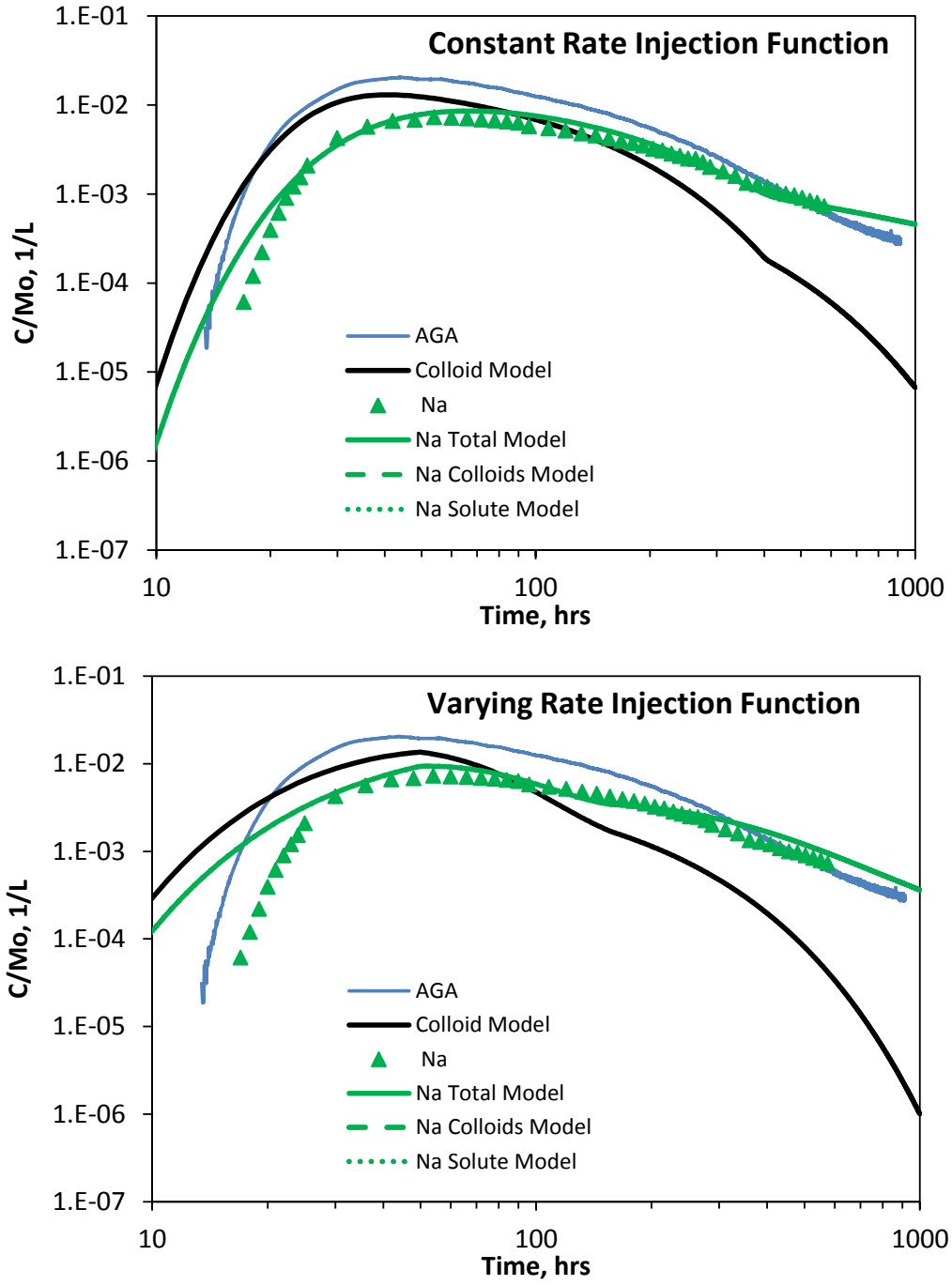

Figure 6-22. Model matches to the Na breakthrough curve of CFM Run 13-05 assuming the two different injection functions. Modeled solute and colloid contributions are shown (note that colloid contribution for varying rate injection function is negligible.

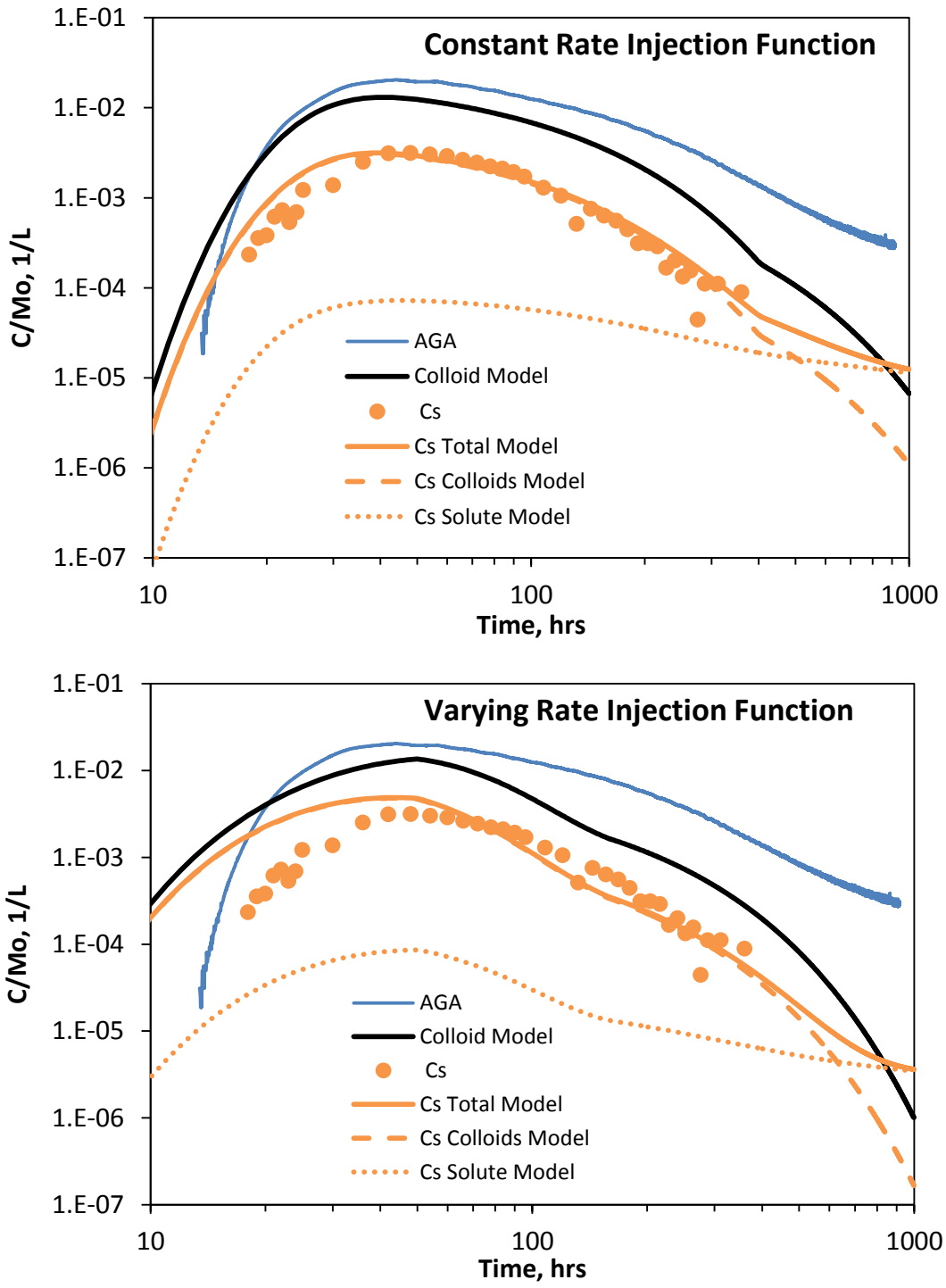

Figure 6-23. Model matches to the Cs breakthrough curve of CFM Run 13-05 assuming the two different injection functions. Modeled solute and colloid contributions are shown.

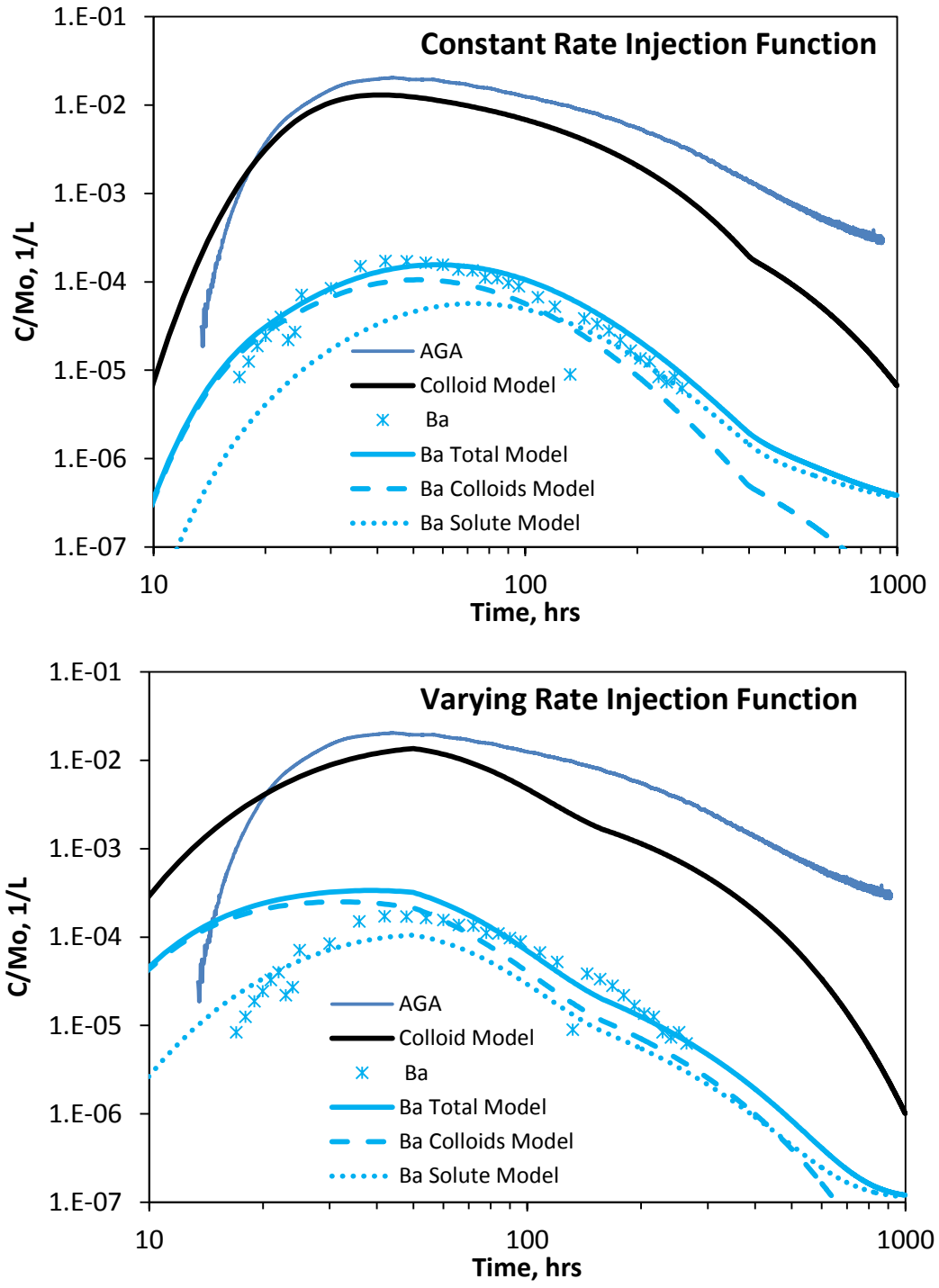

Figure 6-24. Model matches to the Ba breakthrough curve of CFM Run 13-05 assuming the two different injection functions. Modeled solute and colloid contributions are shown.

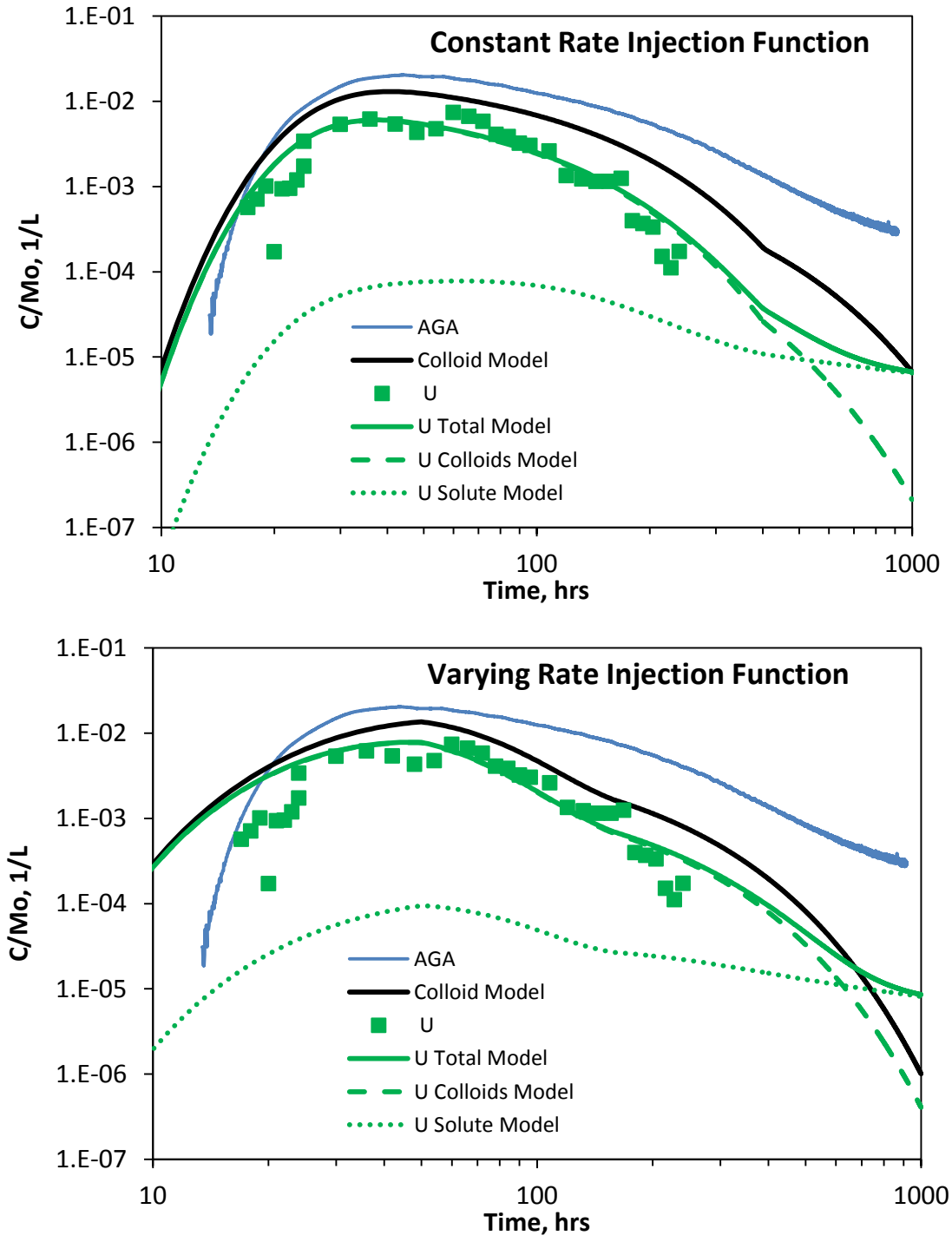

Figure 6-25. Model matches to the U breakthrough curve of CFM Run 13-05 assuming the two different injection functions. Modeled solute and colloid contributions are shown.

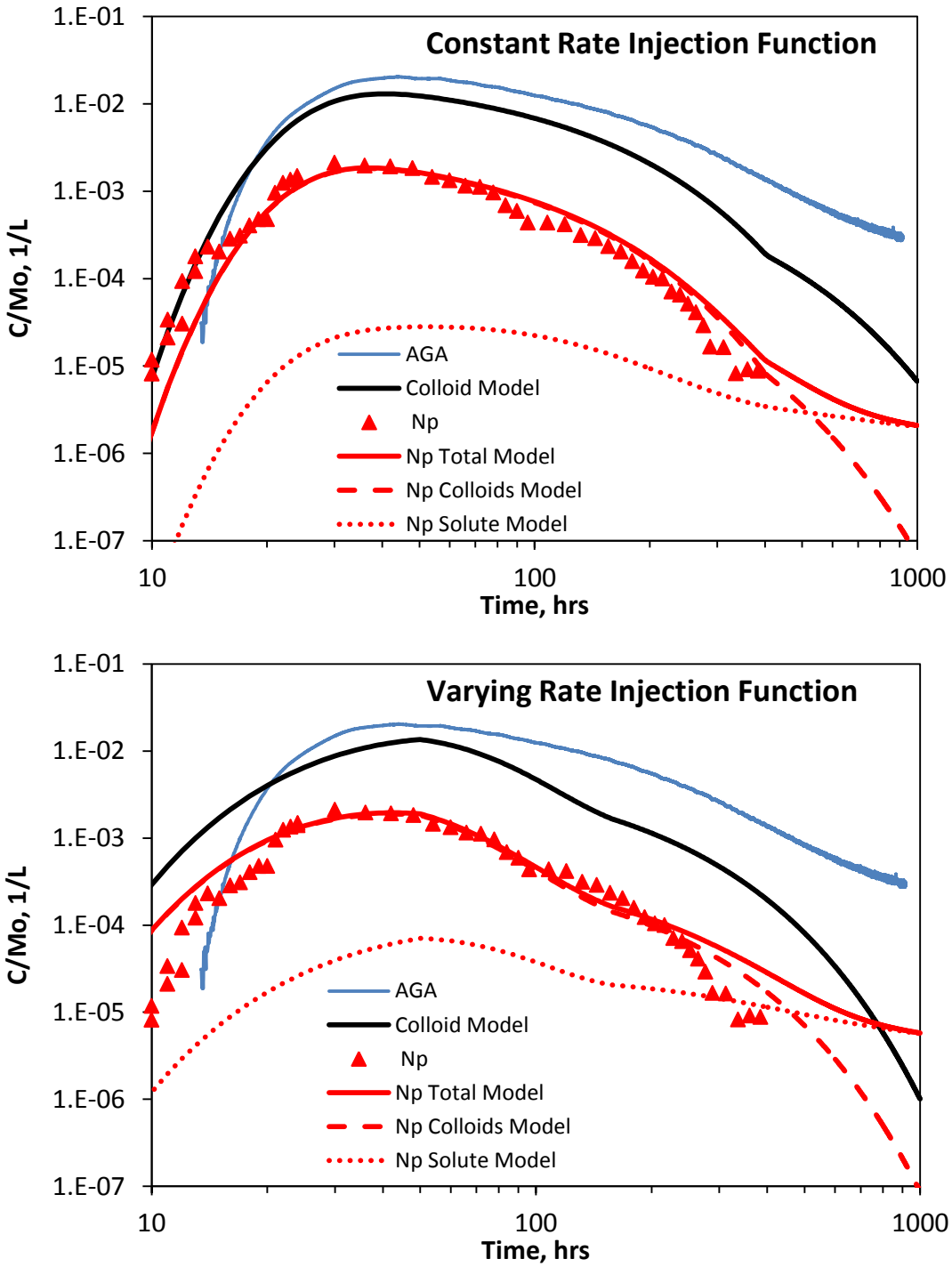

Figure 6-26. Model matches to the Np breakthrough curve of CFM Run 13-05 assuming the two different injection functions. Modeled solute and colloid contributions are shown.

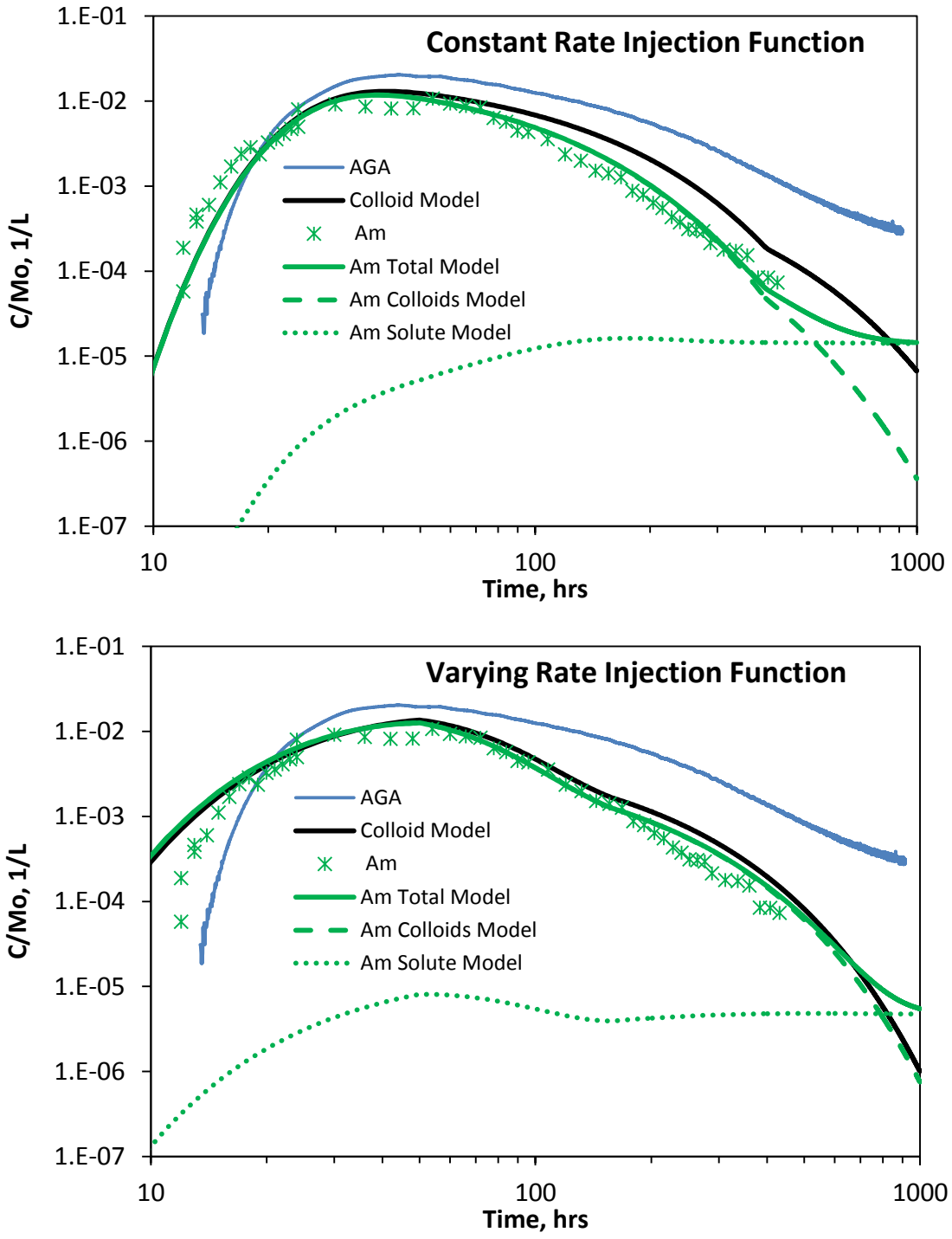

Figure 6-27. Model matches to the Am breakthrough curve of CFM Run 13-05 assuming the two different injection functions. Modeled solute and colloid contributions are shown.

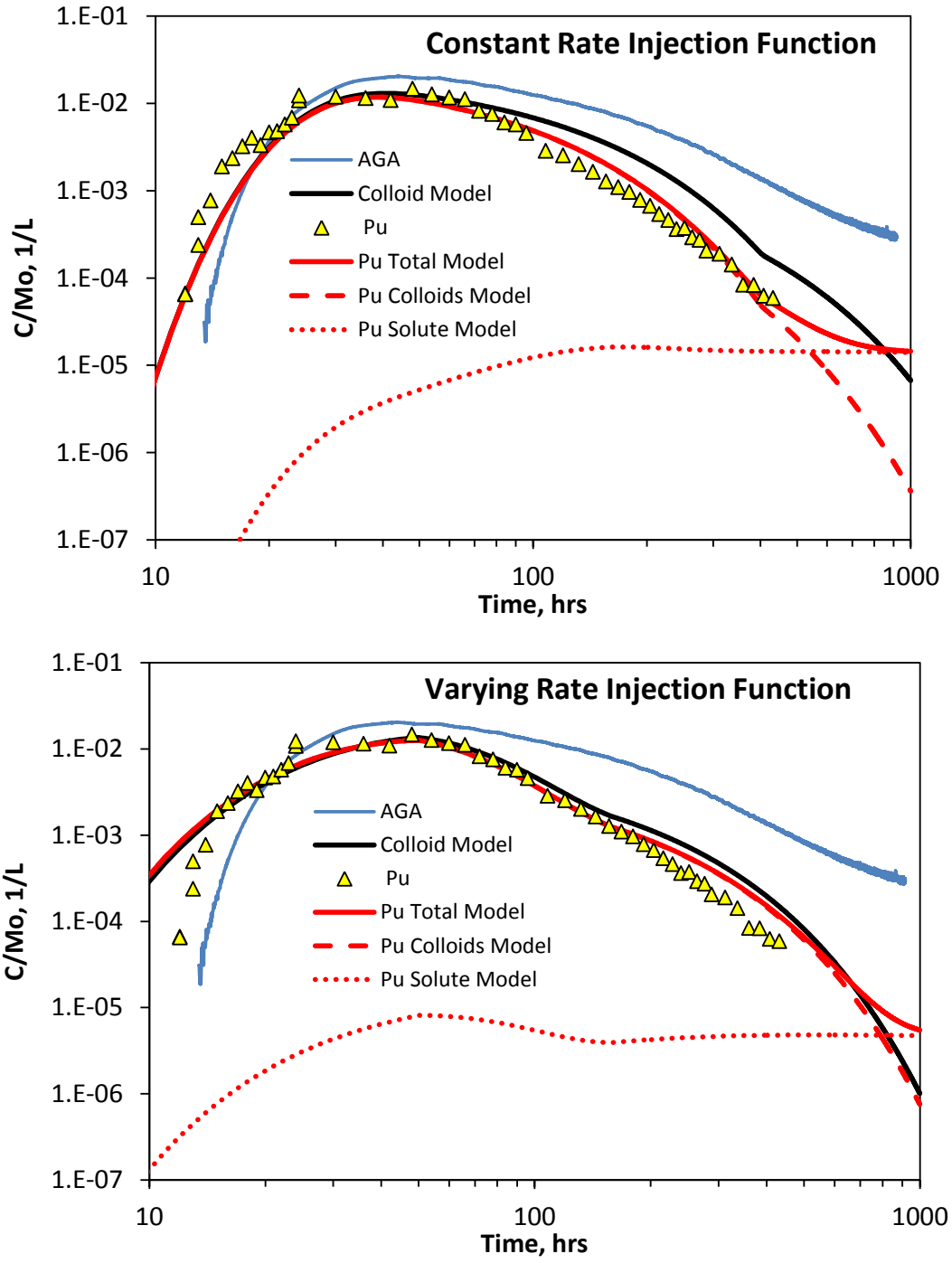

Figure 6-28. Model matches to the Pu breakthrough curve of CFM Run 13-05 assuming the two different injection functions. Modeled solute and colloid contributions are shown.

Table 6-3. Apparent colloid filtration rate constants in all tests (no colloids in CRR Run 31).

Test	k_{fci}^{*}, ml/g-hr
CRR 32	0.0
CFM 12-02	0.013
CFM 13-05 (constant)	0.017-0.12**
CFM 13-05 (varying)	0.02

*k_{fci} = irreversible filtration rate constant; note that it was not necessary to invoke a reversible filtration reaction to match the colloid data in any of the tests.

**In the CFM Run 13-05 with a constant injection rate function, it was necessary to increase the filtration rate constant in linear fashion from 0.017 ml/g-hr at the beginning of the test to 0.12 ml/g-hr at the end of the test to match the colloid data. A single filtration rate constant provided a poor match to the data. The filtration rate constant over the first 200 hours of the test, when most of mass was recovered, was 0.017 to 0.0194 ml/g-hr.

For each radionuclide in each test, the model matches to the breakthrough curves were generally found to be most sensitive to one or two model parameters, with a relatively high degree of insensitivity to all other model parameters. The most sensitive parameters are listed in red text in Tables 6-4 and 6-5. For the radionuclides that were strongly associated with colloids, the most sensitive parameter was generally the rate constant for radionuclide desorption from colloids. For radionuclides that transported mostly in the solute state, the ratio of adsorption to desorption rate constants in the matrix (after diffusion out of the shear zone) was typically the most sensitive parameter, or more specifically, lumped parameter. However, in CRR Run 31, which had no injected colloids, the radionuclides that were generally strongly associated with colloids transported either as if they strongly interacted with shear zone surfaces or as if they transported as intrinsic colloids that were filtered. The results from all the tests are discussed in the rest of this section by colloids or radionuclide.

Colloids: It is apparent from visual inspection of Fig. 6-15 that the bentonite colloids transported effectively without any filtration in CRR Run 32, so a filtration rate constant of zero is listed in Table 6-3 for this test. The colloid recovery was slightly greater than the ^{131}I recovery in this test, which supports a zero filtration rate constant. However, when the filtration rate constants deduced for the CFM tests were used to model the colloid transport in CRR Run 32, only a few percent of the colloids were predicted to be filtered, and the model match to the data was essentially no different than the match with a filtration rate constant of zero. Thus, apparent lack of colloid filtration in CRR Run 32 could be considered consistent with the observations in the CFM tests.

Table 6-4. Adorption and desorption rate constants in the shear zone, on matrix surfaces and on colloids for reactive radionuclides that are not strongly associated (or variably associated) with colloids in different tests. Red numbers indicate parameters that model matches were most sensitive to.

	Shear Zone	Matrix	Colloids
Test/Radionuclide*	**k_{fa} (ml/g-hr), k_{ra} (1/hr)**	**k_{fam} (ml/g-hr), k_{ram} (1/hr)**	**k_{1f} (ml/g-hr), k_{1r} (1/hr)**
^{22}Na / 12-02	0, 0	1, 3.76	0.1, 1
^{22}Na / 13-05(C)	0, 0	1, 2	0.1, 1
^{22}Na / 13-05(V)	0, 0	1, 2.7	0.1, 1
^{85}Sr / CRR 31	0, 0	2000, 5.1	N/A
^{85}Sr / CRR 32	0, 0	2000, 5.9	0, 0
^{99}Tc / CRR 32**	0.11, 0.0003	0, 0	10, 0.3
^{133}Ba / 12-02	3, 1	5, 0.00005	5000, 0.28
^{133}Ba / 13-05(C)	3, 1	5, 0.00005	5000, 0.28
^{133}Ba / 13-05(V)	3, 1	5, 0.00005	5000, 0.2
^{137}Cs / CRR 32	0, 0	100000, 3.5	5000, 1.6
^{137}Cs / 12-02	0, 0	100000, 3.5	30000, 0.1
^{137}Cs / 13-05(C)	0, 0	100000, 3.5	30000, 0.075
^{137}Cs / 13-05(V)	0, 0	100000, 3.5	30000, 0.04
U / CRR 31	0, 0	100, 3.2	N/A
U / CRR 32	0, 0	100, 5.0	0.1, 10
U / 13-05(C)	0, 0	100000, 1	30, 0.02-0.15***
U / 13-05(V)	0, 0	10000, 1	30, 0.02
^{237}Np / CRR 31	0, 0	100, 4.1	N/A
^{237}Np / CRR 32	0, 0	100, 3.1	0.1, 10
^{237}Np / 12-02	0.041, 0.00001	40, 40	30, 0.035
^{237}Np / 13-05(C)	0.041, 0.00001	100000, 1	30, 0.028-0.15***
^{237}Np / 13-05(V)	0.041, 0.00001	1000, 1	30, 0.035

*(C) refers to constant-rate injection function and (V) refers to varying rate injection function for CFM Run 13-05.

**For ^{99}Tc, the breakthrough curve could be matched equally well assuming either a slow, nearly irreversible sorption reaction in the shear zone, or by assuming the ^{99}Tc was initially associated with colloids and desorbed from colloids with a rate constant of 0.3 hr^{-1}.

***First number is initial desorption rate constant from colloids and second number is final desorption rate constant. When the constant-rate injection function was assumed for CFM Run 13-05, the desorption rate constants had to be varied linearly with time between these two values from beginning of test to end of test to achieve good model matches to the data.

For CRR Run 32, a slightly different mean residence time and Peclet number were used for the colloids than for the ^{131}I when interpreting this test (2 hrs and 8, respectively, for colloids vs. 1.8 hrs and 9.5 for ^{131}I) to achieve a better match to the colloid data. This approach was considered reasonable given that the colloids would be expected to have greater dispersion in the shear zone because of their much smaller free-water diffusion coefficient than solutes. The greater expected dispersion for the colloids is consistent with Taylor dispersion theory in laminar flow (Taylor, 1953), particularly for the relatively short residence times of the CRR tests, where colloid diffusion across the width of a flow channel would be limited. This limited diffusion, in principle, will result in some colloids experiencing faster residence times and some experiencing slower residence times than a more diffusive solute would experience (because solutes can rapidly diffuse across all streamlines of different velocity in a flow channel and thus experience more of an average velocity).

Table 6-5. Sorption and desorption rate constants in the shear zone, on matrix surfaces and on colloids for Th, Am, and Pu (radionuclides strongly associated with colloids) in the different tests. Red numbers indicate parameters that model matches were most sensitive to.

	Fracture	Matrix	Colloids
Test/Radionuclide	**k_{fa} (ml/g-hr), k_{ra} (1/hr)**	**k_{fam} (ml/g-hr), k_{ram} (1/hr)**	**k_{1f} (ml/g-hr), k_{1r} (1/hr)**
Th / CRR 31	0.3, 0.0008	0, 0	N/A
Th / CRR 32	10, 0.01	10, 0.01	10, 0.23
Am / CRR 31	0.264, 0.035	0, 0	N/A
Am / CRR 32	10, 0.01	10, 0.01	10, 0.29
Am / 12-02	10, 0.01	10, 0.01	10, 0.018
Am / 13-05(C)	10, 0.01	10, 0.01	30, 0-0.15*
Am / 13-05(V)	10, 0.01	10, 0.01	30, 0.01
Pu / CRR 31	0.415, 0.032	0, 0	N/A
Pu / CRR 32	10, 0.01	10, 0.01	10, 0.07
Pu / 12-02	10, 0.01	10, 0.01	10, 0.005-0.04 (0.01)*
Pu / 13-05(C)	10, 0.01	10, 0.01	30, 0-0.15*
Pu / 13-05(V)	10, 0.01	10, 0.01	30, 0.01

* First number is initial desorption rate constant from colloids and second number is final desorption rate constant. When the constant-rate injection function was assumed for CFM Run 13-05, the desorption rate constants had to be varied linearly with time between these two values from beginning of test to end of test to achieve good model matches to the data. A time-varying colloid desorption rate constant was also found to improve the match to the Pu breakthrough curve in CFM Run 12-02. The number in parentheses for Pu in CFM Run 12-02 is the best-fitting time-invariant desorption rate constant for this test.

The colloid filtration rate constants in CFM Runs 12-02 and 13-05 are in relatively good agreement, with a slightly greater apparent filtration rate in Run 13-05. The uncertainty in the colloid data for these two tests is likely smaller than for CRR Run 32 because the colloid concentrations in the CFM tests were quantified by ICP-MS measurements of Ni, which the bentonite colloids were doped with (Reinholdt et

al., 2013). This offered higher precision measurements than the LIBD method used to measure the concentrations of undoped bentonite colloids used in CRR Run 32.

The colloid filtration rate constant for CFM Run 13-05 when assuming a constant-rate injection function is specified in Table 6-3 as a range that starts at 0.017 ml/g-hr at time zero and increases linearly with time to 0.12 ml/g-hr at the end of the test. It was necessary to specify such a time-dependent filtration rate constant to avoid significant over-prediction of the colloid concentrations at the end of the test. This time dependence intuitively seems implausible, which perhaps serves as an independent indication that the varying-rate injection function (which does not require a time-dependent filtration rate constant) is a more accurate injection function to use for CFM Run 13-05 than the constant-rate injection function. However, it is also possible that a time-dependent filtration rate constant may reflect some filtration of colloids in the injection loop during the test and thus a greater decrease in injected colloid concentrations over time than were assumed in the model.

Sodium-22: ^{22}Na was used in both CFM tests, but not in the CRR tests. It transported as though it were not facilitated at all by the bentonite colloids, which was not surprising given that it had very weak association with the colloids in the injection cocktails (Table 6-1). Its breakthrough curves were best matched by assuming rapid but weak and reversible adsorption in the matrix adjacent to the shear zone flow pathways. Assuming sorption in the shear zone flow pathways did not improve the model matches to the breakthrough curves. Also, parameters that assume rapid desorption from colloids of the little bit of ^{22}Na that was initially associated with colloids provide good matches to the data. However, in both tests there is so little ^{22}Na initially associated with colloids that the model matches are quite insensitive to values of the colloid adsorption and desorption rate constants provided the adsorption rate constant is relatively small.

The matrix sorption parameters for ^{22}Na were in relatively good agreement for the two CFM tests, and also for the two different injection functions assumed for CFM Run 13-05 (Table 6-4). In each case, it was the ratio of the adsorption and desorption rate constants in the matrix that dictated the quality of the model matches to the data. Larger rate constants than those listed in Table 6-4 provided equally good matches to the data provided the ratio of the two constants remained the same. Note that this ratio is equivalent to an equilibrium partition coefficient, or K_d value (ml/g), if both rates are fast relative to transport rates through the shear zone. In this case, the estimates of the ^{22}Na K_d values ranged from about 0.25 to 0.5 ml/g when the matrix adjacent to the shear zone was assumed to have a porosity of 0.02, the half-aperture of the shear zone was assumed to be 1 mm, and the matrix diffusion coefficient for ^{22}Na was assumed to be 1 x 10^{-6} cm^2/sec. The deduced K_d values should not be considered well-constrained estimates because they are highly dependent on the assumptions made for the matrix porosity, matrix diffusion coefficient and shear zone aperture in the system, which are not well known. The estimated K_d value is approximately inversely proportional to the assumed matrix diffusion coefficient and the square of the assumed matrix porosity, and approximately directly proportional to the square of the assumed aperture.

It was found that if the ^{22}Na matrix sorption-desorption rate constants were much smaller than those of Table 6-4, the matches to the breakthrough curves became worse even if the ratio of the rate constants was preserved because too much of the ^{22}Na was then predicted to move through the shear zone without interacting with the matrix, and the ^{22}Na concentrations thus became over-predicted.

Inspection of the two plots of Fig. 6-22 suggests that assuming the constant-rate injection function for CFM Run 13-05 yields a better match to the ^{22}Na breakthrough curve than the varying-rate injection function. However, most of the mismatch in the case of the varying-rate injection function occurs early in the test and is a result of the very small Peclet number in the shear zone that yields the best match to the conservative tracer (AGA) data when this injection function is used. This mismatch is also apparent for

the AGA in Fig. 6-21, and it is a recurring theme throughout Figs. 6-23 to 6-28 when CFM Run 13-05 radionuclide responses are matched using the varying-rate injection function. Little weight is given to this early mismatch because it is taken to be an artifact of assuming only a single flow pathway in the shear zone, which forces this pathway to have a very small Peclet number that is dictated by the tail of the breakthrough curve. If multiple flow pathways were assumed (i.e., splitting the injected mass between two pathways with different mean residence times and Peclet numbers), this early mismatch would disappear. In the case of the constant-rate injection assumption for CFM Run 13-05, the best-matching mean residence time and Peclet number for a single flow pathway results in a much narrower deduced conservative tracer residence time distribution in the shear zone (Fig. 6-10), which makes it inherently easier to match the early breakthrough of any constituent in the test.

Strontium-85: ^{85}Sr was used only in the two CRR tests. It had very weak association with colloids in Run 32, and its transport in both tests was deduced to be dominated by adsorption/desorption in the matrix with negligible adsorption to shear zone surfaces and colloids. ^{85}Sr was modeled as having a much stronger interaction with the matrix than ^{22}Na. Good matches to the ^{85}Sr data in both CRR runs were obtained using similar values of the matrix adsorption and desorption rate constants, and as with ^{22}Na, the model matches were insensitive to the absolute values of the rates as long as the ratio of the rates stayed the same and the rates were relatively fast compared to transport rates through the shear zone. The model matches degraded if the rate constants became much lower than those of Table 6-4, and this was dictated by the much smaller desorption rate constant. The deduced matrix K_d value ranged from about 340 to 390 ml/g, or nearly 2 orders of magnitude greater than for ^{22}Na for the same assumptions of matrix porosity, shear-zone aperture and matrix diffusion coefficient.

Technetium-99: ^{99}Tc was used only in CRR Run 32, although it had only a 12% association with colloids in the injection cocktail. Despite this weak association with colloids, it transported as if it were colloidal, or at least as if it did not interact with the matrix, because the assumption of reversible matrix sorption did not improve the matches to the ^{99}Tc breakthrough curve. Reversible matrix sorption should result in longer tailing relative to ^{131}I than was observed for ^{99}Tc (see, for example, the breakthrough curves of U and Np in CRR Run 32 in Fig. 6-17, which exhibit a classic matrix sorption response). Instead, ^{99}Tc behaved as if its observed transport was governed by an essentially irreversible reaction in the shear zone with a rate constant of about 0.11 ml/g-hr, assuming an effective porosity of 0.5 within the shear zone. This translates to a normalized rate constant of 0.3 hr^{-1} if the rate constant is multiplied by the mass of solids per mL of water in the shear zone, assuming a solids density of 2.65 g/ml. Given that ^{99}Tc(VI) in the form of pertechnetate anion (the form injected) is normally considered a conservative specie, the presumption is that the deduced rate constant reflects the rate of reduction of Tc(VI) to Tc(IV) in the shear zone, with the reduced oxidation state readily adsorbing or precipitating once it forms. However, this is a rather rapid rate constant for a reduction reaction that involves electron transfers, so it is unknown whether this is an appropriate explanation for the observed rate of ^{99}Tc removal from the system.

Note that if all the ^{99}Tc were associated with colloids, the deduced normalized rate constant of 0.3 hr^{-1} would correspond to the desorption rate constant of ^{99}Tc from the colloids (as indicated in Table 6-4, with a corresponding footnote). However, given that only 12% of the ^{99}Tc was initially associated with the colloids, the model results are relatively insensitive to the ^{99}Tc desorption rate constant from colloids, and in fact the desorption rate constant can vary from zero to a very large value without changing the deduced solute adsorption rate constant (or reduction rate constant) in the shear zone by very much.

Barium-133: ^{133}Ba was used only in the two CFM tests, and its observed transport behavior could be matched reasonably well using almost the same set of parameters for each test and for each assumed injection function (in the case of Run 13-05). The only parameter that differed to achieve a match in the different tests or for the different injection functions in CFM Run 13-05 was the rate constant for desorption of ^{133}Ba from the colloids. ^{133}Ba had the lowest recovery of any radionuclide in the two tests

in which it was used. It was also the only radionuclide that was best matched when adsorption and desorption was assumed to occur in the shear zone, the matrix, and on colloids (all 3 possible locations). With sorption only in the matrix, as was assumed for most other radionuclides that were not strongly associated with colloids, ^{133}Ba was consistently predicted to break through and tail too early, and this malady could only be addressed by invoking weak reversible adsorption in the shear zone. Also, it is noteworthy that the sorption of ^{133}Ba in the matrix was essentially modeled as being irreversible because the desorption rate constant providing a good match to the data was exceedingly small (Table 6-4). The assumption of very strong but reversible sorption (over test time scales) in the matrix resulted in somewhat poorer matches to the data.

Interestingly, for CFM Runs 12-02 and 13-05, it was deduced that both the solute fraction of ^{133}Ba and the fraction adsorbed to colloids contributed significantly to the observed breakthrough curves. This also represents a departure from the modeled behavior of other radionuclides in most tests, which were deduced to either be dominated by colloid-facilitated transport or by solute transport and generally did not have significant contributions from both modes of transport. The colloid-associated fraction of ^{133}Ba was slightly more dominant in Run 12-02 than in Run 13-05 - despite the fact that the initial mass fraction associated with colloids was greater in Run 13-05 (see Figs. 6-19 and 6-24).

Cesium-137: ^{137}Cs was used in all tests in which colloids were injected, but it was not used in the colloid-free CRR Run 31. It exhibited a bimodal breakthrough curve in CRR Run 32, which is readily explained by the colloid-associated fraction in the injection cocktail accounting for the first peak and the solute fraction accounting for the second peak. Only 8% of the ^{137}Cs mass was associated with colloids in the injection cocktail, and a majority of this mass was deduced to exit the flow system with the colloids before having a chance to desorb from the colloids. The transport of the remaining 92% of the ^{137}Cs that was injected in the solute phase was modeled as being governed by strong, fast and reversible sorption in the matrix, with effectively no adsorption occurring on shear zone surfaces. As with ^{22}Na and ^{85}Sr, the matrix adsorption and desorption rate constants listed in Table 6-4 could both be increased as long as their ratio stayed the same, but they could not both be decreased without degrading the model match to the data. The effective ^{137}Cs K_d value in the matrix was about 28,500 ml/g, assuming a matrix porosity of 0.02, a matrix diffusion coefficient of 1 x 10^{-6} cm^2/sec, and a shear zone half-aperture of 1 mm (the same assumptions used throughout this section).

For the two CFM tests, the observed ^{137}Cs breakthrough curve had only a single peak, and the ^{137}Cs transport was deduced to be dominated by colloid-facilitated transport. This result differs from CRR Run 32 mainly because there were much greater colloid associations of the ^{137}Cs in the CFM injection cocktails compared to the CRR Run 32 cocktail (see Table 6-1). These differences in colloid associations are likely attributable to the significantly lower ^{137}Cs concentrations and greater colloid concentrations in the two CFM cocktails relative to the CRR cocktail (see Table 6-1). Missana et al (2004) showed that there are abundant weak sorption sites and much less abundant strong sorption sites for ^{137}Cs onto bentonite colloids. Thus, when ^{137}Cs concentrations are low relative to colloid concentrations, most of the ^{137}Cs will become adsorbed to strong sites, but when ^{137}Cs concentration are high, the more abundant weaker sorption sites will dominate the observed bulk adsorption-desorption behavior. The predominant influence of the weaker bentonite sorption sites for the colloid-facilitated transport of relatively high ^{137}Cs concentrations in the Grimsel system was demonstrated in column experiments reported in Chapter 8 of Wang et al. (2015).

As Table 6-4 shows, whereas all the solute sorption parameters were kept identical in the model interpretations for each of the tests involving ^{137}Cs, the rate constants for the desorption of ^{137}Cs from the bentonite colloids were deduced to be over an order of magnitude smaller for the two CFM tests than for CRR Run 32. This result is considered a further reflection of the predominant influence of the stronger ^{137}Cs sorption sites on the colloids at the lower ^{137}Cs concentrations of the two CFM tests and the greater

influence of the weaker sites at the higher ^{137}Cs concentrations (and somewhat lower colloid concentrations) in the CRR test. This behavior is entirely consistent with the two-site ^{137}Cs sorption model onto bentonite colloids of Missana et al (2004).

A two-site sorption-onto-colloids model was not invoked to simulate ^{137}Cs transport in the CRR and CFM tests because the initial fractions of ^{137}Cs adsorbed to weak and strong sorption sites on the colloids was not known. Rather, a single sorption site on the colloids was assumed when interpreting the tests, and the desorption rate constants were taken as a reflection of the dominant behavior of either the weak (CRR) or strong (CFM) sorption sites. It would be an interesting exercise to determine if a single set of adsorption-desorption parameters could be found for both the weak and strong sorption sites in a two-site model to predict both the initial colloid associations and the observed colloid-facilitated transport behavior of the ^{137}Cs in all the tests. Such an exercise would have to include the specification of a limited number of strong sorption sites on the colloids so that the strong sites would lose their influence at higher ^{137}Cs concentrations, as shown in Chapter 8 of Wang et al. (2015).

Uranium Isotopes: Uranium (U), as either ^{233}U or ^{238}U, was injected in both CRR tests and in CFM Run 13-05. It was not used in CFM Run 12-02. Interestingly, U was weakly associated with colloids in CRR Run 32, but it was strongly associated with colloids in the CFM Run 13-05 injection cocktail. The explanation for the stronger colloid association in CFM Run 13-05 is probably analogous to the explanation for the stronger association of ^{137}Cs in the CFM tests relative to CRR Run 32; i.e., the U concentrations in the CRR Run 32 injection cocktail were significantly higher than in the CFM Run 13-05 cocktail (and the colloid concentrations were slightly lower), which resulted in a greatly reduced influence of relatively low-abundance strong colloid sorption sites in the CRR test. Thus, there was essentially no colloid-facilitated transport of U in the CRR test, but colloid-facilitated transport appeared to be dominant in CFM Run 13-05. However, unlike ^{137}Cs, which could be matched in all tests using the same matrix adsorption and desorption rate constants (or K_d values), the matrix sorption parameters for U differed significantly in the CRR and CFM tests, with much stronger matrix sorption needed to match the data in the CFM tests (Table 6-4). It seems plausible that the matrix had an abundance of weak U sorption sites and a small number of strong U sorption sites, analogous to the colloids. This would explain why the apparent matrix K_d value (ratio of adsorption to desorption rate constants) for U in the two CRR tests ranged from about 20 to 30 ml/g whereas the range was 10,000 to 100,000 in CFM Run 13-05 (depending on the injection function used). Such a dramatic difference, particularly in the same dipole configuration within the shear zone, suggests an increased influence of less-abundant, stronger matrix sorption sites in CFM Run 13-05 because of the much lower U injection concentrations. The model matches to the U breakthrough curves in all tests were not improved by assuming U sorption to surfaces within the shear zone. This was even true for CRR Run 31, which had no colloids.

The rate constants for U desorption from colloids for the two different assumed injection functions for CFM Run 13-05 were in reasonably good agreement (Table 6-4), although it was necessary to increase the U desorption rate constant linearly with time throughout the test in the case of the constant-rate injection function to avoid a significant over-prediction of colloid-facilitated U transport at the end of the test. This time-dependent increase in the desorption rate constant was superimposed on a similar time-dependent increase of the colloid filtration rate constant when the constant-rate injection function was used. In contrast, a time-invariant desorption rate constant was sufficient to obtain a reasonable match to the U data when the varying-rate injection function was assumed in CFM Run 13-05. These results would seem to lend additional support to the superiority of the varying-rate injection function over the constant rate injection function for Run 13-05. However, they might also suggest that some desorption of U from the colloids occurred in the injection circulation loop prior to injection of the cocktail into the shear zone.

Neptunium-237: The ^{237}Np transport behavior in both CRR tests and in CFM Run 13-05 was very similar to the U transport behavior in these tests. Essentially everything that was stated for U in the preceding section also applies to ^{237}Np, with the values of best-matching rate constants (or K_d values) differing only slightly for the two different actinides. ^{237}Np seemed to desorb from the colloids slightly faster than U in CFM Run 13-05.

^{237}Np was also used in CFM Run 12-02, which did not include the injection of a U isotope. The ^{237}Np was much less strongly associated with colloids in the Run 12-02 injection cocktail than in the Run 13-05 injection cocktail (Table 6-1), so desorption rates from colloids had little influence on the model matches to the ^{237}Np breakthrough curve in Run 12-02 as they did for Run 13-05. Rather, the ^{237}Np transport behavior in CFM Run 12-02 seemed to be dominated by a slow, essentially irreversible adsorption process occurring on shear zone surfaces, with much weaker matrix sorption interactions than in all the other tests. This slow, irreversible sorption process is considered to be indicative of ^{237}Np reduction from the Np(V) oxidation state (injected) to the Np(IV) oxidation state, which is much less soluble and more strongly adsorbing than the higher oxidation state. Reduction reactions involving electron transfers are typically slower than reactions that don't involve electron transfers. Note that the deduced normalized rate constant for the irreversible shear zone reaction in Run 12-02 was 0.11 hr^{-1}, which corresponds to a characteristic reaction time of 9.2 (1/0.11) hrs. This means that 63% of the ^{237}Np was predicted to be irreversibly sorbed/reduced in the shear zone in 9.2 hours, and 63% of the remaining ^{237}Np was predicted to react in the next 9.2 hours, and so on.

Because residence times in the shear zone were similar in CFM Runs 12-02 and 13-05, the slow, irreversible process in the shear zone (with same rate constant) was also assumed to occur for ^{237}Np in Run 13-05. However, this process had much less influence on the predicted ^{237}Np behavior in CFM Run 13-05 because ^{237}Np transport in that test was modeled as being dominated by the colloid-associated ^{237}Np, which was not a factor in Run 12-02.

The much weaker deduced matrix adsorption of ^{237}Np in CFM Run 12-02 compared to all the other tests (Table 6-4) is difficult to explain. CFM Run 12-02 was conducted in a different part of the shear zone than the other tests (Fig. 6-1), but such differences in matrix adsorption-desorption parameters were not necessary for any of the other radionuclides that were used in both shear zone locations. Attempts to achieve reasonable matches to the ^{237}Np breakthrough curve in CFM Run 12-02 using the same matrix parameters as other tests were not successful. Adjusting colloid sorption parameters had little effect because very little of the ^{237}Np in the injection cocktail was associated with colloids, and only a limited amount of adjustment of the shear zone adsorption/reduction rate could be tolerated before it became impossible to achieve good matches to the ^{237}Np data. The truncated tail of the ^{237}Np breakthrough curve in CFM Run 12-02, coupled with the lack of association of ^{237}Np with colloids, precluded a strong reversible matrix interaction for ^{237}Np because such a strong reversible interaction results in extended tailing. Also, the inclusion of an irreversible sorption/reduction reaction in the matrix (which seems logical if such a reaction is occurring the shear zone) did not improve the model matches. In fact, the inclusion of such a reaction actually forced the reversible matrix sorption reaction to become weaker to compensate, which increased the difference between the matrix parameters in CFM Run 12-02 and all other tests.

Thorium-232: ^{232}Th was analyzed only in the two CRR tests. It was also injected into CFM Run 13-05, but as of the writing of this report, reliable results had not been reported. Although there were no colloids present in CRR Run 31, the ^{232}Th transported very much like it was facilitated by colloids with a finite desorption rate from the colloids. The ^{232}Th transport could also be interpreted as though the ^{232}Th itself was colloidal (i.e., an intrinsic colloid), with partial filtration of these colloids occurring in the shear zone. However, the observed ^{232}Th behavior is also consistent with a slow, irreversible solute adsorption

reaction occurring in the shear zone, and because of the lack of colloids in CRR Run 31, the parameters listed for ^{232}Th in this test in Table 6-5 reflect this interpretation. Nonetheless, it is possible that the ^{232}Th was partially in colloidal form in the Run 31 injection cocktail, either as intrinsic colloids or as a colloidal precipitate, or perhaps adsorbed to a small (unintentional) concentration of pre-existing colloids. Indeed, Kosakowski and Smith (2004) speculated that the transport of ^{232}Th in CRR Run 31 may have been at least partially colloidal.

It is clear from comparing the ^{232}Th breakthrough curves and recoveries in CRR Runs 31 and 32 (especially relative to ^{131}I – see Figs. 6-14 and 6-18, respectively) that the bentonite colloids in Run 32 facilitated the transport of ^{232}Th through the CRR dipole (even if part of the ^{232}Th transport in Run 31 was colloidal). Given that the ^{232}Th was almost entirely associated with colloids in the Run 32 injection cocktail, the ^{232}Th breakthrough curve in this test was interpreted as being governed by the rate of desorption of ^{232}Th from the colloids. The ^{232}Th sorption parameters for the shear zone and matrix in CRR Run 32 were set so that any ^{232}Th that desorbed from the colloids rapidly became associated with these surfaces for the remainder of the test. Note that the ^{232}Th parameters listed in Table 6-5 for CRR Run 32 reflect that the ^{232}Th that was desorbed from colloids in this test did not follow the same shear zone transport behavior as in CRR Run 31 (i.e., a slow, irreversible reaction in the shear zone). If this slow, reversible reaction was assumed to apply, it would have the effect of increasing the colloid desorption rate constant in Run 32 because some of the ^{232}Th desorbed from colloids would then be predicted to transport through the system as a solute.

It should be noted that the colloid-facilitated transport of ^{232}Th was evaluated in 3 other CFM tests conducted in the same flow configuration as CFM Run 12-02, but without other radionuclides (CFM Runs 08-01, 10-01 and 10-03). Interpretations of these tests are reported in Chapter 2 of Wang et al. (2013). In general, it was found that the governing rate constant for desorption of ^{232}Th from the colloids in these tests was about an order of magnitude smaller than the rate constant reported for CRR Run 32 in Table 6-5 and similar in magnitude to the rate constants deduced for Am and Pu in CFM Runs 12-02 and 13-05 that are listed in Table 6-5.

Americium Isotopes: Americium (Am) isotopes (either ^{241}Am or ^{243}Am) were injected in all the tests. Am transported in a very similar manner as ^{232}Th, with its transport in CRR Run 31 (without colloids) interpreted as being governed by a slow, irreversible adsorption reaction in the shear zone, and its transport in all other tests as governed by a slow desorption reaction from colloids with rapid and strong adsorption of the Am to both shear zone and matrix surfaces once it desorbed from colloids. As for ^{232}Th, transport of Am partially in a colloidal state cannot be ruled out for CRR Run 31; this possibility was also speculated by Kosakowski and Smith (2004). Am was interpreted as having a slightly slower solute shear-zone reaction rate in CRR Run 31 than ^{232}Th but as having a slightly faster desorption rate from colloids than ^{232}Th in CRR Run 32 (Table 6-5). However, these differences may not be significant, as they could be swamped by errors associated with analytical measurements, including measurements of radionuclide associations with colloids in the Run 32 injection cocktail (which can have a significant impact on the deduced desorption rate constants).

The interpretations of Am transport in CFM Runs 12-02 and 13-05 were generally consistent with that of CRR Run 32, although the rate constant for Am desorption from colloids was notably smaller in the CFM tests than in the CRR test. Whereas differences in the observed colloid-facilitated transport of Cs and U in the CRR and CFM tests were qualitatively explained by the greater influence of strong colloid sorption sites at the lower injection concentrations in the CFM tests, no such explanation can be invoked for Am because its injection concentrations in all the tests were quite similar. Nonetheless, it is still possible that there were both strong and weak Am sorption sites on the colloids, or more specifically, sites with slower and faster desorption rate constants. In this case, the faster sites would have more influence on the bulk behavior observed in the shorter-duration CRR test, and the slower sites would have greater influence in

the CFM tests with longer shear-zone residence times. The fact that the colloid concentrations were about five times lower in the CRR test than in the CFM tests may have also resulted in a greater influence of weaker colloid sorption sites on Am transport (expressed as faster Am desorption rates from colloids) in the CRR tests.

The Am desorption rate constant from colloids in CFM Run 13-05 was smaller than in CFM Run 12-02 despite the fact that the residence time for the majority of the injected mass was shorter in the former test than the latter test. Although the differences in the desorption rate constants may not be significant because of errors and uncertainties in the data, one possible explanation for this result is that the CFM Run 13-05 injection cocktail was "aged" for 401 days before its injection whereas the Run 12-02 injection cocktail was injected within 7 days of its preparation. This would have given the Am more time to become associated with strong sorption sites on the colloids in the Run 13-05 cocktail, thus resulting in a slower apparent rate constant for desorption from colloids in this test. However, it is also possible that the desorption rate constants were different in the two tests simply because the tests were conducted in different parts of the shear zone.

Finally, it should be noted that, as for U and Np in CFM Run 13-05, the Am rate constant for desorption from colloids when a constant-rate injection function was assumed in Run 13-05 had to be specified as steadily increasing with time to obtain a reasonable match to the Am breakthrough curve. Without such a time-dependent desorption rate constant, the Am concentrations near the end of the test were significantly over-predicted.

Plutonium Isotopes: Plutonium (Pu) isotopes (either ^{238}Pu, ^{242}Pu or ^{244}Pu, or some combination of these) were injected in all the tests. Pu transported in a manner very similar manner to ^{232}Th and Am, with its transport in CRR Run 31 (without colloids) interpreted as being governed by a slow, irreversible adsorption reaction in the shear zone, and its transport in all other tests as being governed by a slow desorption reaction from colloids with rapid and strong adsorption of the Pu to both shear zone and matrix surfaces once it desorbed from the colloids. Pu was interpreted as having the fastest shear-zone solute reaction rate of these three radionuclides in CRR Run 31, and also as having the slowest rate of desorption from colloids in all the other tests (Table 2-5). However, its desorption rate from colloids was indistinguishable from that of Am in CFM Run 13-05.
All of the statements in the last two paragraphs about Am transport also apply to Pu, so they are not repeated here. However, one exception is that the rate constants for desorption of Pu from colloids were deduced to be almost identical in CFM Runs 12-02 and 13-05, whereas this desorption rate constant for Am was deduced to be somewhat smaller in Run 13-05 than in Run 12-02.

6.5 DISCUSSION AND CONCLUSIONS

The comprehensive model interpretations presented in this report for all the CRR and CFM tests involving reactive radionuclides at the Grimsel Test Site yield some valuable insights for modeling of radionuclide transport, and particularly of colloid-facilitated radionuclide transport, in saturated fractured crystalline rocks. Nonuniqueness in the model interpretations was reduced by minimizing the differences in the reactive transport parameter estimates for a given radionuclide in different tests, with the rationale being that all the tests were conducted within a few meters of each other in the same shear zone, so the model parameters for a given radionuclide should be similar in all tests. However, nonuniqueness in the parameter estimates could not be completely eliminated, particularly for parameters for which the model simulations of a given radionuclide were insensitive. Also, it should be made clear that a rigorous parameter estimation algorithm was not applied, so the parameter estimates of Tables 6-3 through 6-5 should not be considered formally optimized.

For the most part, a relatively consistent set of reactive transport parameter estimates was obtained for each radionuclide, and these could be readily applied to all CRR or CFM tests in which that radionuclide was injected. However, adjustments to the most sensitive reactive transport parameters were inevitably necessary to improve model matches to breakthrough curves for a given radionuclide when interpreting different tests. Some of these adjustments can be readily justified as being attributable to differences in injection concentrations of the radionuclides or to differences in the locations of the tests in the shear zone.

The transport of the FEBEX bentonite colloids in all the tests involving radionuclides could be explained quite well with an irreversible filtration rate constant, which was deduced to be similar in magnitude in each of the tests. No colloid filtration was apparent in the very short-duration CRR Run 32, but the predicted amount of filtration in this test was negligible when the filtration rate constants deduced from the longer-duration CFM tests were applied, so the lack of observed filtration in the CRR test is considered to be consistent with the CFM test results. In effect, CRR Run 32 was too short to provide constrained estimates of colloid filtration rate constants, and this test should not be used to draw any conclusions about colloid filtration rates in the MI shear zone other than placing an upper bound on what the filtration rate might be.

The transport of radionuclides that were not strongly associated with colloids but nevertheless had significant interactions with rock surfaces (^{22}Na, ^{85}Sr, ^{133}Ba, U and Np in tests other than CFM Run 13-05, and ^{137}Cs at high concentrations or in the absence of colloids) appeared to be dominated by sorption and desorption in the matrix (after diffusion out of the shear zone), rather than by sorption and desorption within the shear zone itself. This was true despite the relatively small matrix porosity of the Grimsel granodiorite, which should presumably limit diffusion of radionuclides into the matrix. In most cases, the matrix adsorption and desorption rates could be considered rapid relative to conservative tracer residence times in the tests, so the sorptive interaction in the matrix could be approximated with a partition coefficient, or K_d value (ml/g), rather than explicitly accounting for rate-limited adsorption and desorption reactions. This result is consistent with the observations of Andersson et al. (2002) in the fractured granite system at the Aspö site in Sweden, where it was also observed that strongly-adsorbing radionuclides tended to behave as if sorption in the matrix dominated their transport behavior despite a small matrix porosity.

The transport of radionuclides that were strongly associated with colloids (^{232}Th, Am, Pu) tended to be governed by their rates of desorption from the colloids, with the assumption that once the radionuclides desorbed from the colloids, they quickly became strongly associated with immobile surfaces in the system (either in the shear zone or in the matrix), thus removing them from further participation in the test. The mass recoveries of these radionuclides were governed by their colloid desorption rate constants, with larger desorption rate constants resulting in lower recoveries.

In the absence of colloids (CRR Run 31), the transport of radionuclides that were otherwise strongly associated with colloids (^{232}Th, Am, Pu) appeared to be governed by a slow, essentially irreversible reaction occurring in the shear zone. There was little evidence that these radionuclides interacted at all with the matrix, although a limited amount of matrix interaction cannot be ruled out. The transport behavior of these radionuclides in the absence of colloids was also consistent with colloid-facilitated transport with a finite desorption rate from the colloids or with transport of intrinsic colloids (e.g., colloidal precipitates) with a finite filtration rate of the colloids. These possibilities are considered plausible, particularly given the low solubilities and apparent lack of matrix interactions of these radionuclides despite the strong matrix interactions observed for other radionuclides.

The injection function for CFM Run 13-05 had more uncertainty than any other CFM tracer test previously conducted with a circulating injection loop (see Chapter 2, Wang et al., 2013), because the

deduced conservative tracer mass associated with the injection function was about 20% higher than the reported injection mass. This uncertainty was addressed by performing model interpretations assuming (1) a varying-rate injection function that closely followed the observed injection function behavior but with concentrations scaled down by 20% to preserve mass and (2) a mass-conserving constant-rate injection function at the injection rate observed over the last several hundred hours of the test. Because the model interpretations assuming the latter injection function required both a time-dependent colloid filtration rate constant and time-dependent colloid desorption rate constants for U, ^{237}Np, Am and Pu, the varying-rate injection function is considered to be the more plausible function. It is recommended that the reactive transport parameters for radionculides deduced assuming this injection function in CFM Run 13-05 be given more credence than those obtained assuming the constant rate function.

Although it was hoped that the tests would provide some insights into the time and distance scaling behavior of colloid filtration rate constants, it appears that little can be said about such scaling behavior. The colloid filtration rate constants in the CFM tests were deduced to be quite similar in the two test configurations. The CRR tests had much shorter time scales than the CFM tests, but there was no observed colloid filtration in CRR Run 32, so it was not possible to obtain a constrained estimate of the colloid filtration rate constant in this test. The reader is referred to the Chapter on CFM test interpretations in Chapter 2 of Wang et al. (2013) for a discussion of apparent time-scale dependence of colloid filtration rate constants observed in non-radionuclide CFM tests that were conducted in the same configuration as CFM Run 12-02 but with varying residence times. That discussion, which includes CFM Run 12-02 as one of the tests considered, provides more insights into the scaling behavior of colloid filtration rates than can be gleaned from the radionuclide tests described in this report.

The rate constants for desorption of radionuclides from bentonite colloids were consistently greater for ^{137}Cs, Am and Pu in the shorter-duration CRR Run 32 than in either of the longer-duration CFM tests. These were the only colloid-facilitated radionuclides for which comparisons between the CRR and CFM tests were possible. The suggested time-scale dependence of the desorption rate constants may be an artifact of the assumption in the interpretative modeling that there was only a single type of radionuclide sorption site on the colloids. For ^{137}Cs, there is independent evidence (Missana et al., 2004; Chapter 2 in Wang et al., 2013) that at least two different sorption sites of different strengths exist on the bentonite colloids, with the stronger sorption site having much lower abundance on the colloid surfaces. In this case, the observed ^{137}Cs behavior can be at least partially attributed to the much higher concentration of Cs in the injection cocktail in the CRR test than in the CFM tests. The higher Cs concentration in the CRR test would be expected to result in a predominant influence of the more abundant weaker sorption sites on the colloids, whereas there would be expected to be a greater influence of the less-abundant, stronger sorption sites on the colloids in the CFM tests. The fact that the Cs was much more strongly associated with colloids in the CFM injection cocktails than in the CRR injection cocktail is consistent with this explanation. For Am and Pu, the reasons for the larger apparent desorption rate constants in the CRR test cannot be attributed to differences in concentrations of the radionuclides in the injection cocktails because the concentrations in all cocktails were similar. However, the smaller concentration of colloids in the CRR Run 32 cocktail relative to the CFM tests (by about a factor of five) may have still resulted in a greater percentage of Am and Pu in the CRR test being associated with weaker colloid sorption sites than in the CFM tests.

The model interpretations documented in this report are generally consistent with the interpretations of CRR Runs 31 and 32 reported by Kosakowski and Smith (2004), who did a somewhat more sophisticated set of analyses that included both 1-D and 2-D models, with the latter accounting for 2-D flow through the shear zone around the CRR dipole.

It is of interest to compare the Am and Pu desorption rate constants from colloids in the GTS field tests to the rates measured in the laboratory experiments of Huber et al. (2011). Huber et al. (2011) measured

desorption rate constants for Am and Pu from colloids in a ternary system involving the bentonite colloids, fracture fill material from GTS, and a synthetic GTS ground water at two different starting concentrations of the nuclides. Using the Am and Pu injection concentrations in the GTS tests, the desorption rate constants predicted by the experiments of Huber et al. (2011) would be approximately 0.01 hr^{-1} for Am and 0.002 hr^{-1} for Pu. The desorption rate constants deduced in CFM Runs 12-02 and 13-05 were in reasonably good agreement with these values, although they tended to be slightly higher than in the laboratory tests. This agreement is nonetheless considered to be quite good, and the higher rates in the field experiments could just reflect that the shear zone surface area available for competitive sorption with the colloids was somewhat higher in the field test than in the lab experiments.

Generally speaking, the results of the GTS colloid-facilitated radionuclide transport tests indicate that the actinides Th, Pu and Am, and the fission product ^{137}Cs, are the most likely radionuclides to experience colloid-facilitated transport over long time and distance scales (at least for bentonite colloids in a fractured crystalline setting). However, the time and distance scales of the GTS tests were very short relative to time and distance scales of relevance for nuclear waste repository performance assessments, so it should not necessarily be concluded that colloid-facilitated transport of these radionuclides will be a concern in such performance assessments. The GTS results collectively suggest that colloid-facilitated radionuclide transport is likely to be more efficient at lower radionuclide concentrations than at higher concentrations because a greater fraction of the radionuclide mass will then tend to become associated with strong, low abundance adsorption sites on the colloids. Stated differently, the GTS results suggest that colloid-facilitated transport over very long time and distance scales is much more likely to involve very small concentrations of radionuclides rather than large concentrations.

6.6 REFERENCES

Andersson P., Byegard J., Dershowitz W., Doe T., Hermanson J., Meier P., Tullborg E., and Winberg A. (2002) *TRUE Block Scale project. Final report 1(4). Characterisation and model development*. Technical Report 02-13, Swed. Nucl. Fuel and Waste Management Co., Stockholm.

Huber F., Kunze P, Geckeis H., and Schäfer T. (2011) Sorption reversibility kinetics in the ternary system radionuclide-bentonite colloids/nanoparticles-granite fracture filling material, *Appl. Geochem.*, 26, 2226-2237.

Kontar K. and Gräfe K. (2012) *GTS Phase VI CFM Project Tracer Test Run 12-02, Quick-Look Report,* AN 12-302, CFM Project, Switzerland.

Kontar K., Gräfe K., and Rösli U. (2013) *GTS Phase VI, CFM Phase 2, Tracer Test Run 13-05, Quick-Look Report,* AN 13-617, CFM Project, Switzerland.

Kontar K. and Rösli U. (2014) *GTS Phase VI, CFM Project, Long-Term In-Situ Test (LIT): Bentonite source term packer system, surface equipment extension, QA and installation report*, AN 14-362, CFM Project, Switzerland.

Kosakowski G. and Smith P. (2004) *Modelling the Transport of Solutes and Colloids in a Water-Conducting Shear Zone the Grimsel Test Site*, Nagra Techncial Report 04-01, Nagra, Wettingen, Switzerland.

Missana T., Garcia-Gutierrez M., and Alonso U. (2004) Kinetics and irreversibility of cesium and uranium sorption onto bentonite colloids in a deep granitic environment, *Appl. Clay Sci.*, 26, 137-150.

Möri A. (Ed.) (2004) *The CRR final project report series I: Description of the Field Phase – Methodologies and Raw Data*. Nagra Technical Report NTB 03-01. Nagra, Wettingen, Switzerland.

Reimus P. W., Pohll G., Mihevc T., Chapman J., Papelis L., Lyles B., Kosinski S., Niswonger R., and Sanders P. (2003) Testing and parameterizing a conceptual model for radionuclide transport in a fractured granite using multiple tracers in a forced-gradient test, *Water Resour. Res.*, 39(12), 1350, doi:10.1029/2002WR001597.

Reinholdt M. X., Brendle J., Tuilier M-H., Kaliaguine S., and Ambroise E. (2013) Hydrothermal synthesis and characterization of Ni-Al montmorillonite-like phyllosilicates, *Nanomaterials*, 3, 48-69, doi:10.3390/nano3010048.

Taylor G. I. (1953) Dispersion of soluble matter in solvent flowing slowly through a tube, *Proc. Roy. Soc.* A., 219, 186–203.

Wang Y., et al. (2013) *Used Fuel Disposition Campaign Milestone Report FCRD-UFD-2013-000628; Chapter 2, Interpretations of Colloid-Facilitated Transport Experiments at the Grimsel Test Site from 2008 through 2012*. Natural System Evaluation and Tool Development – International Collaborations: FY13 Progress Report.

Wang Y., et al. (2015) *Used Fuel Disposition Campaign Milestone Report FCRD-UFD-2015-000125; Chapter 8, Laboratory Investigation of Colloid Facilitated Transport of Cesium by Bentonite Colloids in a Crystalline Rock System*. Used Fuel Disposal in Crystalline Rocks: FY15 Progress Report.

7. DEVELOPMENT AND CAPABILITY DEMONSTRATION OF DISCRETE FRACTURE NETWORK MODEL

7.1 INTRODUCTION

In this section we report recent technical and scientific developments of the Los Alamos National Laboratory computational suite, dfnWorks, for simulating flow and transport in fractured rocks such as the Crystalline rocks that are the focus of this work package. dfnWorks can be used to stochastically generate three-dimensional discrete fracture networks where fracture geometry is retained and flow and transport are simulated therein without using one-dimensional pipe network approximations.

In the first part of this section, we show results of our recent study on fracture size and fracture transmissivity correlation. We characterize how different fracture size-transmissivity relationships influence flow and transport simulations through sparse three-dimensional discrete fracture networks, loosely based on Forsmark fracture characteristics provided by SKB. Although it is generally accepted that there is a positive correlation between a fracture's size and its transmissivity/aperture, the functional form of that relationship remains a matter of debate. Relationships that assume perfect correlation, semi-correlation, and non-correlation between the two have been proposed. To study the impact that adopting one of these relationships has on transport properties, we generate multiple sparse fracture networks composed of circular fractures whose radii follow a truncated power law distribution. The distribution of transmissivities is selected so that the mean transmissivity of the fracture networks are the same and the distributions of aperture and transmissivity in models that include a stochastic term are also the same. We observe that adopting a correlation between a fracture size and its transmissivity leads to earlier breakthrough times and higher effective permeability when compared to networks where no correlation is used. While fracture network geometry plays the principal role in determining where transport occurs within the network, the relationship between size and transmissivity controls the flow speed. These observations indicate DFN modelers should be aware that breakthrough times and effective permeabilities can be strongly influenced by such a relationship in addition to fracture and network statistics.

In the second part of this section, we present an analysis and visualization prototype using the concept of a flow topology graph (FTG) for characterization of flow in constrained networks, with a focus on DFN. Our method allows users to understand and evaluate flow and transport in DFN simulations by computing statistical distributions, segment paths of interest, and cluster particles based on their paths. The new approach enables to evaluate the accuracy of the simulations, visualize features of interest, and compare multiple realizations over a specific domain of interest. It allows to simulate complex transport phenomena modeling large sites for networks consisting of several thousand fractures without compromising the geometry of the network. However, few tools exist for performing higher-level analysis and visualization of simulated DFN data. The prototype system we present addresses this need. We demonstrate its effectiveness for increasingly complex examples of DFNs, covering two distinct use cases – hydrocarbon extraction from unconventional resources and transport of dissolved contaminant from a spent nuclear fuel repository.

7.2 FRACTURE SIZE AND TRANSMISSIVITY CORRELATIONS: IMPLICATIONS FOR TRANSPORT SIMULATIONS IN SPARSE THREE-DIMENSIONAL DISCRETE FRACTURE NETWORKS FOLLOWING A TRUNCATED POWER LAW DISTRIBUTION OF FRACTURE SIZE

7.2.1 Introduction

Interconnected networks of fractures are the primary pathway for fluid flow and the associated transport of dissolved contaminants through low permeability rocks. These fracture networks are common in hydrocarbon extraction, aquifer storage and management, geothermal energy extraction, environmental restoration of contaminated fractured rock sites, and the disposal of spent nuclear fuel (Adler et al., 2012; Berkowitz, 2002; Faybishenko, 2005; Karra et al., 2015; National Research Council,1996; Neuman, 2005). However, the limited amount of available information leads to significant uncertainty when trying to determine the influence of fracture properties on flow and transport through the subsurface (Bonnet et al., 2001). Models used to simulate flow and transport through fractured rock address these uncertainties in different ways and each has its own advantages and disadvantages (Molz et al., 2004; National Research Council, 1996; Neuman, 2005). The two main methodologies in use are continuum models, where the rock mass is represented as a porous medium and the hydraulic conductivity is a scale-dependent correlated stochastic field, and discrete fracture network (DFN) models, where the geometry and properties of individual fractures are explicitly represented. Other models that consider the combined effect of fracture and matrix have also been recently developed (Ahmed et al., 2015a, b; Roubinet et al., 2010; Willmann et al., 2013). Although DFN models can typically represent a wider range of transport phenomena than continuum models (Painter and Cvetkovic, 2005; Painter et al., 2002), the inclusion of detailed features introduces additional layers of uncertainty because more parameters have to be calibrated (Neuman, 2005). For example, it is possible to include in-fracture aperture variability into high fidelity DFN simulations (de Dreuzy et al., 2012; Makedonska et al., 2016) but constraining the in-fracture variability requires detailed knowledge of the particular rock formation.

One source of uncertainty in DFN modeling is the relationship between a fracture's size and its transmissivity. A correlation between size and aperture implicitly define a correlation between a fracture size and its transmissivity if one assumes that the aperture controls flow rate through a fracture, e.g., if the cubic law (Witherspoon et al., 1980) or variant thereof is used. However, in comparison to studies on fracture length, there are relatively few on aperture distributions. Although it is generally accepted that there is a positive correlation between fracture length and aperture (Bonnet et al., 2001), a functional form of that relationship remains a matter of debate. Proposed relationships between a fracture's length and its aperture include: Lévy stable (Belfield, 1998), lognormal (Charlaix et al., 1987; de Dreuzy et al., 2001; Margolin et al., 1998), and power law (Gudmundsson et al., 2001; Hatton et al., 1994; Patriarche et al., 2007; Vermilye and Scholz, 1995; Walmann et al., 1996). Each of these models exhibit a range of parameter values based on scale and site data. In particular, an extensive range of exponent values in power law relationships, the most widely used relationship, has been reported in the literature, cf. section 6.4.2 in Bonnet et al. (2001). Moreover, any calibrated exponent is likely not universal at all scales (Hatton et al., 1994; Renshaw and Park, 1997).

A direct link between fracture size and transmissivity is also difficult to obtain from field observations and proper characterization of this relationship is essential for upscaled flow and transport behavior if a correlation is adopted (Frampton and Cvetkovic, 2010). The influence of adopting a correlation between fracture size and aperture (transmissivity) on effective network permeability was investigated using two-dimensional fracture networks by de Dreuzy et al.

(2004) and Baghbanan and Jing (2007), but they did not consider transport processes. de Dreuzy et al. (2004) observed that the effective permeability of the networks was enhanced when a correlation between fracture size and aperture width was included and Baghbanan and Jing (2007) observed that the overall permeability of the DFN was controlled by large fractures that were assigned higher apertures. Joyce et al. (2014) and Follin et al. (2014) performed a site-specific study using three-dimensional networks and calibrated three different size-transmissivity models by matching specific capacities. They found that uncorrelated models had higher mean transmissivity values when compared to correlated models.

We characterize the influence that selecting a particular relationship between fracture size and transmissivity (aperture) has on transport processes in large (kilometer-scale) semi-generic sparse discrete fracture networks. We use the dfnWorks (Hyman et al., 2015a) computational suite to create three-dimensional fracture networks loosely based on the fractured granite at the Forsmark site in Sweden, a potential host for spent nuclear fuel (Svensk Kärnbränslehantering AB , 2011), and resolve flow and transport therein. We select four different relationships and quantify the impact that each of them has on flow and transport observables. The four relationships we consider are: 1) a positively correlated power law, 2) a log-normal distribution around a positively correlated power law, 3) a log-normal distribution around a prescribed mean, and 4) constant (all fractures have the same transmissivity). Each of these models represents various degrees of uncertainty about the relationship between fracture size and transmissivity. Adoption of a positively correlated power law model assumes a fairly low degree of uncertainty, log-normal distribution around a positively correlated power law includes a stochastic term to account for variability of transmissivities in fractures of the same size, and the log-normal distribution around a prescribed mean assumes a high degree of uncertainty asserting that there is no correlation between the fracture size and transmissivity; the constant relationship is used for comparison. Their influence on observables is compared in terms of the effective permeability of the network, transport properties of a conservative solute passing through DFN, and where transport occurs in the network.

We observe that networks with a correlated relationship have consistently higher effective permeability values and earlier breakthrough times than networks without correlation. Specifically, fracture network geometry plays a principal role in determining where transport occurs within the network and the adopted relationship between fracture size and transmissivity controls the speed of flow and transport times. The results suggest the breakthrough times and effective permeabilities are influenced by the adopted relationship in addition to fracture and network statistics.

7.2.2 Methods

In the DFN approach, geologic field investigations are used to create a network of fractures where the geometry and properties of individual fractures are explicitly represented as $N-1$ dimensional objects in an N dimensional space, e.g., lines in two dimensions or planar polygons in three dimensions. Fractures in the network are assigned a shape, location, and orientation based on distributions obtained in a site characterization. Once a network is constructed, the individual fractures are meshed for computation and the flow equations are numerically integrated on the resulting computational mesh. In most DFN methodologies, the matrix is considered impervious due to its low permeability (Trimmer et al., 1980). Examples of the various DFN methodologies and their applications are found in Cacas et al. (1990); de Dreuzy et al. (2004, 2012); Dershowitz (2014); Erhel et al. (2009); Hyman et al. (2015b); Ji et al. (2011); Mustapha and Mustapha (2007); Pichot et al. (2010, 2012) and Xu et al. (2006).

Transmissivity Models: Under the assumption of aperture uniformity, flow through the fractures is equivalent to flow through two parallel plates, and the volumetric flow rate Q per unit fracture width normal to the direction of flow is given by the Boussinesq equation (Boussinesq, 1868):

$$Q = -b^3 \frac{\rho g}{12\upsilon} \nabla h \tag{7-1}$$

where b is the fracture aperture, ρ is the fluid density (which we assume is constant), ν is the fluid viscosity, and h it the hydraulic head. This relationship between aperture and flow rate can be used to derive a similar relationship between aperture and transmissivity:

$$T = b^3 \frac{\rho g}{12\upsilon} \tag{7-2}$$

referred to as the cubic law (Witherspoon et al., 1980). For heterogeneous fracture apertures with significant fracture roughness and/or fracture closing, measured values of transmissivity can deviate from predictions obtained using the cubic law (Konzuk and Kueper, 2004; Zimmerman and Bodvarsson, 1996). A host of corrections and reformulations of the cubic law have been proposed. There are reformulations based on other powers of aperture such as the quadratic law $T \propto b^2$ (Uchida, 1994) and the quintic law $T \propto b^5$ (Klimczak et al., 2010). Cvetkovic et al. (2004) and Cvetkovic and Frampton (2012) investigated the influence that adoption of either the cubic law or the quadratic law had on transport properties in three-dimensional DFN. They determined the selection of how aperture relates to transmissivity can influence transport and retention properties. Others have proposed correction factors based on geometric and empirical considerations (Renshaw, 1995; Witherspoon et al., 1980). We only consider the cubic law because it is already established the choice of aperture-transmissivity relationship can influence transport properties. Additionally, using a similar computational setup, Makedonska et al. (2016) found that in-fracture aperture variability has little effect on transport properties in sparse three-dimensional fracture networks. In light of their field each fracture is assigned a uniform aperture representative of the mean value of variable apertures within a fracture plane.

We consider four different size-transmissivity relationships and quantify the impact that their adoption has on flow and transport observables. The four relationships are: 1) a positively correlated power law, 2) a log-normal distribution around a positively correlated power law, 3) a log-normal distribution around a prescribed mean, and 4) constant. The functional forms of the relationships between transmissivity T and radius r are the following. The first model we consider is a positively correlated power law relationship with parameters α and β:

$$\log(T) = \log(\alpha \cdot r^{\beta}) \tag{7-3}$$

We refer to this model as *correlated.*

The second model includes a stochastic term into (5):

$$\log(T) = \log(\alpha \cdot r^{\beta}) + \sigma_T N(0,1) \tag{7-4}$$

to account for uncertainty and variability between fractures of the same size. The strength of the stochastic term is determined by the variance of a log-normal distribution σ_T and the stochastic term is an independent identically distributed random variable sampled from a normal distribution with mean 0 and variance 1, N (0, 1). This model results in a log-normal distribution of fracture transmissivities around a positively correlated power law mean. We refer to this model as *semi-correlated*.

The third model assumes that there is no correlation between the fracture size and transmissivity and all values are independent identically distributed random variables from a log-normal distribution with specified mean μ_T and variance σ_T:

$$\log(T) = \mu_T + \sigma_T N(0, 1) \tag{7-5}$$

We refer to this model as *uncorrelated*.

The fourth model represents an assumption that in addition to no relationship between r and T, and there is no variation between fractures:

$$\log(T) = \mu_T \tag{7-6}$$

We refer to this model as *constant*. Equation (7-6) provides a control case for comparison between the other models.

Each of these models represents various degrees of uncertainty about the relationship between fracture size and transmissivity. Adoption of the perfectly correlated model (7-3) implicitly assumes a fairly low degree of uncertainty about the relationship between fracture size and transmissivity. While there are indications that such a relationship between size and transmissivity is useful (Dershowitz et al., 2003), the deterministic formulation is an idealization where all fractures of the same size are assigned the same transmissivity. Such a model disregards all mechanical, chemical, and hydrological processes that can result in variation between transmissivity of fractures of the same size. However, the formulation is convenient because each realization of network geometry requires a single realization of the transmissivity field Frampton and Cvetkovic (2010) calibrated the parameters of a perfectly correlated model in a DFN representation of fractured crystalline rock at Laxemar, Sweden using soft conditioning based on Posiva flow logs (PFL). The conditioning is soft in the sense that the objective is to match the distribution of borehole flows with the distribution PFL flows rather than specific data. Other research teams have also used the perfectly correlated model (Bogdanov et al., 2007; de Dreuzy et al., 2002; Joyce et al., 2014; Wellman et al., 2009). The semi-correlated model (1-4) attempts to address the some of the issues associated with its deterministic counterpart. While still not resolving the physical processes that cause variations between the transmissivities of fractures of the same size, it includes a stochastic term to account for these variations (Hartley et al., 2006). While this term might increase realism of the network, it is more cumbersome than the perfectly correlated model, both in terms of computational demands (multiple transmissivity field realizations for the same network geometry are required) and calibration data (the semi-correlated model requires additional support from field data to constrain its additional parameters (Frampton and Cvetkovic, 2010)). The semi-correlated model is the least common of the models considered here, even though some researchers consider it the most realistic (Follin et al., 2014). In the uncorrelated model (7-5), a lognormal distribution around a prescribed mean transmissivity is used to include variability between fractures. Here the mechanical, chemical, and

hydrological processes are assumed principally responsible for variations between fracture transmissivities rather than assuming a correlation between a fracture's size and its transmissivity. In other words, this model is the opposite extreme of the perfectly correlated model and the semi-correlated is a combination of the two. Examples of studies that use the uncorrelated DFN models are Cacas et al. (1990); Cvetkovic et al. (2004); de Dreuzy et al. (2001); Dverstorp and Andersson (1989) and Kang et al. (2015).

We begin by comparing all four models on a single DFN realization to explore what differences occur due to assumptions of correlation and the inclusion of stochastic terms. Because there is no randomness in the correlated and constant models, only one transmissivity field is generated for each network for these models. To sample the stochastic term in the semi-correlated and uncorrelated models, thirty independent transmissivity fields are generated on a fracture network geometry for each relationship. The average statistics are studied for each set, as well as those obtained for individual realizations. This results in sixty-two flow solutions for this particular fracture network. Next, we compare the correlated and constant models using thirty independent network realizations to determine what variation exists between realizations of the fracture networks. These two relationships, correlated and constant, are selected because statistics obtained from the semi-correlated and uncorrelated center around their deterministic counterparts. In sum 112 different flow field on 31 different network geometries are considered.

The adopted parameters of the four different relationships for the single DFN realization are provided in Table 7-1. The parameters are selected so that the mean transmissivity of the fracture networks are all the same and that the distributions of aperture and transmissivity in models that include a stochastic term are also the same. In all cases the P_{32} values are nearly identical; differences between samples are less than 10^{-5}. The parameter values and variances are taken from those provided in Table 6-75 in the SKB report TR-10-52 (Svensk Kärnbränslehantering AB, 2010). Figure 7-1 shows the distributions of fracture apertures and transmissivities for the correlated (blue), semi-correlated (red), and uncorrelated models (green). The values are normalized by the aperture of the constant model for comparison. Figure 7-1 (a) shows the distribution of apertures for the correlated, semi- correlated, and uncorrelated models. Even though the mean values of aperture are all the same, there is a clear difference between the distributions of the deterministic model (correlated) and the two stochastic models (semi-correlated and uncorrelated) due to the stochastic term. In the correlated case, the apertures (and transmissivities) are determined by the power law distribution for the fracture radius, which has a hard cutoff. This lower bound results in distributions with a sharp cutoff in the distribution of apertures as well, reminiscent of a power law distribution. The stochastic term in the semi-correlated and uncorrelated models results in wider distributions with heavier tails. Figure 7-1 (b) shows the distribution of transmissivities for the correlated, semi-correlated, and uncorrelated models. The distributions of the two stochastic models different from the correlated model, but are nearly indistinguishable from one another. The distribution of transmissivities for the stochastic models have a much fatter tail at high values of transmissivity, include more small transmissivity values, and have a higher variance than the deterministic model.

Table 7-1. DFN generation parameters. The values are loosely based on fractured granite at the Forsmark repository site in Sweden (Svensk Kärnbränslehantering AB, 2010). The domain is a cube with sides of length (L) 1000 [m]. Parameters of the Fisher distribution for fracture orientation, Eq. 1: Mean Trend (θ^1), Mean Plunge (φ^1), and the concentration parameter (κ). Parameters for the power law distribution of fracture radii, power law exponent (α), upper cutoff (r_u/L) [-], and lower cutoff (r_0/L) [-]. The required number of fractures from each increased to reach the percolation threshold. Mean P_{32} (surface area of the fractures over the total volume) value for the fracture network that connects the inflow and outflow boundaries of this DFN is 0.057 m^{-1}.

Set	Fisher Distribution			Power Law Distribution			Fracture Density
	θ^1	φ^1	κ	γ	r_u/L [-]	r_0/L [-]	Number of fractures
1. (NS)	90.0°	0.0°	21.7	2.5	560	15	2093
						20	1019
						25	583
2. (NE)	135.0°	0.0°	21.5	2.7	560	15	2000
						20	919
						25	503
3. (HZ)	360.0°	90.0°	8.2	2.38	560	15	7711
						20	3887
						25	2285

Table 7-2. Four different relationships between fracture radius r and transmissivity T. Parameters are selected so that all models have the same mean and the two stochastic relationships have similar distributions.

Model	Relationship	Parameters
Correlated	$\log(T) = \log(\alpha \cdot r^{\beta})$	$(\alpha, \beta) = (1.3 \cdot 10^{-9}, 0.5)$
Semi-Correlated	$\log(T) = \log(\alpha \cdot r^{\beta}) + \sigma_T N(0,1)$	$(\alpha, \beta, \sigma_T) = (1.3 \cdot 10^{-9}, 0.5, 0.7)$
Uncorrelated	$\log(T) = \mu_T + \sigma_T N(0,1)$	$(\mu_T, \sigma_T) = (-18.79, 0.8)$
Constant	$\log(T) = \mu_T$	$\mu_T = -18.79$

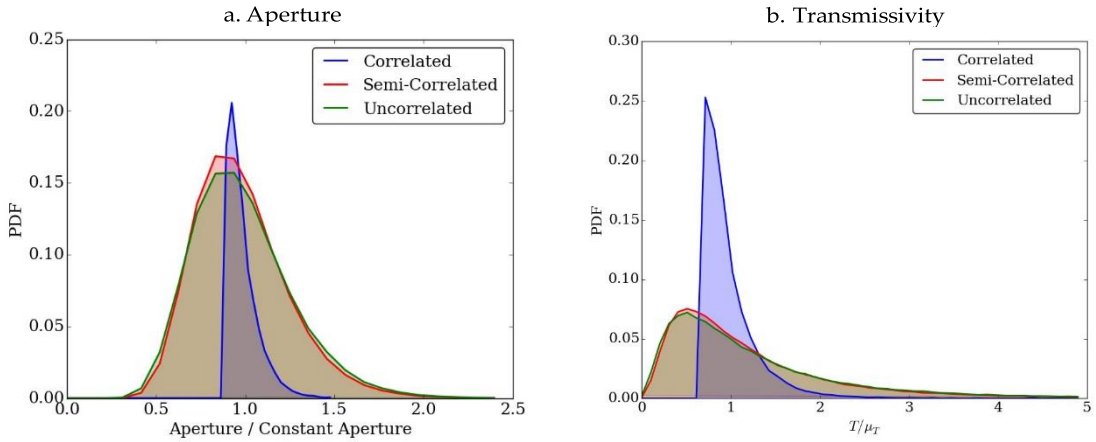

Figure 7-1. Empirical probability density functions of the (a) fracture apertures and (b) transmissivities for the correlated (blue), semi-correlated (red), and uncorrelated models (green). Model parameters, provided in Table 7-2, are selected so that the mean transmissivity of the fracture networks are all the same and that the distributions of aperture and transmissivity in models that include a stochastic term are similar. Values are normalized by the value of the constant model for comparison. (a) Even though the mean values of aperture are all the same, there is a clear difference between the distributions of the deterministic model (correlated) and the two stochastic models (semi-correlated and uncorrelated) due to the stochastic term. The stochastic term in the semi-correlated and uncorrelated models results in wider distributions with heavier tails that do not exhibit a sharp cutoff in the distribution, which occurs in the correlated case due to the truncated power law distribution of fracture radii. (b) The distributions of transmissivity for the two stochastic models different from the correlated model, but are close to one another. The distribution of transmissivities for the stochastic models display a much fatter tail at high values of transmissivity, include more small transmissivity fractures, and have a higher variance than the deterministic model**.**

7.2.3 Results

In this section we report how the adopted relationships between fracture size and transmissivity influence flow and transport behavior in terms of the effective permeability of the network, particle breakthrough times and transport resistance curves, and network backbone. We begin with a single DFN realization to focus our discussion and presentation of results and then report observations for multiple fracture networks.

Effective Permeably: To estimate the effective permeability of each network in the direction of flow, we compute the Darcy velocity at the outlet plane and then invert Darcy's law using the imposed pressure gradient and domain size. Values of mean, variance, minimum and maximum for the samples are reported in Table 7-3. For comparison, effective permeability values are normalized by the effective permeability of the constant fracture network. Figure 7-2 shows a scatter plot of the semi-correlated and uncorrelated values along with a black dotted line of the effective permeability of the constant fracture network and a blue dotted line for the effective permeability of the perfectly correlated network.

Table 7-3. Effective permeabilities. Values are normalized by the effective permeability of the constant fracture network for comparison.

Model	Mean	Variance	Minimum	Maximum
Correlated	2.56	-	-	-
Semi-Correlated	2.62	0.13	3.35	2.03
Uncorrelated	0.98	0.04	1.46	0.66

The effective permeabilities of the networks are within a factor of two to three of one another. The perfectly correlated model resulted in a value of effective permeability two and one-half times that of the constant network even though the mean values of transmissivity in the two networks are the same. The reported value of the semi-correlated model center around that of the perfectly correlated value, which is expected because the semi-correlated relationship is based on the perfected correlation relationship, and the uncorrelated networks' effective permeabilities center around that of the constant network, which is expected because the uncorrelated relationship is based on the constant relationship. There is more variation between realizations using the semi-correlated relationship when compared to the uncorrelated relationship.

The observed difference between effective permeability values of the correlated/semi-correlated and constant/uncorrelated models demonstrates that correlation between fracture size and transmissivity influence the effective permeability of a DFN. Considering that the mean values of the fracture based transmissivities are the same and the distributions of the two stochastic models are nearly identical, cf. Fig. 7-1 (b), it appears that correlations between fracture size and transmissivity impact upscaled transport properties in a manner that cannot be known *a priori* when considering only the distributions of aperture and transmissivity. In other words, fracture network geometry also plays a key role in determining upscaled flow properties. *de Dreuzy et al.* (2004) observed similar results in two-dimension DFN simulations, but the impact on transport, which we consider in the next section, was not investigated.

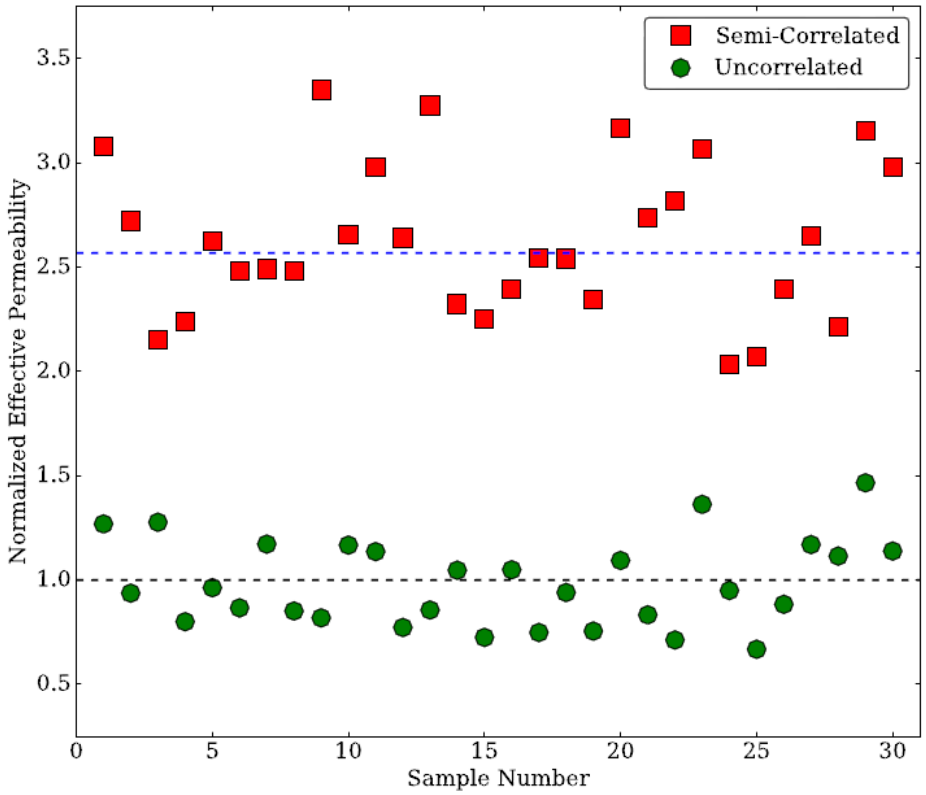

Figure 7-2. Effective permeability of the fracture networks. Values are normalized by the effective permeability of the constant fracture network for comparison (black dotted line). The effective permeability for the perfectly correlated model (blue dotted line) is 2.56 times that of the constant fracture network. Values for the uncorrelated model center around the value of the constant model. Values for the semi-correlated model are higher than the constant and center around the value of the correlated model and exhibit more variation than the uncorrelated model.

Travel Time and Transport Resistance Distributions: Figure 7-3 (a) reports the empirical cumulative distribution function (CDF) for the particle travel times (breakthrough curves). Figure 7-3 (b) reports the compliment of the cumulative distribution function (CCDF) on a log-log plot. Semi-translucent lines represent individual realizations and thick lines are the aggregate of all realizations for a given relationship. DFN with semi-correlated relationships are red, uncorrelated: green, correlated: blue, and constant: black. For comparison, time (ordinate) is rescaled by the 50% breakthrough of particles in the constant fracture network.

Breakthrough times for the correlated and semi-correlated networks are significantly earlier than those observed for constant and uncorrelated networks. Table 7-4 reports the 50% breakthrough times and exponent of a power law field to CCDF tail. The earliest breakthroughs are observed in semi-correlated networks and the latest breakthrough times are observed in the uncorrelated model. The aggregate values of the semi-correlated networks are very close to the correlated values, similarly for the uncorrelated and constant networks. This is not surprising however, because the semi-correlated relationship is based on the correlated and the uncorrelated relationship is based on the constant model. However, at early times the stochastic models have slightly earlier breakthroughs than their deterministic counterparts. This deviation is more pronounced in the uncorrelated/constant case. There are particular

realizations of the semi-correlated model where the 50% breakthrough is later than particular realizations of the uncorrelated model. While it is already known that the effect of transmissivity variability on the DFN scale can be significant, these distributions provide evidence that the effect it is increased when transmissivity is correlated with fracture size. The exponent of the power laws fit to the tail of the distributions are all approximately the same ≈ 2. These observations suggest that a correlated relationship between fracture size and transmissivity leads to earlier breakthrough time but the scaling of the distribution at later times is not significantly influenced.

Considering each fracture network as a homogenous permeability field with an effective permeability k_e, a straightforward calculation using Darcy's law shows that increase of effective permeability by a factor of 2.5, as reported in Table 1-3 for the correlated cases, results in a decrease of travel time by 60%, i.e., breakthrough in the higher permeability fields is 0.4 times the breakthrough in the lower permeability field. This analytical value is quite close to the observed values that are reported in Table 7-4 where the median breakthrough of particles in the perfectly correlated network is 0.34 times the breakthrough of that observed in the constant network. This similarity is not surprising because both the effective permeability and breakthrough curves are upscaled observables of the networks. However, the reported value is slightly smaller than what is expected analytically indicating that particles in the correlated networks move faster than what would be expected in an equivalent continuum representation.

Table 7-4. 50% breakthrough times and exponent of power law fit for particle travel time and retention parameter. Times are normalized by the 50% breakthrough time for the constant network.

Model	**Correlated**	**Semi-Correlated**	**Uncorrelated**	**Constant**
τ 50% Breakthrough	0.34	0.31	1.01	1.00
power law Exponent	1.95	1.90	2.00	2.18
β 50% Breakthrough	0.27	0.24	1.02	1.00
power law Exponent	1.87	1.84	1.96	2.18

In general, the CDF and CCDF of β are rather similar to those of τ and thus are not shown. There are a few differences worth commenting on however. The mean values of the semi-correlated networks is rather close to that of the correlated network, similarly for the constant and uncorrelated networks, but less so than for values of τ. Deviations of the stochastic models are more pronounced in the CDF of β than of τ. Distributions of β are more sensitive to changes in aperture than τ, because b is used in the computation of β. Therefore, variations in aperture along the pathlines are more reflected in plots of β than of τ, which likely leads to these deviations. At early times, the models that include a stochastic component have slightly earlier breakthroughs than their deterministic counterparts. All tails exhibit roughly the same power law scaling suggesting that the adopted fracture-size transmissivity relationship influences the early retention times more than long-term transport behavior in the DFN. Table 1-4 reports the 50% breakthrough times and exponent of a power law fit to CCDF tail, which are nearly identical to those reported for τ.

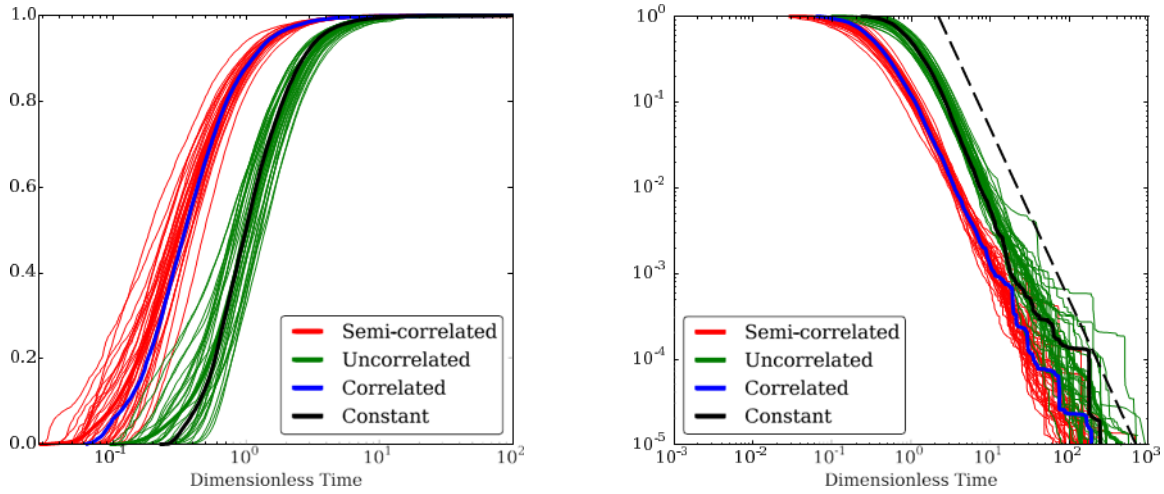

Figure 7-3. Breakthrough times (τ). Semi-correlated relationships between fracture size and transmissivity are red, uncorrelated: green, correlated: blue, and constant: black. For comparison, time on the ordinate is rescaled by the 50% breakthrough of the constant fracture network. (a) Cumulative distribution of travel times. Breakthrough times for the correlated and semi-correlated networks are much earlier than that observed for constant and uncorrelated. The earliest breakthroughs are observed in semi-correlated networks, and the latest breakthrough times are observed in the uncorrelated model. The aggregate values of the semi-correlated networks are very close to the correlated values, similarly for the uncorrelated and constant networks. (b) Compliment of cumulative distribution of travel times. All tails exhibit the similar exponents of power law scaling (Table 7-4) suggesting that the adopted relationship does not influence long-term transport behavior in the DFN. The dashed black line is a power law with an exponent of two.

Active Specific Surface Area: Although the distributions of τ and β are quite similar, their relationship with one another varies with the adopted size-transmissivity model. Figure 7-4 shows scatter plots of β as a function of τ for the (a) perfectly correlated model, (b) the semi-correlated model, and (c) the uncorrelated model. Values of τ and β are normalized by the median value of the constant model for comparison. The constant model is not included because $\beta = 2\ \tau$ /b, as b is constant. A linear model fits the data well; R2 greater than 0.9 for all size-transmissivity relationships. The specific surface area associated with each model is approximated by taking the median value of β / τ across all particles. Relative to the active surface area of the constant model, the active surface area of perfectly correlated model is 0.82 (variance of 0.003), 0.84 (variance of 0.02) for the semi-correlated, and 1.04 (variance of 0.02) for the uncorrelated models. In other words, the active surface area in the two correlated models is around 15-20% lower than the uncorrelated models. Such values indicate that size-transmissivity relationship could influence transport mechanisms like diffusion, retention and fracture-matrix exchanges because the active surface area available for these processes depends on the adopted model.

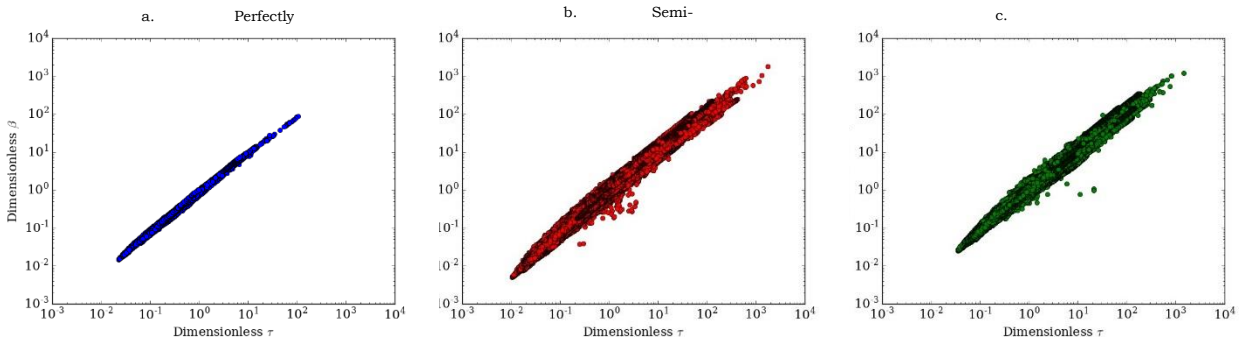

Figure 7-4. Scatter plots of β as a function of τ for the (a) perfectly correlated model, (b) the semi-correlated model, and the uncorrelated model (c). Values of τ and β are normalized by the median values from the constant model for comparison. Best linear fits to the scatter plots provide an estimate of the active specific surface area associated with each model.

Multiple Geometry Realizations: We generate thirty additional fracture networks using the same statistics (Table 7-1) and compare breakthrough curves assuming either a correlated or constant fracture size- transmissivity relationship. This results in an additional sixty flow solutions. These two relationships, correlated and constant, are selected because breakthrough curves of the semi-correlated and uncorrelated center around these values respectively, cf. Fig. 7-3. Therefore, general differences in overall flow and transport for the stochastic models in these DFN can be inferred by their deterministic counterparts.

Figure 7-5 (a) shows the CDF for the ten DFN realizations and (b) shows the CCDF. One hundred thousand particles are tracked through each DFN for both the constant and correlated cases. Time is normalized by the fifty percent breakthrough time of the aggregate constant breakthrough times. Semi-transparent lines are single realizations and thick lines are the aggregate of all realizations. Differences between realizations are more pronounced in the correlated networks. Similar to what is observed in Fig. 7-3, these plots indicate that including correlations between size and transmissivity results in significantly earlier breakthroughs than if correlations are not included. The aggregate 50% breakthrough time of the trajectories through correlated networks is about 50% faster than through the constant networks. The standard error for the 50% breakthrough time for the constant networks is 0.018 and 0.013 for the perfectly correlated indicating that the observed differences in 50% breakthrough times are not a result of an insufficient number of realizations. The CCDF for these curves is shown in Figure 7-5 (b) and demonstrates that these differences persist at later times. The dashed black line is a power law with exponent of two and shows that both relationships exhibit similar power law scaling suggesting that scaling of the distribution at later times is not significantly influenced by the adopted relationship. These plots demonstrate that the large discrepancies in travel times resulting from the adopted size and transmissivity relationships do not depend on the particular realization.

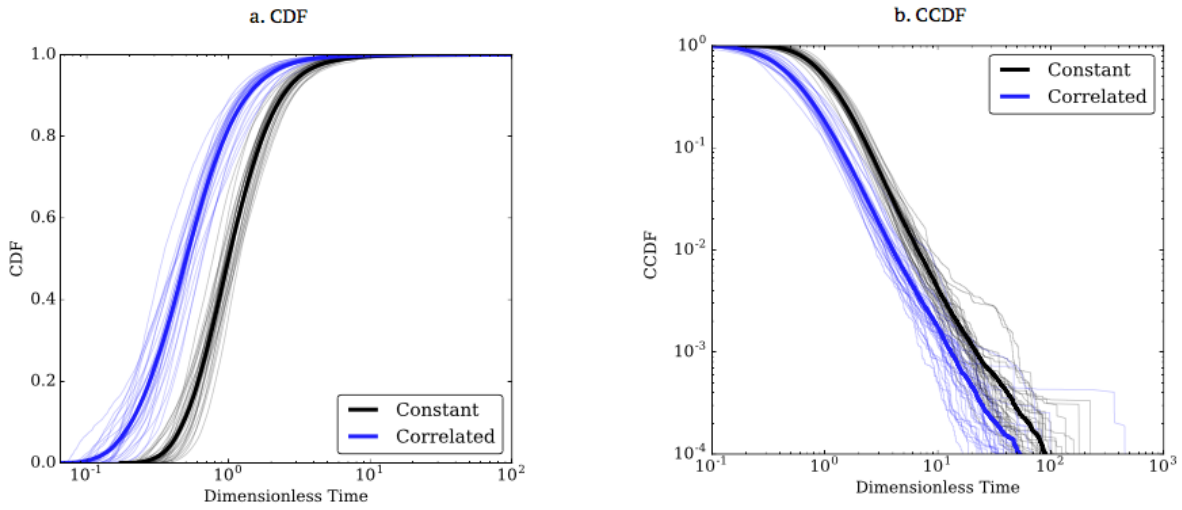

Figure 7-5. Breakthrough time distributions for thirty independent DFN realizations. Time is normalized by the fifty percent breakthrough of the aggregate constant breakthrough times. Semi-transparent lines are single realizations and thick lines are the aggregate of all realizations. For the same fracture network geometry, correlating transmissivity with size results in earlier breakthrough times when compared to simulations where no correlation is adopted.

7.2.4 Discussion

We have characterized the influence that selecting a particular relationship between fracture size and aperture has on flow and transport processes in a large-scale sparsely fractured three-dimensional networks. We compared four different fracture size-transmissivity relationships to investigate the potential impact that each model has on flow and transport. Comparisons are made in terms of the network effective permeability, transport properties including travel time, retention, active surface area, and fracture network backbone structure.

The principal observation of this study is that adopting a correlation between fracture size and transmissivity in a three-dimensional DFN can result in significantly earlier breakthrough times and higher effective permeabilities than if a correlation is not included. We also found that fracture network geometry has a stronger influence in determining where transport occurs within a sparsely fractured DFN network than the adopted relationship between fracture size and transmissivity, which controls the speed of flow and transport. The following list summarizes our key observations:

1. Even though the mean values of the fracture transmissivities are the same for all models and the distribution of transmissivities of the two stochastic models are nearly identical (Fig. 7-1) the perfectly correlated and semi-correlated relationships resulted in consistently higher effective permeability values than the constant and uncorrelated relationships (Fig. 7-2 and Table 7-3). These results suggest that correlations between fracture size and transmissivity influence upscaled transport properties in a manner that cannot be predicted by solely considering distributions of aperture and transmissivity due to the constraints put on the flow field by the fracture network geometry.

2. Breakthrough times for the correlated and semi-correlated networks are consistently and significantly earlier than those observed in the constant and uncorrelated models (Fig. 7-3, Table 7-4). These observations suggest that flow moves faster through the entire network when larger fractures are assigned higher values of transmissivity.
3. The distribution of particle travels times in the correlated and semi-correlated networks are very close, as are the constant and uncorrelated networks (Fig. 7-3 (a) and Table 7-4). This is not surprising however, because the semi-correlated relationship is based on the correlated and the uncorrelated relationship is based on the constant model. Models that include a stochastic component, semi-correlated and uncorrelated, have earlier breakthroughs than their deterministic counterparts.
4. The tails of the travel time and retention parameter distributions exhibit the same power law scaling behavior, with exponents that are close to 2 (Fig. 7-3 (b) and Table 7-4). This similarity suggests that the adopted fracture-size transmissivity relationship does not have a pronounced influence on long-term transport scaling behavior.
5. The active surface area, computed using τ and β, for the two correlated models is between 15 to 20% lower than the uncorrelated models. These differences could have significant impact on reactive transport modeling because the active specific surface area indicates the amount of surface area available for a dissolved solute.
6. Flow channeling occurs in all of the fracture networks. If correlations between fracture size and transmissivity are included, then it is more pronounced.
7. Fractures that make up the primary backbones of the networks are similar regardless of the adopted relationship between fracture size and transmissivity. Fracture network backbones are comprised of relatively large fractures that are primarily aligned with the direction of flow. These results indicate that the fractures where the majority of transport through the network occurs are primarily determined by the network geometry and the adopted relationship between fracture size and transmissivity is a secondary effect with respect to determining where flow occurs.

7.2.5 Conclusions

A possible explanation for the deviation between the models in terms of flow and transport observables is that the majority of flow and transport occurs in big fractures due to geometrical induced channeling. In the case of the perfectly correlated and semi-correlated models this channeling is further encouraged by the reduced resistance offered by the higher transmissivity values associated with these large fractures. This flow channeling results in higher effective permeability values and faster breakthrough times for these two relationships. Another possibility is that including a correlation between fracture size and aperture influences the overall fracture volumes, which could partially account for the observed differences. In the case of the correlated relationships, the total volume of the fracture network is higher than the uncorrelated, averaging $1.5 \cdot 10^{-4}$ [m^3/m^3] compared to $1.2 \cdot 10^{-4}$ [m^3/m^3]. Recall that the mean transmissivity and P_{32} values were constant between realizations, but not total fracture volume. This difference can thus explain some of the differences between the breakthrough curves. It is more likely that the increased volume of the large fractures, resulting in higher transmissivity in the principal flow regions, is more responsible for the differences, than the overall increase in volume fraction.

Within any DFN simulation several assumptions and conceptualizations have to be invoked. For this study, we assumed that: fracture aperture is constant within each fracture, transmissivity is controlled by the cube of the aperture, a relatively low variability of transmissivity is considered, particles are inserted

according to flux weighting, the network is sparse, fractures are circles, fracture radii follow a truncated power law distribution with hard upper and lower cutoffs, and fracture centers are uniformly distributed. Some of these assumptions, such as uniform fracture aperture; network sparsity; and the adoption of the cubic law, could influence the magnitude of the observed differences due to adoption of a particular size-aperture relationship. For example, it is possible that discrepancies between size-transmissivity models might be exacerbated/reduced if different aperture-transmissivity relationships are considered. The adoption of the cubic law has been shown to influence the computation of τ and β (Cvetkovic et al., 2004; Cvetkovic and Frampton, 2012) and combining our results with those of Cvetkovic and Frampton (2012), who found that adopting the cubic law can lead to early breakthrough up to 4 times faster than those obtained using the quadratic law, it could be possible that the same fracture network geometry could produce mean breakthrough times that are an order of magnitude different from one another, e.g., a perfectly correlated model using the cubic law compared to a uncorrelated model using the quadratic law. Whether these assumptions combine in a linear or non-linear fashion is an open area of research. A better understanding of both the hydraulic relationship between aperture and transmissivity and size-transmissivity relationships and their joint sensitivity is imperative for robust modeling using discrete fracture networks. Similarly, although Makedonska et al. (2016) found that in-fracture variability had little effect on global transport properties in similar networks it is possible that different internal aperture structures representative of various physical processes such as channelization of apertures due to erosion, could have more significant impacts when combined with a correlation relationship between size and aperture. Furthermore, our problem setup was designed so that distributions of transmissivity were identical, albeit with low variance. While the similarity between the constant and uncorrelated networks under such setup is not terribly remarkable, it is remarkable that a single fracture network geometry with identical transmissivity distributions (Fig. 7-1) but different size-transmissivity correlation relationships can produce differences of mean breakthrough times that can be up to half an order of magnitude different. While it is already known that the effect of transmissivity variability on the DFN scale can be significant, this study provides evidence that the effect is increased when transmissivity is correlated with fracture size.

Regardless of the assumptions made here, the observed differences between transport properties serves as a warning for DFN modelers. If fracture network statistics are such that geometrically induced flow channeling through a few large fractures parallel to the primary direction of flow are common, then the differences resulting from the use of different fracture-size transmissivity relationships will likely be more pronounced than networks where fractures sizes are relatively uniform. Thus the DFN modeler should take care to not only consider the distribution of transmissivities in the network, but also the distributions of fracture size, transmissivity, and orientation relative to the flow domain if they want different size-transmissivity relationships to result in similar flow behaviors. In the absence of good estimates of aperture (T) distributions, then using flow measurements is the only viable option to calibrate DFN parameters. Another project comparing these models using data from the Laxemar site, similar to the study of Frampton and Cvetkovic (2010), could help shed light on the variations induced by adoption of one these models. However, calibration of model parameters by matching specific capacities and flow has resulted in higher values of mean transmissivity for uncorrelated models when compared to correlated models (Joyce et al., 2014; Follin et al., 2014). The calibrated values resulted in a significant difference of mean log transmissivities between models. In light of the findings reported here, the higher values likely compensate for the increased flow channeling encouraged by the correlated relationships by globally increasing the transmissivity of the entire model to match flow parameters. While this modification might decrease the difference between model outputs in terms of effective permeability and breakthrough curves, the absence of a physical reason for these higher permeabilities warrants further consideration. If there are aperture distributions to match against flow as well, an analysis similar to that presented here could be used to determine which correlation model is most plausible for a given site. Explicitly, when trying to honor aperture (T) distributions, it may not be possible to also match observed flow properties, which would identify poor quality models.

The prevalence of flow channeling indicates that there is a large percentage of these sparse networks which is fairly stagnant, and that percentage is increased when a correlation between size and transmissivity is included in the model setup. The transport of solutes in these stagnant regions could result in increased matrix diffusion, retention and fracture-matrix exchanges due to the additional amount of time that solutes would remain there. Therefore, it is not unreasonable to expect that reaction of a solute with the fracture walls would be highly variability throughout the network and that variability would depend on the assumed correlation between size and transmissivity. Through the use of particle tracking methods and the analysis tools used here it should be possible to identify these flow channeling pathways, as well as their compliment, to potentially investigate their field relevance and perhaps identify them a priori for a given hydraulic setup. The approximation of active surface area was a first step in this direction and we are currently designing additional studies to investigate such properties.

7.3 ANALYSIS AND VISUALIZATION OF DISCRETE FRACTURE NETWORKS USING A FLOW TOPOLOGY GRAPH

7.3.1 Introduction

We present a method for the analysis and visualization of constrained flow networks driven by applications in computational simulation of fluid flow and transport in fractured rock. Determining how subsurface fractures control flow and transport has various applications in engineering and scientific endeavors including hydrocarbon extraction, aquifer storage and management, geothermal energy extraction, environmental restoration of fractured rock contaminated sites and the disposal of spent nuclear fuel (Middleton et al., 2015; National Research Council, 1996; Neuman, 2005). Figure 7-7 shows a caricature of flow and transport in fractured porous media.

Discrete fracture networks (DFN) are one methodology that computational subsurface scientists use to simulate fluid transport within such fracture networks. Although DFN models were introduced over two decades ago, they are fairly novel to the visualization community. The need for this collaboration between the visualization researchers and geoscientists is the result of recent developments in the DFN community where three-dimensional fracture networks consisting of tens of thousands of fractures are now common. Accumulating local and global transport statistics such as the distribution of traversal times, velocities, and tortuosity of advected particles is not terribly difficult, but the analysis of these flow features and determining their relation to properties of the simulation domain is a demanding task. The large amount of data resulting from these physics based simulations has created a need for advanced analysis and visualizations techniques to more efficiently process and interpret model outputs. Our team has addressed this need by developing, implementing, and testing a new visualization workflow.

We identified three areas of analysis research needed by geoscientists concerned with flow and transport in fractured media: statistical analysis, topological path analysis, and topological trace clustering. Figure 7-6 shows an outline of the methodology we developed, which is described in this paper, to address these needs. Using particle trajectories in the DFN (Left) we build a flow topology graph (FTG) (Center Top) that embeds information about transport through the fracture network into a graph. This representation enables us to develop and use graph analytics based algorithms, which combine feature and statistical analysis, to analyze the simulation output. The analysis results are stored in the FTG and are used to generate geometry files and statistical plots which can be explored by the user (Right). Using this information, we evaluate and refine the FTG analysis to investigate specific features of flow and transport through each DFN (Center Bottom). Embedding analysis from the FTG directly into geometry files for the DFN allows for integration of the FTG data with standard visualization tools. Furthermore, these tools allow for the identification of backbones in the DFN, which are connected subsets of fractures on which a majority of flow and transport occurs.
The key contributions of this methodology development are:

- Advanced visualization for the analysis of fluid transport in DFN simulations.
- The direct transformation of the simulation results to a flow topology graph (FTG) with one-to-one correspondence with DFN geometry.
- A novel graph analysis algorithm for detecting back- bone paths on FTG.
- A new algorithm for clustering particle trajectories based their path topology that can be used to identify and quantify flow channeling within the DFN.

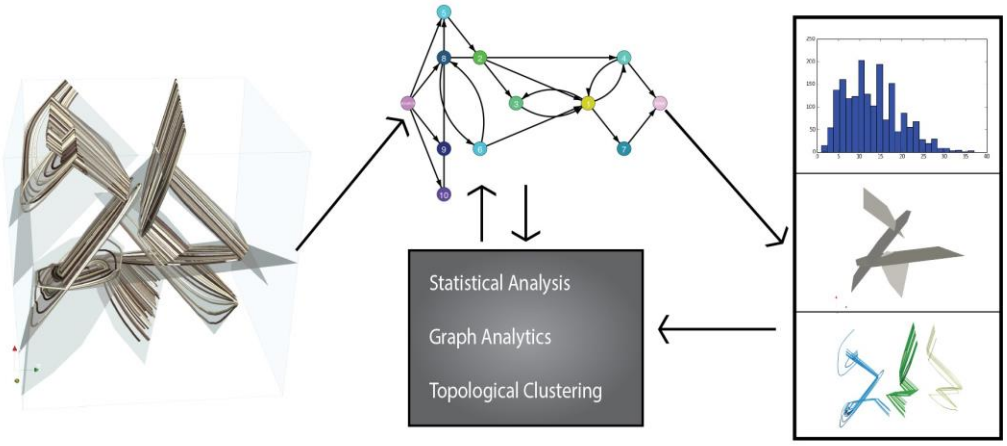

Figure 7-6. Overview of our analysis and visualization methodology. (Left) Transport through a discrete fracture network (DFN) is simulated using particle advection through a steady-state flow field. (Center Top). Pathlines obtained in the transport simulation are used to construct a flow topology graph (FTG) that embeds flow and transport information into a graph. (Right) Analysis of the FTG using statistics, graph theory, and topological clustering provides detailed information about various features of interest. Using this information, we can evaluate and refine the FTG analysis to investigate specific features of flow and transport through each DFN (Center Bottom).

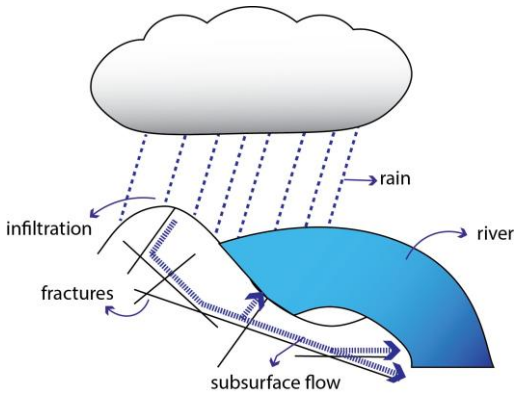

Figure 7-7. A caricature of a two-dimensional fracture network embedded within impermeable rock. Fractures are the principal pathway for flow and transport through low-permeability rocks in the subsurface. Beyond the difficulties associated with determining flow and transport within such networks, efficient and effective ways for the analysis of the data sets produced via such simulations are still lacking. Existing general data analysis and visualization methods must be specialized for the needs of particle tracking through fracture network data.

7.3.2 Analysis and Visualization of DFN

Using the FTG representation, we provide a workflow that produces three types of analysis products for DFN, namely statistical analysis, path analysis, and topological clustering. Statistical analysis can be used for debugging and to compare multiple fracture networks based on the same geological distributions to address questions of ergodicity and resolve global and local trends in the flow field. Path analysis allows us to use a Lagrangian viewpoint to find features in the flow field and link them to the fracture geometry. One key feature of interest within a DFN are backbones, which are connected subsets of fractures on which a majority of flow and transport occur. Backbones are believed to be responsible for flow channelization in fractured media, where flow is concentrated in certain regions of fractured rock, and have been qualitatively identified (Hyman et al., 2015b; de Dreuzy et al., 2002). In this section, we provided a systematic methodology to identify them using the FTG. We describe a method of topological clustering to group particles which take similar paths through the network. This clustering allows us to better visualize and segment particle traces as well as verify backbones defined using path analysis.

Statistical Analysis: The construction of each DFN is stochastic, relying on randomly sampling known distributions of fracture size, orientation, aperture and shape; multiple realizations of a given site must therefore be created. Statistical analysis can be used to verify that an ensemble of fracture networks with different topologies, but modeling the same formation of rock, produce similar results. Sampling constraints in both time and space limit what experiment data can be obtained in the field; local measurements of key phenomena are not possible throughout a site. Therefore, upscaled quantities, are used for verification of flow and transport simulations at site specific locations. Statistical analysis can also be used to compare transport behavior on selected sets of fractures or paths (such as backbones) to global transport for the system.

By appending fracture and intersection attributes as well as statistics to the FTG for a transport simulation, we can readily accumulate global statistics for a single DFN, a local subset of the DFN, or multiple realizations. While global statistics are important for comparison between transport simulations, localized statistics taken from a subset of the network are useful for characterizing specific flow attributes. For example, the user can segment the parts of the network that are never reached by particles, find the set of fractures responsible for the fastest or slowest transport times, or segment the DFN into topological layers by finding all fractures where particles must travel through at least N fractures before entering.

Several attributes are stored in the FTG that are of interest to the domain experts analyzing the transport simulations of a DFN. Per-fracture attributes include the size; topological distances (E^i, S^i); the number of transported particles ($|P^i|$); and mean fracture tortuosity ($\bar{T}^i$). For each particle, we store both per-fracture and total transport time, path length, velocity, and particle tortuosity (T_j). For these integral values, we are also interested in how they change as particles traverse the network. To accomplish this investigation, we parameterize the derived values for each particle over time, trace-path length, and topological distance. For example, in Figure 1-9 the tortuosity is shown for all particles in a simulation that uses the DFN shown in Figure 1-8. In the top plot of Figure 1-9, the maximum path length for all particle trajectories is calculated L_{max}, and then divided evenly by the number of sample points. We parameterize each trajectory and sample the tortuosity starting at these points along the curve, discarding trajectories that have a shorter overall path length than the sample point. The result is a two-dimensional histogram, which we display as a heat map, in shades of blue. In addition, the mean tortuosity curve is plotted in green, and the number of particles sampled at that point (the occupancy) is plotted in magenta. When plotting the results, we add a negative value to the distances that indicates the path length to the exit, as opposed to from the source. We can interpret from these plots that the

farther a particle travels through the DFN, the more direct its path towards the exit becomes. In the bottom plot, the change in fracture tortuosity over topological distance to the exit, E^i, is shown. This parameterization is necessarily much coarser, and the number of fractures at each distance is given for reference. From this graph we show that fractures closer to the DFN exit, provide a more direct path.

Most often the statistical data is displayed by producing plots and graphs, however we also allow the user to directly visualize these distributions on the original geometry. For large DFN, rendering the entire network using a colormap to identify attributes is less useful, due to occlusion. However, this method of visualization is still relevant when applied to meaningful subsets of the DFN.

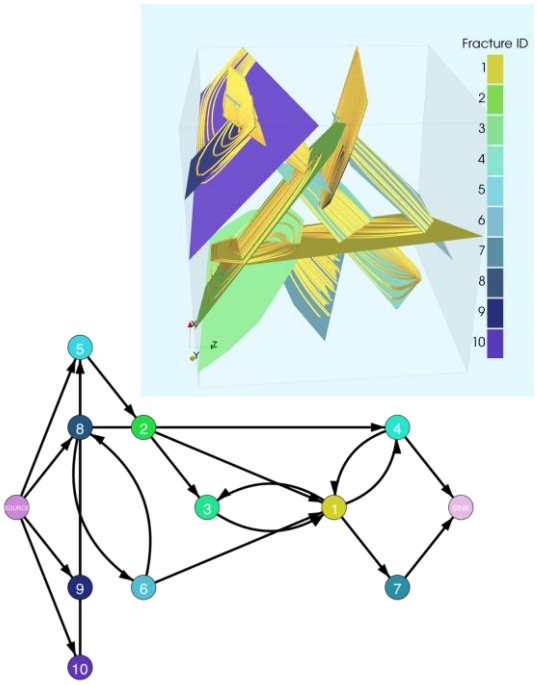

Figure 7-8. The flow topology graph (FTG) derived from the transport simulation. In the FTG each fracture polygon is represented by a vertex in the graph. Each edge represents particles that travel between two fractures over an intersection. We also add a "SOURCE" and "SINK" node (at the far left and right respectively) to the FTG from which all particles enter and exit.

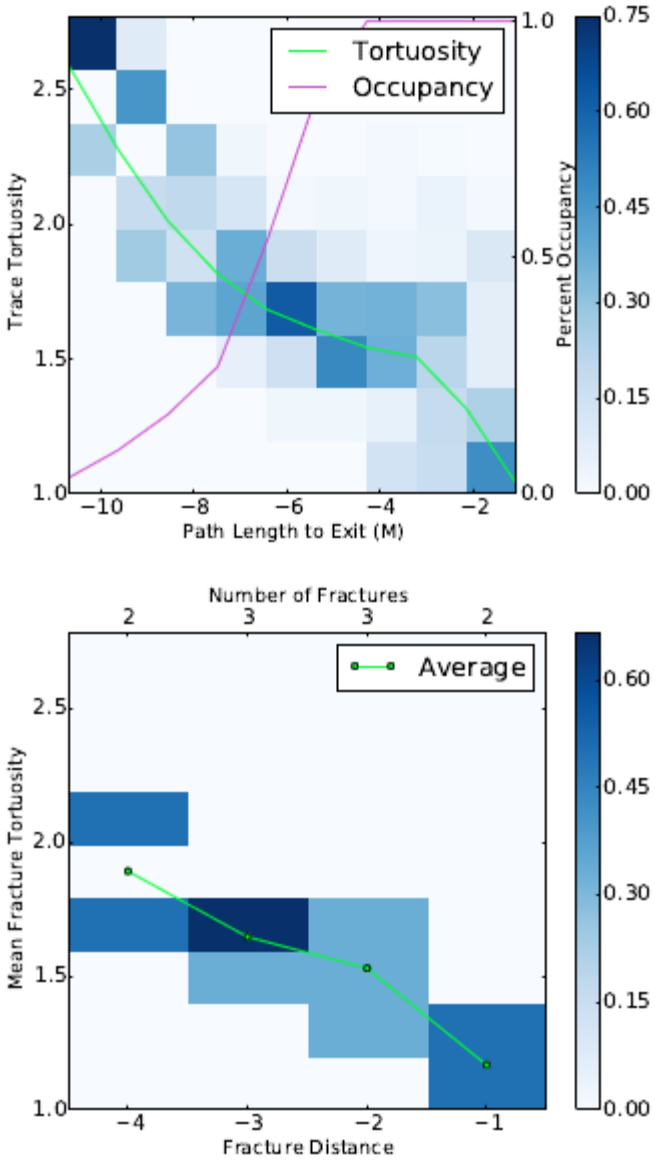

Figure 7-9. Plots of statistical qualities from a transport simulation in a DFN made up of ten fractures. Around 150 particles are advected through the DFN to produce these statistics. (Top) A blue heat map represents the two-dimensional histogram of tortuosity values sampled at discrete path lengths along particle traces (blue gradient), as well as the mean curve (green). The particle occupancy, or number of particles in the system at each sampled point is also shown in magenta. The coarseness of the plot is due to the simplistic nature of our example. (Bottom) Particle tortuosity distribution are sampled over topological distance indicating that as particles reach fractures closer to the exit, they take more direct, less tortuous, paths.

Topological Trace Clustering: Visually differentiating large numbers of integrated paths leads to an occlusion problem. A common approach to resolve this issue is to compare traces using a similarity metric and then apply a clustering algorithm to associate them with groups in accordance with their similarity. Once split into groups, particle traces can be visualized either through rendering each group in a different color, by rendering a smaller but representative subset of the particles, or a combination of both techniques. This allows users to better understand the coherency between particle

traces and observe trends in the flow field or network. Previous research has focused on defining similarity metrics by properties of the curves themselves, such as curvature (McLoughlin et al., 2013), shape (Yu et al., 2012), or statistical distributions (Lu et al., 2013). However, similarity in shape or structure of individual trajectories is less important for our application.

We define a similarity function using network topology in terms of the ordered set of fractures each trace traverses. By representing the trace path of a particle using the ordered set of fractures that it visits while traversing a DFN, and comparing the paths each trace takes through the FTG the similarity of traces can be readily computed. Explicitly, any two traces that travel on the same ordered set of fractures are considered topologically equivalent when clustering. Similarly, if two particles have nearly the same trace path, deviating only slightly in the fractures they traverse, then they will be considered to have small distance value between them. Finally, if two particles have completely different trace paths then they will be assigned a very large or infinite distance.

This trace distance function is inspired by the Levenshtein distance function for string-based comparisons (Levenshtein, 1966). The Levenshtein distance function finds the shortest edit distance between two strings by recursively comparing the ordered set of characters in the string and produces the minimum number of changes needed to convert one string into the other. The possible changes include insertion, removal or replacement of single characters. For example, when comparing 'skip' and 'sip' or 'show' and 'slow', the Levenshtein distance is one in both cases (a removal and a replacement, respectively). Wilson et al. (2004) used an adaptation of this metric to compare spectral representations of graphs. We have adapted this algorithm by considering strings of fracture IDs, F_i, representing the trace paths of particles, rather than strings of characters. For example, a particle could have the trace path, $\{F1, F3, F10\}$, which would indicate that it entered the DFN on fracture $F1$, was transported to fracture $F3$ and exited the DFN through fracture $F10$. A pseudocode implementation of the distance function is given in Algorithm 1.

The major difference between our algorithm and the original is the use of a topological cost function for making edits; $\phi(i, j)$ in Algorithm 1. In the Levenshtein distance, all edits are given a cost of 1, while we calculate the cost of replacing fractures in a trace path using the topological distance information encapsulated by the FTG. We define the cost function for replacing a fracture, F_i with another fracture F_j, $\phi(i, j)$, to be the number of edges in the shortest path from vertex v_i to v_j in the associated FTG. In other words, the replacement cost is represented by the minimum number of fractures that would be traversed for a particle on F_i to reach F_j. If no path exists in the FTG, then $\phi(i, j)$ = infinity. This definition also implies that the cost of insertion or deletion of a fracture is 1. This can be explained as follows: if there existed two trace paths, $R_a = \{F_a, F_b, F_c\}$ and $R_b = \{F_a, F_c\}$, then the FTG would have to contain edges $e_{a;b}$, $e_{a;c}$. Therefore, the cost to either remove F_b from R_a or add it to R_b is 1, as that is the minimum distance between the associated vertices. The resulting algorithm uses a recursive function that returns the minimum cost.

Algorithm 1 Trace Distance Function

Let R_a be the ordered set of fracture ids, F_i, for trace a

Let $|R_a|$ be the number of fracture ids in R_a

Let $R_{a|k}$ be the k_{th} fracture id

Let $\phi(F_i, F_j)$ be the cost function for replacing IDs s.t.

$\phi(F_i, F_j) \equiv$ the shortest path from v_i to v_j in the FTG

Initially $L_a \leftarrow |R_a|$

Initially $L_b \leftarrow |R_b|$

procedure TDF(R_a,L_a,R_b,L_b)

if $L_a = 0$ **then**

return L_b

end if

if $L_b = 0$ **then**

return L_a

end if

if $R_a|_{L_a} = R_b|_{L_b}$ **then**

$RC \leftarrow 0$

else

$RC \leftarrow \min(\phi(R_a|_{L_a}, R_b|_{L_b}), \phi(R_b|_{L_b}, R_a|_{L_a}))$

end if

return MIN(

TDF(R_a,$L_a - 1$,R_b,L_b) +1,

TDF(R_a,L_a,R_b,$L_b - 1$) +1,

TDF(R_a,$L_a - 1$,R_b,$L_b - 1$) +RC

)

end procedure

To identify trace clusters given their mutual distances, we use the agglomerative hierarchical clustering (AHC) algorithm (Defays, 1977). This is one of the most commonly used method for clustering path traces and other integral curves (Salzbrunn et al., 2008; Pobitzer et al., 2011; McLoughlin et al., 2013; Yu et al., 2012; Lu et al., 2013). AHC builds a hierarchy by recursively merging pairs of clusters (initially each trace being its own cluster), until all clusters are merged. The resulting hierarchy can then be 'cut' by setting a maximum distance value for pairs of particle traces included in the same cluster. This gives the user control to define how similar the paths of particles must be. In practice we choose several distances and allow the user to select the most appropriate one during exploratory visualization.

In Figure 7-10(a) we show the results of our clustering algorithm for the ten-fracture system 2. Here, each cluster is rendered in a unique color. In Figure 7-10(b) we show only the two largest clusters to emphasize the paths taken by traces in each group. In particular, the largest (yellow) cluster consists of particles that take similar, but not the same, path through the network. We note that the largest clusters lie primarily along the *backbone* path shown in Figure 7-10. By grouping and then visualizing large clusters of particles that take similar paths through the network, users are better able to observe and differentiate areas where channelization occurs. If a larger number of clusters is seen, then a single representative trace of each cluster will be rendered to further reduce occlusion retaining key information. The representative trace is chosen at random from particles which take the most common path in the cluster.

While our algorithm on its own performs well and produces clusters as expected, we have included two optional modifications to accommodate specific needs of DFN simulations. First, we allow users to disregard cycles in the fracture path by collapsing them in the trace path i.e., $\{\ldots, F_a, F_b, F_c, F_d, F_b, F_e, \ldots\} \rightarrow \{\ldots, F_a, F_b, F_e, \ldots\}$. In the context of a DFN, this corresponds to a particle that leaves a fracture, but later then returns to it and continues to travel therein.

The second modification accounts for potential bias due to initial conditions. To do so, we disregard the first several (typically 1 to 3) fractures in the trace path when computing clusters. Disregarding the first fractures in a trace path limits the influence that the initial seeding has on clusters by allowing particles to initially disperse/coalesce in the system prior to being subject to analysis. Hyman et al. (2015b) observed that is took particles uniformly distributed across an inlet plane 250 meters before they exhibited strong flow channeling characteristics. Trimming initial fractures is an optional step in the clustering algorithm and only useful for certain use cases and under certain initial conditions. However, it provides flexibility for domain experts.

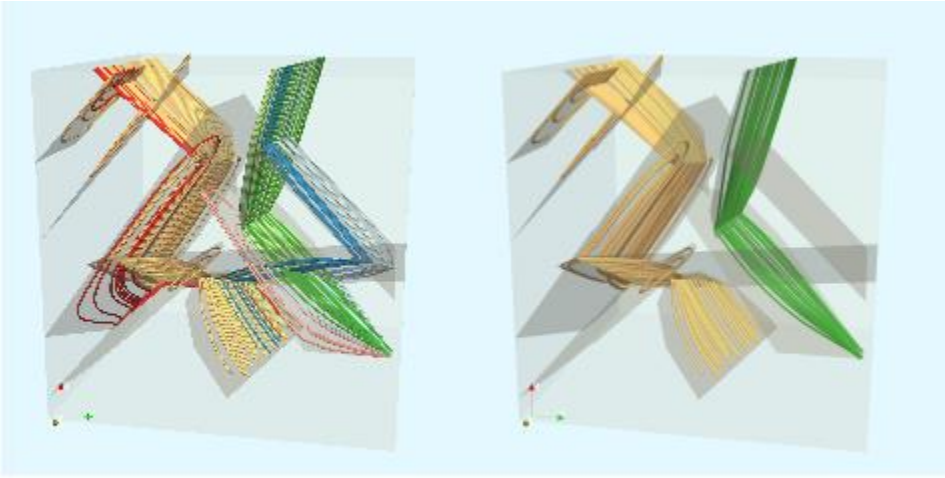

Figure 7-10. We use agglomerative hierarchal clustering to segment particles which take similar topological paths through the network. For this DFN the clustering is readily apparent, and each cluster is rendered with a unique color. In (b) we show the largest two clusters emphasizing that clustered particles take similar paths while traversing the DFN.

By visualizing the large clusters of particles, channelization becomes more apparent. This is an important tool for validating the candidate backbones and observing the global behavior of the flow network.

Analysis Driven Visualization: Exploratory visualization of the analysis results produced by our framework plays an integral role in evaluating the results of a DFN simulation. We have chosen to decouple visualization from the analysis process to maintain both flexibility and interactivity. Statistical plots are produced directly from the FTG using python scripts that generate plots either for the entire system, a subset of fractures representing candidate backbones, or sets of clustered particles. These plots can be combined and overlaid for comparison purposes. This is especially useful for comparing multiple simulated data sets. While we provide predefined python- based scripts to produce these plots, custom plots can also be created. Direct geometric visualization is handled through embedding analysis results directly into geometry files for both the DFN and particle traces. The one-to-one mapping between the FTG and DFN allows us to add per-fracture attributes to the DFN geometry files. Similarly, the statistical and clustering information for each particle is added as an attribute to the trace geometry files. To allow users to explore the results of parameter value changes, we sample a selected parameter space and embed all of the results into the output files. For example, when generating clusters, we select multiple minimum distances to cut the agglomerative clustering hierarchy and allow users to select from clusters generated at each level. The number of cuts and minimum distance are user-defined options. By default, the mean distance between particles is used as a base. Five subsequent cuts are also made by linearly sampling between the mean distance and one-tenth that distance. The candidate backbones are embedded in two different ways, to aid users in identifying the most meaningful ones. Paths can be selected by the method and order that they are extracted or by the amount of flow occurring on each. The former allows users to better understand why the algorithm produced each candidate path and the latter gives a more natural ordering of the candidates. Individual traces and each fracture on a selected path retain their statistical properties along with cluster information. This allows each feature to be compared visually and the selections can be used to generate plots for the subset.

The decision to decouple visualization from analysis, rather than integrating both steps into a custom tool, makes possible the use of many standard visualization tools, such as the Paraview data analysis and visualization platform (Ahrens et al., 2005). Our target user group, computational geoscientists studying flow in DFN simulations, preferred to leverage preexisting tools that they are already familiar with. By using well-maintained visualization tools, we ensure easy use and that the analysis tools can remain usable without support for a new software interface. Furthermore, by encapsulating the analysis methods in an offline process, large amounts of data can be processed. As the field continues to develop, DFNs are expected to become larger, more complex and are likely to require and increasing number of realizations to capture properties of the stochastic system.

We have a minimal set of requirements for visualization tools to effectively visualize the analysis files produced by our system. The first, and most important, is the ability to select subsets of data by setting thresholds for embedded attributes. This enables users to select particle traces by the cluster they belong to or the size of the cluster, and the particular cut in the hierarchy that the clusters are produced from. Thresholding also allows users to select candidate backbones by the method used and order in which they are extracted, or by the amount of flow occurring on each path. The second requirement is to overlay multiple geometry files using the absolute positions of vertices. Finally, the tool must allow users to apply colormaps to the geometry which corresponds to embedded per-cell attributes. Other features that we use to generate the examples provided in this section, though not necessarily required for analysis, include: rendering lines as tubes of varying thickness and assigning glyphs to represent points and vectors.

7.3.3 Examples

We demonstrate our methodology by analyzing the flow and transport in DFN simulations at various scales. We begin with a medium sized DFN made up of two hundred fractures. Then we demonstrate our approach in two sub- surface applications with networks made up of thousands of fractures. The first of these is used to study unconventional hydrocarbon extraction based on a shale formation in the Tuscaloosa, Alabama. The second DFN model is loosely based on a subset of fractures in Forsmark, Sweden (a potential host location for spent civilian nuclear fuel). We selected these two site characterizations because they highlight different transport scenarios. The primary direction of flow in the hydrocarbon extraction model is radial, towards a horizontal well at the center of the domain, while in the DFN based on the Forsmark site, the imposed pressure gradient drives flow in one primary direction aligned with the Z-axis. We also use the method to compare multiple DFN realizations based on the same statistical distributions.

Two Hundred Fracture network: We created a medium sized DFN of two hundred circular and rectangular fractures constrained to a 12-meter cubed domain. This network is used to demonstrate how the combination of statistical and visualization analysis allows us to characterize transport behavior for DFN. A pressure gradient is applied along the X-direction to create flow through the network and about 500 particles are used to simulate fluid transport.
Figure 7-11 shows three backbones identified in the network along with particle trajectories. Backbones are large fractures aligned with principal direction of flow. The backbone along the bottom of the domain, colored purple, is primarily a single large fracture while the other two are composed of several fractures. On the left, each path is represented by a different color and the clustered particles traveling along each path are represented by tubes whose colors indicate their cluster ID. On the right, fractures are colored by the mean tortuosity of particles on those fractures. The tortuosity values are close to one, indicating that particles traveling on these paths take a direct path towards the exit rather than dispersing into the rest of the network.

Figure 7-12 shows various particle based observables. Figure 7-12 (a) shows a scatter plot of particle density as a function of relation to the fracture area and reveals that a large percentage of transport in the network occurs on a single large fracture. Fracture radii are determined by sampling a power law distribution so there are a lot of small fractures and few large ones. There are a disproportionate number of particles on the largest fracture(s) when compared to the number of large fractures. Figure 7-12 (b) shows particle tortuosity and occupancy as a function of particle length from the exit plane, sampled at discrete points along particle traces. Most particles travel between 15 and 25 meters as they traverse the network; recall that minimum distance to traverse the cube is 12 meters. The tortuosity values indicate that most particles take a relatively direct path through the network. This is further emphasized by the graph in Figure 7-12 (c), which relates fracture tortuosity and the topological distance of each fracture from the exit. The graph also shows that the majority of particles travel along seven fractures or less and that after each transition to a new fracture their path becomes more direct towards the exit.

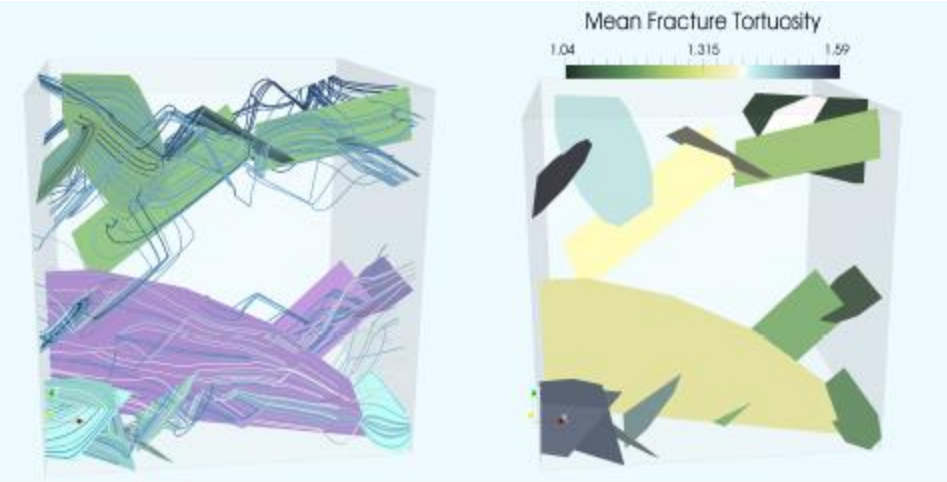

Figure 7-11. Three backbones in a 200 fracture network. On the left, each path is represented by a different color and the clustered particles traveling along each path are represented by tubes whose colors indicate their cluster ID. On the right, backbone fractures are colored by the mean tortuosity of the particles traversing these fractures (fracture tortuosity). The tortuosity values are close to one indicating that particles on the backbones take direct paths towards the exit, rather than dispersing throughout the network.

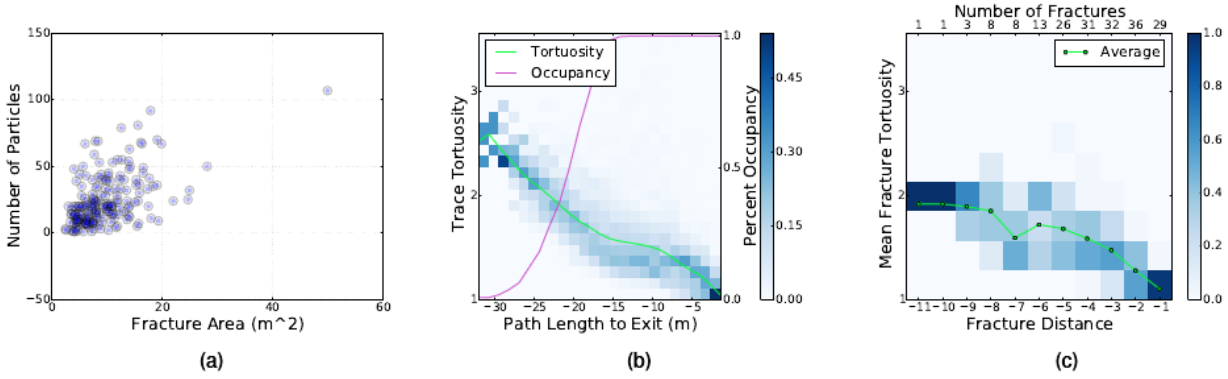

Figure 7-12. We produce statistical results based on the particle behavior in a 200 fracture DFN with around 500 advected particles. The scatter plot in (a) shows the number of particles that traverse through fractures of different sizes. This image indicate that particles are well distributed over fractures of different sizes, except for a single outlying fracture that is significantly larger than the rest on which a large portion of the transport occurs. We calculate a series histogram for the tortuosity by sampling particles at regular intervals of time, path length (b), or mean distance and topological distance (c).

Kilometer DFN of fractured granite: The Swedish Nuclear Fuel and Waste Management Company (SKB) has undertaken a detailed investigation of the fractured granite at the Forsmark site, Sweden as a potential host formation for a subsurface repository for spent nuclear fuel (SKB, 2011). We adopt a semi-generic subset of the statistical fracture model determined by SKB, details of the site

characterization are provided in (SKB, 2011). Our fracture model uses three fracture sets whose radii are determined by a truncated power-law distribution and varying orientations. The largest fractures have a radius of 560 meters and the smallest have a radius of 15 meters. An example network is shown in Figure 7-13 (a). The domain is a cubic kilometer and each realization contains approximately five thousand circular fractures. The fractures colored orange are not visited by a particle during the transport simulation; only 30% of fractures in the domain are touched by a particle during transport simulations. These results indicate that the strong flow channeling is occurring along backbones in the DFN. Figure 7-13 (b) shows the backbones of the network along with the largest particle clusters for verification. The backbones are made up of large fractures and the particle trajectories tend to arrive on a fracture in a backbone and remain then remain along that path.

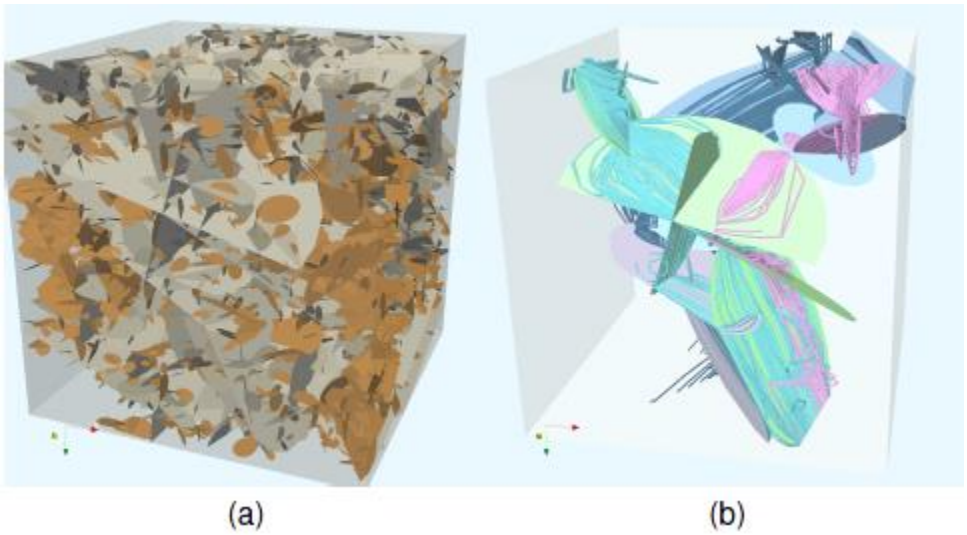

Figure 7-13. (a) A DFN realization based on the fractured granite at the Forsmark site in Sweden. The domain is a cubic kilometer and contains approximately five thousand circular fractures whose radii are sampled from a truncated power-law distribution. The fractures highlighted orange indicate that these fracture have not been visited by any particle during the transport simulation. (b) The backbones of the DFN along with the three largest trace clusters colored by the cluster ID. The backbones are primarily comprised of larger fractures that act as conduits for flow and transport through the network, as shown by the clustering of traces.

Network Comparison: DFN are generated stochastically and thus multiple realizations using the same underlaying statistics are required and these multiple DFN are compared to one another. This type of comparative analysis is desirable when trying to demonstrate ergodic behavior in upscaled transport distributions. For example, identifying universal fracture characteristics that lead to flow channeling, which is equivalent to particle clustering, requires numerous realizations. To demonstrate the utility of the proposed methodology in this regard, we compare networks generated using the same underlaying statistics. Comparisons between the networks are performed both visually and analytically to identify features and clusters in the networks.

Three independent DFN realizations based on the Forsmark site are created and the backbone of each network is determined, shown in Figure 7-14 (a-c). In the first and third realization, there is one large fracture that dominates transport through the system. In the second realization, shown in the middle, the backbone is made up of numerous medium sized fractures rather than a single large fracture.

The methodology allows us to characterize and identify the key fracture characteristics that lead to flow channeling. One possible use of this methodology is to identify the characteristics of the fractures that make up the backbone and then create reduced DFN models that retain these backbones but omit fractures that do not significantly contribute to transport.

Figure 7-15 shows the particle tortuosity and percent occupancy of particles for the three DFN realizations. Although the backbones are different, particle ensemble statistics appear to have stabilized. Observed tortuosity values all scale linearly with path length to exit and little variability is observed between realizations. However, there are discrepancies in the observed cumulative distributions of percent of occupancy. Most notable, at large distances from the exit plane. One realization has fewer particles with long distances from the exit plane, and this is likely the result of the large fracture that dominants the backbone of DFN, cf. Figure 7-14 (a). In general, we can use such statistical comparisons to ensure that any given realization of the network topology is equally valid. If there are major discrepancies between networks, we can use the feature analysis and clustering to determine where these differences stem from.

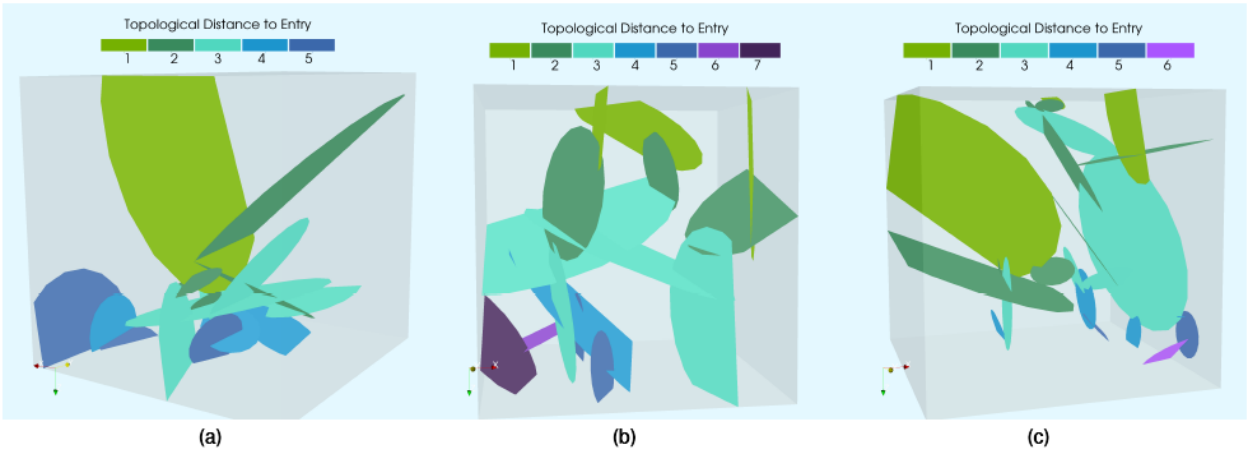

Figure 7-14. The backbones in three realizations of the DFN network topology, all modeling the same physical domain of the Forsmark repository site. Each network has different types of main backbones. This type of comparison, between DFN modeling the same physical site, is important due to the stochastic nature in which DFN are produced.

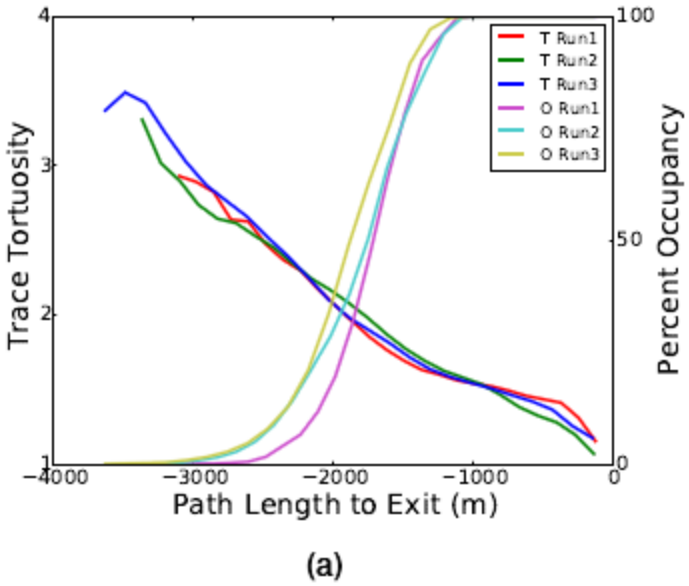

Figure 7-15. Particle tortuosity and percent occupancy of particles for the DFN used in Figure 7-14, which are generated by sampling the same fracture statistics. Similarities and differences in the curves can be explained by the backbone structures developed in each realization.

7.3.4 Conclusions and Future Work

We have introduced a flow topology graph method for the analysis of flow and transport in fractured rock that allows users to analyze simulated flow and transport in discrete fracture networks. Recent advancements in DFN simulation tools have made it possible to model and simulate flow at realistic scales with networks containing thousands of fractures. The methods presented here are part of a prototype system and toolset supporting the interactive, detailed exploration of simulated Lagrangian transport data. The methodology is both modular and flexible, allowing for rapid prototyping and modification of capabilities with changing goals and application needs. Visualization is decoupled from analysis, allowing users to interactively explore the results using tools they are familiar with.

Our FTG-based framework supports both global and localized statistical analysis, feature analysis for discovering channelization due to backbones, and intuitive clustering of particle paths in these large fracture networks. The methodology addresses the three main areas of analysis research identified by geoscientists concerned with flow and transport in fractured media: statistical analysis, topological path analysis, and topological trace clustering. The provided statistical analysis can be used to gain a better understanding of system-wide trends as well as identify potential problems in the simulation. The topological path analysis allows for the identification of important regions within the network, namely backbones, and allows for a systematic, integrative approach to identifying fracture characteristics that lead to flow channeling in fractured rock. The topological trace clustering identifies groups of particles that travel along similar paths and verify backbones. In combination, these tools can be used to identify geological structures that dictate flow and transport in the fractured rock. This characterization can potentially be utilized in the modeling of both static and adaptive control of subsurface processes, being relevant for areas including carbon sequestration, geothermal energy, contamination remediation, and unconventional oil and gas extraction.

While the results demonstrated with our prototype sys- tem are promising, it is important to note that more detailed case studies are needed to evaluate results more conclusively. More research needs to be

done concerning the establishment of better metrics for improved path analysis, topological trace clustering, and comparative analysis. We have identified several metrics that produce reasonable results, and we currently allow a user to select what set of metrics to use. More studies are needed to determine which ones are most meaningful for a given DFN application. This aspect is especially relevant when performing comparative analysis, where a proper metric for measuring similarities and differences between multiple realizations of a DFN is crucially important (ensemble simulation and analysis). We do not currently directly visualize the graph as part of our analysis framework. However, developing a scalable algorithm for laying out the graph, especially for quickly comparing between multiple FTG, is the focus of ongoing research. Allowing users to directly interact with the FTG, and highlight features that may be difficult to describe algorithmically is also a future goal. Similarly, directly linking statistical plots with the geometry in a painting and linking style will be considered for future systems. This would require a more customized system, and thus some flexibility in the visualizing tools would be lost, however the benefit may outweigh the cost. Currently our prototype system is used for performing data analysis in a post-processing step. Considering the increasing size and complexity of simulated DFNs, we will consider *in situ* use of our analyses. We have kept this goal in mind during the development of our prototype to minimize the amount of implementation that will need to be done when transitioning our system from a post-processing to an *in situ* analysis system.

7.4 TASK 9: INCREASING THE REALISM IN SOLUTE TRANSPORT MODELLING – MODELLING THE FIELD EXPERIMENTS OF LTDE-SD AND REPRO USING DISCRETE FRACTURE NETWORK MODELING

Task 9 focuses on the realistic modelling of coupled matrix diffusion and sorption in heterogeneous crystalline rock matrix at depth. This is done in the context of inverse and predictive modelling of tracer concentrations of the in-situ experiments performed within LTDE-SD at the Äspö HRL in Sweden, as well as within the REPRO project at ONKALO in Finland, focusing on sorption and diffusion. The ultimate aim is to develop models that in a more realistic way represent retardation in the natural rock matrix at depth.

7.4.1 Task 9A: Long-Term Diffusion Sorption Experiment (REPRO)

Here we focus on REPRO (**R**ock matrix r**E**tention **PRO**perties) experiment, which is presently carried out by Posiva at the ONKALO underground rock characterisation facility in Finland. Today, LANL team has all necessary modelling capabilities to simulate matrix diffusion processes observed during REPRO experiment: computational tool for producing high quality mesh, and control volume HPC flow solver for water phase diffusion and sorption study. In the current section we start from brief explanation of REPRO experiment, giving previously in Task 9 description (Löfgren, 2014), and continue with algorithm of high quality computational mesh generating process.

REPRO Experiment: The description of REPRO experiment is given in Löfgren (2014). A number of boreholes have been drilled into the non-fractured rock matrix from the REPRO niche at ONKALO underground rock characterisation facility, at about 400 m depth (see Figure 7-16). Borehole ONK-PP323 is utilised for the Water Phase Diffusion (WPDE) series of experiments, which are advection-diffusion-sorption experiments. They are carried out between ~18-20 m from tunnel wall. A 1.9 m long section has been packed off, and in this section a dummy has been placed. Its diameter is 54 mm whereas the borehole diameter is 56 mm, leaving a 1 mm gap between the borehole wall and the dummy. This gap is regarded as an artificial fracture of relatively well-defined geometry. In this gap a very low steady state water flow has been applied, directed towards the tunnel. This is achieved by injecting the water at the far end of the packed-off section, as shown to the upper right in Figure 7-16. In this water flow the tracers HTO, Na-22, Cl-36, and I-125 were injected in WPDE-1, and HTO, Na-22, Cl-36, Sr-85 and Ba-133 in

WPDE-2. Injection was made as a few hours long pulse at the far end of the experimental section. As the pulse travels with the water flow, its tracers will diffuse into the rock matrix. As the pulse passes, the concentration gradients are reversed and the tracers will diffuse out of the rock matrix and into the flowing water. To date, two experiments have been performed at different flow rates; WPDE-1 (20 µL/min) and WPDE-2 (10 µL/min). The tracer concentrations were measured in water flowing out of the experimental section, both by on-line Na(Tl)I-scintillation detection and by analysing water samples in the laboratory. Breakthrough curves have been obtained over half a year and about one and a half a year for WPDE-1 and WPDE-2, respectively. The rock volume surrounding the experimental section, affected by in-diffusion, is not planned to be overcored.

The Through Diffusion Experiment (TDE) will be carried out between three parallel boreholes situated perpendicular to each other, in 1 m long packed-off sections, at a distance of about 11 to 12 m from the tunnel wall. Borehole ONK-PP326 will be used as the injection hole and boreholes ONK-PP324 and ONK-PP327 as observation holes (see Figure 1-16, upper left corner). The distances between the boreholes are between 10 and 15 cm. Any advective flow between the boreholes is foreseen to be insignificant, as the experiment takes placed in a rock volume that lacks in water-bearing fractures. The tracers HTO, Na-22, Cl-36, Ba-133, and probably Cs-134 are planned to be injected. The decreasing and (foreseen) increasing tracer concentrations in the injection hole and observations holes, respectively, will be analyzed. This is done on extracted samples in the laboratory; by liquid scintillation counting and High Resolution GXRS (gamma measurements). Furthermore, on-line measurements will be performed in the injection hole and observation holes by a High Performance Germanium detector and a Na(Tl)I-scintillation detector, respectively. Tracer concentrations in the injection hole will be measured at a higher frequency at the first part of the experiment, while focus will be shifted towards analyzing breakthrough concentrations in the observation holes as the experiment progresses. Breakthroughs of non-sorbing tracers are foreseen within the timeframe of Task 9, although unexpectedly low pore diffusivities may prevent this from happening. The tracers were chosen to make overcoring and analysis of tracer penetration profiles possible, although this option is presently not included in the REPRO planning. As the REPRO project is on-going, it offers the possibility of both inverse and predictive modelling. The in-situ part of REPRO aims to tackle the topics of diffusion, sorption, anion exclusion, and rock matrix anisotropy. The laboratory part has, in addition, focused on small scale rock characterisation. This provides a wealth of input data that can be incorporated in the modelling.

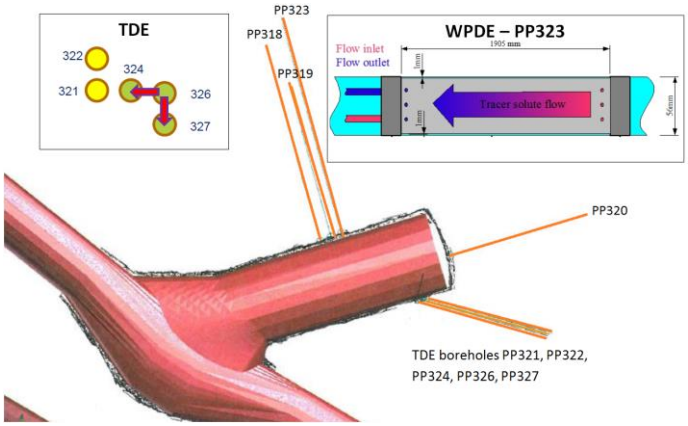

Figure 7-16. The REPRO niche at the 401 m level at ONKALO, and the nine boreholes drilled from the niche. Borehole PP323 is utilized for WPDE-1&2, and boreholes PP324, PP326, and PP327 for TDE.

Modeling of REPRO experiment. Phase 1: Producing high quality computational mesh on REPRO model: In order to simulate water and tracer sorption into rock matrix the high quality computational mesh is required. We use Los Alamos Gridding Tool (LaGriT, 2013), meshing capability developed at LANL, to produce three dimensional computational mesh.

A cube of size 1.9 m x 1.9 m x 1.9 m is generated for WPDE experiment modeling, where only one borehole, drilled into non-fractured rock matrix, is considered (Figure 7-17). First, the structured tetrahedral mesh is produced in the cube. Then, the hole of 56 mm diameter is created on the center of the cube (Figure 7-18, right panel). Producing the cylindrical hole, which represents the borehole in the rock, requires to reform the structural grid to unstructured circular grid around the borehole. The mesh of the borehole is generated separately (Figure 7-18, left panel). The cylinder of 54 mm diameter represents the filled with dummy borehole. The last step is to merge three dimensional unstructured mesh of the cylinder with the cube, generating 1 mm meshed layer between dummy filled borehole and the rock matrix.

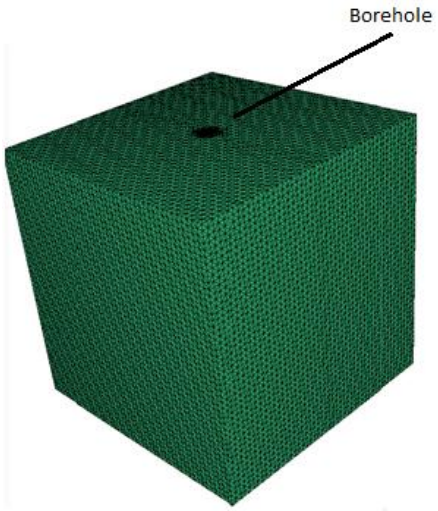

Figure 7-17. The cube with 1.9 m side length is generated with structured tetrahedral mesh. The borehole is modelled in the center of the cube along the z direction.

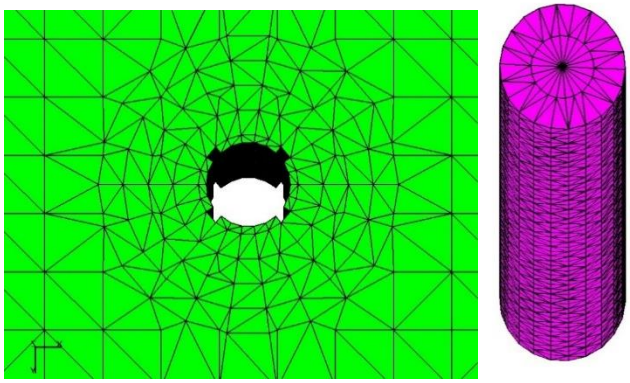

Figure 7-18. The first two steps of computational mesh generation for WPDE experiment modeling. On left side the part of the cube is shown, where the unstructured cylindrical mesh is merged to structural mesh of the cube, and the cut of the cylindrical hole is in the center of the cube. The right panel shows the cylindrical mesh created separately.

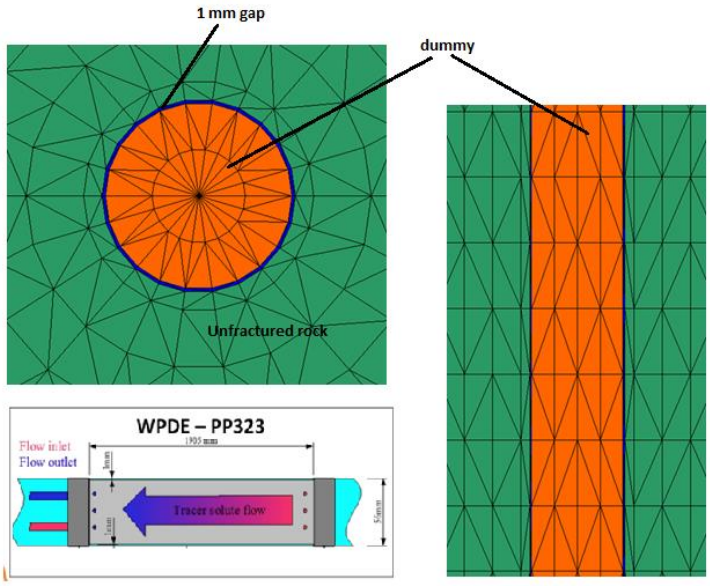

Figure 7-19. The final computational mesh for WPDE experiment modeling.

The final mesh for WPDE modeling is shown in Figure 7-19. The right upper panel shows the top view of the borehole inside the rock matrix. The dummy (orange mesh) is surrounded by 1 mm meshed layer (blue), representing gap between dummy and non-fractured rock. This layer will be used for applying boundary conditions and obtaining steady state water flow solution, as well as the source of tracer injections (as it is shown in figure 4 right bottom panel or Figure 7-16 right top panel). On the left panel in Figure 7-19 the cross section along the borehole in z direction is shown: dummy is colored by orange, 1 mm layer is blue and structured mesh of surrounding rock is colored by green. The final mesh consists of 2450 nodes and 11515 tetrahedral elements.

Similar procedure is applied to generate the mesh for TDE experiment, where three boreholes are considered in non-fractured rock. Figure 7-20 shows the top view of the parallelepiped, initially meshed structurally, with three cylindrical holes in it, where the distance between cylinder centers is 0.15 m. The meshed separately cylinders are merged into the parallelepiped creating a 1 mm layer around each borehole. Figure 7-21 (right panel) shows the whole mesh with three boreholes, which represent ONK-PP326, ONK-PP324, and ONK-PP327 boreholes in TDE experiment (Figure 7-21, left panel). Figure 1-22 shows the cross section along the boreholes and zoom in on borehole mesh, where the region filled with dummy is separated by 1 mm layer from the rock matrix. The entire mesh consists of 133650 nodes and 740174 tetrahedral elements.

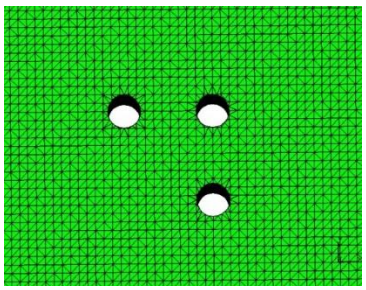

Figure 7-20. The top view of parallelepiped of size 0.7m x 0.7 m x 1.9 m. Three cylindrical holes are cut in 0.15 m distance between centers.

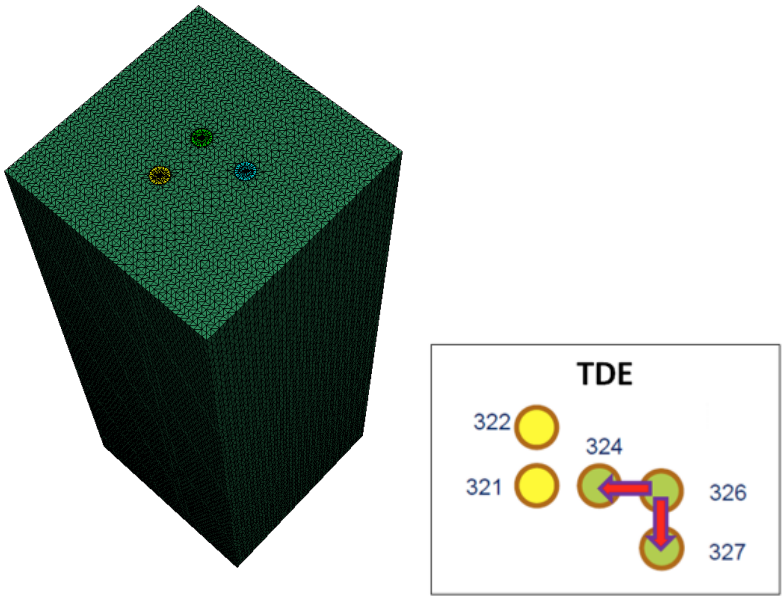

Figure 7-21. Right panel shows the whole mesh with three boreholes, which represent ONK-PP326, ONK-PP324, and ONK-PP327 boreholes in TDE experiment (left panel).

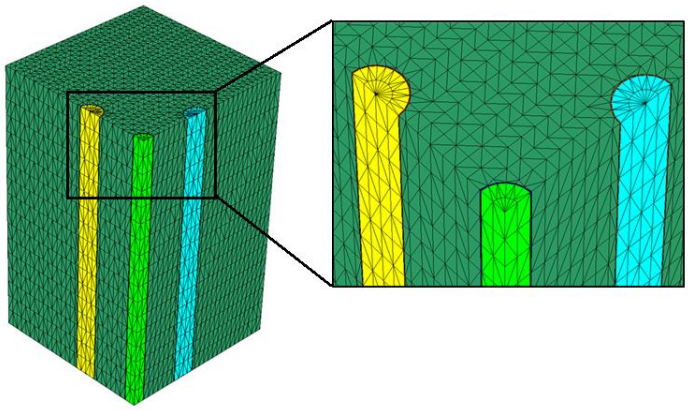

Figure 1-22. The cross section of the entire mesh along the boreholes, along z direction. The distance between central borehole and two others is 0.15 m. the zoom in figure shows the mesh of dummy filled boreholes and 1 mm layer between dummy and rock matrix.

7.4.2 Task 9B: Increasing the Realism in Solute Transport Modelling – Modelling the Field Experiments of LTDE-SD

Long Term Sorption Diffusion Experiment (LTDE-SD): The description of LTDE experiment is given in Löfgren (2014). One of few recent in-situ studies focusing on tracer transport in the stagnant pore water of the rock matrix has been conducted in Sweden at the Äspö Hard Rock Laboratory, within the LTDE-SD campaign (Long Term Sorption Diffusion Experiment). In this study, a cocktail of both sorbing and non-sorbing tracers was allowed to contact a natural fracture surface, as well as the unaltered rock matrix, for a time period of 200 days. The decline in tracer concentration in the water phase was monitored. Thereafter the rock was overcored and analysed in regard to tracer concentration profiles in the rock matrix.

The illustration in the lower right of Figure 7-23 shows the location of LTDE-SD in the Äspö HRL tunnel system. In the centre of the figure, the local tunnel section is shown together with the different boreholes drilled from the site. These boreholes include the LTDE-SD borehole and the closely located pilot borehole. These two boreholes intersect a water-conducting natural fracture at a distance of about 11 m from the tunnel wall, which is the experiment's target fracture. The LTDE-SD borehole was drilled with different diameters, roughly described as follows. Up to the fracture plane the borehole has a large diameter and beyond the fracture plane a small diameter was used. This is simplistically illustrated in the lower left of Figure 7-23. The borehole is indicated by the solid black line and the intersected fracture is indicated by the curved blue line. Orange areas indicate packed-off volumes, whereas blue areas indicate volumes of the tracer cocktail. The red arrows symbolise in-diffusion of tracers from the large-diameter borehole through the fracture surface and into the underlying altered rock matrix. They also symbolise diffusion into the unaltered rock matrix from the small-diameter borehole. The dashed black line indicates the rock volume that was overcored at the end of the tracer test.

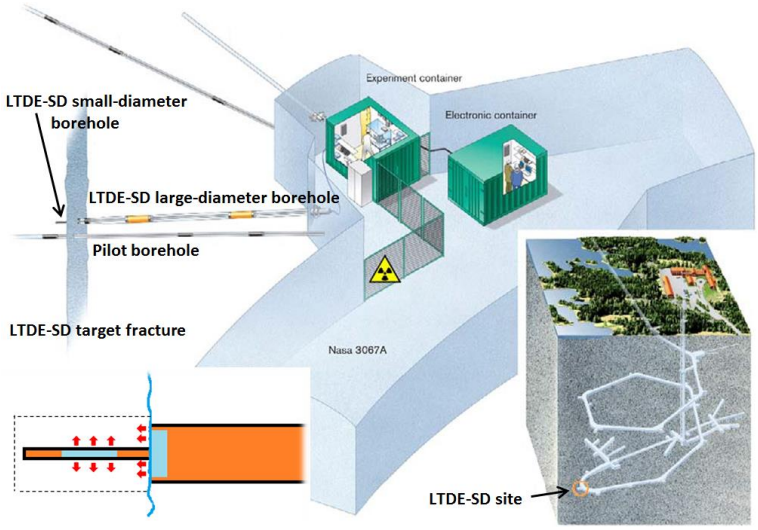

Figure 7-23. Illustrations of the LTDE-SD experimental setup.

The tracers injected were Na-22, S-35, Cl-36, Co-57, Ni-63, Se-75, Sr-85, Nb-95, Zr-95, Tc-99, Pd-102, Cd-109, Ag-110, Sn-113, Ba-133, Cs-137, Gd-153, Hf-175, Ra-226, Pa-233, U-236, and Np-237. Speciation calculations were made using PHREEQC. PEEK tubing connected the tracer cocktail volumes with experimental equipment in the tunnel. Hence, the decreasing tracer concentrations, as well as environmental parameters, could be monitored during the 200 days the tracer test progressed. After that the surrounding rock volume was overcored, and from the overcored volume a number of smaller drill cores were excavated, as illustrated on the left in Figure 7-24. Here the natural fracture surface is located on the right-hand side of the overcored rock volume.

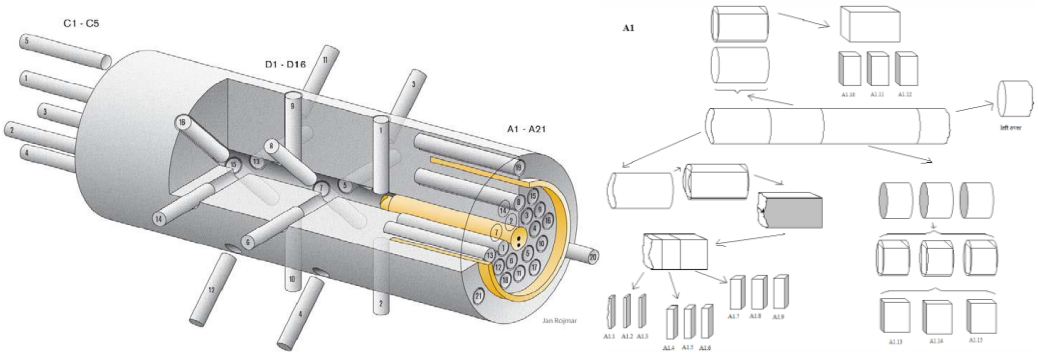

Figure 7-24. Illustration of the sampling of the overcored rock volume in LTDE-SD.

A large number of the drill core samples of Figure 7-24 were cut into subsamples as indicated to the right in Figure 1-24, enabling the obtaining of tracer penetration profiles. Tracer concentrations (or activities) in the rock were obtained by a number of analysis methods, including autoradiography on intact samples; direct activity measurements on intact and crush samples; and leaching or dissolution of intact and crush samples, followed by water phase measurements.

Problem Statement: Although the methodology and results from the experimental campaign have been reported, the outcomes have not yet been subjected to the scrutiny of a broader community of researchers and modellers. Concerning the shape of the penetration profiles, the predicted general shape discussed in the above paragraph was not observed; neither for the natural fracture surface nor for the unaltered rock matrix. Figure 7-25 shows the experimental shapes of the in-diffusing tracer Cs are shown by symbols, as well as the modelled profile by the dashed curve.

The following hypothesis is advanced during LTDE-SD experiment performance: the major diffusion of injected tracer into crystalline rock occurs through multiple micro fractures, which are observed in the rock samples. We propose to use dfnWorks modeling tool to inspect this hypothesis and to simulate diffusion and sorption processes detected by LTDE-SD experiments.

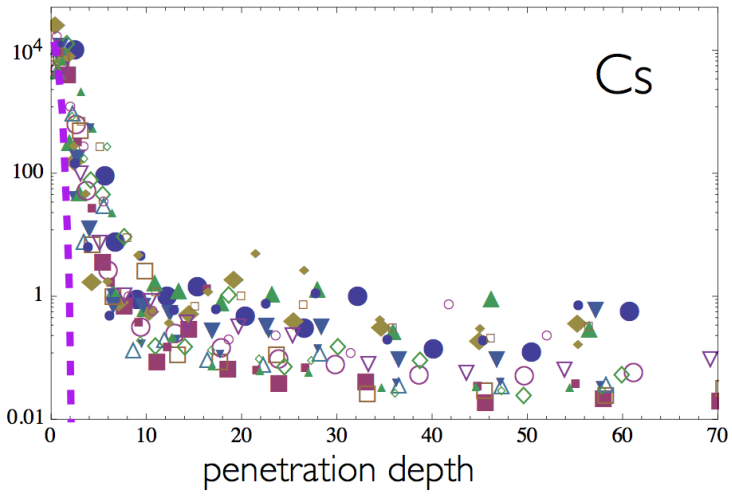

Figure 7-25. The measured experimental shapes of Cs penetration profile (symbols) do not satisfy modeled penetration profile (dashed line) (Data provided by V. Cvetkovic, TF Task9 meeting, Finland, 2015).

We use massively parallel reactive flow and transport model PFLOTRAN (Lichtner et al., 2015) to simulate flow in DFNs. PFLOTRAN allows to model transient multiphase flow, and tracer diffusion into rock matrix can be accurately measured.

In spite of the fact that dfnWorks was verified and used for large scale site simulations (e.g. Hyman et al., 2015b, Karra et al., 2015) it can be easily adapted to small scale micro fracture networks with given micro fracture statistical characteristics. Preliminary results, shown by Paolo Trinchero team, *AMPHOS 21, October 2015*, who are using DarcyTools and PFLOTRAN for modeling solute diffusion into crystalline rock (REPRO experiment, Task9A), indicate the importance of large fractures in interaction between flowing fractures and the matrix. Moreover, it is shown that the small fractures, represented by inter granular porosity in DarcyTool model, are dominating in the rock matrix. The conceptual model used in DarcyTool is shown in Figure 7-26. This concept gives us a confidence that LTDE-SD experiment can be modeled using discrete fracture network model, and dfnWorks software will provide realistic transport simulations.

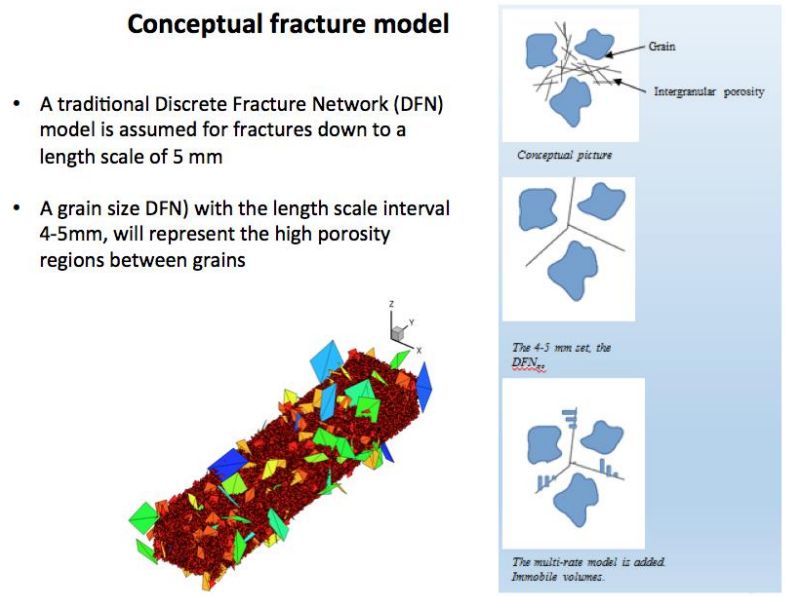

Figure 1-26. The conceptual fracture model used by AMPHOS 21 team to simulate LTDE-SD experiment.

Modeling Procedure: Base on conceptual fracture model, presented in Figure 1-26, the fracture network is generated, which represents connected micro fractures observed on the rock samples at small scale. These micro fractures are the porous spaces between grains and provide paths for tracer through the rock samples.

The domain size is 2 cm^3, where total volume of the simulation domain is 0.08m^3. There are three sets of square fractures, with fracture's orientation following Fisher Distribution and fracture's length based on Truncated Power Law distributions. The fracture statistical characteristics are presented in Table 7-5, and base on Äspö characteristics for the fracture data. Aperture of fractures is set to be uniform, 2.0×10^{-6} m. The example of obtained DFN realization is shown in Figure 7-27. There are 36169 fractures in the DFN, the fracture intensity P_{32} = 864.718 1/m, fracture porosity P_{33} =0.0032, or 0.32%.

Table 7-5. Fracture characteristics that are used to generate micro fracture networks.

Set	Trend	Plunge	Kappa	R_{Min}	R_{Max}	Alpha	P_{32}
1	280	20	10	0.002	0.01	2.6	110
2	20	10	15	0.002	0.01	2.6	200
3	120	50	10	0.002	0.01	2.6	75

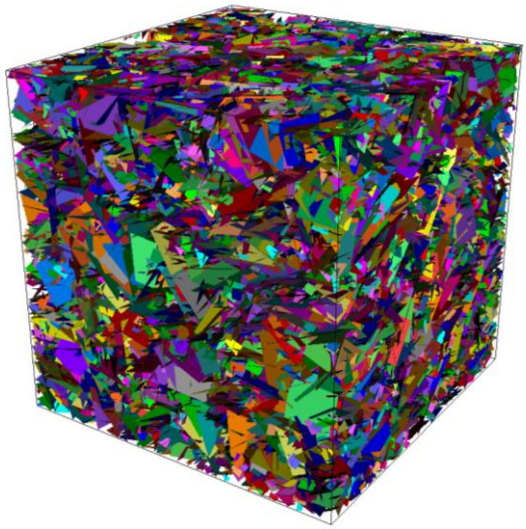

Figure 7-27. The example of DFN realization, where each micro fracture is shown by its own color. The size distribution follows truncated power low distribution. Fracture characteristics are given in Table 7-5.

In order to verify that obtained DFN represents fractured rock sample, we compare two dimensional slice of the DFN with muscovite granite picture. Figure 7-28 shows the DFN slice (left) and granite picture (right), where black lines show the porous paths between grains. This visual verification allows us to proceed with flow and transport simulation for LTDE-SD modeling.

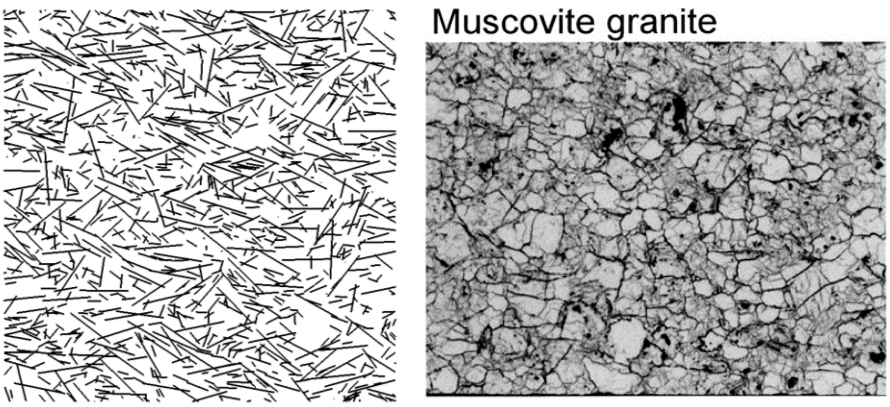

Figure 7-28. (Left) Two dimensional snapshot of a DFN realization, compared to (Right) picture of muscovite granite, where grains boundaries are black lines. Granite picture is from Maikki Siitari-Kauppi, TF #32.

DFN model represents fractures individually, where each fracture has its own permeability value. However, it completely neglects any interaction with rock matrix. LTDE experiment, on the contrary, is focused on diffusion processes. Therefore, the next step of the modeling is mapping connected micro fracture network into continuum model with following ADE simulation, where both, advective and diffusive transport processes can be modeled.

As the fracture network structure of the DFN is mapped into regular voxel mesh, each voxel is defined a permeability equal to fracture permeability that is crossing the voxel, or, if there is no fracture crossing, given rock matrix permeability value. The size of each voxel is chosen as 0.5 mm^3, what makes side length 4 times smaller than the smallest fracture length in the DFN (2mm). Figure 7-29 shows the continuum model, where red cells represent voxel crossed by fracture and blue cells represent the rock matrix. Obtained permeability and porosity profiles are shown in Figure 7-30.

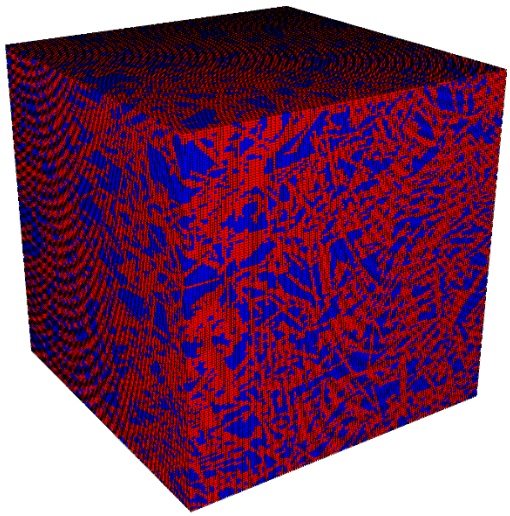

Figure 7-29. The DFN model is mapped into continuum. Red cells represent voxel crossed by fracture and blue cells represent the rock matrix.

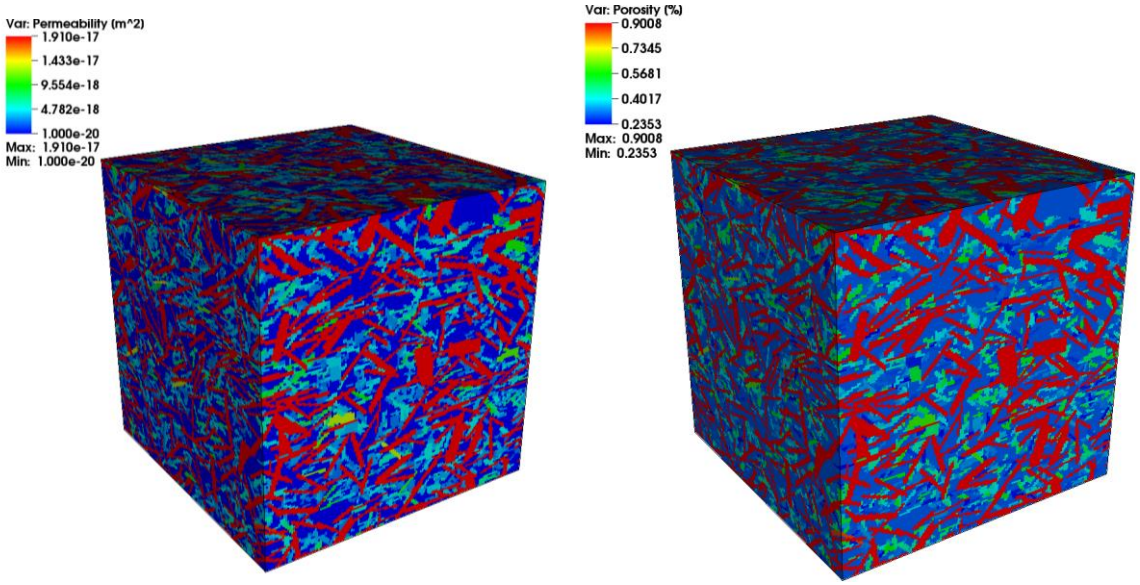

Figure 7-30. Permeability (Left) and porosity (Right) profiles are shown in the continuum simulation.

Preliminary Results: We use PFLOTRAN to run transport through the simulation domain. The tracer is injected uniformly on top face and moving toward bottom face along Z axis according ADE equation. The simulation is run for 25 days. One-time frame is shown in Figure 7-31. We can see that tracer concentration is not uniform along fluid flow direction; the micro fracture cells provide faster paths for tracer than rock matrix cells due to higher permeability and higher porosity, and also advetive term.

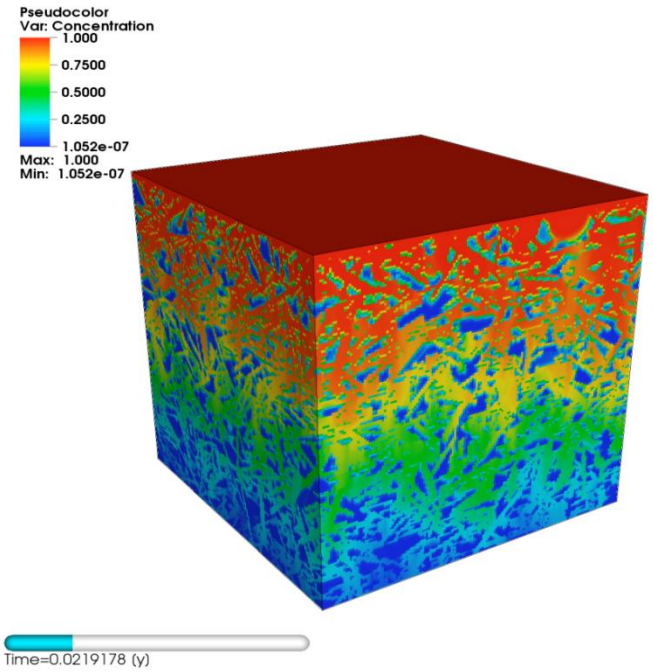

Figure 7-31. The tracer concentration of transport modeling in fractured continuum.

We measure tracer concentration and plot it versus penetration depth (Figure 7-32.) Left plot of Figure 7-32 shows our simulation results in two modeled cases: fractured system, where DFN is mapped into continuum (blue line) and uniform continuum (dashed green line). The same simulation settings, such as initial tracer location, boundary conditions and flow rates, are applied to both continuum models. This way we can clearly observe the role of micro fractures and advection part in transport. Right panel of Figure 7-32 repeats the plot of Figure 7-25 and placed here for comparison. We can see that pure diffusion case in uniform continuum model, shown in both plots by dashed lines, behave very similar and show a big difference with fractured continuum and experimental results.

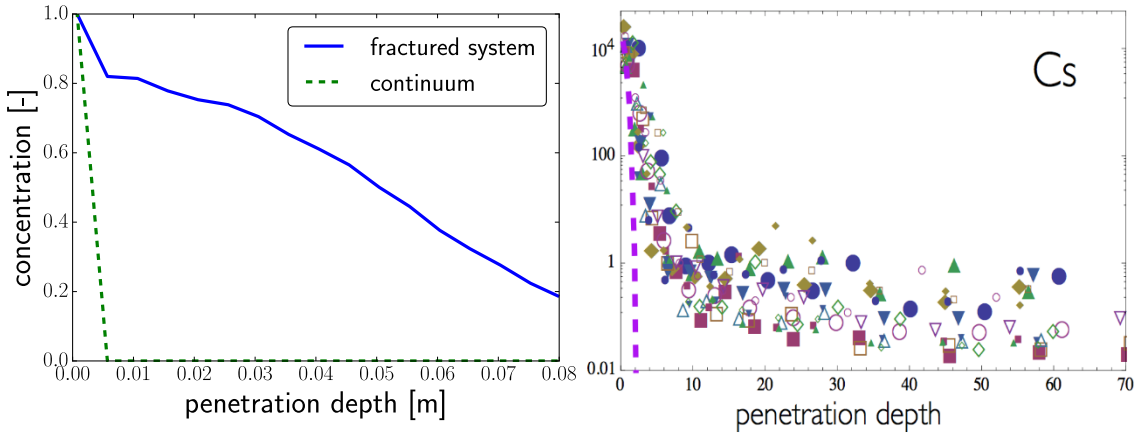

Figure 7-32. Left: the simulation results of tracer concentration plotted versus tracer penetration depth. Blue line corresponds to fractured continuum model with simulated ADE, dashed green line shows results for uniform continuum with simulated pure diffusion process. Right panel repeats plot of Figure 7-25 for comparison. Here dashed line corresponds to continuum pure diffusion modeling and symbols show the results of LTDE experiment.

Future Work: As a future work of modeling LTDE experiment using fracture network we propose following:

1. Understanding the difference between ADE simulated tracer concentration curve using fractured continuum model and the experimental results. Perhaps, the rock sample used in the experiment is a combination of both characteristics: it is fractured on boundaries, where micro fractures were induced at the stage of extracting rock sample, and it gets less fractured and become more homogeneous closer to the center. In order to check this hypothesis, we can produce continuum model that will have both fractured and homogeneous parts, with following transport simulation and results comparison.
2. We have to verify several uncertainties, such as flow rate. We are not sure that flow rate observed in the experiment is similar to the flow rate we used in the simulation. Another uncertain parameter is the time: at what time the tracer concentration is shown.
3. Continuing improving our modeling tool, upgrade the procedure of mapping DFN into continuum. Moreover, in order to avoid statistical bias of stochastically generated fracture network, multiple DFN realizations required. We also need to explore the sensitivity of DFN input parameters and simulation settings.

7.5 REFERENCES

Adler P. M., Thovert J. F., and Mourzenko V. V. (2012) *Fractured porous media*. Oxford University Press.

Ahmed R., Edwards M. G., Lamine S., Huisman B., and Pal M. (2015a) Control-volume distributed multi-point flux approximation coupled with a lower-dimensional fracture model, *J. Comput. Phys.*, 284, 462–489.

Ahmed R., Edwards M. G., Lamine S., Huisman B. A., and Pal M. (2015b) Three-dimensional control-volume distributed multi-point flux approximation coupled with a lower-dimensional surface fracture model, *J. Comput. Phys.*, 303, 470–497.

Ahrens J., Geveci B., and Law C. (2005) 36 paraview: An end-user tool for large-data visualization, *The Visualization Handbook*, 717.

Baghbanan A. and Jing L. (2007) Hydraulic properties of fractured rock masses with correlated fracture length and aperture, *Int. J. Rock Mech. Min.*, 44(5), 704–719.

Belfield W. C. (1998) Incorporating spatial distribution into stochastic modelling of fractures: multifractals and Lévy-stable statistics, *J. Struct. Geol.*, 20(4), 473–486.

Berkowitz B. (2002) Characterizing flow and transport in fractured geological media: A review, *Adv. Water Resour.*, 25(8-12), 861–884.

Bogdanov I., Mourzenko V., Thovert J.-F., and Adler P. (2007) Effective permeability of fractured porous media with power-law distribution of fracture sizes, *Phys. Rev. E*, 76(3), 036,309.

Bonnet E., Bour O., Odling N. E., Davy P., Main I., Cowie P., and Berkowitz B. (2001) Scaling of fracture systems in geological media, *Rev. Geophys.*, 39(3), 347–383.

Boussinesq J. (1868) Mémoire sur l'influence des frottements dans les mouvements réguliers des fluids, *J. Math. Pures Appl*, 13(377-424), 21.

Cacas M. C., Ledoux E., De Marsily G., Barbreau A., Calmels P., Gaillard B., and Margritta R. (1990) Modeling fracture flow with a stochastic discrete fracture network: Calibration and validation: 2. The transport model, *Water Resour. Res.*, 26(3), 491–500.

Charlaix E., Guyon E., and Roux S. (1987) Permeability of a random array of fractures of widely varying apertures, *Transport Porous Med.*, 2(1), 31–43.

Cvetkovic V. and Frampton A. (2012) Solute transport and retention in three-dimensional fracture networks, *Water Resour. Res.*, 48(2).

Cvetkovic V., Painter S., Outters N., and Selroos J. (2004) Stochastic simulation of radionuclide migration in discretely fractured rock near the Äspö hard rock laboratory Äspö hard rock laboratory, *Water Resour. Res.*, 40(2).

de Dreuzy J.-R., Davy P., and Bour O. (2001) Hydraulic properties of two-dimensional random fracture networks following a power law length distribution 2. Permeability of networks based on lognormal distribution of apertures, *Water Resour. Res.*, 37(8), 2079–2095.

de Dreuzy J.-R., Davy P., and Bour O. (2002) Hydraulic properties of two-dimensional random fracture networks following power law distributions of length and aperture, *Water Resour. Res.*, 38(12).

de Dreuzy J.-R., Darcel C., Davy P., and Bour O. (2004) Influence of spatial correlation of fracture centers on the permeability of two-dimensional fracture networks following a power law length distribution, *Water Resour. Res.*, 40(1).

de Dreuzy J.-R., Méheust Y., and Pichot G. (2012) Influence of fracture scale heterogeneity on the flow properties of three-dimensional discrete fracture networks, *J. Geophys. Res.- Sol. Ea.*, 117(B11).

Defays D. (1977) An efficient algorithm for a complete link method, *The Computer Journal*, 20 (4), 364–366, online Available: http://comjnl.oxfordjournals.org/content/20/4/364.abstract

Dershowitz W. (2014) *FracMan version 7.4-Interactive discrete feature data analysis, geometric modeling, and exploration simulation: User documentation,* http://fracman.golder.com/.

Dershowitz W., Winberg A., Hermanson J., Byegård J., Tullborg E., Andersson P., and Mazurek M., Äspö hard rock laboratory. Äspö task force on modelling of groundwater flow and transport of solutes. Task 6c. (2003) *A semi-synthetic model of block scale conductive structures at the Äspö HRL,* International Progress Report IPR-03-13, Swedish Nuclear Fuel and Waste Management Co., Stockholm.

Dverstorp B., and Andersson J. (1989) Application of the discrete fracture network concept with field data: Possibilities of model calibration and validation, *Water Resour. Res.,* 25 (3), 540–550.

Erhel J., De Dreuzy J.-R., and Poirriez B. (2009) Flow simulation in three-dimensional discrete fracture networks, *SIAM J. Sci. Comput.*, 31(4), 2688–2705.

Faybishenko B. (2005) *Dynamics of fluids and transport in fractured rock,* 162, American Geophysical Union.

Follin S., Hartley L., Rhén I., Jackson P., Joyce S., Roberts D., and Swift B. (2014) A methodology to constrain the parameters of a hydrogeological discrete fracture network model for sparsely fractured crystalline rock, exemplified by data from the proposed high-level nuclear waste repository site at forsmark, sweden, *Hydrogeology Journal*, 22 (2), 313–331.

Frampton A. and Cvetkovic V. (2010) Inference of field-scale fracture transmissivities in crystalline rock using flow log measurements, *Water Resour. Res.*, 46(11).

Gudmundsson A., Berg S. S., Lyslo K. B., and Skurtveit E. (2001) Fracture networks and fluid transport in active fault zones, *J. Struct. Geol.*, 23(2), 343–353.

Hartley L., Hunter F., Jackson P., McCarthy R., Gylling B., and Marsic N. (2006) *Regional hydrogeological simulations using connectflow*, Preliminary site description Laxemar subarea–version, 1.

Hatton C., Main I., and Meredith P. (1994) Non-universal scaling of fracture length and opening displacement, *Nature*, 367(6459), 160–162.

Hyman J. D., Karra S., Makedonska N., Gable C. W., Painter S. L., and Viswanathan H. S. (2015a) dfnWorks: A discrete fracture network framework for modeling subsurface flow and transport, *Comput. Geosci.*, 84, 10–19.

Hyman J. D., Painter S. L., Viswanathan H., Makedonska N., and Karra S. (2015b) Influence of injection mode on transport properties in kilometer-scale three-dimensional discrete fracture networks, *Water Resour. Res.*, 51(9), 7289–7308.

Ji S.-H., Park Y.-J., and Lee K.-K. (2011) Influence of fracture connectivity and characterization level on the uncertainty of the equivalent permeability in statistically conceptualized fracture networks, *Transport Porous Med.*, 87(2), 385–395.

Joyce S., Hartley L., Applegate D., Hoek J., and Jackson P. (2014) Multi-scale groundwater flow modeling during temperate climate conditions for the safety assessment of the proposed high-level nuclear waste repository site at forsmark, sweden, *Hydrogeol. J.*, 22(6), 1233–1249.

Kang P. K., Dentz M., Le Borgne T., and Juanes R. (2015) Anomalous transport on regular fracture networks: Impact of conductivity heterogeneity and mixing at fracture intersections, *Phys. Rev. E*, 92(2), 022,148.

Karra S., Makedonska N., Viswanathan H. S., Painter S. L., and Hyman J. D. (2015) Effect of advective flow in fractures and matrix diffusion on natural gas production, *Water Resour. Res.*, 51(10), 8646–8657.

Klimczak C., Schultz R. A., Parashar R., and Reeves D. M. (2010) Cubic law with aperture-length correlation: implications for network scale fluid flow, *Hydrogeol. J.*, 18 (4), 851–862.

Konzuk J. S. and Kueper B. H. (2004) Evaluation of cubic law based models describing single-phase flow through a rough-walled fracture, *Water Resour. Res.*, 40(2).

LaGriT (2013) *Los Alamos Grid Toolbox, (LaGriT)*, Los Alamos National Laboratory, http://lagrit.lanl.gov.

Levenshtein V. I. (1966) Binary codes capable of correcting deletions, insertions, and reversals, *Soviet physics doklady*, 10 (8), 707–710.

Lichtner P., Hammond G., Lu C., Karra S., Bisht G., Andre B., Mills R., and Kumar J. (2015) *PFLOTRAN user manual: A massively parallel reactive flow and transport model for describing surface and subsurface processes*, Tech. rep., (Report No.: LA-UR-15-20403) Los Alamos National Laboratory.

Löfgren M. (2014) *Increasing the realism in solute transport modelling – Modelling the field experiments of REPRO and LTDE-SD*, SKB Task force on Modelling of Groundwater Flow and Transport of Solutes.

Lu K., Chaudhuri A., Lee T.-Y., Shen H.-W., and Wong P. C. (2013) Exploring vector fields with distribution-based streamline analysis, *PacificVis*, 257–264.

Makedonska N., Hyman J. D., Karra S., Painter S. L., Gable C. W., and Viswanathan H. S. (2016) Evaluating the effect of internal aperture variability on transport in kilometer scale discrete fracture networks, *Adv. Water Resour.*, 94, 486-497.

Margolin G., Berkowitz B., and Scher H. (1998) Structure, flow, and generalized conductivity scaling in fracture networks, *Water Resour. Res.*, 34(9), 2103–2121.

McLoughlin T., Jones M. W., Laramee R. S., Malki R., Masters I., and Hansen C. D. (2013) Similarity measures for enhancing interactive streamline seeding, *Visualization and Computer Graphics, IEEE Transactions on*, 19 (8), 1342–1353.

Middleton R. S., Carey J. W., Currier R. P., Hyman J. D., Kang Q., Karra S., Jiménez-Martínez J., Porter M. L., and Viswanathan H. S. (2015) Shale gas and non-aqueous fracturing fluids: Opportunities and challenges for supercritical CO2, *Appl. Energ.*, 147, 500–509.

Molz F. J., Rajaram H., and Lu S. (2004) Stochastic fractal-based models of heterogeneity in subsurface hydrology: Origins, applications, limitations, and future research questions, *Rev. Geophys.*, 42(1).

Mustapha H. and Mustapha K. (2007) A new approach to simulating flow in discrete fracture networks with an optimized mesh, *SIAM J. Sci. Comput.*, 29, 1439.

National Research Council (1996) *Rock fractures and fluid flow: contemporary understanding and applications*, National Academy Press.

Neuman S. (2005) Trends, prospects and challenges in quantifying flow and transport through fractured rocks, *Hydrogeol. J.*, 13(1), 124–147.

Painter S. and Cvetkovic V. (2005) Upscaling discrete fracture network simulations: An alternative to continuum transport models, *Water Resour. Res, 41*, W02, 002.

Painter S., Cvetkovic V., and Selroos J.-O. (2002) Power-law velocity distributions in fracture networks: Numerical evidence and implications for tracer transport, *Geophys. Res. Lett.*, 29 (14), 20–1–20–4.

Patriarche D., Pili E., Adler P. M., and Thovert J.-F. (2007) Stereological analysis of fractures in the roselend tunnel and permeability determination, *Water Resour. Res.*, 43(9).

Pichot G., Erhel J., and De Dreuzy J. (2010) A mixed hybrid mortar method for solving flow in discrete fracture networks, *Appl. Anal.*, 89(10), 1629–1643.

Pichot G., Erhel J., and De Dreuzy J. (2012) A generalized mixed hybrid mortar method for solving flow in stochastic discrete fracture networks, *SIAM J. Sci. Comput.*, 34 (1), B86–B105.

Pobitzer A., Peikert R., Fuchs R., Schindler B., Kuhn A., Theisel H., Matković K., and Hauser H. (2011) The state of the art in topology- based visualization of unsteady flow, *Computer Graphics Forum*, 30 (6), 1789–1811.

Renshaw C. E. (1995) On the relationship between mechanical and hydraulic apertures in rough-walled fractures, *J. Geophys. Res.-Sol. Ea.*, 100(B12), 24,629–24,636.

Renshaw C. E. and Park J. C. (1997) Effect of mechanical interactions on the scaling of fracture length and aperture, *Nature*, 386(6624), 482–484.

Roubinet D., Liu H.-H., and De Dreuzy J.-R. (2010) A new particle-tracking approach to simulating transport in heterogeneous fractured porous media, *Water Resour. Res.*, 46(11).

Salzbrunn T., Jänicke H., and Wischgoll T. (2008) The State of the art in flow visualization: Partition-based techniques, *SimVis*, 75–92.

SKB (2011) *Long-term safety for the final repository for spent nuclear fuel at forsmark, main report of the sr-site project*, SKB TR-11-01.

Svensk Kärnbränslehantering AB (2010) *Data report for the safety assessment SR-site (TR-10-52)*, Tech. rep., Svensk Kärnbränslehantering AB.

Svensk Kärnbränslehantering AB (2011), *Data report for the safety assessment SR-site (TR-11- 01)*, Tech. rep., Svensk Kärnbränslehantering AB.

Trimmer D., Bonner B., Heard H., and Duba A. (1980) Effect of pressure and stress on water transport in intact and fractured gabbro and granite, *J. Geophys. Res.-Sol. Ea.*, 85 (B12), 7059–7071.

Uchida M. (1994) *Discrete-fracture modelling of the Äspö LPT-2, large-scale pumping and tracer test*, Svensk kärnbränslehantering AB.

Vermilye J. M. and Scholz C. H. (1995) Relation between vein length and aperture, *J. Struct. Geol.*, 17(3), 423–434.

Walmann T., Malthe-Sørenssen A., Feder J., Jøssang T., Meakin P., and Hardy H. H. (1996) Scaling relations for the lengths and widths of fractures, *Phys. Rev. Lett.*, 77, 5393–5396.

Wellman T. P., Shapiro A. M., and Hill M. C. (2009) Effects of simplifying fracture network representation on inert chemical migration in fracture-controlled aquifers, *Water Resour. Res.*, 45(1).

Willmann M., Lanyon G., Marschall P., and Kinzelbach W. (2013) A new stochastic particle-tracking approach for fractured sedimentary formations, *Water Resour. Res.*, 49 (1), 352–359.

Wilson R. and Hancock E. (2004) Levenshtein distance for graph spectral features, *Pattern Recognition, 2004. ICPR 2004. Proceedings of the 17th International Conference on*, 2, 489–492.

Witherspoon P. A., Wang J., Iwai K., and Gale J. (1980) Validity of cubic law for fluid flow in a deformable rock fracture, *Water Resour. Res.*, 16(6), 1016–1024.

Xu C., Dowd P., Mardia K., and Fowell R. (2006) A connectivity index for discrete fracture networks, *Math. Geol.*, 38(5), 611–634.

Yu H., Wang C., Shene C.-K., and Chen J. H. (2012) Hierarchical streamline bundles, *Visualization and Computer Graphics, IEEE Transactions on*, 18(8), 1353–1367.

Zimmerman R. W. and Bodvarsson G. S. (1996) Hydraulic conductivity of rock fractures, *Transport Porous Med.*, 23(1), 1–30.

8. FRACTURE CONTINUUM MODEL AND ITS COMPARISON WITH DISCRETE FRACTURE NETWORK MODEL TO REPRESENT CRYSTALLINE FRACTURED ROCK

Numerical modeling of disposal of nuclear waste in fractured crystalline rock requires characterization of fractures. Various fracture representations are used in modeling for different applications. Two of these methods are the Discrete Fracture Network (DFN) and the Fracture Continuum Model (FCM). The DFN is based on characterization of individual fractures, while the FCM uses a geostatistical approach to assign fracture data to grid blocks. Details of both the DFN and the FCM approaches are described below.

This study is a continuation of the work started in FY15 documented in the 2015 milestone report (Wang et al., 2015). The objectives of this study are to evaluate both the DFN and FCM methods for use in flow and transport modeling of a generic deep geologic disposal of used fuel in crystalline rocks. Section 1.1 describes the DFN model and model setup. Section 8.2 describes the FCM model and recent modifications as part of the DFN-FCM comparison. Section 8.3 describes FCM Model setup and results of DFN-FCM comparison.

8.1 DISCRETE FRACTURE NETWORK (DFN) MODEL SETUP FOR DFN-FCM COMPARISON

Subsurface flow and transport through fractured rock can be modeled and predicted using several simulation tools. In frame of the current project the two conceptual models are used: the FCM and the DFN. While FCM uses a continuum approach, where different 3D cells represent either high permeability fracture or low permeability matrix, the DFN model explicitly represents individual fractures and ignores low permeability rock matrix. In spite of the fact that fractures provide the main paths for subsurface flow and transport, there are hydrological mechanisms between fracture surfaces and rock matrix, which cannot be ignored in flow and transport predictions. The current task is focused on the comparison of (1) pure advective transport modeled with DFN and particle tracking, (2) advection-diffusion modeled with DFN and advection-diffusion equation, and (2) advection-diffusion simulated with FCM using advection-diffusion equation. The quantities that we are interested in FCM - DFN comparison are: 1) effective permeability of the simulated fractured domain, and 2) breakthrough curves of the transport.

8.1.1 Fracture Distributions

The property of the fracture network considered in this comparison study is loosely based on the property of the SKB site in Sweden. Three fracture sets were considered. The properties of these fracture sets are summarized in Table 8-1.

It is assumed that the fracture radius follows a truncated power law distribution as follows:

$$R = R_0 \cdot \left[1 - u + u \cdot \left(\frac{R_0}{R_u}\right)^{\alpha}\right]^{-1/\alpha}, \tag{8-1}$$

with the parameters shown in Table 8-1.

It was assumed that fracture orientations follow a Fisher distribution:

$$f(\theta) = \frac{\kappa \cdot sin\theta \cdot e^{\kappa \cdot cos\theta}}{e^{\kappa} - e^{-\kappa}}, \tag{8-2}$$

where θ is the deviation of the fracture pole orientation from the mean orientation and the parameter $\kappa > 0$ is the concentration parameter also given in Table 8-1.

Fracture transmissivity, σ, is estimated using a power-law relationship of a correlated transmissivity model [SKB, 2011]:

$$\log(\sigma) = \log(\gamma \cdot R^{\omega}), \quad (8\text{-}3)$$

with parameters γ=1.6×10^{-9}, ω=0.8. The fracture aperture, *b*, is correlated to fracture size and calculated using the cubic law [e.g. Adler, 2012]

$$\sigma = \frac{b^3}{12}\frac{\rho g}{\mu} \quad (8\text{-}4)$$

In Eq. (8-4), ρ is a water density, g is gravity acceleration and μ is a water viscosity. The fracture permeability is defined from fracture aperture as k = b^2/12.

Table 1. Fracture set statics used in the model based on Table 6-75 SKB report TR10-52. Note that the fracture statistics of NE in the SKB report are now being used for EW.

Set	Mean trend (deg)	Mean plunge (deg)	κ	a	R_u	R_0	Number of fractures in 1 km^3
NS	90	0	22	2.5	500	15	2100
EW	0	0	22	2.7	500	15	2000
HZ	360	90	10	2.4	500	15	2300

8.1.2 DFN Model Workflow

This section describes the DFN model set-up and the new technique on the mapping of the fracture network geometry into continuum model is also presented.

DFNWorks description: The general workflow of DFNWorks software is shown in Figure 8-1a.

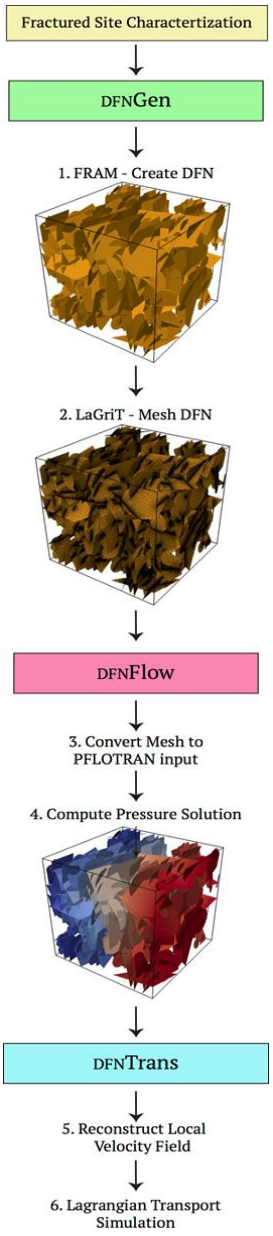

DFNGEN: The Feature Rejection Algorithm for Meshing

Figure 8-1a. DFNWORKS Workflow. From top: The input for DFNWORKS is a fractured site characterization that provides distributions of fracture orientations, radius, and spatial locations. DFNGEN: 1) FRAM - Create DFN: Using the fractured site characterization that networks are constructed using the feature rejection algorithm for meshing. 2) LAGRIT - Mesh DFN: The LAGRIT meshing toolbox is used to create a conforming Delaunay triangulation of the network. DFNFLOW: 3) Convert Mesh to PFLOTRAN input: Control volume information is formatted for PFLOTRAN. 4) Compute Pressure Solution: The steady-state pressure solution in the DFN is obtained using PFLOTRAN. dfnTrans: 5) Reconstruct Local Velocity Field: Darcy fluxes obtained using dfnFlow are used to reconstruct the local velocity field, which is used for particle tracking on the DFN. 6) Lagrangian Transport Simulation: An extension of the walkabout method is used to determine pathlines through the network and simulate transport.

DFNGEN: The Feature Rejection Algorithm for Meshing: Each three-dimensional DFN is generated and meshed using the feature rejection algorithm for meshing (FRAM) methodology of Hyman et al., (Hyman et al. 2014). Each DFN is constructed so that all features in the network, e.g., length of intersections between fractures; distance between lines of intersection of a fracture, are larger than a user-defined minimum length scale. This restriction provides a firm lower bound on the required mesh resolution, and special care is taken so that prescribed geological statistics are not affected by this restriction. Once the DFN is generated, the LAGRIT (LaGriT, 2013) meshing toolbox is used to create a high resolution computational mesh representation of the DFN in parallel. An algorithm for conforming Delaunay triangulation is implemented so that meshes along intersections coincide and Voronoi control volumes suitable for finite volume solvers such as FEHM, TOUGH2, and the fully parallelized PFLOTRAN are produced. Because the mesh conforms to fracture intersections, the method does not require solving additional systems of linear equations, which is needed if a non-conforming mesh is used.

Network Generation and Meshing: The principal issue in meshing a DFN is that to resolve a tiny feature in the network, the edges of the mesh surrounding the feature must be the size of the feature or smaller, if the physics are to be properly resolved. Various methods have been proposed to address this issue, and others, associated with meshing a DFN. In one methodology, pathological cases that degrade mesh quality, e.g., an arbitrarily short line of intersection between two fractures, are systematically removed after an unconstrained fracture network is generated and meshed. However, such adjustments can deform the network, resulting in fractures that may no longer be planar. Another methodology does not require the mesh to coincide at the line of intersection, and the difficulty is pushed forward by the inclusion of additional linear systems that must be solved to impose continuity of pressure and flux along fracture intersections. These additional linear systems make this methodology computationally more expensive when solving for flow than when the meshes are forced to align. In addition, a non-aligned grid at fracture intersections may complicate solute transport calculations.

In contrast to these methods, DFNGEN uses FRAM to constrain the generation of the network so that it only contains features greater than or equal to a user-prescribed minimum length scale h. Each fracture in our DFN is a planar straight-line graph (PSLG) made up of the set of line segments that represent the boundary of the fracture and the line segments that represent where other fractures intersect it. Given a set of PSLGs $\mathcal{X}$ with arbitrary orientation in R3, one can define a *local feature size at a point p* as the radius of the smallest sphere centered at p that intersects two non-incident vertices of segments of $\mathcal{X}$ (Ruppert 1995). In a three-dimensional DFN, examples of a measurable feature include: the length of the line of intersection between two fractures, the distance from the end of a fracture intersection that is interior to the polygon boundary to the polygon boundary, and the distance between two fracture intersection line segments. During the generation process, we require that the DFN never generate a fracture with a feature of size less than h, which provides a firm lower bound on the required resolution of the mesh. When the resulting network is meshed, all features can be resolved by generating triangular cell edges with a minimum length slightly less than h.

By constraining the network so that all features in the network are greater than h, FRAM ensures that pathological cases which degrade mesh quality are not present in the network. Under these conditions, a conforming Delaunay triangulation algorithm can be used to ensure that the line of intersection between any two fractures is preserved in the mesh so long as the lines of intersection are discretized in steps less than h. The conforming Delaunay triangulation algorithm procedure results in meshes that are coincident along the common line of intersection between fractures. Because computational control volumes (Voronoi polygons) are based on vertices and the triangular meshes are coincident along intersections, the Voronoi cells also conform at the fracture boundaries. This results in Voronoi control volumes that span both of the intersecting fractures. However, the neighbors of these Voronoi cells are still two-dimensional. The need to check for a feature size less than h means that the fracture generation process is computationally more demanding than methods that do not impose the minimum feature size constraint.

The tradeoff is a streamlined/parallelized process of mesh generation, numerical integration of the pressure solution, and simplifying particle tracking through the resulting flow field.

Mesh Examples: In figure 8-1b three intersecting fractures show the intersecting conforming Delaunay triangulations. Two of the fractures are colored by distance from lines of intersections (traces) with each other and other fractures that intersect these fractures, and the other is semi-transparent for clarity. The mesh is optionally coarsened away from intersections with pressure gradients will be lower. The inclusion of the semi- transparent fracture illustrates how FRAM creates a mesh that adheres to multiple intersections on the surface of a single fracture. Two additional fractures intersect the elliptical fracture, and intersect one another on the surface of that fracture, as shown by the intersecting white colored regions. The inset shows that the Delaunay mesh conforms all of these lines of intersection.

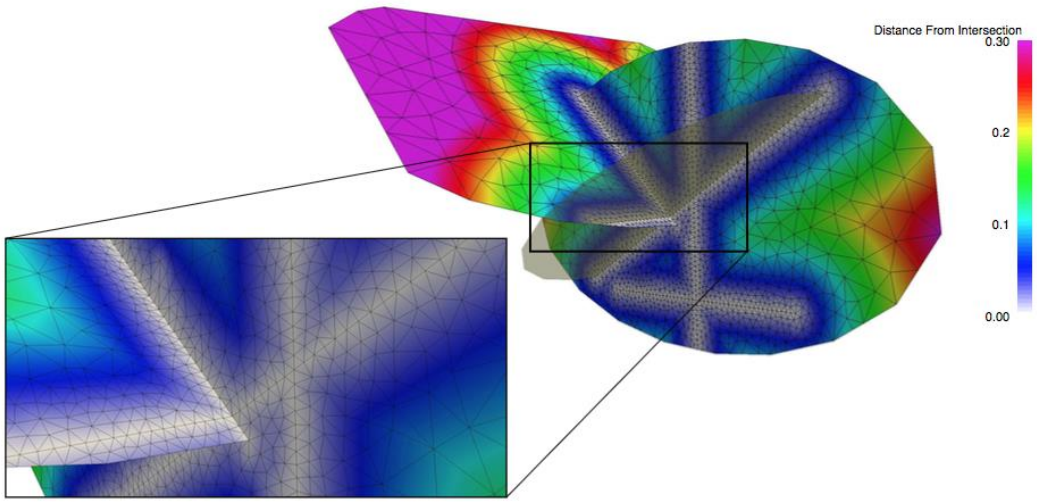

Figure 8-1b. Three intersecting fractures show the intersecting conforming Delaunay triangulations. Two of the fractures are colored by distance from lines of intersections (traces) between fractures, and the other is semi-transparent. The mesh is optionally coarsened away from intersections with pressure gradients will be lower. The inclusion of the semi-transparent fracture illustrates how FRAM creates a mesh that adheres to multiple intersections on the surface of a single fracture. Two additional fractures intersect the elliptical fracture, and intersect one another on the surface of that fracture, as shown by the intersecting white colored regions. The inset shows that the Delaunay mesh conforms all of these lines of intersection.

Remarks about FRAM: Decisions about the minimum length scale h that will be represented in a DFN are made a priori; which is typically the case in scientific computing and not unique to FRAM. When adopting the FRAM methodology the choice of the h will be reflected in the generated network. If h is chosen to large with respect to fracture and domain size, then it will be difficult to generate a DFN that meets the density requirements. If h is chosen too small, then computational cost associated with meshing and solving the governing equations will increase. The choice of h should be made so that all physical phenomena of interest are greater than h, so they can be well resolved by the computational mesh, while limiting computational expenses. The tradeoff between spatial resolution and computational expediency inherent in the choice of h in FRAM is the familiar tradeoff in most branches of scientific computing.

Due to the rejection nature of FRAM some of the desired distributions in the network, e.g. fracture length, will not be properly represented due to over rejection unless certain criteria are met. For example, larger

fractures generate more measurable features in the network than smaller ones and can be rejected a disproportionate amount. However, modifying the procedure by which fracture lengths are sampled can alleviate the issue of bias in the represented fracture length distribution. This is only necessary when sampling from a distribution with a broad range of lengths, such as a truncated power law distribution. An alternative solution is decreasing h to loosen the acceptation criteria. In the limit of $h \rightarrow 0$, all prescribed distributions will be recovered exactly because no fractures are rejected. Details about these procedures are in (Hyman et al. 2014).

8.1.3 DFNWorks results for DFN-FCM comparison

We consider simulation domain size of 1 km x 1 km x 1 km. Figure 8-1c shows an example of one DFN realization according to fracture parameter given in Table 8-1.

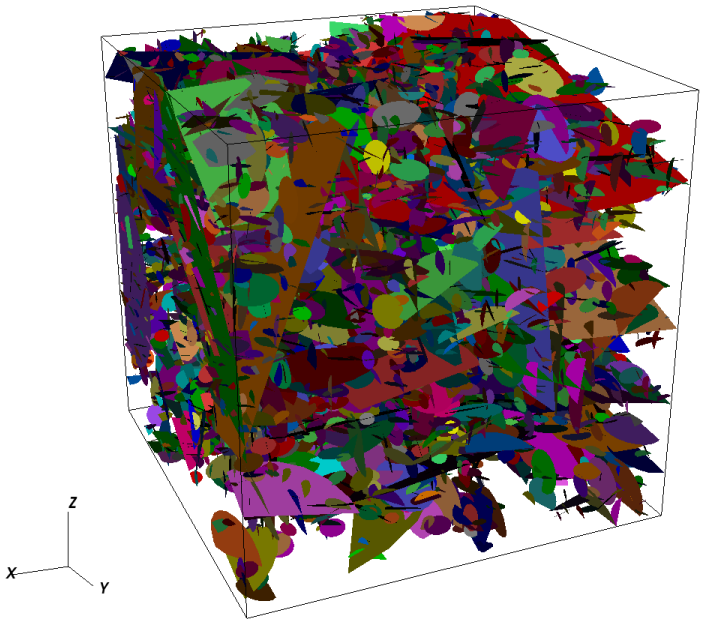

Figure 8-1c. Example of DFN that is generated according to fracture characteristics given in Table 1. This realization consists of 6531 fractures, 6.092.806 control volume cells and 12.421.385 triangular elements. Fracture intensity, area of fractures per unit volume, P_{32}=0.0257.

The CDF distribution of fracture radii, aperture and permeability are shown in Figures 8-2, 8-3, and 8-4, respectively.

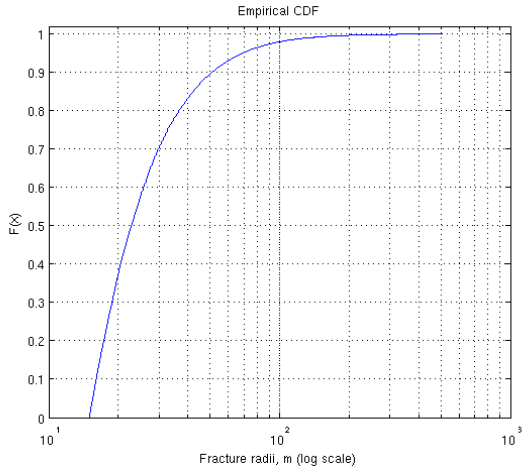

Figure 8-2. CDF of fracture radii of the DFN realization shown in Figure 8-1c.

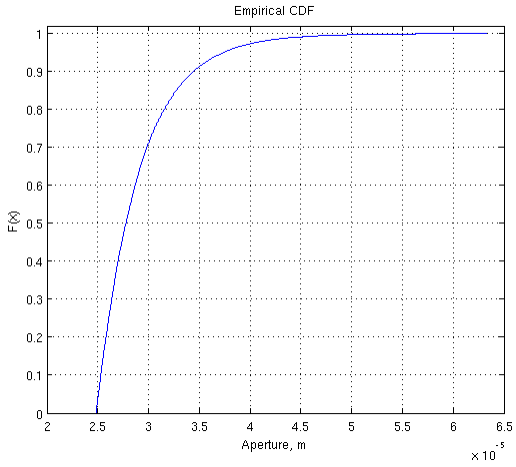

Figure 8-3. Fracture aperture distribution defined by Eq. (8-4).

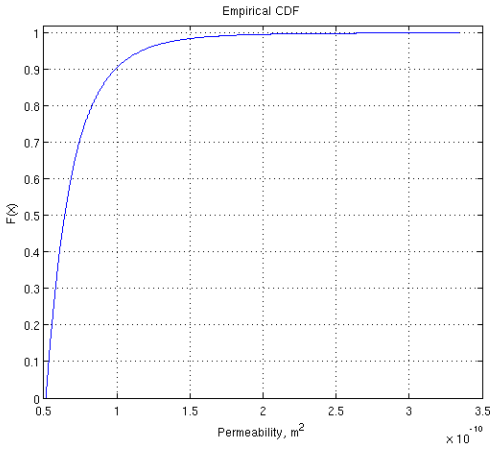

Figure 8-4. Fracture permeability distribution defined from fracture aperture as $k=b^2/12$.

The flow is driven from west to east (x = 1 km) with a constant pressure of 1.001 MPa on the west face (x = 0) and constant pressure of 1 MPa on the east face. Note that we assume that gravity is turned off and that these constant pressures are applied throughout the faces (not hydrostatic). The rest of the faces have no flow boundary conditions. Steady-state flow is solved for here (therefore, do not need initial conditions). The example of obtained steady-state pressure solution is shown in Figure 8-5. Figure 8-6 shows a permeability profile of the same DFN realization.

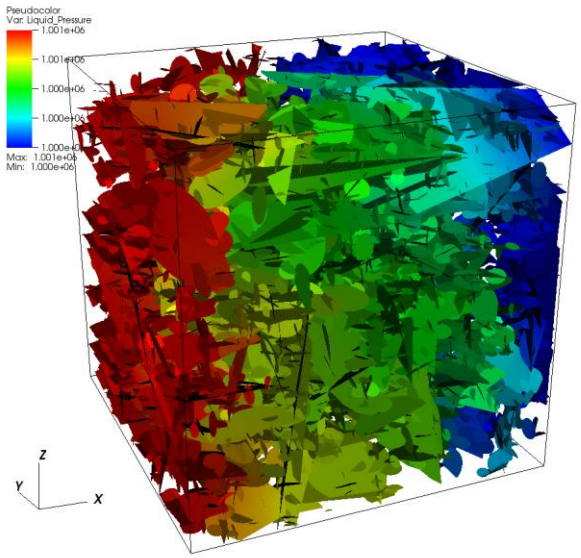

Figure 8-5. Steady state pressure solution, where flow direction is from west (-x face) to east (+x face).

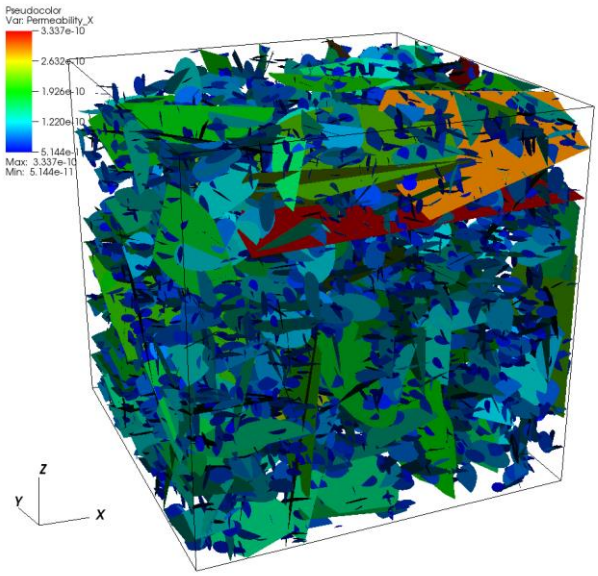

Figure 8-6. Permeability profile of one of DFN realizations.

We consider the origin of particles/tracer being located along entire west face of the domain as a pulse. The boundary conditions for transport are outlet on east face and no flux on the rest of the boundaries. Steady state solution is evaluated for the flow and then effective permeability is calculated using Darcy's law and the east face flux. The fluxes from a steady state flow are used to drive the transport, and the breakthrough curve on the east face is calculated for comparing DFN and FCM approaches. Figure 8-7 shows BTCs of particle tracking results through 25 DFN realizations. Figure 8-8 shows BTCs of tracer runs using PFLOTRAN.

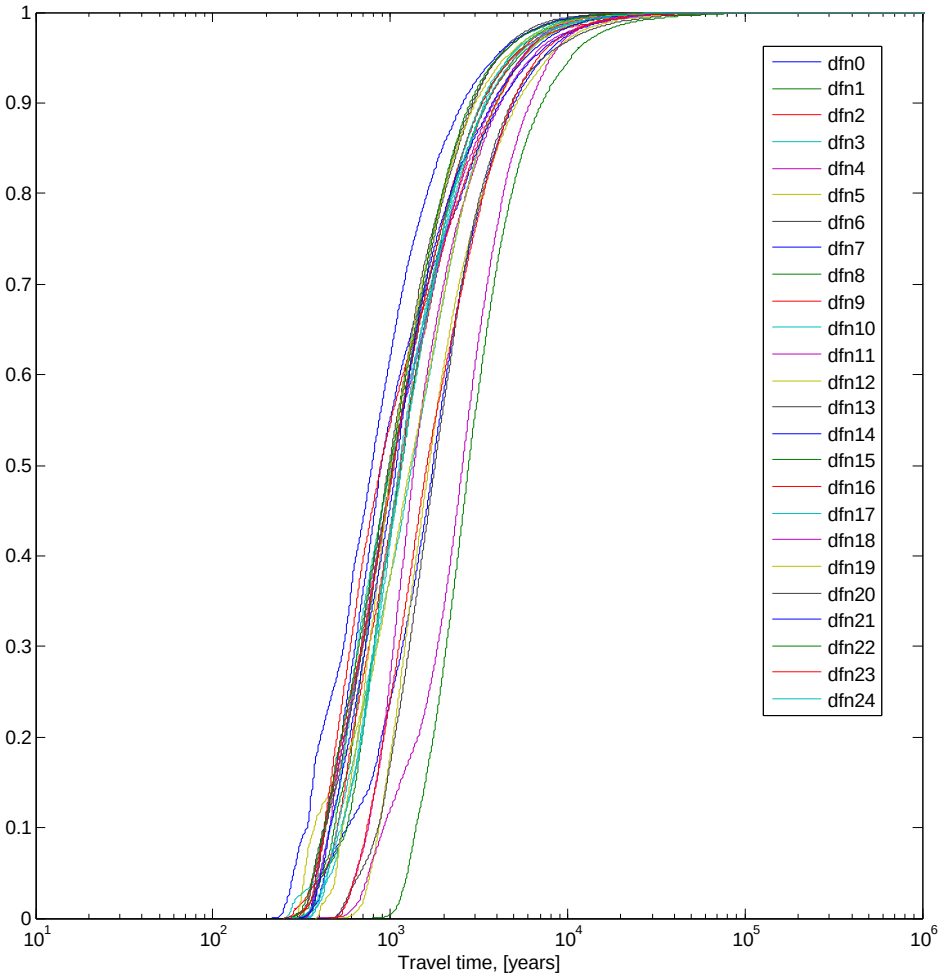

Figure 8-7. BTCs of particle tracking in 25 DFN realizations.

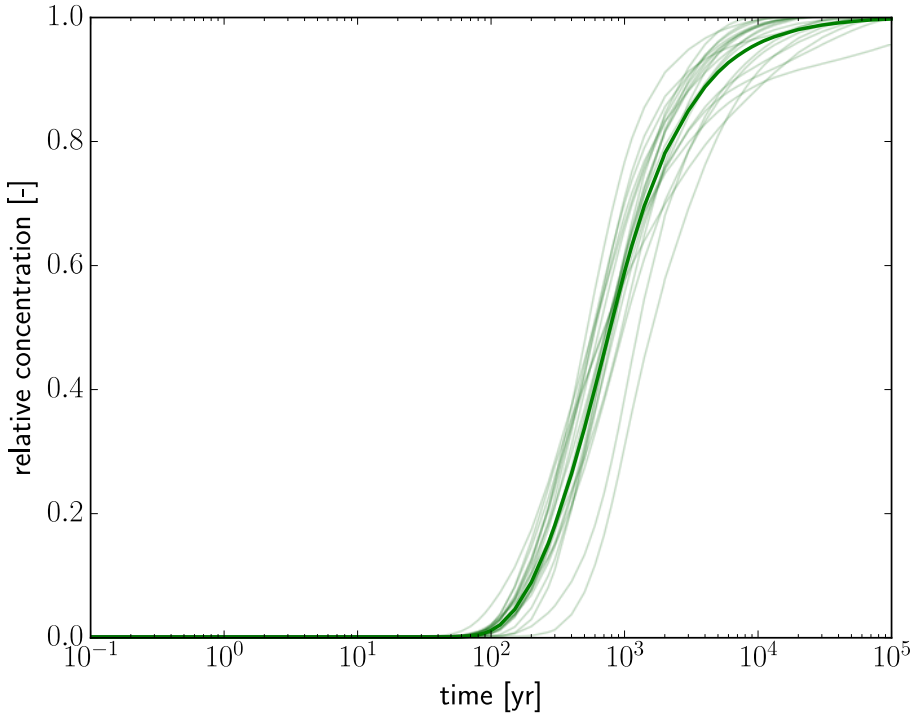

Figure 8-8. BTCs of tracer transport results using PFLOTRAN.

8.1.4 Mapping DFN geometry into continuum model for FCM simulations

One of the main uncertainty in DFN-FCM comparison is the fracture connectivity and percolation of fractures from in-flow boundary to out-flow boundary. While the DFN approach guarantees the existence of fracture clusters that connect boundary faces, FCM has difficulties with assurance of fracture percolation between boundary faces. In the case that there is no connected fracture path between in-flow and out-flow boundary, the BTCs of the transport cannot be compared with DFN results. In order to overcome this issue, we propose a new technique of mapping a DFN fracture geometry into a continuum model. The main algorithm of the mapping consists of the following steps:

1. Generate a DFN realization.
2. Create 3D continuum uniform mesh of the same size as DFN simulation domain.
3. For each fracture in DFN identify the list of a corresponding 3D cells that are crossing the fracture in 3D space. Output the list of cells for each fracture. This list is used by the FCM to set up a proper permeability.

Figure 8-9 shows an example of continuum mesh with simplified permeability profile. As the fracture network structure of the DFN is mapped into regular voxel mesh, each voxel is defined a permeability equal to fracture permeability that is crossing the voxel, or, if there is no fracture crossing, given rock matrix permeability value. If a few fractures with different permeability cut across the same cell, the highest permeability value is chosen for the cell. The size of each voxel is chosen as $10m^3$. Figure 8-9 shows the continuum model, where non-blue cells represent voxel crossed by fracture and blue cells represent the rock matrix.

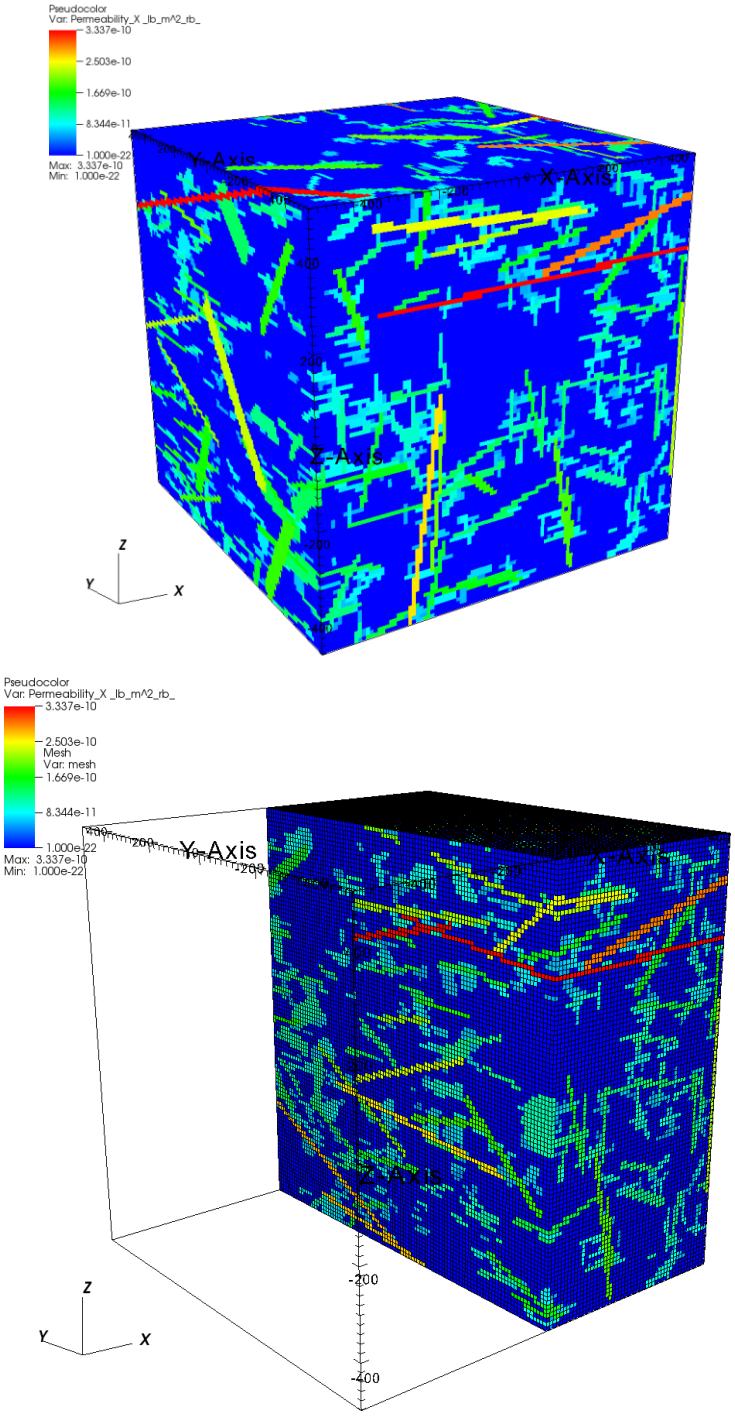

Figure 8-9. We undertake a simple simulation to map the DFN into continuum model. Here the hex mesh is uniform, each cell is $10m^3$. The permeability of each cell is equal to permeability of the fracture that crosses the cell. If there is no fracture, then the permeability is equal to matrix permeability. The top figure shows the obtained permeability profile, the bottom one shows the slice of right part of the same simulation domain.

8.2 THE FRACTURE CONTINUUM MODEL AND RECENT MODIFICATIONS

This section provides a description of the fractured continuum model (FCM) and the methods developed to generate fracture networks for FCM. It also discusses the fracture networks generated for FCM-DFN comparison.

8.2.1 Fractured Continuum Model

A number of different techniques were proposed to translate individual fracture properties into a continuum model (Botros et al. 2008, McKenna and Reeves, 2005, Reeves 2008). The method used in this study is an extension of the method described in McKenna and Reeves (2005) and Reeves (2008). The method is based on mapping fracture properties into a continuum model regular grid (Figure 8-10). The resulting model is called fracture continuum model (FCM).

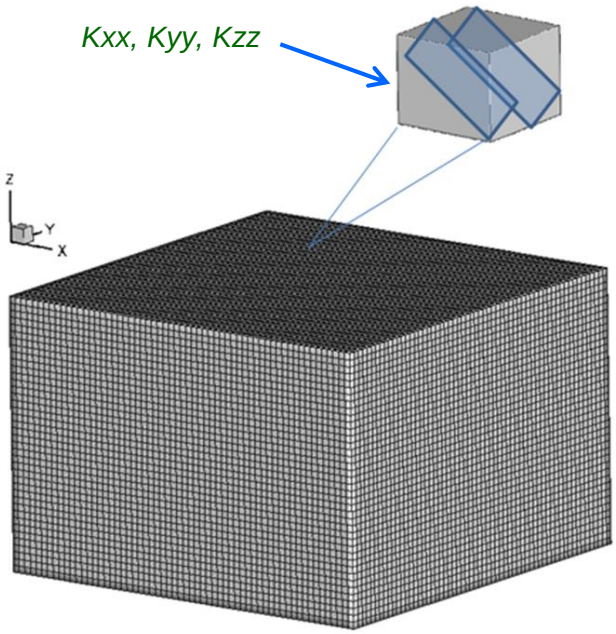

Figure 8-10. Schematic Representation of the Fractured Continuum Approach.

The FCM calculates permeability of each grid block from the following fracture properties:

- Strike
- Dip
- Aperture
- Spacing

If a few fractures that belong to the same fracture set are present in a grid block, they are assumed to be parallel (have the same properties).

To calculate the effective permeability of a grid block, the parallel plate flow methods, originally presented by Snow (Snow, 1968 and Snow, 1969), were extended to include multiple fracture sets at arbitrary fracture orientation following the method developed by Chen et al. (1999). The effective permeability is the permeability of a FCM grid block that results in the same flow between the opposite block sides as the flow through all the fractures located inside this block under the same pressure difference.

The permeability tensor for each grid cell in the model domain for one fracture set is calculated as follows (Chen et al., 1999):

$$k_{ij} = \frac{b^3}{12d}\begin{bmatrix} (n_2)^2 + (n_3)^2 & -n_1 n_2 & -n_3 n_1 \\ -n_1 n_2 & (n_3)^2 + (n_1)^2 & -n_2 n_3 \\ -n_3 n_1 & -n_2 n_3 & (n_1)^2 + (n_2)^2 \end{bmatrix} \quad (8\text{-}5)$$

where k_{ij} is the permeability tensor, b is fracture aperture, d is fracture spacing, and $n_{1,2,3}$ is the unit normal to the fracture plane in the x, y, and z direction, respectively.

The unit normal components to the fracture plane are calculated as:

$$\begin{aligned} \mathrm{n_1} &= \cos\left(\alpha\frac{\pi}{180}\right) * \sin(\omega\frac{\pi}{180}) \\ \mathrm{n_2} &= \cos\left(\alpha\frac{\pi}{180}\right) * \cos(\omega\frac{\pi}{180}) \\ \mathrm{n_3} &= -\sin(\alpha\frac{\pi}{180}) \end{aligned} \quad (8\text{-}6)$$

where α is the fracture plunge (90^0 - dip) and ω is the fracture trend (strike - 90^0).

In the case of multiple fracture sets, the permeability tensor can be computed by summing the permeability tensors for individual fracture sets as follows:

$$\mathrm{k_{ij}^{*}} = \sum_{\mathrm{m=1}}^{\mathrm{N}} \mathrm{k_{ij}^{m}} \quad (8\text{-}7)$$

where N is the number of fracture sets and k_{ijm} is defined by Equation (8-5). This is schematically shown in Figure 8-11 for two fracture sets.

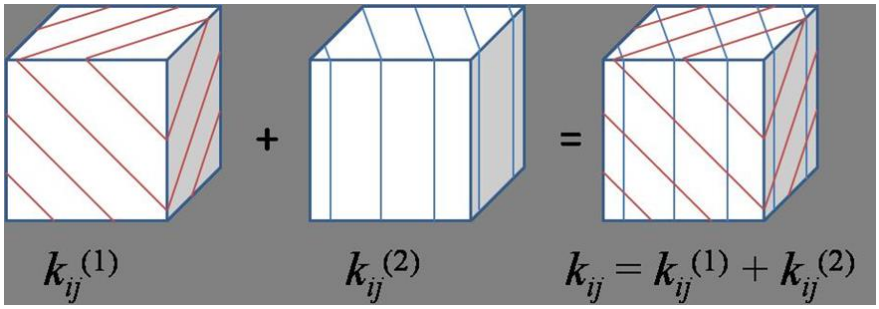

Figure 8-11. Permeability of a Grid Block with Two Fracture Sets.

Note that only k_{xx}^*, k_{yy}^*, and k_{zz}^* components of the permeability tensor are used in the flow and transport model. The k_{xxm}, k_{yym} and k_{zzm} values are calculated for each grid block based on the fracture aperture, spacing, strike, and dip as described by Eqs. (8-5) - (8-7).

In FY16 the FCM was modified to incorporate calculation of the effective porosity of the FCM grid blocks with fractures. This modification is important for transport simulations. The effective porosity of a grid block (n_i) is calculated as:

$$n_i = \frac{\sum V_f}{V_{gr}} \qquad V_f = A_f \cdot b_f \tag{8-8}$$

Where $\sum V_f$ is the total volume of all the fractures in the grid block, V_{gr} is the volume of the grid block ($dx \cdot dy \cdot dz$), A_f is the fracture area, and b_f is the fracture aperture. The fracture area is calculated based on the fracture orientation in the grid block. Consequently, the transport in the grid blocks with fracture is only within the fraction of the grid block representing the total fracture volume in this block. The transport in the grid block without fractures is within the pore volume defined by the matrix porosity. Same value of matrix porosity is defined for all matrix blocks.

As it was described above, FCM calculates effective permeability and porosity of each grid block from specified fracture properties. It is important to understand that the assumptions and conceptual representation of fracture network from which these properties are derived are very different.

8.2.2 Generation of Fracture Network for FCM

In the FY15 study, the modified Sequential Gaussian Simulation (SGSIM) approach was used to generate fracture properties of each grid block of FCM. The SGSIM method does not require an assumption regarding the fracture shape. Fracture aperture, spacing, and orientation are defined based on the probability distributions obtained as a part of field observations. Spatially correlated features (continuation of fracture in the direction of the orientation) are created using spatially correlated random numbers generated with SGSIM code.

The original SGSIM method was modified to be more comparable to the DFN assumptions. The Poison distribution was used to calculate the number of fractures in a grid block. Correlation ranges were set equal to a representative fracture radius. Correlation angle was set equal to a representative fracture set orientation. Fracture aperture was calculated from fracture radius. Fracture strike and dip were defined with univariate Fisher's distribution. Even with these modifications, FCM and DFN were hard to compare (Wang et al., 2015).

The major goal of the FY16 study was to develop, test, and incorporate into FCM the fracture generating methods that would use the same or very similar assumptions as the DFN. Two such methods were developed. The first method uses modified ELLIPSIM (Deutsch, 1998) to generate fracture network. The second method uses the fracture network generated by DFN. The properties of the fracture network are converted into the FCM inputs (fracture aperture, spacing, dip, and strike), which are then used to calculate the effective permeability and porosity of the FCM grid blocks. The conceptual diagram of this process is shown in Figure 12. The details of the two methods are provided below.

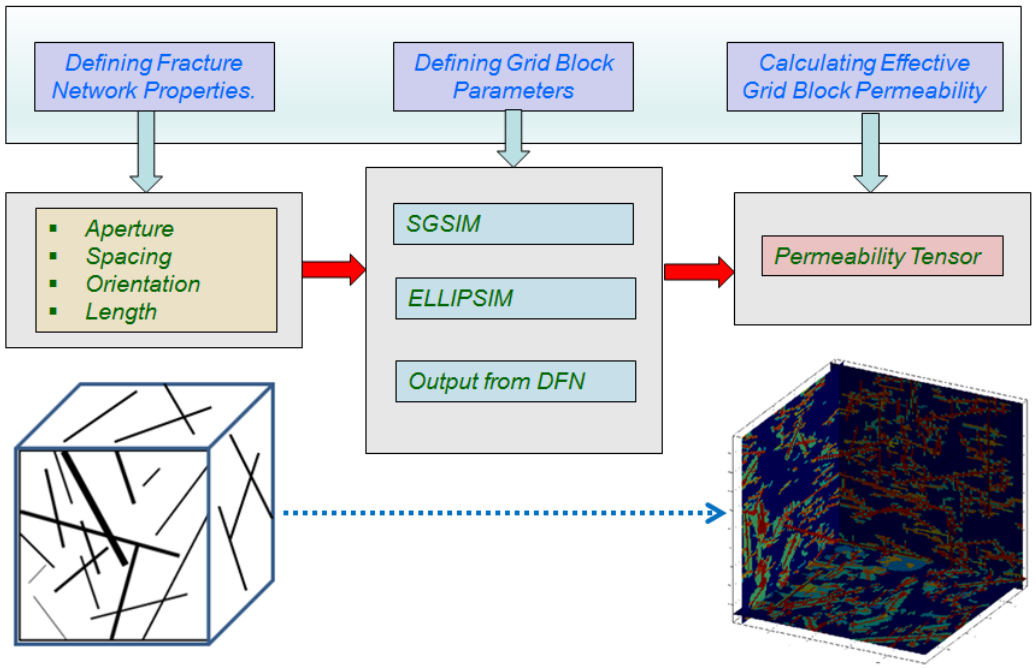

Figure 8-12. Diagram of FCM Methods for Generating Permeability Field from Fracture Network Parameters.

Generating Fracture Network with ELLIPSIM: ELLIPSIM is a Boolean simulation program available from GSLIB library (Deutsch, 1998). The program generates ellipsoids of various sizes and anisotropies and places them at random until target proportion of points in the domain is filled with ellipsoids. A number of modifications were done to ELLIPSIM to incorporate the fracture network generation algorithm similar to DFN.

The new version of ELLIPSIM generates a specified number of ellipses (fractures in the fracture set). The ellipse radius is drawn from the truncated power-law distribution (Eq. 8-1): The ellipse orientation is drawn from the triangular distribution approximating Fisher's distribution (Eq. 8-2). The grid blocks located within a specific ellipse are assigned the radius and orientation of this ellipse. The grid blocks that do not belong to any ellipse are considered to be matrix blocks.

Figure 8-13 (top) shows the examples of three ELLIPSIM runs. The first run generated vertical north-south trending fractures. The second run generated vertical east-west trending fractures. The third run generated horizontal west-east trending fractures. Figure 8-13 (bottom) shows all three fracture sets combined. Figure 8-14 shows the triangular distribution that approximates Fisher's distribution (Eq.8-2) with κ =22.

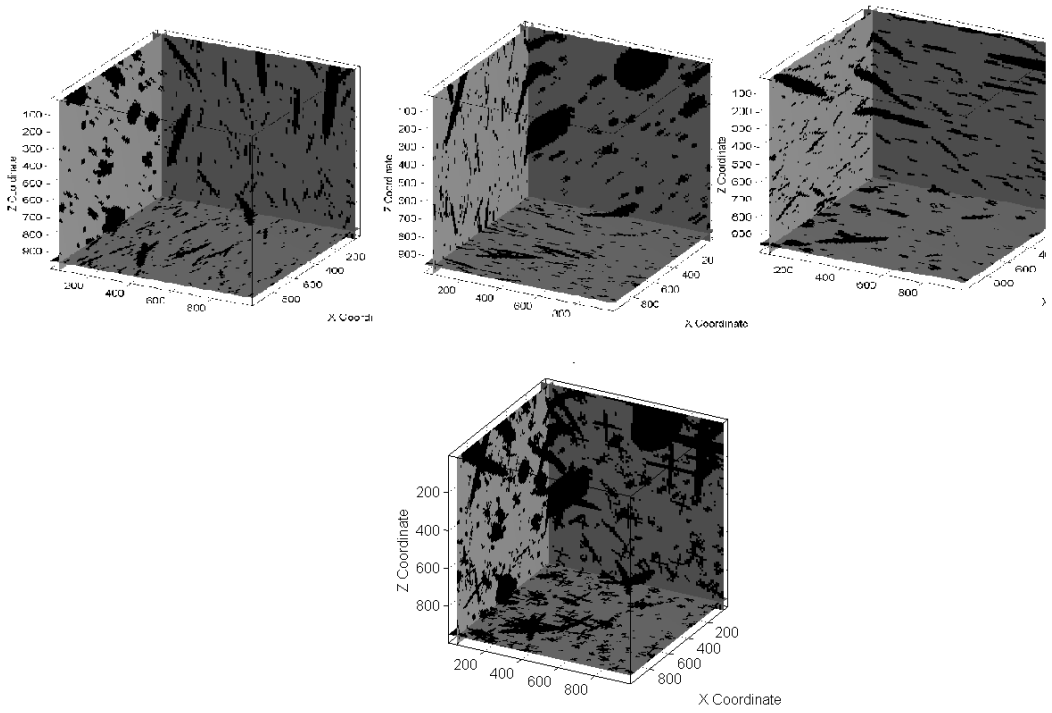

Figure 8-13. Example of Three Fracture Sets Generated with ELLIPSIM.

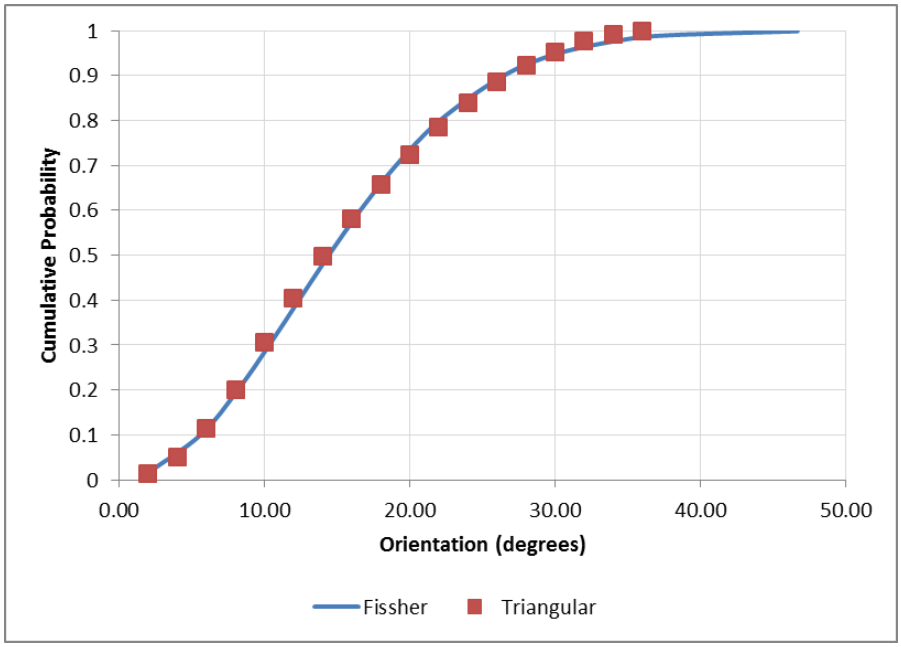

Figure 8-14. Triangular and Fisher's Cumulative Probability Distributions of Fracture Orientation.

The output from ELLIPSIM contains fracture radius and orientation for each grid block with ellipse for one fracture set. This fracture orientation is converted to the fracture dip and strike. The fracture radius (R) is used to calculate fracture aperture (b) with Eq. (8-3) and (8-4). The fracture spacing is assumed to be equal to the block size. This equals to having one fracture in the grid block.

FCM uses these data (aperture, dip, strike and spacing for each fracture set) to calculate the effective permeability values [Eq. (8-5) - (8-7)] and effective porosity [Eq. (8-8)] of the grid blocks with fractures. This process is schematically shown in Figure 8-15. The grid blocks without fractures are assigned permeability equal to matrix permeability and porosity equal to matrix porosity.

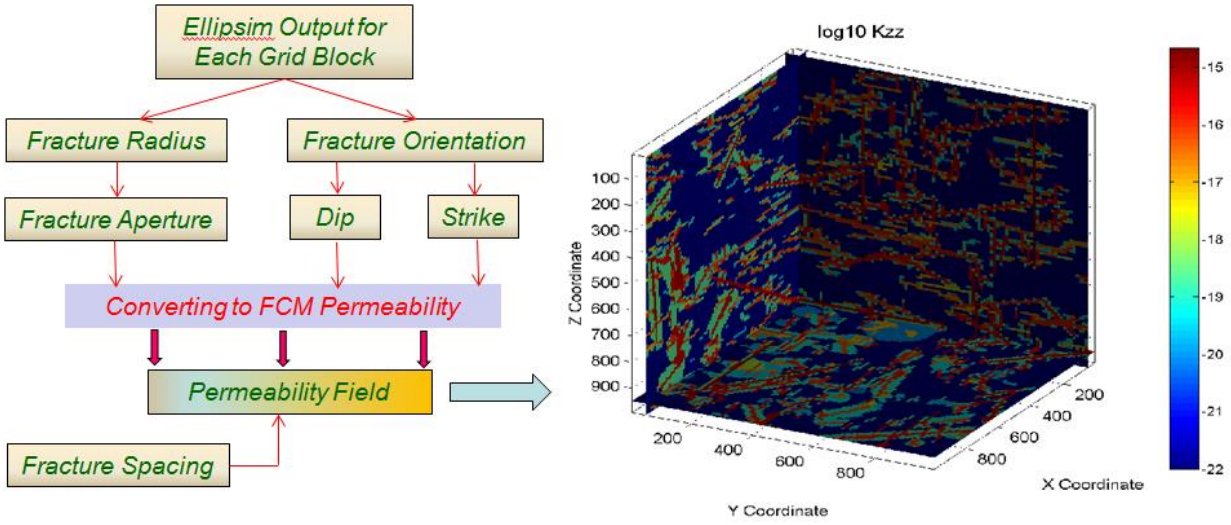

Figure 8-15. Converting ELLIPSIM Output to FCM Effective Grid Block Permeability and Effective Grid Block Porosity.

An example of the permeability field calculated for the fracture network shown in Figure 8-13 is demonstrated in Figure 8-16. The k_{xx}, k_{yy}, and kzz permeability values are shown. The matrix permeability is 1×10^{-22} m^2.

Note that permeability fields generated using output from ELLIPSIM does not necessarily assure that the grid blocks with fractures are connected from one side of the modeling domain to another. The matrix grid blocks provide the continuity of the flow and transport. Conceptually, the matrix blocks can represent the smaller fractures that are not included in DFN.

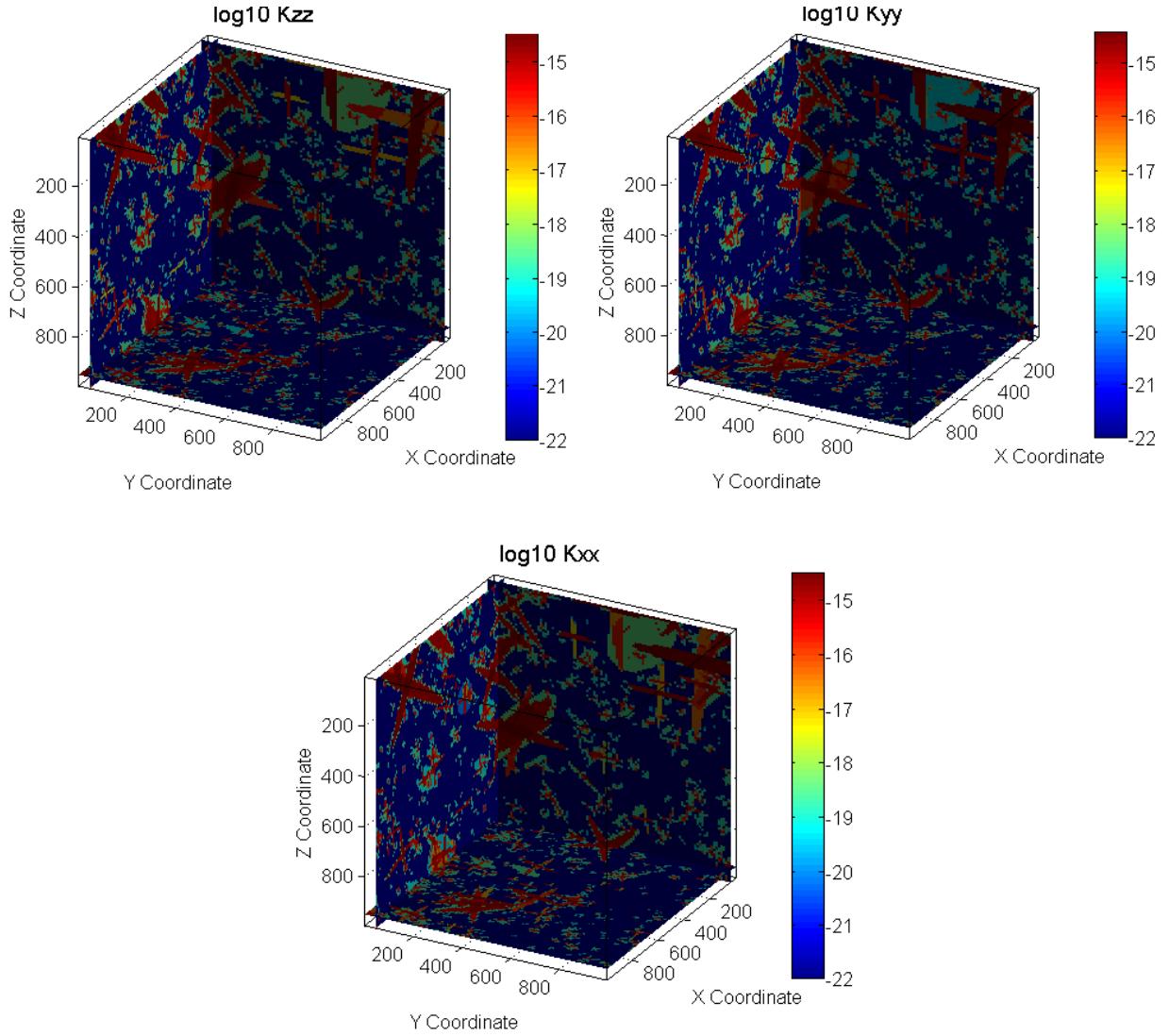

Figure 8-16. k_{xx}, k_{yy}, and k_{zz} Permeability Fields for the Fracture Network Shown in Figure 8-13.

Generating Fracture Network from DFN Output: The fracture networks generated with ELLIPSIM are based on the same assumptions as DFN with one exception. As it was discussed in the previous section, the connectivity of the grid blocks with fractures from one side of the modeling domain to another side is not warranted. For the sake of more direct comparison with DFN, the capability of converting the fracture network generated by DFN into the inputs for FCM was developed. This capability also allows for comparing the same realization of the fracture network.

The fracture network generated with DFN is first converted into a continuum grid as described in Section 8.1.4. The output of this conversion contains fracture aperture and normal components to the fracture plane for each grid block with fractures. These data are converted into the FCM input (fracture aperture, dip, strike and spacing) and used to calculate the effective permeability and effective porosity values of the grid blocks with fractures. This process is schematically shown in Figure 8-17. The grid blocks without fractures are assigned permeability equal to matrix permeability and porosity equal to matrix porosity.

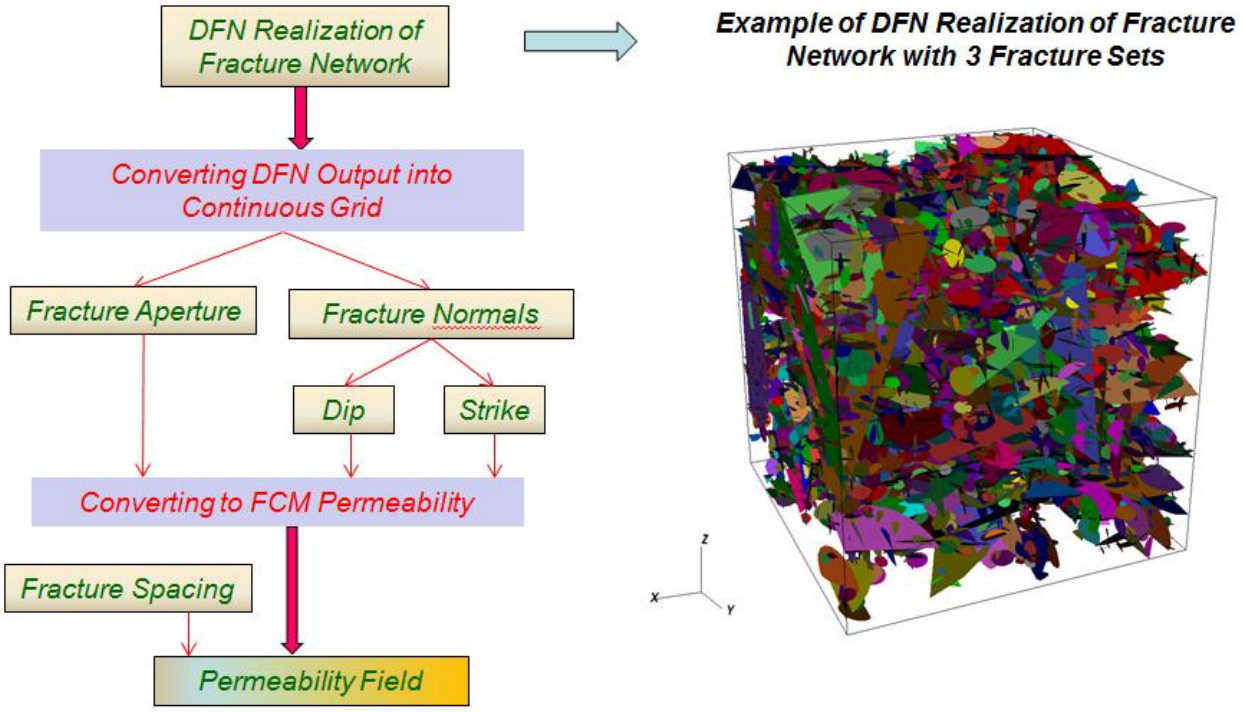

Figure 8-17. Converting DFN Output to FCM Effective Grid Block Permeability and Effective Grid Block Porosity.

8.2.3 Generating Fracture Networks for FCM-DFN Comparison

The fracture networks for FCM were generated using a few different methods as described below. This was dictated by the different approaches used to compare FCM and DFN. The first approach used to compare FCM and DFN is the most direct one. In this approach a DFN realization of the fracture network is used to generate the FCM permeability and porosity fields (Section 8.2.2). This approach eliminates uncertainty in generating fracture network. The only difference is between explicit (DFN) and effective (FCM) representation of fracture network. Effective permeability of the modeling domain and breakthrough curves can be compared for each realization. Because the DFN generates connected fracture network, the FCM network is also connected. Five DFN realizations were selected for this comparison.

The second approach is indirect one. It compares 25 realizations of the fracture network generated with DFN (Section 8.2.2) to 25 realizations generated with ELLIPSIM. This approach evaluates the major difference in the conceptual models, for example, fracture network connectivity. As it was discussed earlier, the DFN fracture networks are directly connected and the FCM connectivity might be partially through matrix. The effective permeability of the modeling domain and breakthrough curves have to be compared statistically.

Note that the probability distributions of fracture radius defined in Table 8-1 for three fracture sets need to be modified to produce fracture networks similar to DFN. This is because DFN fracture network is generated iteratively. The process starts with number of fractures significantly larger than the number of fractures in the fracture sets (~18,000 fractures compared to 6,400). The iterations are needed to remove not connected clusters of fractures and assure fracture connectivity. This process changes the original probability distributions of fracture radius.

An example is shown in Figure 8-18. The original fracture radius distributions are power-law distributions with parameter *a* equal to 2.5, 2.7 and 2.4 for north-south vertical, east-west vertical, and west-east horizontal fracture sets respectively. The power-law distribution with parameter *a* =2.5 is compared in Figure 8-18 to the radius distributions sampled in the five DFN realizations. The sampled radius distributions are closer to the power-law distribution with parameter *a* =1.9. However, the sampled distribution deviates from power-law as well. The new distributions have larger proportion of longer fractures and smaller proportion of shorter fractures. The final number of fractures generated by DFN is slightly different than in Table 8-1. The differences between the sampled distributions are very small. This indicates that the iterative process is stable.

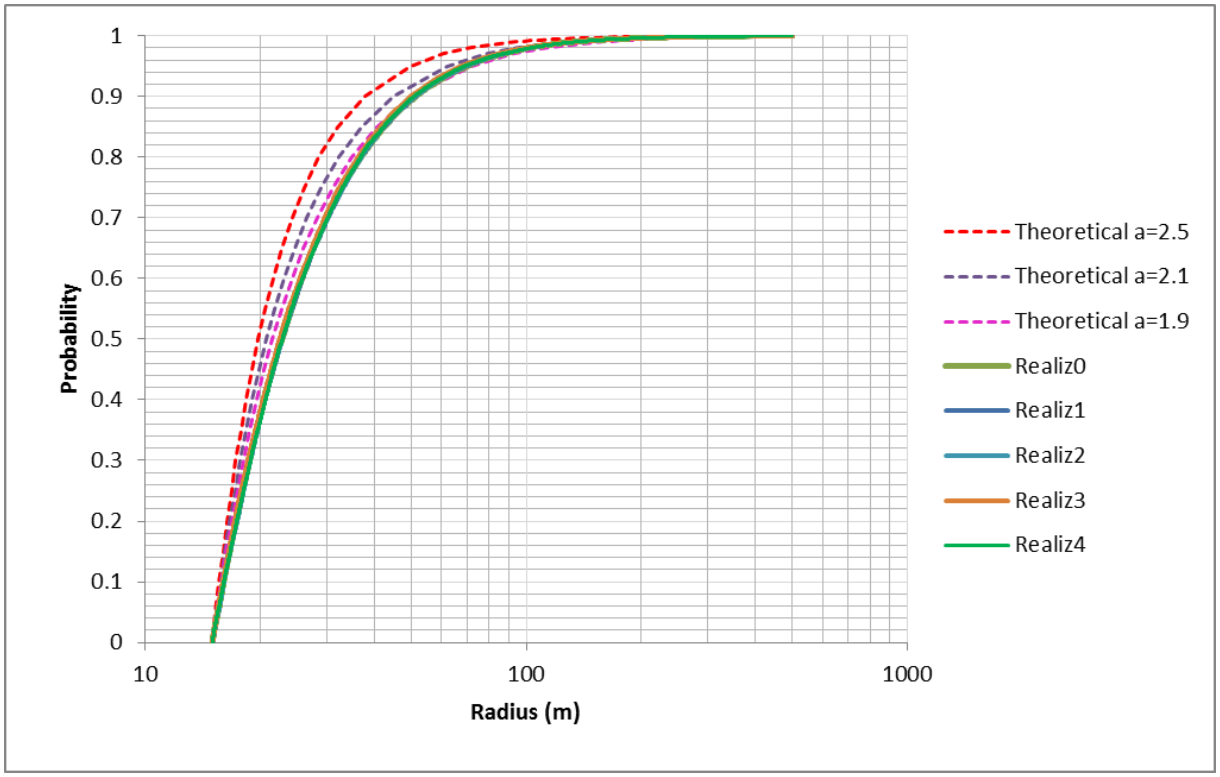

Figure 8-18. Theoretical Power-Law Distributions with Different Parameter and Sampled by DFN Distributions of Fracture Radius.

Table 8-2 summarizes the property of the five DFN generated fracture networks. Note that the number of grid blocks with fractures is approximately 34% of the total number of grid blocks.

Table 8-2. Fracture Properties of the Five DFN Generated Fracture Networks.

Realization	**0**	**1**	**2**	**3**	**4**
Number of fractures	6,531	6,700	6,523	6,715	6,574
Number of grid blocks with fractures	334,154	343,390	332,334	339,531	335,832
Effective permeability (m^2)	3.77E-17	4.24E-17	4.28E-17	3.81E-17	3.35E-17
Total volume of fractures (m^3)	977.84	988.32	994.07	1,008.30	1,022.94

To make an adequate comparison with DFN, the radius distributions and the number of fractures used to generate fracture networks with ELLIPSIM have to be modified. The effective permeability of the modeling domain can serve as the indicator of comparability.

The fracture parameters were modified iteratively. Each network generated with ELLIPSIM was then used in the PFLOTRAN flow simulation to determine the effective permeability. The parameters that were varied from one iteration to another were the parameter *a* and the number of fractures in the fracture set. The fracture sets had the same *a* and number of fractures. The fracture parameters that resulted in the effective permeability of 3.99 m^2 (*a* equal to 2.3 and number of fractures equal to 4,600) were then used to generate 25 realizations of the fracture network. The discussion of the results for these realizations is provided in Section 8.2.

Finally, ELLIPSIM was used to generate the fracture network with the original fracture parameters as defined in Table 8-1. The example of one of the realizations is shown in Figure 8-19. Also shown in this figure is the fracture network obtained with the modified radius distribution described above. The same seed was used to generate these networks. All the parameters, except parameter *a* and number of fractures in the set were the same as well. The original distribution results in a significantly more sparse fracture network.

50 realizations were generated then using the fracture network with the original fracture parameters. Only 6 realizations out of 50 resulted in the effective permeability noticeably higher than the matrix permeability. This is the indication of sufficient connectivity between the fractures. Based on these preliminary results, the probability of the fracture network to be connected (convey flow from one side of the model to another one) is about 12%. The discussion of the results for these realizations is provided in Section 2.3.

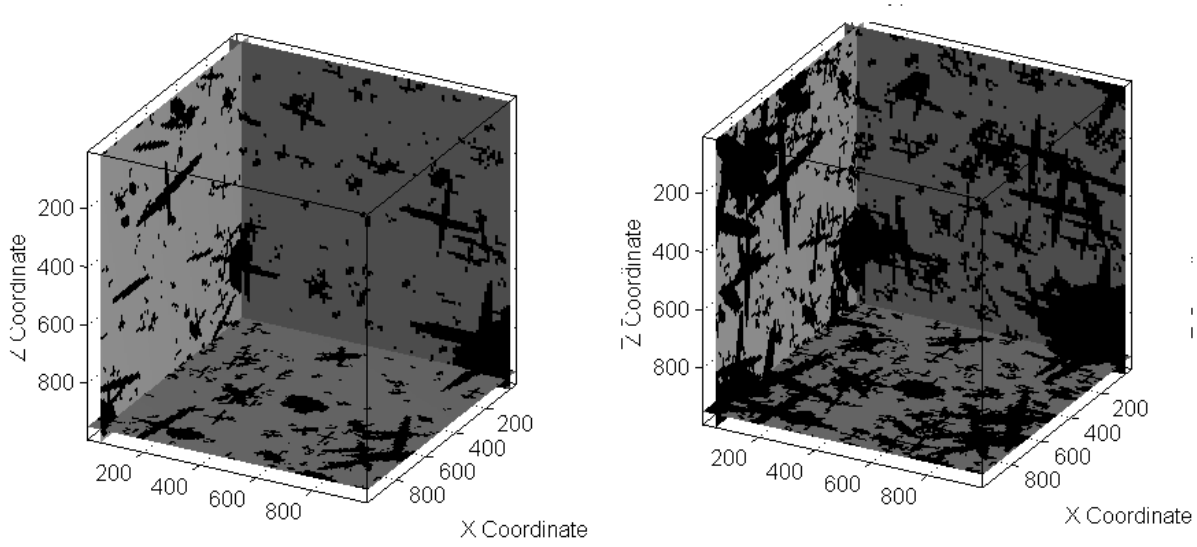

Figure 8-19. Fracture Network with Original (left) and Modified (Right) Fracture Parameters.

8.3 FRACTURE CONTINUUM MODEL SET-UP AND RESULTS OF DFN-FCM COMPARISON

For the DFN-FCM comparison a model geometry of 1 km x 1 km x 1 km was selected. For the FCM approach a constant grid block size of 10 m x 10 m x 10 m was used resulting in a mesh size of 10^6 grid blocks. Figure 8-20 shows the mesh used for the FCM approach. Fracture parameters and statistical data used for the different modeling tasks are described in Section 8.2.

Flow boundary conditions
For both the DFN and FCM fluid moves in the fractured rock from west face (x=0) to east face (x=1 km) as a result of applied pressure gradient. The flow boundary condition used includes a pressure of 1.001 MPa on the west face and 1.0 MPa on the east face. The rest of the faces are at no flow boundary condition. For this work the system is assumed to be at isothermal conditions of 25°C temperature. Flow and transport in the DFN model are through fractures-only while the FCM allows both fracture and matrix participation. To allow comparison of DFN and FCM results advection through matrix rock was minimized by using matrix permeability of 10^{-22} m^2. The boundary conditions set for flow and transport include outlet on the east face and no flux on the rest of the faces. For the comparison steady state flow solution will be obtained and the flow field will be used for the transport part of the simulations. For the DFN-FCM comparison the effective permeability will be calculated using Darcy's law and steady state east face flux.

Transport boundary Conditions
For the FCM approach tracer is transported by advection through fractures and diffusion through matrix rock. The DFN-FCM comparison requires minimizing matrix diffusion. For transport a pulse injection of tracer was applied at the center of the west face in the region (0,450,450) - (0,550,550). A concentration of 1 mol/L was prescribed at the pulse injection location. A background concentration of 1e-8 mol/L was applied elsewhere in the domain. Transport in the fractured rock is simulated using the steady state flow field and the concentration gradient. For DFN-FCM comparison breakthrough curves (relative concentration) on the east face will be analyzed.

For the FCM simulations the PFLOTRAN numerical software (Hammond et al., 2014) was used. Use of PFLOTRAN allowed for high performance parallel computing utilizing many processors. To summarize, the quantities of interest for the FCM and DFN comparison are: 1) effective permeability, and 2) east face breakthrough curves.

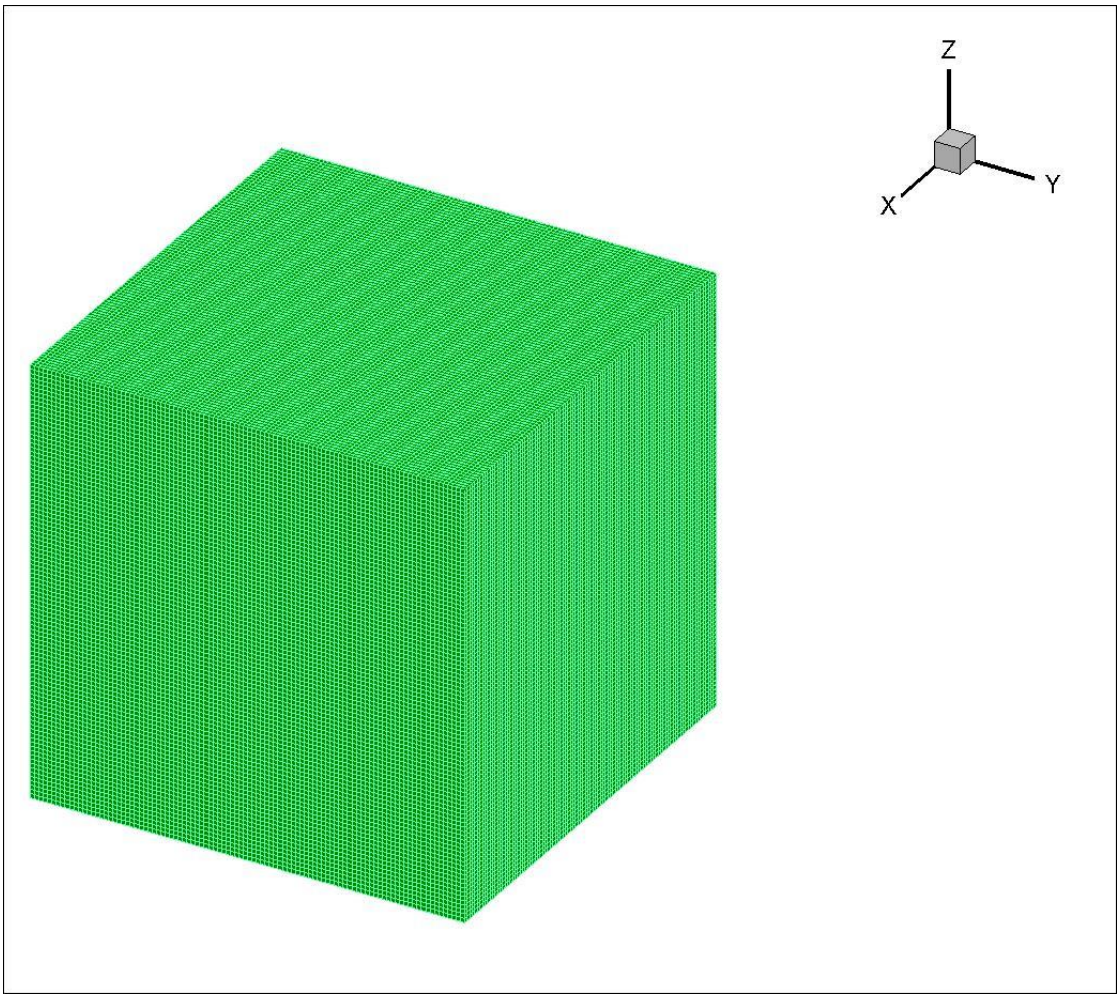

Figure 8-20. Structured mesh with 10^6 grid blocks

The simulation analysis utilized various modeling methods to test capabilities of the DFN and FCM fracture models. For the FCM simulations the different fracture characterization methods described in Section 8.2 were used. Simulations using each method is described below.

8.3.1 Direct DFN-FCM comparison using DFN Generated Fracture Output

DFN generated fracture data were used to obtain FCM permeability and porosity fields for direct comparison between DFN and FCM output (Section 8.2.3). As an example permeability and porosity fields for Realization 0 are shown in Figures 8-2 and 8-3, respectfully. PFLOTRAN flow and transport simulations were carried out using the resulting permeability and porosity fields. As outlined above one of the metrics for DFN and FCM comparison is the effective permeability. Effective permeability was calculated using Darcy's law and liquid flux at steady state:

$$q = \frac{-k_{eff}\Delta P}{\mu L} \qquad (8\text{-}9)$$

where

q = flux,
k_{eff} = effective permeability,

ΔP = pressure difference between west and east faces (1000 Pa)
μ = dynamic viscosity
L = distance between west and east faces (1000 m)

Equation (8-9) was then used to estimate the effective permeability values using flux output on the east face for the 5 DFN realizations. Table 8-3 shows the effective permeability values predicted for the 5 DFN realizations using DFN and FCM output. The calculated values of DFN and FCM are in excellent agreement indicating that the modified FCM reproduced the fracture network as in DFN. The slight differences reflect the difference between explicit (DFN) and effective (FCM) representation of fracture network. The DFN method was then used to generate effective permeability values for an additional 20 realizations. Table 8-4 shows DFN effective permeability values for the total 25 realizations. The values of the additional 20 realizations are in the same range as the first 5.

Figure 8-21 compares the DFN and FCM effective permeability for 25 realizations. The mode of the distributions is the same. The difference is on the high end of the distribution tails. As it was explained in Section 8.2.3, the fracture distributions used in ELLIPSIM to generate fracture network were modified to match the radius distributions sampled by DFN. However, the modified distributions in ELLIPSIM are the power-law distributions. The DFN radius distribution deviates from power-law.

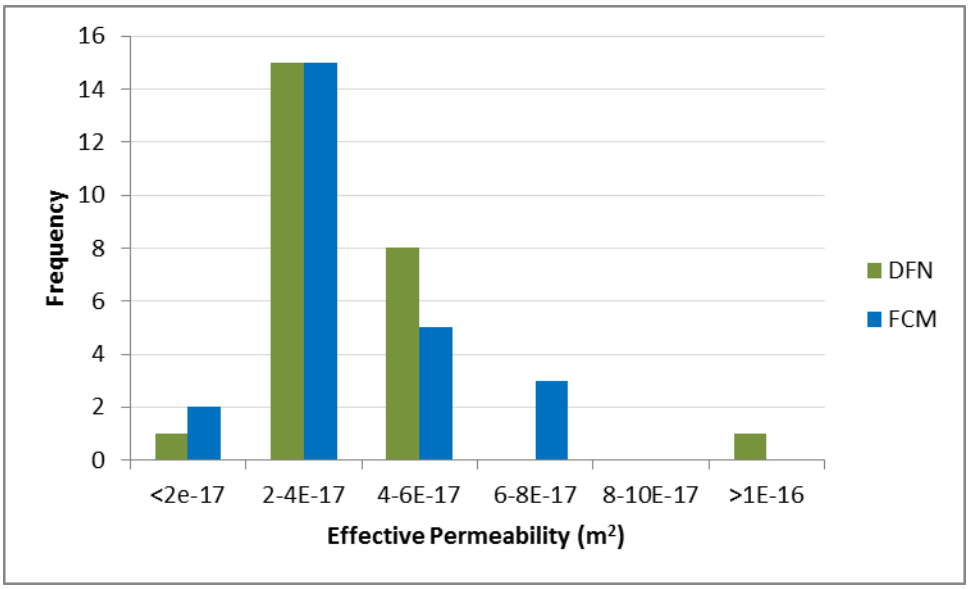

Figure 8-21. Comparison of the Effective Permeability Values Calculated with DFN and FCM.

The steady state flow fields and generated porosity fields were utilized in the simulation of transport. To make a comparison of DFN and FCM transport output the matrix rock was deactivated in the FCM simulations. This is because as porosity is important for transport it was necessary to make sure that matrix diffusion did not occur. This was done by either through the use of very small diffusion coefficient or deactivating the matrix blocks (with permeability = 10^{-22} m^2), which is one of the features of PFLOTRAN. Figures 8-22 to 8-24 show tracer distributions at different simulation times for Realization 0. Notice that transport occurs in the fractures only because of the deactivation of the matrix rock. For the comparison of transport output of DFN and FCM tracer concentrations at the east face as a function of time were reported. Normalized breakthrough (concentration at east face divided by concentration at west face at each time) for each realization was then plotted for FCM. Breakthrough output of the DFN method using both advection-diffusion (PFLOTRAN) and particle tracking options were also obtained. The

results for the 5 realizations are shown in Figures 8-25 to 8-29. As with the effective permeability values the breakthrough curves are in close agreement. This indicates that the modified FCM code can reproduce DFN output when DFN generated fracture data are used. This is one of the capabilities described in Section 8.2.2. Note that the first arrival times of FCM and DFN particle tracking curves are very similar for most of the 5 realizations. The late times for FCM look delayed and smeared compared to DFN with particle tracking which could be a result of numerical dispersion. In addition, the DFN advection-diffusion results seem to indicate numerical dispersion when compared to the DFN with particle tracking. Further study will be needed to analyze the differences among the different methods. Breakthrough curves for the 25 DFN realizations have also been obtained for both advection-diffusion method (using PFLOTRAN) and particle tracking method. The results are shown in Figures 8-7 and 8-8.

Table 8-3. DFN and FCM Effective Permeability Values for 5 Realizations.

Realization	DFN Effective Permeability m^2	FCM Effective Permeability m^2
0	3.77E-17	4.60e-17
1	4.24E-17	3.91e-17
2	4.28E-17	4.18e-17
3	3.81E-17	3.62e-17
4	3.35E-17	3.81e-17

Table 8-4. DFN Effective Permeability Values for 25 Realizations.

DFN Run	DFN effective permeability
0	3.77E-17
1	4.24E-17
2	4.28E-17
3	3.81E-17
4	3.35E-17
5	2.54E-17
6	3.82E-17
7	3.68E-17
8	3.26E-17
9	4.41E-17
10	1.48E-16
11	3.98E-17
12	2.54E-17
13	4.95E-17
14	3.61E-17
15	1.79E-17
16	4.20E-17
17	4.77E-17
18	2.34E-17
19	4.69E-17
20	3.12E-17
21	3.78E-17
22	5.38E-17
23	2.43E-17
24	3.88E-17

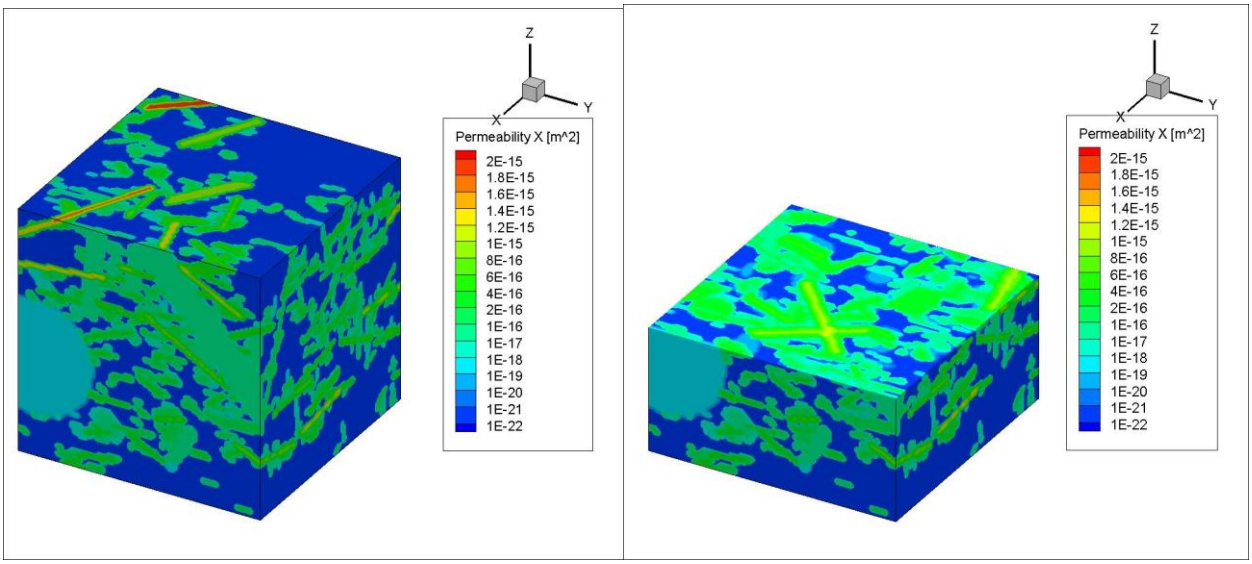

Figure 8-22. FCM permeability field for DFN Realization 0.

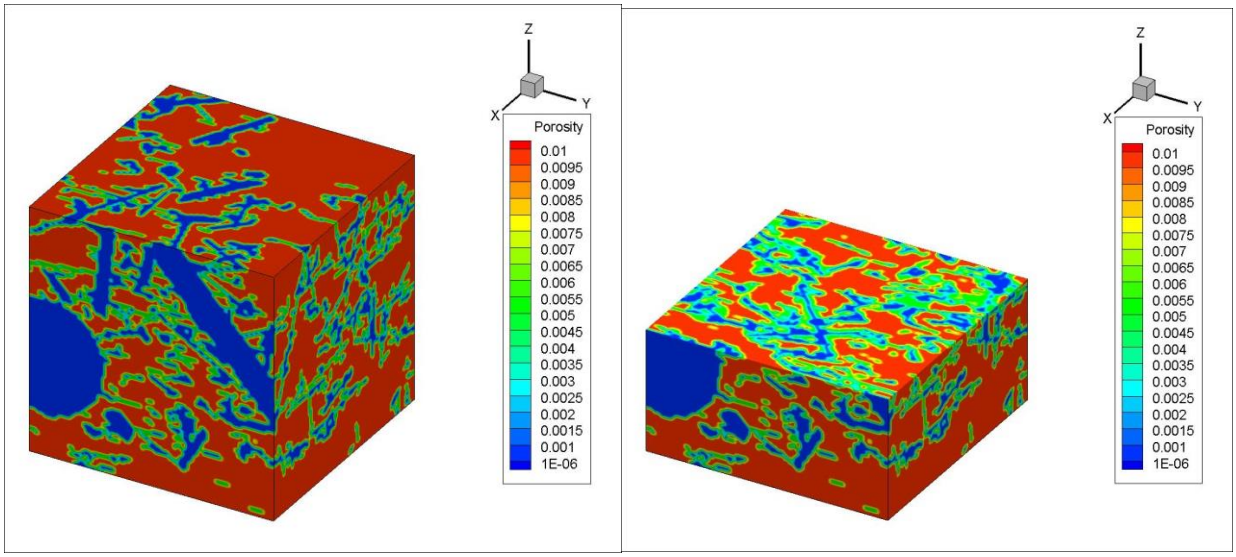

Figure 8-23. FCM porosity field for DFN Realization 0.

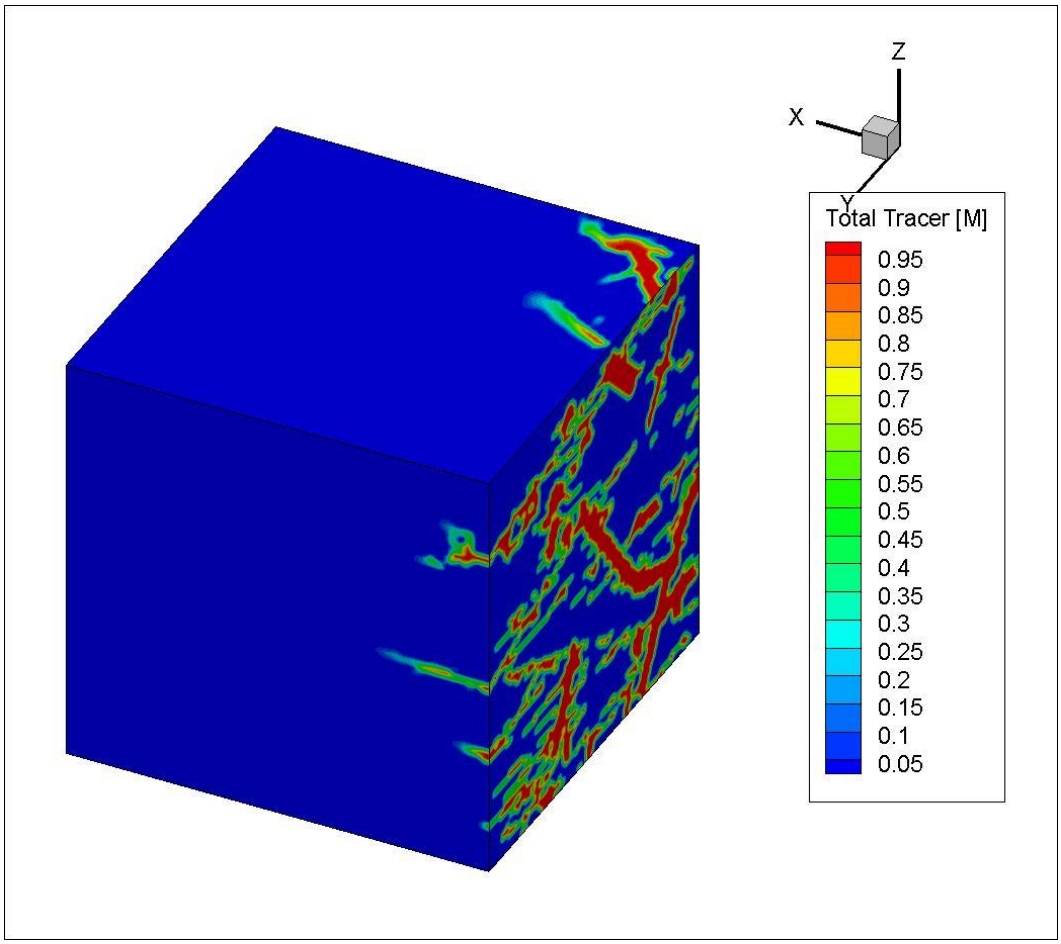

Figure 8-24. FCM tracer transport results for DFN Realization 0 after 70 years of simulation time.

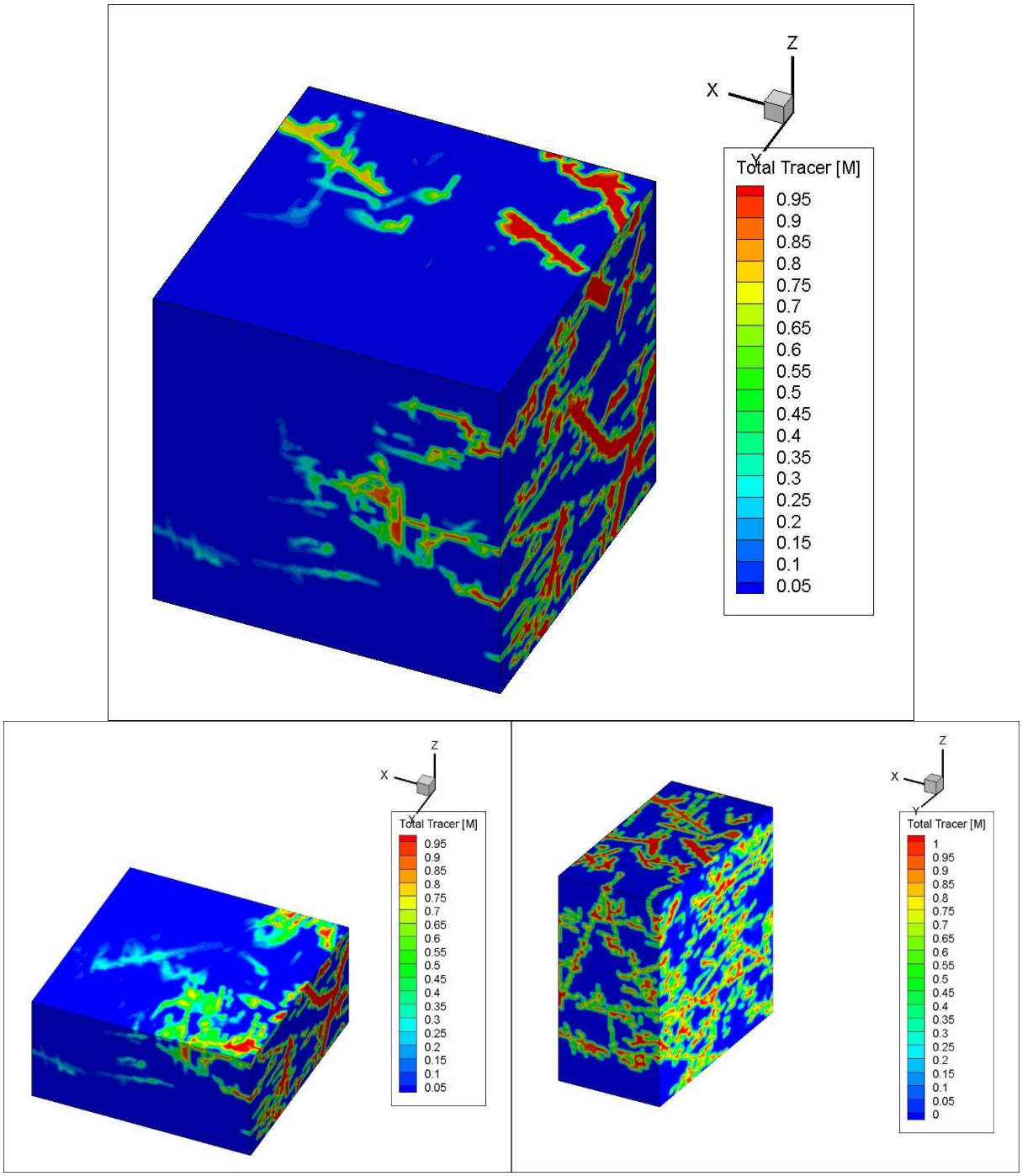

Figure 8-25. FCM Tracer Transport Results for DFN Realization 0 after 400 years of Simulation Time.

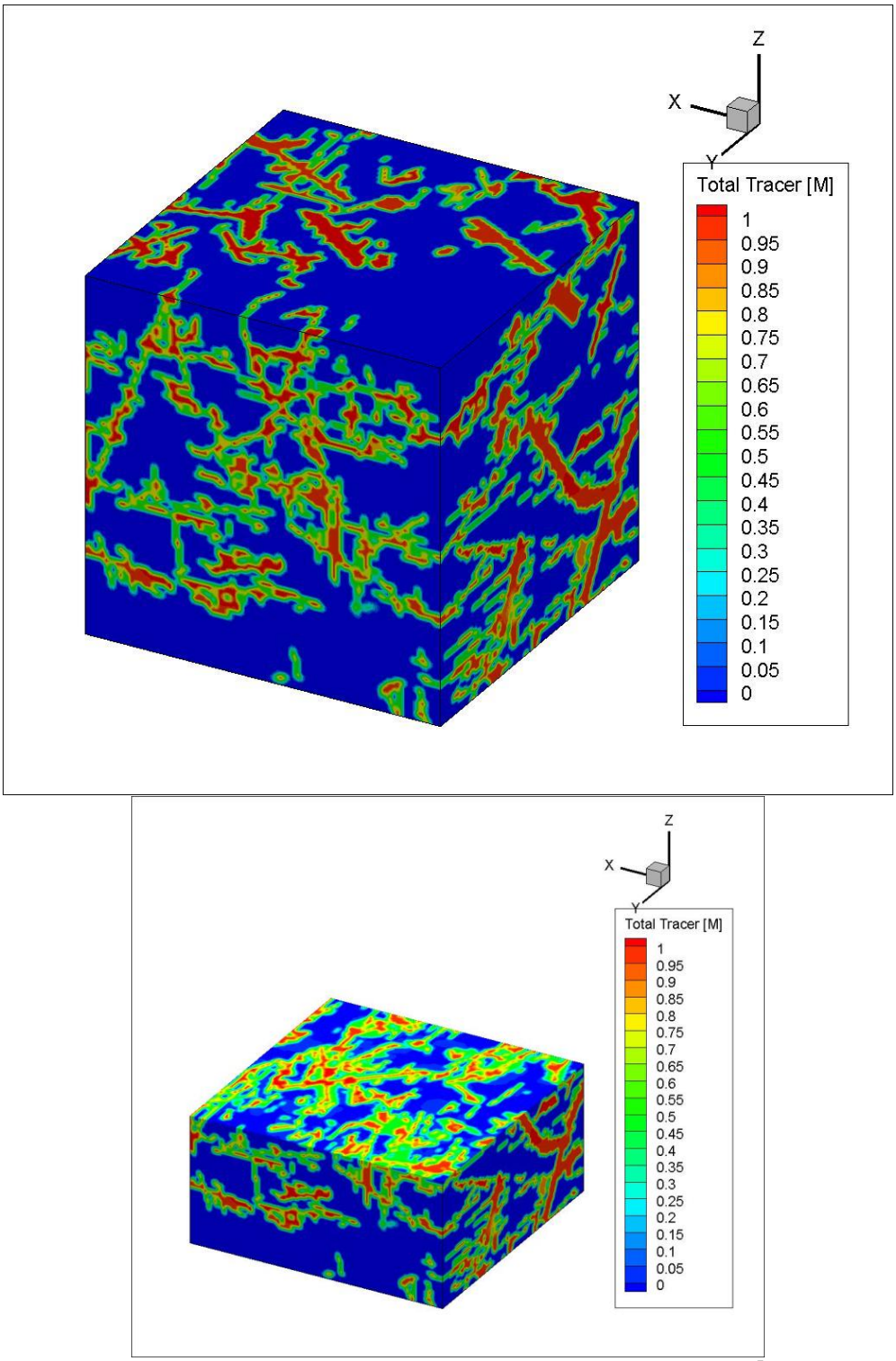

Figure 8-26. FCM Tracer Transport Results for DFN Realization 0 after 1 x 10^5 years of Simulation Time.

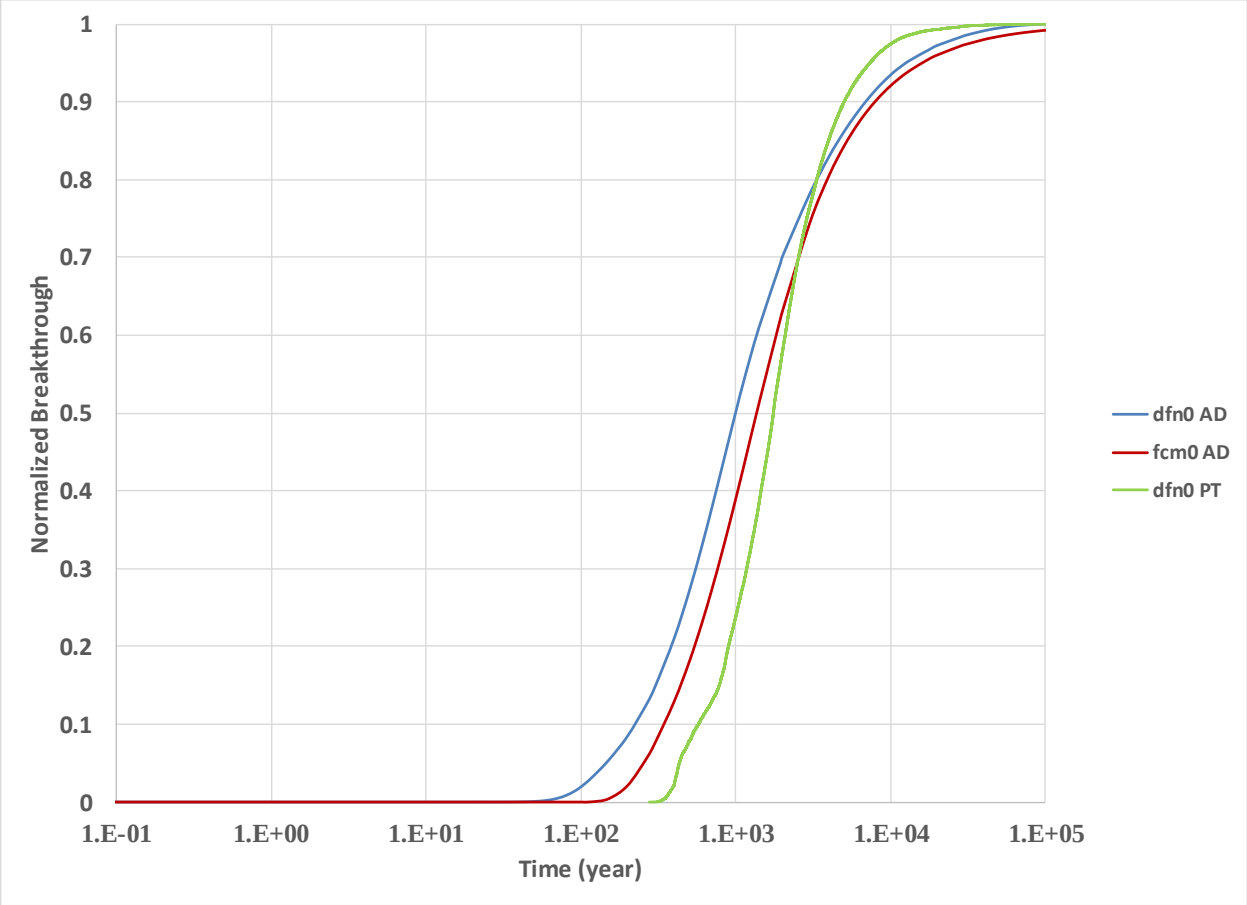

Figure 8-27. Comparison of DFN (Particle Tracking), DFN (Advection-Diffusion, PFLOTRAN) and FCM (Advection-Diffusion, PFLOTRAN) Breakthrough Curves for DFN Realization 0.

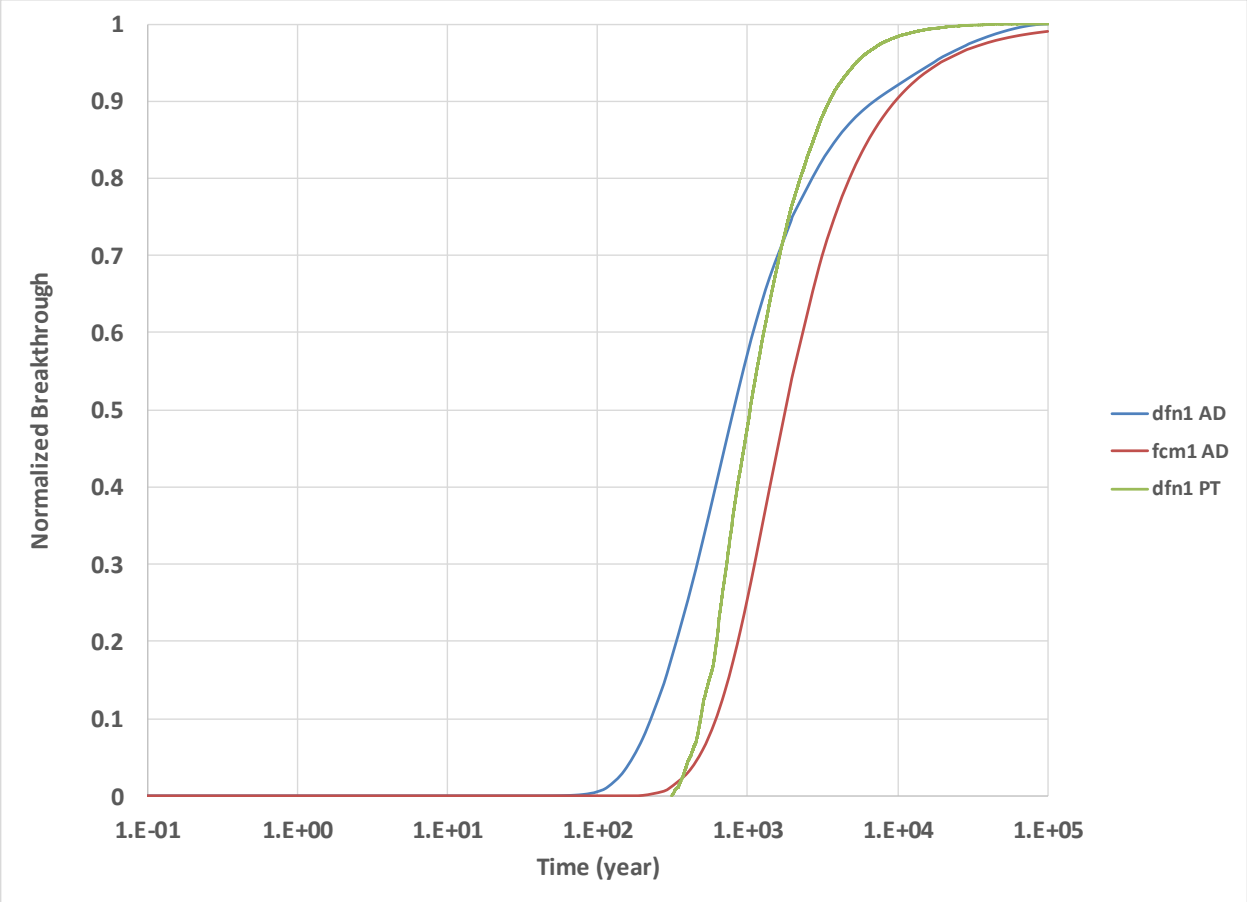

Figure 8-28. Comparison of DFN (Particle Tracking), DFN (Advection-Diffusion, PFLOTRAN) and FCM (Advection-Diffusion, PFLOTRAN) Breakthrough Curves for DFN Realization 1.

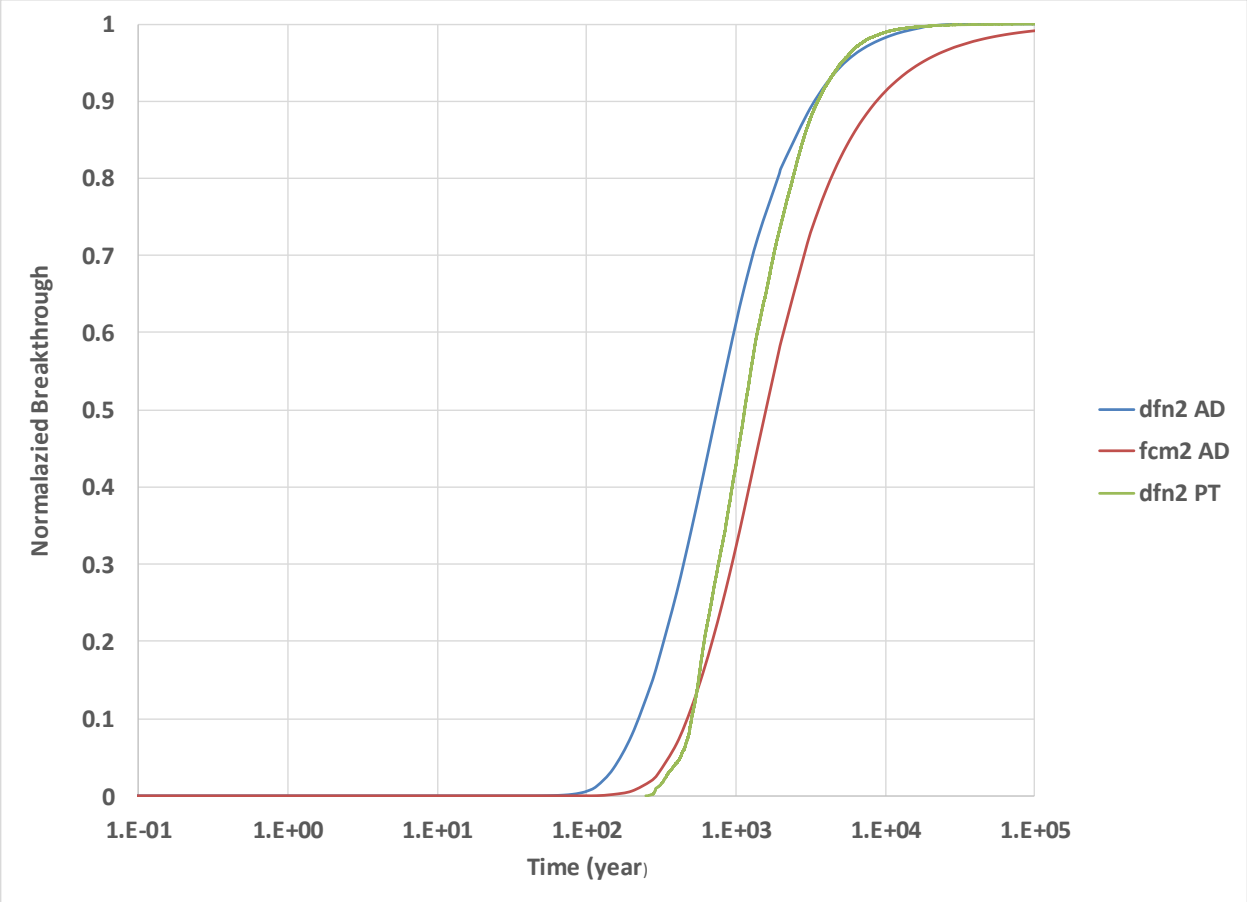

Figure 8-29. Comparison of DFN (Particle Tracking), DFN (Advection-Diffusion, PFLOTRAN) and FCM (Advection-Diffusion, PFLOTRAN) Breakthrough Curves for DFN Realization 2.

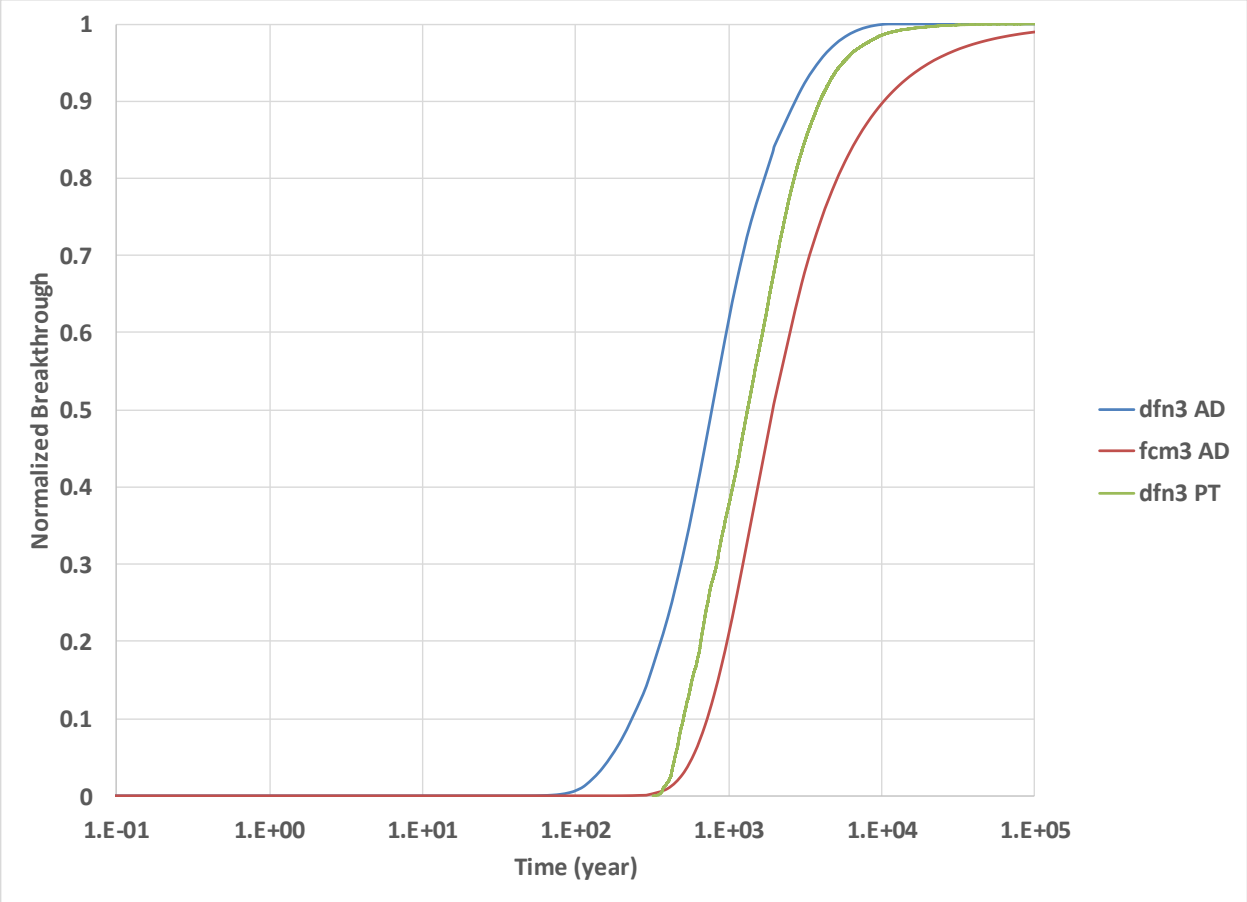

Figure 8-30. Comparison of DFN (Particle Tracking), DFN (Advection-Diffusion, PFLOTRAN) and FCM (Advection-Diffusion, PFLOTRAN) Breakthrough Curves for DFN Realization 3.

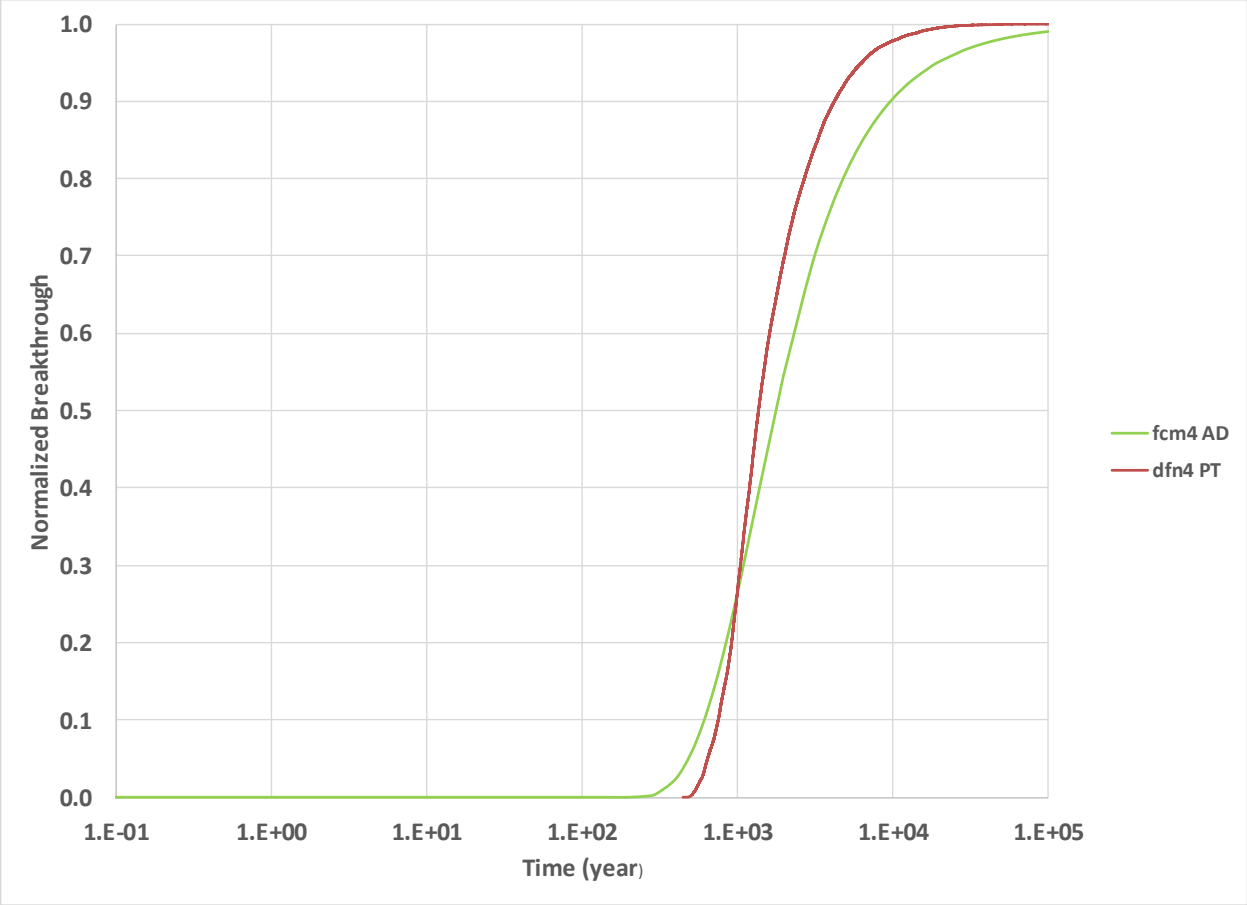

Figure 8-31. Comparison of DFN (Particle Tracking) and FCM (Advection-Diffusion, PFLOTRAN) Breakthrough Curves for DFN Realization 4. DFN (Advection-Diffusion, PFLOTRAN) results were not available for this realization.

8.3.2 Indirect DFN-FCM comparison using DFN and FCM ELLIPSIM

As described in Section 8.2.3, for FCM the original fracture statistical distributions of parameters were modified to generate similar fracture network as in DFN. The modified fracture statistics data were then used to generate 25 realizations of permeability and porosity fields. Flow and transport runs were carried out using the 25 generated permeability and porosity fields as outlined in Section 8.3. As was done in Section 8.3.1 steady state flow in the east face of the domain was used to generate effective permeability for each realization (Table 8-5). The calculated effective permeability values are very similar to those of the DFN approach (Table 8-4 and Figure 8-21). Figure 8-32 shows plots of breakthrough curves from three sources: DFN (Advection Diffusion, PFLOTRAN), modified FCM and the 5 DFN realizations described in Figures 8-27 to 8-31. All the breakthrough curves are very similar. Comparison of the mean DFN and FCM curves based on the advection-diffusion simulation option (PFLOTRAN) indicates that the FCM is slightly delayed.

Table 8-5. Effective Permeability Values for 25 FCM Realizations with Modified Parameter Distributions.

Run for Modified FCM	DFN effective permeability
1	4.96E-17
2	2.47E-17
3	6.15E-17
4	2.76E-17
5	3.87E-17
6	3.87E-17
7	2.51E-17
8	6.86E-17
9	5.39E-17
10	5.54E-17
11	3.24E-17
12	3.19E-17
13	4.97E-17
14	7.22E-18
15	4.02E-17
16	7.91E-18
17	2.01E-17
18	3.35E-17
29	6.35E-17
20	3.40E-17
21	3.26E-17
22	3.33E-17
23	2.46E-17
24	3.24E-17
25	2.76E-17

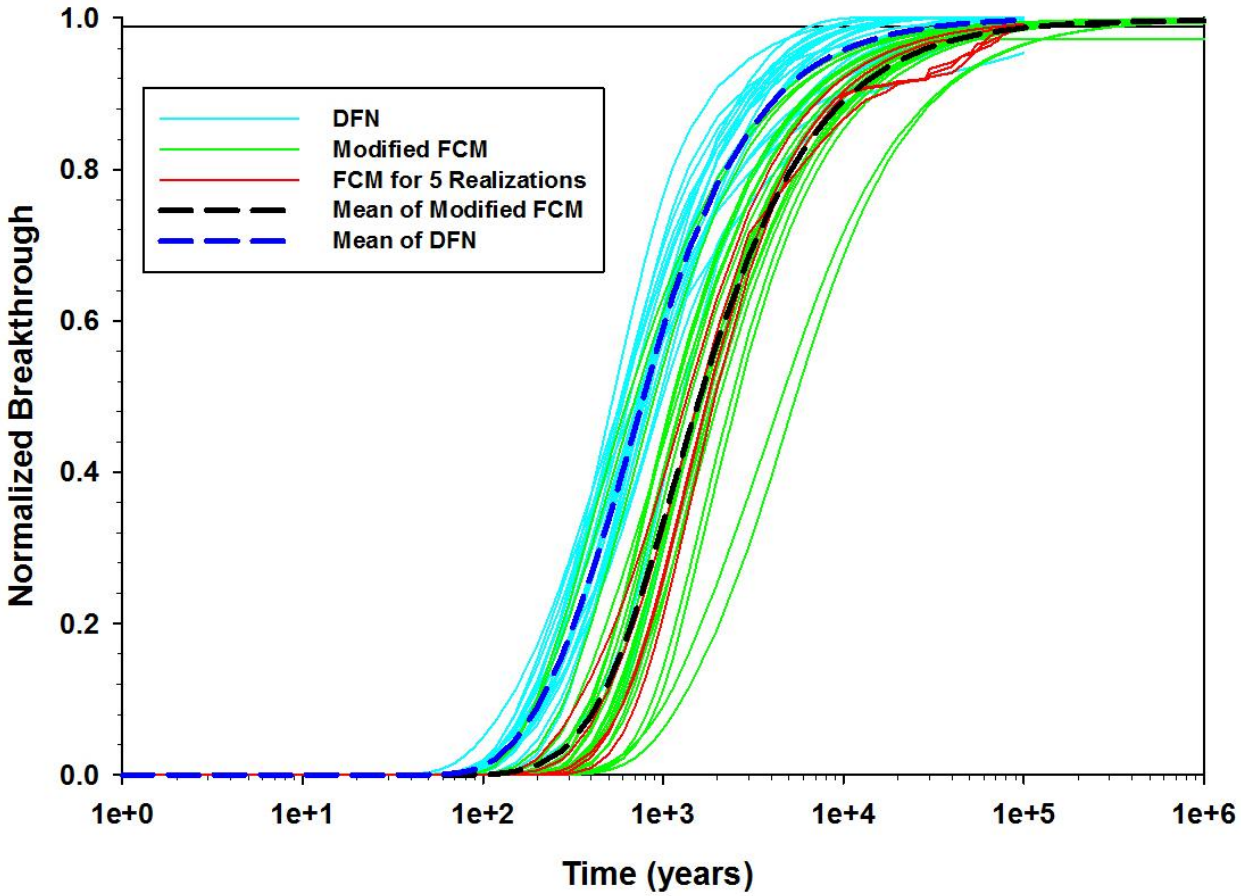

Figure 8-32. FCM (PFLOTRAN) breakthrough curves for DFN (cyan), modified fracture parameters (green) and the five realizations of Figures 37 – 31 (red).

8.3.3 50 Realizations of Fracture Network with the Original Parameter Distributions

As outlined in Section 8.2.3 the fracture networks were also generated using ELLIPSIM with the original fracture parameter distributions as defined in Table 8-1. For this case two groups of 25 realizations were generated to check statistical stability of the sample size. Flow and transport simulations were conducted using the fracture parameters generated as outlined in Section 8.2.3. Note that matrix rock permeability of 10^{-22} m^2 was used, effectively suppressing any matrix flow. The calculated effective permeability values for the two groups are shown in Tables 8-6 and 8-7. Highlighted rows represent the runs with above background effective permeability values. The effective permeability values calculated for the two groups showed that only two realizations from the first group and four realizations from the second group had effective permeability values above matrix permeability. This indicates that without the manipulation of each realization to create fracture connectivity and use of more realistic matrix permeability, the chances of fracture connectivity are low (12%). The analysis also indicates that the sample size of 25 generated different counts of above background effective permeability values. More realizations might be required to be statistically representative (stable).

Transport results for some of the realizations with effective permeability above matrix permeability are shown in Figures 8-33 to 8-35. Two sets of transport simulations were carried out: with the use of default diffusion coefficient of 10^{-9} m^2/s and without the use of diffusion coefficient. Figure 8-33 shows breakthrough curves for the realizations with above matrix effective permeability, with and without

diffusion. The figure also includes mean breakthrough curve for the FCM modified case. The breakthrough curves with diffusion represent advection in fractures and diffusion in the matrix rock. The curves with no diffusion represent advection in fractures. Run103 (Table 8-6) which has effective permeability of the order of the modified FCM runs has breakthrough curve very close to the mean of the modified FCM case. Thus, when matrix diffusion is not suppressed the breakthrough curves represent both advection and matrix diffusion. Note that using original fracture parameter distributions shifts the breakthrough to later times.

Figures 8-34 and 8-35 show distributions of tracer for Run 103 at different times, for the case with diffusion included. The figures show that at early times tracer transport is mainly through advection in fractures. Results at later times show pronounced matrix diffusion, in line with the breakthrough curves on Figure 8-33.

Table 8-6. Effective Permeability Values for 25 Realizations of Fracture Network Generated with the Original Parameter Distributions.

Run for Modified FCM	DFN effective permeability
70	3.33E-22
71	5.83E-22
72	3.01E-22
73	5.10E-22
74	2.51E-22
75	2.28E-22
76	3.20E-22
77	2.81E-22
78	6.82E-22
79	4.51E-22
80	2.37E-22
81	2.51E-22
82	5.87E-22
83	4.56E-22
84	5.04E-22
85	4.33E-22
86	**4.54E-19**
87	2.50E-22
88	3.99E-22
89	3.07E-22
90	3.26E-22
91	3.27E-22
92	**4.72E-19**
93	3.96E-22
94	3.38E-22

Table 8-7. Effective Permeability Values for the Additional 25 Realizations of Fracture Network Generated with the Original Parameter Distributions.

Run for Modified FCM	DFN effective permeability
95	7.13E-22
96	3.25E-22
97	1.79E-22
98	**1.36E-19**
99	2.47E-22
100	2.97E-22
101	2.48E-22
102	4.33E-22
103	**1.39E-17**
104	2.63E-22
105	3.03E-22
106	4.17E-22
107	5.32E-22
108	2.69E-22
109	4.16E-22
110	5.70E-22
111	2.27E-22
112	3.17E-22
113	3.85E-22
114	3.20E-22
115	**7.72E-19**
116	4.26E-22
117	**1.09E-18**
118	2.42E-22
119	2.79E-22

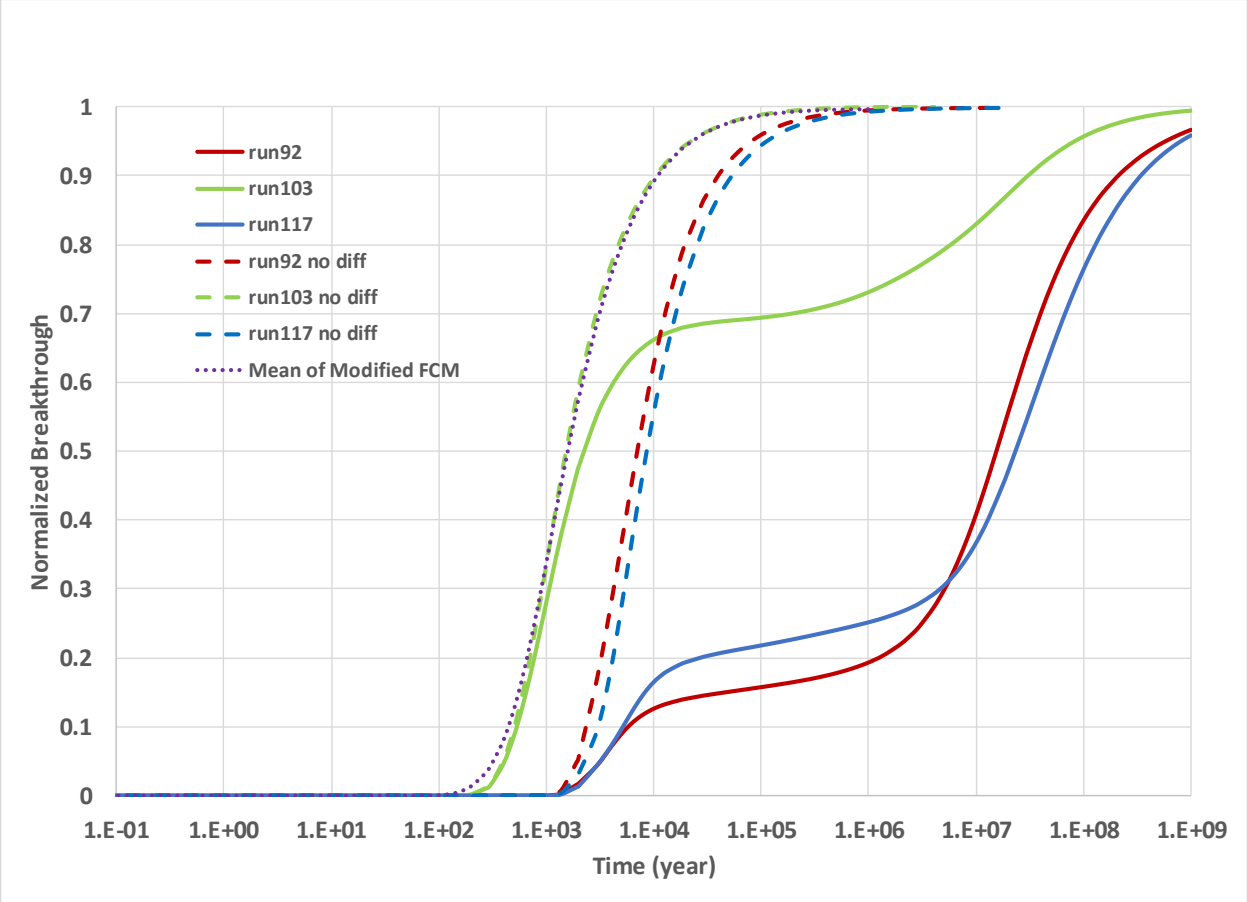

Figure 8-33. FCM (PFLOTRAN) Breakthrough Curves for Fracture Network Generated with the Original Fracture Parameter Distributions.

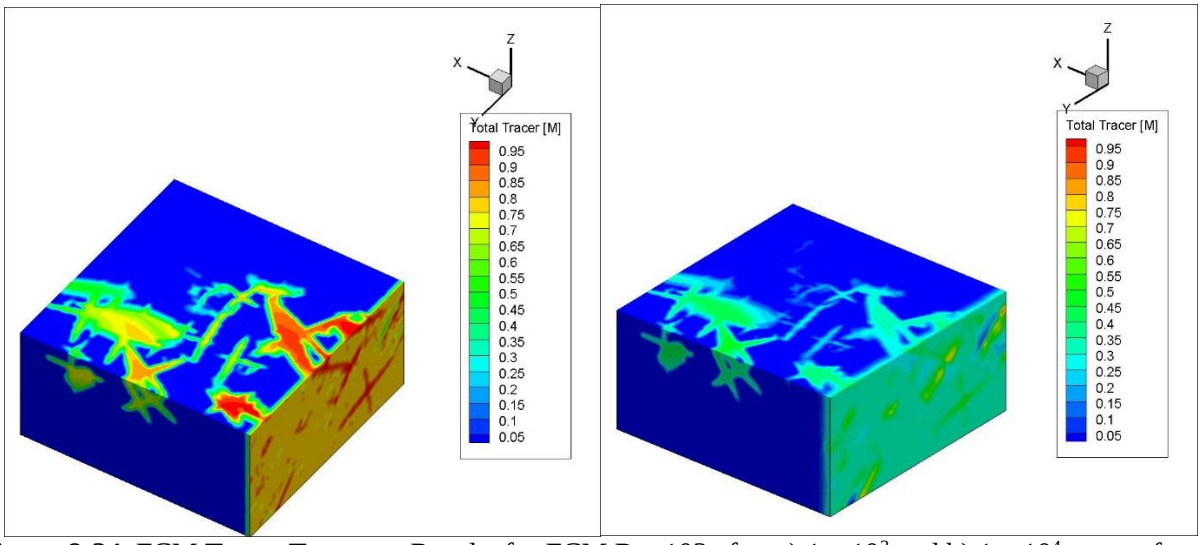

Figure 8-34. FCM Tracer Transport Results for FCM Run103 after a) 1 x 10^3 and b) 1 x 10^4 years of simulation times (Fracture Network Generated with the Original Fracture Parameter Distributions).

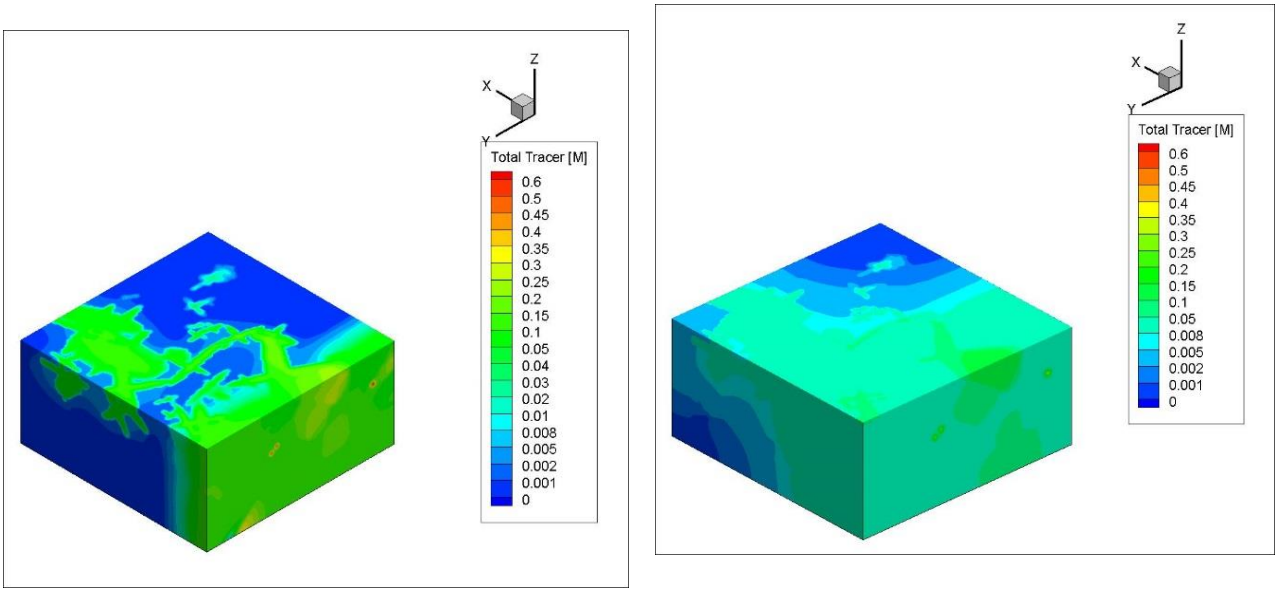

Figure 8-35. FCM Tracer Transport Results for FCM Run103 after a) 1 x 10^5 and b) 1 x 10^6 years of simulation times ((Fracture Network Generated with the Original Fracture Parameter Distributions).

8.4 CONCLUSIONS AND RECOMMENDATIONS FOR FUTURE WORK

Both the DFN and FCM fracture models can be used to characterize fractures in crystalline rock. DFN is based on flow and transport in fractures only. FCM is based on both matrix and fracture flow and transport. Comparison of the two models required significant upgrades in the FCM codes. As part of the comparison the FCM codes were modified to include two fracture generating methods that are close to the DFN model. The first method uses representation of fractures with ellipses to generate fracture network. The second method uses the fracture network generated by DFN. For the second case the properties of the DFN fracture network are converted into the FCM inputs (fracture aperture, spacing, dip, and strike), which are then used to calculate the effective permeability and porosity of the FCM grid blocks. DFN and FCM comparison was made on a domain size of 1 km^3 and common fracture data. The property of the fracture data used for the comparison study are loosely based on the property of the SKB site in Sweden. Use of the common fracture data for the DFN model are described in Section 8.1. For the FCM method the fracture data were used in various ways, described in Sections 8.2 and 8.3. Comparisons of effective permeability and breakthrough curves from the two fracture methods are described in Section 8.3. Results of the two fracture models are close when the FCM methods with modified fracture parameters are used. Results are largely different when the FCM method with original fracture parameters is used with matrix diffusion included. It is shown that the rock matrix could play a role in advection as well as in diffusion when it is assigned low permeability values but higher than the value of 10^{-22} m^2 used in this report. The validity of that can be tested using simulations with the use of measured field data. Recommendations for future work are further testing of the fracture models using field data, and analysis of numerical dispersion.

8.5 REFERENCES

Adler (2012) Adler, P. M., Thovert, J. F. and V. V. Mourzenko (2012), Fractured porous media. Oxford University Press.

Botros FE., Hassan AE, Reeves DM, and Pohll G (2008) On mapping fracture networks onto continuum. Water Resour. Res., vol 44, W08435.

Chen M, Bai M, Roegiers J-C (1999) Permeability tensors of anisotropic fracture networks. Mathematical Geology, 31, 4.

Deutsch CV and Journel AG (1998) GSLIB Geostatistical software library and user's guide. 2nd ed. Oxford Univ. Press, New York.

G. E. Hammond, P.C. Lichtner and R.T. Mills, "Evaluating the Performance of Parallel Subsurface Simulators: An Illustrative Example with PFLOTRAN", *Water Resources Research*, 50, doi:10.1002/2012WR013483 (2014).

LaGriT (2013) *Los Alamos Grid Toolbox, (LaGriT)*, http://lagrit.lanl.gov, Los Alamos National Laboratory.

Hammond, G.E., P.C. Lichtner and R.T. Mills, 2014. Evaluating the Performance of Parallel Subsurface Simulators: An Illustrative Example with PFLOTRAN, *Water Resources Research*, 50, doi:10.1002/2012WR013483.

Hyman J. D., Gable C. W., Painter S. L., and Makedonska N. (2014) Conforming Delaunay triangulation of stochastically generated three dimensional discrete fracture networks: A feature rejection algorithm for meshing strategy, *SIAM Journal of Scientific Computing*, 36(4), A1871–A1894.

McKenna SA and Reeves PC (2005) Fractured continuum approach to stochastic permeability modeling in Coburn TC, Yarus JM, Chambers RL, eds. Stochastic Modeling and Geostatistics: Principles, Methods, and Case Studies, II, 1–14

Reeves DM, Benson DA, and Meerschaert MM (2008) Transport of conservative solutes in simulated fracture networks: 1. Synthetic data generation, Water Resour. Res., vol 44, W05404.

SKB (2011) *Long-term safety for the final repository for spent nuclear fuel at Forsmark. main report of the SR-site project*, Technical Report SKB TR-11-01, Swedish Nuclear Fuel and Waste Management Co., Stockholm, Sweden.

Snow DT (1968) Rock fracture spacings, openings, and porosities. Journal of the Soil Mechanics and Foundations Division, Proceedings of American Society of Civil Engineers, 94, 73-91.

Snow DT (1969) Anisotropic permeability of fractured media. Water Resources Research, 5, 1273–1289.

Trimmer, D., B. Bonner, H. C. Heard, and A. Duba. (1980) Effect of pressure and stress on water transport in intact and fractured gabbro and granite. *Journal of Geophysical Research: Solid Earth*, 85, 7059-7071.

Y. Wang, T. Hadgu, E. Matteo, J. N. Kruichak, M. M. Mills, R. Tinnacher, J. Davis, H. Viswanathan, S. Chu, T. Dittrich, F. Hyman, S. Karra, N. Makedonska, P. Reimus, M. Zavarin, P. Zhao, C. Joseph, J. Begg, Z. Dai, A. B. Kersting, J. Jerden, J. M. Copple, T. Cruse, and W. Ebert, 2015: *Used Fuel Disposal in Crystalline Rocks: FY15 Progress Report*, FCRD-UFD-2015-000125. U.S. Department of Energy, Used Fuel Disposition R&D Campaign.

9. SUMMARY

Significant progress has been made in FY16 in both experimental and modeling arenas in evaluation of used fuel disposal in crystalline rocks. The work covers a wide range of research topics identified in the R&D plan. The major accomplishments are summarized below:

- *Development of Fuel Matrix Degradation Model (FMDM):* We have formulated, coded and tested an electrochemical steel corrosion module that couples in-package steel corrosion with fuel degradation through the common solution. This module provides the kinetic source of H_2 that may control the used fuel dissolution rates under repository relevant conditions. We have updated and optimized FMDM to improve the efficiency of integration with the GDSA PA model. We have also performed scoping electrochemical tests to build confidence in modeling the H_2 effect mechanism, which has been shown by both experiment and electrochemical modeling to significantly impact source term calculations when in-package steel components are corroding simultaneously with used fuel. It has been shown that the corrosion of steel canister materials will have a significant impact on the radionuclide source terms calculated by PA because of its role as the major source of the H_2, which attenuates the fuel degradation rate. The test runs with the updated FMDM indicate that the peak radionuclide source term from a breached waste package will likely be attenuated by the H_2 effect and the corrosion of steel components (the dominant source of H_2 in the system). In addition, we have shown a potential effect of ferrous iron from waste package corrosion on hydrogen peroxide generation.
- *Uranium Interaction with Engineered Materials:* We developed a new surface complexation model (SCM) that specifically accounts for the 'spillover' of the electrostatic surface potential of basal cation exchange sites on the surface potential of neighboring edge sites. This model allows us to simulate U(VI) adsorption onto Na-montmorillonite over a wide range of chemical solution conditions with a lower number of fitting parameters than previous SCM concepts, and without including a second site type or the formation of ternary U(VI)-carbonato surface complexes. This SCM allows us to simulate U(VI) sorption onto montmorillonite as a function of chemical solution conditions, while minimizing the number of fitting parameters in subsequent uranium(VI) diffusion models. Modeling results suggest that an accurate description of the unique characteristics of electrostatic surface potentials on montmorillonite edge sites is highly important, in order to accurately predict U(VI) sorption and transport behavior at larger field scales. Similar modeling approaches may also be useful for other charge-unbalanced, layered mineral phases. Our modeling results further emphasize the strong influence of dissolved carbonate ligands on U(VI) sorption, which is driven by the competition between U(VI)-carbonate complexation reactions in solution and U(VI) surface complexation reactions on montmorillonite edge sites.
- *Colloid-Facilitated Radionuclide Transport:* A comprehensive literature review and data synthesis has been conducted on colloid-facilitated radionuclide transport (CFRT), and a scheme for the implementation of the CFRT model in performance assessment has been proposed (the results are reported in a separated report). A comprehensive model interpretation has been performed for the Grimsel Test Site (GTS) CFRT tests, yielding valuable insights for modeling of radionuclide transport, and particularly of CFRT, in saturated fractured crystalline rocks. It is shown that the actinides Th, Pu and Am, and the fission product ^{137}Cs, are the most likely radionuclides to experience colloid-facilitated transport over long time and distance scales (at least for bentonite colloids in a fractured crystalline setting). However, the time and distance scales of the GTS tests were very short relative to time and distance scales of relevance for nuclear waste repository performance assessments, so it should not necessarily be concluded that colloid-facilitated transport of these radionuclides will be a concern in such performance assessments. The GTS results collectively suggest that CFRT is likely to be more efficient at lower radionuclide concentrations than at higher concentrations because a greater fraction of the

radionuclide mass will then tend to become associated with strong, low abundance adsorption sites on the colloids.

- D*evelopment and demonstration of Discrete Fracture Network (DFN) model:* We have evaluated the correlation between fracture size and fracture transmissivity. We have characterized how different fracture size-transmissivity relationships influence flow and transport simulations through sparse three- dimensional discrete fracture networks, based on Forsmark fracture characteristics provided by SKB. We observe that adopting a correlation between a fracture size and its transmissivity leads to earlier breakthrough times and higher effective permeability when compared to networks where no correlation is used. While fracture network geometry plays the principal role in determining where transport occurs within the network, the relationship between size and transmissivity controls the flow speed. These observations indicate DFN modelers should be aware that breakthrough times and effective permeabilities can be strongly influenced by such a relationship in addition to fracture and network statistics. We have developed an analysis and visualization tool for the characterization of flow in constrained networks using the concept of a flow topology graph (FTG). Our method allows users to understand and evaluate flow and transport in DFN simulations by computing statistical distributions, segment paths of interest, and cluster particles based on their paths. The new approach enables to evaluate the accuracy of the simulations, visualize features of interest, and compare multiple realizations over a specific domain of interest. It allows to simulate complex transport phenomena modeling large sites for networks consisting of several thousand fractures without compromising the geometry of the network.
- *Comparison of Fracture Continuum Model (FCM) with DFN model:* Both the DFN and FCM fracture models can be used to characterize fractures in crystalline rock. DFN is based on flow and transport in fractures only. FCM is based on both matrix and fracture flow and transport. Comparison of the two models required significant upgrades in the FCM codes. As part of the comparison the FCM codes were modified to include two fracture generating methods that are close to the DFN model. The first method uses representation of fractures with ellipses to generate fracture network. The second method uses the fracture network generated by DFN. For the second case the properties of the DFN fracture network are converted into the FCM inputs (fracture aperture, spacing, dip, and strike), which are then used to calculate the effective permeability and porosity of the FCM grid blocks. DFN and FCM comparison was made on a domain size of 1 km^3 and common fracture data. The property of the fracture data used for the comparison study are loosely based on the property of the SKB site in Sweden. Results of the two fracture models are similar when the FCM methods with modified fracture parameters are used. Results are largely different when the FCM method with original fracture parameters is used with matrix diffusion included. It is shown that the rock matrix can play a role in advection as well as in diffusion when it is assigned low permeability values but higher than the value of 10^{-22} m^2 used in this report. The validity of that can be tested using simulations with the use of measured field data. Recommendations for future work are further testing of the fracture models using field data and analysis of numerical dispersion. Two groups of 25 realizations were generated to check statistical stability of the sample size of fracture networks. The effective permeability values calculated for the two groups show that only two realizations from the first group and four realizations from the second group had effective permeability values above matrix permeability. This indicates that without the manipulation of each realization to create fracture connectivity and use of more realistic matrix permeability, the chance of fracture connectivity is low (12%) and therefore the sample size of 25 may not be large enough to generate meaningful statistics for fracture networks. It is anticipated that a relatively large number of realizations might be required for a performance assessment of a crystalline rock geologic repository.

Based on the work accomplished in FY16 and the prior years, the future work is recommended to:

- Continue to focus on two key topics related to deep geologic disposal of spent fuel in crystalline rocks: better characterization and understanding of fractured media and fluid flow and transport in such media, and designing effective engineered barrier systems (EBS) for waste isolation. Specific attention will be given to the development of next-generation buffer materials for waste isolation and to a mechanistic understanding of alteration products (e.g. iron oxides) of EBS components as secondary waste forms for radionuclide retention.
- Help the generic disposal system analysis (GDSA) team to develop a total system performance assessment model and provide the parameter feeds to the model. One goal of this effort is to have a PA model matured enough over next two years to be able to simulate a typical thermal-hydrologic-chemical evolution history of a repository in a crystalline medium. Once such as a model becomes available, various disposal concepts will be explored.
- Continue to synthesize technical results obtained in FY17 and prior years in a few selected areas to demonstrate tangible progress in the research. The focus areas will include thermal limits of bentonite and smectite illitization and modeling approaches of fluid flow and transport in fractured geologic media.
- The modeling work will move towards model demonstrations and applications using actual field data. For the process model development, an emphasis will be placed on the integration with total system model development.
- Fully leverage international collaborations, especially with Sweden Underground Research Lab and DECOVALEX.
- Closely collaborate and integrate with other work packages, especially those on disposal in argillite, deep borehole disposal, and DOE-managed high-level waste (HLW) and spent nuclear fuel (SNF) Research.